INFLUENCE OF YTTRIUM ADDITION ON TEXTURE AND DEFORMATION BEHAVIOR IN AN EXTRUDED ZM31 ALLOY

By

Nabila Tahreen

Bachelor of Science in Industrial and Production Engineering

Bangladesh University of Engineering and Technology, 2009

Master of Science in Industrial and Production Engineering

Bangladesh University of Engineering and Technology, 2011

A dissertation

presented to Ryerson University

in partial fulfillment of the

requirements for the degree of

Doctor of Philosophy

in the Program of

Mechanical and Industrial Engineering

Toronto, Ontario, Canada, 2016

AUTHOR'S DECLARATION

I hereby declare that I am the sole author of this dissertation. This is a true copy of the dissertation, including any required final revisions, as accepted by my examiners.

I authorize Ryerson University to lend this dissertation to other institutions or individuals for the purpose of scholarly research.

I further authorize Ryerson University to reproduce this dissertation by photocopying or by other means, in total or in part, at the request of other institutions or individuals for the purpose of scholarly research.

I understand that my dissertation may be made electronically available to the public.

Influence of Yttrium Addition on Texture and Deformation Behavior in an Extruded ZM31 Alloy

Nabila Tahreen

Doctor of Philosophy, 2016

Mechanical and Industrial Engineering

Ryerson University

ABSTRACT

The current "storm" of lightweighting, a revolution in materials, processes, and business models, which is brewing on the horizon of the auto industry, inspires researchers and engineers to develop and apply new wrought magnesium alloys with improved properties. For wider applications in the automotive and aerospace industries, the enhancement of strength, thermal stability and formability of magnesium alloys is required. In recent years, Mg-Zn-Y series alloys have received a considerable attention from the research community due to their improved mechanical properties. The present study was aimed at evaluating the influence of Y addition to Mg-Zn-Mn system based on phase formation, mechanical response and texture development with special attention paid to recrystallization, hot characterization and relative activity.

The dissertation evaluated the strain hardening and deformation behavior of as-extruded Mg-Zn-Mn (ZM31) magnesium alloy with varying Y contents via compression testing at room temperature, 200°C and 300°C. Alloy ZM31+0.3Y consisted I-phase (Mg_3YZn_6); alloy

ZM31+3.2Y contained I-phase and W-phase ($Mg_3Y_2Zn_3$); alloy ZM31+6Y had long-period stacking-ordered (LPSO) X-phase ($Mg_{12}YZn$) and $Mg_{24}Y_5$ particles. With increasing Y content the basal texture became weakened significantly. While alloys ZM31+0.3Y and ZM31+3.2Y exhibited a skewed true stress-true stain curve with a three-stage strain hardening feature caused by the occurrence of $\{10\bar{1}2\}$ extension twinning, the true stress-true strain curve of alloy ZM31+6Y was normal due to the dislocation slip during compression.

The evolution of flow stress, texture and microstructure during the compression tests has been studied under various conditions of temperature and strain rates. Optical metallography, EBSD techniques and X-ray diffraction were employed to study the microstructural development and texture evolution. The deformation activation energy was calculated and the processing maps were generated to determine the optimum hot working parameters. In addition, viscoplastic self-consistent model was successfully used to predict the experimental textures.

Lastly, the strengthening mechanisms in each Mg-Zn-Mn-Y material are established quantitatively for the first time to account for grain refinement, thermal mismatch, dislocation density, load bearing, and particle strengthening contributions. The present work laid the foundations for a better understanding the role of Y elements on deformation behavior in magnesium alloys.

ACKNOWLEDGEMENTS

First of all, I am profoundly indebted to my parents Late Quazi Fariduddin and Bilkis Begum, for their unconditional love, dedication and the many years of support that provided the foundation for this work. They are the rock upon which all of my current and future success has been and will be built.

I would like to express my deepest gratitude to my supervisor Professor Dr. Daolun Chen for his unwavering support, collegiality and mentorship throughout this work. It is not often that one finds an advisor who always finds the time for listening to the little problems and roadblocks that unavoidably crop up in the course of performing research. The completion of this project would not have been possible without his continued guidance and support.

I am grateful to my committee members Dr. Ahmad Ghasempoor, Dr. Vincent Chan and Dr. Don Oguamanam for their precious time in evaluating and subsequently raising several valuable points during the course of this work. Their constructive criticism has greatly helped me to improve the quality of this thesis.

I extend my sincere word of thanks to Dr. Sarah Thompson and Dr. Joanna Barlas, who have been there as loving mentors, through a very difficult period of my life. I would never be able to pay back the love and affection showered upon me by them.

My acknowledgement will never be complete without the special mention of my fellow labmates, who have taught me the lab culture and have lived by example to make me understand the hard facts of life. I would like to acknowledge A. Machin, Q. Li, J. Amankrah, C. Ma, G. He, and R. Churaman for all their personal and professional help that they have extended to me throughout.

Last, but not least, I would like to thank my husband, Faysal, and sibling, Samiha, who are my champions and who blessed me with a life of joy in the hours when the lab lights were off.

DEDICATION

To

My Beloved Father

Late Mr. Quazi Fariduddin

TABLE OF CONTENTS

LIST OF TABLES

LIST OF FIGURES

NOMENCLATURE

a, c	Lattice parameter
d	Lattice spacing
$CRSS$	Critical Resolved Shear Stress
σ	Stress
ε	Strain
$\dot{\varepsilon}$	Strain rate
n	Strain hardening exponent
K	Strength coefficient
2θ	Bragg angle
$ASTM$	American Society for Testing Materials
ODF	Orientation Distribution Function
MRD	Multiples of Random Distributions
$\varphi_1\ \Phi\ \varphi_2$	Euler angles
SF	Schmid Factor
UCS	Ultimate Compressive Strength
YS	Yield stress
H_c	Hardening capacity
$d\sigma/d\varepsilon$	Strain hardening rate
ED	Extrusion Direction
RD	Radial Direction
RE	Rare Earth

RT	Room Temperature
SEM	Scanning Electron Microscopy
EBSD	Electron Backscatter Diffraction
EDS	Energy-Dispersive X-ray Spectroscopy
IPF	Inverse Pole Figure
LPSO	Long Period Stacking Order
VPSC	Viscoplastic self-consistent
Y	Yttrium
Zn	Zinc
Mn	Manganese
Mg	Magnesium
DRX	Dynamic recrystallization
CDRX	Continuous dynamic recrystallization
DDRX	Discontinuous dynamic recrystallization
SRX	Static recrystallization
m	Strain rate sensitivity
Q	Activation energy
T	Temperature
TEM	Transmission Electron Microscopy
XRD	X-ray diffraction

CHAPTER 1

1. INTRODUCTION

1.1 Background

The concept of lightweighting unveils the use of advanced materials to explore weight reduction solution aiming to improve fuel efficiency while reducing climate-changing, costly and human death-causing* CO_2 emissions [1–7]. It is now even referred to as the "storm" of lightweighting - a revolution in materials, processes, and business models, which is brewing on the horizon of the auto industry [8,9]. It has been reported that the fuel efficiency of ground vehicles can be improved by 6~8% for each 10% reduction in weight [10].

As an ultra-lightweight material, magnesium alloys have a promising prospective of applications in the transportation industry, which is the reason why research and development of high performance magnesium alloys is an important objective [11–14]. In order to meet the pressing demand for improved fuel economy and reducing harmful CO_2 emissions, the utilization of lightweight magnesium alloys must be intensified [1,7,15].

*According to Science News entitled "Air pollution kills 7 million people a year" on March 25, 2014 at http://www.sciencemag.org/news/sifter/air-pollution-kills-7-million-people-year: "Air pollution isn't just harming Earth; it's hurting us, too. Startling new numbers released by the World Health Organization today reveal that one in eight deaths are a result of exposure to air pollution. The data reveal a strong link between the tiny particles that we breathe into our lungs and the illnesses they can lead to, including stroke, heart attack, lung cancer, and chronic obstructive pulmonary disease."

1.2 Motivation

There is a persistent struggle to improve various properties of magnesium alloy where one of scenarios being explored is the addition of rare-earth metals [8,16,17]. It has been recognized that alloying with rare earth elements bring beneficial effects in terms of strengthening, formability and creep resistance [18–20]. In recent years, Mg-Zn-Y series alloys have received significant attention from researchers due to their superior mechanical properties and distinctive microstructures [21–23]. The alloy system is largely acknowledged for being rich in ternary intermetallic phases [24,25]. Such alloys have also been pointed out to have potential for use as a high temperature structural material.

There are three types of ternary equilibrium phases reported in Mg-Zn-Y systems alloys known as I-phase (Mg_3YZn_6), W-phase ($Mg_3Y_2Zn_3$) and LPSO-phase ($Mg_{12}ZnY$) [26–28]. A stable I-phase was first reported by Luo *et al*. [29,30] in Mg-Zn-Y alloys with an icosahedral quasicrystal structure. Quasicrystals are a well-defined ordered phase of solid matter with long-range quasiperiodic translational order and an orientational order [31], but no three-dimensional translational periodicity [32]. The discovery of quasicrystals in 1984, by Shechtman *et al.* [33] in a rapidly solidified Al-Mn alloy brought about a paradigm shift in solid-state physics as this type of atomic arrangements was forbidden for conventional crystallography. The astonishing discovery of quasicrystals presented scientists with a new, puzzling class of materials and involved hundreds of researchers in this realm [34]. As is well-known, quasicrystals possess many special mechanical and physical properties such as high strength, high thermal conductivity, low coefficient of friction and low interfacial energy [35–38]. Though they cannot be applied directly as structural materials for their innate brittleness, they can be used as a strengthening second phase

with other materials [34]. On the other hand, W-phase is generally not considered as a very effective strengthening phase [27,39–41]. It has been recognized that the W-phase with face-centered cubic structure shares a weak bonding with Mg matrix [27,42,43]. In addition, W-phase easily cracks during the tensile testing process in the as-cast Mg-Zn-Y-Zr alloys, which degraded the mechanical properties [27].

The latest development of high-strength magnesium alloys involves the role of the strengthening phases with a novel long-period stacking-ordered (LPSO) structure [44]. It is an excellent reinforcement phase which, to date, has been regarded as the greatest strengthening second phase in magnesium alloys. About fifteen years ago, a study revealed that a nanocrystalline $Mg_{97}Zn_1Y_2$ alloy prepared through a non-equilibrium rapid solidification process, demonstrated superior mechanical properties which seemed to be originated from not only a grain refinement but also from the LPSO phase formed in the alloy [45–49]. The phase was found to be chemical-ordered as well as stacking-ordered. Apart from its unique crystal structure, the phase appeared to be immensely beneficial for magnesium alloy.

Due to limited available slip systems, deforming magnesium alloys at room temperature has been challenging [8,17]. At elevated temperatures, the workability of magnesium alloys significantly increases as additional slip systems become activated which brings superior formability to the alloy [50]. However, the elevated temperature inevitably carries some concerns such as high temperature oxidation, energy consumption, grain growth and particle coarsening [51]. It is, therefore, critical to optimize the processing frame to secure the desired post-deformation properties, based on the knowledge of deformation mechanisms and microstructure evolution. It has been widely recognized that the processing map is an effective tool for optimizing hot

working/processing parameters [52–54]. By using the processing maps, the deformation mechanisms in different deformation conditions can be predicted, and proper/safe processing parameters referring to the occurrence of dynamic recrystallization can be determined via the efficiency of power dissipation [53,55].

Despite the unique crystal structure of I, W and LPSO phases in the recently developed Mg-Zn-Y alloy, little is known about the influence of the alloying element Y on the resulting texture, mechanical response and corresponding recrystallization and deformation mechanisms. It is unclear to what extent the Y-element affects the compressive deformation behavior. The systematic study of processing conditions on the formability of extruded Mg-Zn-Mn-Y alloys comprising dissimilar phases is largely unknown. Therefore, the present work constitutes a benchmark for understanding the impact of the addition of Y to extruded Mg-Zn-Mn alloys based on multiscale investigation and analysis. In addition, a theoretical understanding of the strength improvement associated with individual Mg-Zn-Y phase was established, which is likely to provide valuable insight towards further development of the alloys.

1.3 Objectives of the Research

The following studies were conducted and the specific aims of each study are listed below:

Study 1: Effects of Y Addition on Microstructure, Texture and Phase Formation

The effect of Y addition on microstructure, texture and phase formation was investigated with the following objectives:

i. To investigate the alteration of grain size and shape with varying Y content.

ii. To study the morphology and distribution of various second phase particles arising from different amounts of Y alloying.

iii. To distinguish and characterize the second phase particles developed in the alloys.

iv. To ascertain if the Y addition would affect the texture development.

Study 2: Effect of Y Alloying on Deformation Behavior

The effect of Y addition on flow behavior during uniaxial compression was investigated to obtain the following objectives:

i. To investigate the influence of Y on compressive properties both at ambient and elevated temperatures.

ii. To study strain hardening behavior and to predict possible deformation mode at different stages of compressive loading.

iii. To discuss the effect of both temperature and Y on the deformation mode associated with work hardening.

Study 3: Role of Y on Recrystallization

This study was aimed at investigating the effect of Y on the recrystallization of extruded Mg-Zn-Mn alloys. Specially, the study was aimed to do the following:

i. To examine the static recrystallization activities in the presence of both Y solute and Y-containing second phase particles.

ii. To study dynamic recrystallization in conjunction with Y solutes and Y-containing particles during compression at elevated temperature.

Study 4: Role of Y on Relative Deformation Activity

As-extruded Mg-Zn-Mn alloys with varied amount of Y (α-Mg solid solution + intermetallic) were subjected to compression to investigate the evolution of microstructure and texture to obtain the following objectives:

i. To identify the underlying deformation mechanisms due to Y addition at elevated temperatures.
ii. To understand the alteration of operating deformation mode in relation to the texture evolution and mechanical behavior, ViscoPlastic Self-Consistent (VPSC) polycrystal simulations were performed.

Study 5: Influence of Y on Hot Characterization

The hot deformation characteristics of Mg-Zn-Mn magnesium alloy with different addition of Y have been studied via isothermal compression testing. The study intended to do the followings:

i. To study the evolution of activation energy with increasing Y content.
ii. To determine optimum hot working parameters based on processing maps.

Study 6: Strengthening Improvement due to Y Alloying

The study was designed at predicting the yield strength of as-extruded Mg-Zn-Y alloys with varying amounts of Y to achieve the following objective:

i. To establish the strengthening mechanisms in each material quantitatively accounting for grain refinement, thermal mismatch, dislocation, load bearing, and particle strengthening contributions.

CHAPTER 2

2. LITERATURE REVIEW

2.1 Deformation Modes in Magnesium

Magnesium has a hexagonal close-packed (hcp) crystal structure with a c/a ratio of 1.623. Two types of deformation mechanisms, dislocation-slip and twinning, generally take place in magnesium during deformation.

2.1.1 Dislocation-slip

Dislocation slip is the most important and dominant deformation mechanism in metallic materials. In order for a polycrystal to accommodate homogenous deformation, five independent slip systems need to be activated [56,57]. Unlike FCC lattice, magnesium possessing a hcp crystal structure exhibits poor formability at room temperature due to its limited number of active slip systems. The possible independent slip systems in hcp are: (1) basal slip $(0001)\langle 11\bar{2}0\rangle$; (2) prismatic slip $\{10\bar{1}0\}\langle 11\bar{2}0\rangle$, $\{10\bar{1}0\}[0001]$ and $\{11\bar{2}0\}[0001]$; and (3) pyramidal slip $\{10\bar{1}1\}\langle 11\bar{2}0\rangle$ and $\{11\bar{2}2\}\langle 11\bar{2}3\rangle$. These slip systems are shown in Fig. 2.1 and summarized in Table 2.1.

Table 2.1: Possible slip systems in hcp crystal [57]

Burgers vector	Slip plane	Slip direction	Number of slip systems	
			Total	Independent
$\langle a \rangle$	basal (0001)	$\langle 11\bar{2}0 \rangle$	3	2
$\langle a \rangle$	prismatic $\{10\bar{1}0\}$	$\langle 11\bar{2}0 \rangle$	3	2
$\langle c \rangle$	prismatic $\{10\bar{1}0\}$	$\langle 0001 \rangle$	3	2
$\langle c \rangle$	prismatic $\{11\bar{2}0\}$	$\langle 0001 \rangle$	3	2
$\langle a \rangle$	pyramidal $\{10\bar{1}1\}$	$\langle 11\bar{2}0 \rangle$	6	4
$\langle c+a \rangle$	pyramidal $\{11\bar{2}2\}$	$\langle 11\bar{2}3 \rangle$	6	5

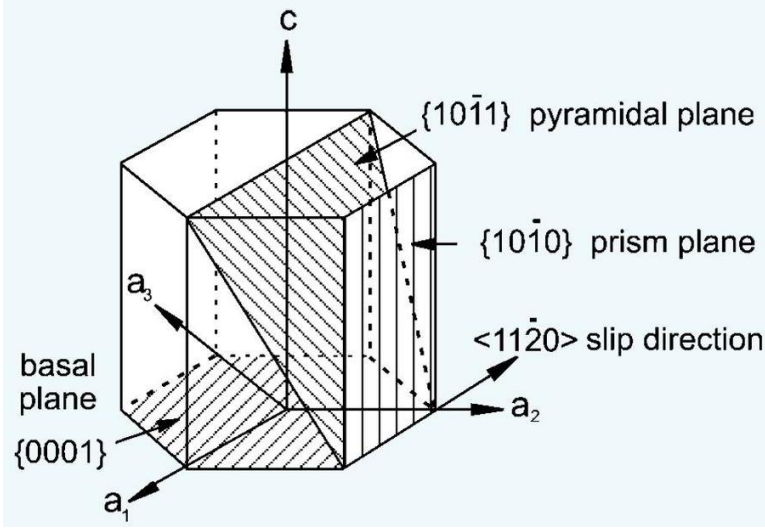

Figure 2.1: Dislocation glide system in hcp alloy [58].

In general, there are several factors affecting deformation modes and the operation of the slip systems in magnesium [57], (1) von Mises criterion, (2) Schmid factors, (3) critical resolved shear stress (CRSS), and (4) temperature dependence of the CRSS.

2.1.2 Twinning

In addition to slip, plastic deformation can occur by the formation of mechanical twins, or *twinning* [59]. Twinning results when a portion of the crystal takes up an orientation that is related to the orientation of the rest of the untwined lattice in a definite, symmetrical way [60]. Then the twinned portion of the crystal would be a mirror image of the parent crystal. The plane of symmetry between the two portions is known as the twinning plane.

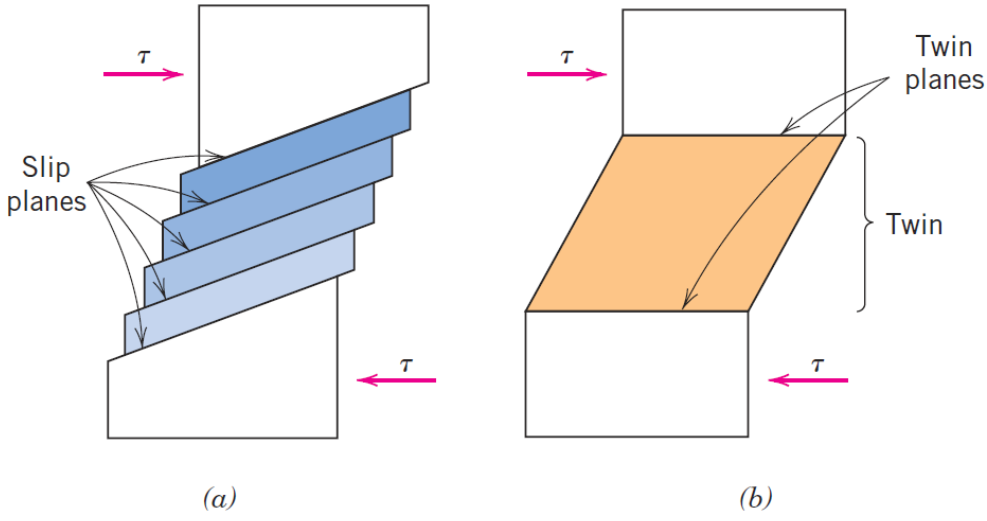

Figure 2.2: For a single crystal subjected to a shear stress τ, (a) deformation by slip; (b) deformation by twinning [59].

Slip and twinning deformation modes are compared in Fig. 2.2(a) and (b) for a single crystal that is subjected to a shear stress τ. These two deformation processes differ from each other in several respects [59]. First, for slip the crystallographic orientation above and below the slip plane is the same before and after the deformation; for twinning there will be a reorientation across the twin

plane. In addition, slip occurs in distinct atomic spacing multiples, whereas the atomic displacements for twinning are less than interatomic separation. The amount of bulk plastic deformation from twinning is normally small relative to that resulting from slip. However, the real importance of twinning lies in the accompanying crystallographic reorientations; twinning may promote new slip systems in orientations that are favorable relative to the stress axis such that the slip process can now take place. Mechanical twinning occurs in magnesium especially at low temperatures and at high rates of loading conditions under which the slip process is restricted; that is, there are few operable slip systems.

2.2 Factors Influencing Deformation Mechanisms

2.2.1 Critical resolved shear stress (CRSS)

The activation of a certain slip or twinning system depends on the critical resolved shear stress (CRSS) on the slip plane and in the slip or twinning direction. The resolved shear stress is orientation-dependent and it is related to external stress by Schmid factor. CRSS is a material property corresponding to the yield strength, and it is related to the chemical composition and deformation conditions (strain rates, deformation temperatures and strain path). The relationship between the resolved shear stress operating on the slip/twinning plane along the slip/twinning direction, the direction of the external applied force, and the specimen dimension is given by the following equation and also is shown in Fig. 2.3:

$$\tau_C = \frac{F}{A}\cos\varphi\cos\lambda = \sigma m, \tag{2.1}$$

where:

- τ_c: resolved shear stress (RSS) on the slip/twinning plane in the shear direction;
- F: externally applied force in the direction of the rod axis;
- A: cross-section area of the rod sample;
- φ: angle between the slip/twinning direction and net force of the external reference system.
- λ: angle between the normal to the slip/twinning plane and the direction of force of the external reference system. The Schmid factor (m) is the product of $cos\varphi$ and $cos\lambda$, with a value ranging from 0 to 0.5.

In hcp metals, the resolved shear stresses of various deformation modes are strongly dependent on the direction of the external applied force, especially with respect to the c-axis of hcp unit cell. When the applied RSS reaches the critical resolved shear stress (CRSS), slip (or twinning) occurs; this is usually called the Schmid law.

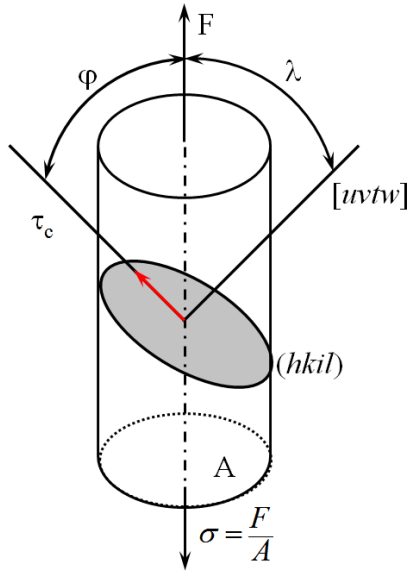

Figure 2.3: Relationship between the resolved shear stress acting on the deformation system and the force applied externally on the single-crystal rod [59].

The slip system with the highest Schmid factor value undergoes the largest resolved shear stress, and therefore will be activated firstly. The ease of deformation in crystalline materials depends on the CRSS applicable to the various slip systems. There is no doubt that the plastic deformation of magnesium will be comprehended firstly by basal slip due to its lowest CRSS value among all the deformation modes. The CRSS for the basal slip in pure magnesium is very low, approximately 0.6-0.7 MPa, which is also nearly independent of temperature. In contrast, the CRSS for the non-basal slip is over 40 MPa at low temperature and drastically decreases to 2-3 MPa with increasing temperature [61].

2.2.2 Temperature

Barnett [62] studied the influence of temperature on the CRSS values of the main deformation modes in magnesium. With increasing temperature, prismatic and pyramidal slip become significant since the CRSS values for these non-basal slip modes decrease rapidly. It is generally known that the CRSS of the various slip and twinning systems vary at room temperature according to the following sequence: $CRSS_{basal} < CRSS_{twinning} < CRSS_{prismatic} < CRSS_{pyramidal}$ [62–66]. Pyramidal $\langle c+a \rangle$ slip is difficult to activate at low temperatures because of its high CRSS and easy dissociation into sessile dislocations to suppress continuous slip [67]. At elevated temperatures, the activation of pyramidal $\langle c+a \rangle$ slip and other non-basal slip occurs due to a lower CRSS. Through these additional systems, cross-slip from basal planes to non-basal planes becomes possible and thus barriers can be overcome. This explains the decreased strength of Mg and its improved formability at elevated temperatures [68]. A number of research work has been devoted to investigate the factors encouraging non-basal slip systems. Reed-Hill and Robertson

[69] investigated non-basal slip in Mg single crystals by tensile testing under conditions of null Schmid factor and no resolved shear stress on the basal planes at temperatures ranging from -190 to 286°C. The decreased yield stress and enhanced ductility of Mg crystal with increasing temperature were attributed to double prismatic slip and/or pyramidal slip at elevated temperatures with a lower CRSS [69]. Kelley and Hosford [70] performed plane strain compression tests on Mg single crystal with different orientations carefully chosen to activate different deformation modes including basal, prismatic and pyramidal slip and $\{10\bar{1}2\}$ twinning. Obara *et al*. [67] verified that the second order pyramidal $<c + a>$ slip in crystals compressed along the *c*-axis gives direct evidence that slip systems other than basal slip can be activated under specific loading orientations and that CRSS for the high order systems is largely dependent on temperature.

2.2.3 Strain hardening

Deformation of metals occurs primarily by the motion of existing dislocations and by the generation of new dislocations [71]. The dislocation density increases when dislocation generation and multiplication occur faster than dislocation annihilation. During deformation, dislocation tangles are formed, which decrease the mean slip distance and result in an increased strength. Therefore, interactions of dislocations cause further deformation to become more difficult thus strengthening the metal through strain hardening. The addition of alloying elements can have a dramatic effect of strain hardening behavior of a material through several possible mechanisms, (i) precipitation during deformation; (ii) increasing the rate of dislocation multiplication, and (iii) reducing the rate of recovery. The strain hardening exponent is a measure of the strain hardening capability of a metal: the larger its magnitude, the greater the strain hardening for a given amount

of plastic strain [59]. The strain hardening exponent reflects the strain hardening behavior of materials more directly than other parameters, such as flow stress and ultimate strength [72]. Hollomon proposed an empirical equation to evaluate the strain hardening exponent in the form of [73],

$$\sigma = K\varepsilon^{n}, \tag{2.2}$$

where n is the strain hardening exponent and K is the strength coefficient. Afrin *et al.* [74] proposed the following equation by only accounting for the net flow stress and net plastic strain of a material after the onset of yielding,

$$\sigma = \sigma_y + K^{*}(\varepsilon - \varepsilon_y)^{n^{*}}, \tag{2.3}$$

where n^*, σ, ε, σ_y and ε_y are the strain hardening exponent, true stress, true strain, yield strength and yield strain of a material, respectively. K^* is the strength coefficient which represents the increment in strength due to strain hardening corresponding to $(\varepsilon - \varepsilon_y) = 1$. Furthermore, the hardening capacity of a material, H_c, has been defined as a normalized parameter [74],

$$H_c = \frac{\sigma_{UTS} - \sigma_y}{\sigma_y} = \frac{\sigma_{UTS}}{\sigma_y} - 1, \tag{2.4}$$

where σ_y is the yield strength, and σ_{UTS} is the ultimate tensile strength of a material.

2.2.4 Initial texture

When a material undergoes a severe amount of deformation during manufacturing processes [75–78] such as rolling, extrusion, forging, wire drawing, etc., it will develop a preferred orientation, also called texture, in which certain crystallographic planes tend to orient themselves in a preferred

manner with respect to the direction of maximum strain [60]. The preferred orientation resulting from plastic deformation is strongly dependent on the slip and twinning systems available for deformation, but it is not generally affected by such processing variables as die angle, roll diameter, roll speed, and reduction per pass. The most important mechanical variables are the geometry of the material flow and the amount of deformation. Thus the same deformation texture is produced whether a rod is made by rolling or drawing.

2.3 Texture Modelling

The viscoplastic self-consistent (VPSC) model [79–83] can be utilized to simulate the experimentally obtained deformation textures. The model helps to understand the contribution of twinning and slip modes to the texture development at different temperatures in respect of the loading direction. In brief, the viscoplastic formulation of the model describes each grain as a viscoplastic ellipsoidal inclusion embedded in a Homogeneous Effective Medium (HEM) that represents the averaged properties of all other grains. Being self-consistent, the model is able to take into account the inherent anisotropy during polycrystal deformation, which makes it advantageous for polycrystal plasticity simulation of low-symmetry crystal structures, such as HCP metals. Additionally, the implementation of different hardening schemes allows accurate prediction of the deformation behavior of hard and soft slip systems, such that the latter can accommodate larger deformation strains during the simulation. This is particularly useful when investigating the influence of alloying elements and temperature on the relative activities of different deformation modes during plastic deformation. A modified Voce empirical hardening scheme was employed for each individual deformation mode in individual grains. The Voce hardening equation is characterized by the evolution of threshold stress with accumulated shear

strain in each grain. Reorientation of grains by twinning was done by the predominant twin reorientation (PTR) scheme [80] defined implicitly in the model.

2.4 Theory of Hot Deformation

Workability is usually used to refer to the shaping of materials by such bulk deformation processes as forging, extrusion, and rolling [84]. The characterization of mechanical properties of a material involves measuring two different types of mechanical property: strength (such as yield strength and peak strength) and ductility (such as percentage elongation). Similarly, the evaluation of workability involves both the measurement of the resistance to deformation (strength) and determination of the extent of possible plastic deformation before failure (ductility). Therefore, a complete description of the workability of a material is specified by its flow stress dependence on processing variables (strain, strain rate, and temperature), its failure behavior, and the metallurgical transformation that describe the alloy system to which it belongs. Flow stress data are essential in the development of constitutive equations and processing maps. The compression test is usually considered as a standard workability test, because the stress system is close to those found in bulk deformation processes [85]. One of the requirements for process modelling is a knowledge of the material flow behavior for defining the deformation maps that delineate 'safe' and 'non-safe' hot working conditions. These maps show in the processing space (axes of temperature T and strain rate $\dot{\varepsilon}$) the processing conditions for stable and unstable deformation. The instability theory to define the regions of unstable flow during hot deformation was established on the basis of microstructural observations for identification of flow instabilities (such as adiabatic shear banding, intercrystalline cracking, prior particle boundary cracking in powder compacts, wedge cracking). A new approach for describing the material behavior under

processing conditions developed by Prasad *et al.* [86] and recently reviewed by Gegel *et al.* [87] is summarized in this section. The approach, called Dynamic Material Modeling (DMM), combines the use of constitutive equations with an understanding of how the applied power is instantaneously dissipated through the workpiece during plastic deformation. According to this model, the workpiece basically dissipates power during hot deformation and the constitutive response of the material at a given temperature depends essentially on the strain rate and to a lesser extent on the strain. The total power *P* (per unit volume) absorbed by the workpiece during plastic flow may be expressed as a sum of two complementary functions [88,89],

$$P = G + J = \int_0^{\dot{\varepsilon}} \sigma d\dot{\varepsilon} + \int_0^{\sigma} \dot{\varepsilon} d\sigma \,, \tag{2.5}$$

where the term *G* represents the power dissipated by plastic deformation, most of which is converted into heat, and the other term *J* represents the dissipation through microstructure evolution such as dynamic recovery, dynamic recrystallization, superplastic flow, phase transformation as well as crack propagation. At any given temperature and strain, the partitioning of power between *J* and *G* is given by,

$$\left(\frac{\partial J}{\partial G}\right)_{T,\dot{\varepsilon}} = \left(\frac{\partial \ln \sigma}{\partial \ln \dot{\varepsilon}}\right)_{T,\dot{\varepsilon}} = m \,, \tag{2.6}$$

where *m* is the strain rate sensitivity of the material which varies with temperature and strain rate. The value of *J* may be normalized with respect to J_{max} to obtain a dimensionless parameter called the efficiency of power dissipation defined as,

$$\eta = \frac{J}{J_{\max}} = \frac{2m}{m+1} \,. \tag{2.7}$$

The variation of η with temperature and strain rate reflects the characteristics of power dissipation occurring through microstructural changes in the work piece, which constitutes a power dissipation map. The map is presented as a contour plot of efficiency variation in the temperature-strain rate field where different domains represent different deformation mechanisms. A continuum instability criterion developed on the basis of extremum principles of irreversible thermodynamics, which is given by [90],

$$\xi(\dot{\varepsilon}) = \frac{\partial \ln(m/m+1)}{\partial \ln \dot{\varepsilon}} + m < 0 . \tag{2.8}$$

It is used to mark out the regions of flow instability. The instability parameter $\xi(\dot{\varepsilon})$ is evaluated as a function of temperature and strain rate and is plotted to obtain an instability map where ξ is negative. It is superimposed onto the power dissipation map to construct a processing map.

2.5 Recrystallization in Magnesium

2.5.1 Dynamic recrystallization (DRX)

It is known that the processing of magnesium alloys at elevated temperatures is predominantly accompanied by recovery and dynamic recrystallization (DRX) [91]. According to the nature of the process, two types of DRX could be distinguished: discontinuous DRX (DDRX) and continuous DRX (CDRX) [92]. DDRX is a classic nucleation and growth process driven by the stored strain energy, whereas CDRX is a process characterized by the formation of subgrain boundaries and their progressive rotation to become high-angle boundaries [93,94]. One of the groundbreaking pieces of work on recrystallization in Mg alloys was by Ion *et al*. [95] on Mg-

0.8%Al during deformation at elevated temperatures (above 423K). Since then, there has been considerable amount of work on dynamic recrystallization (DRX) in magnesium alloys [93,96–99].

Stanford *et al.* [100] processed a series of binary magnesium-based alloys with Gd concentrations between 0.22 and 4.65 wt.% Gd by hot rolling in order to examine the recrystallization behavior. The addition of small amounts of Gd was found to significantly decrease the recrystallized grain size and at higher alloy concentrations nucleation of recrystallization became more strongly inhibited, but the growth rate remained largely unchanged. The effect of Gd concentration on solute strengthening was quantified, and it was found that strengthening of the prismatic slip system above 100 MPa could be achieved through alloying with Gd. A fivefold increase in ductility also resulted from Gd addition, and this was attributed to changes in the recrystallization texture.

2.5.2 Static recrystallization (SRX)

Static recrystallization could potentially be a powerful tool in improving the formability of magnesium alloys by altering their texture for at least two important reasons. First, as recrystallization needs nucleation sites in the deformed structures, deformation twins could offer the possible sites to form recrystallized grains with a modified size and diverse orientations [101]. It would be of particular interest to study the recrystallization activities in the presence of both deformation twins and RE-containing second phase particles. Second, it has been observed that magnesium alloys exhibit extremely high strain hardening rates for orientations where the *c*-axis is perpendicular during compression [102,103]. As recrystallization requires a minimum amount

of stored energy [101], the high strain hardening rates should provide the necessary driving force to initiate recrystallization at low strains, and result in a larger processing window to explore the effects of static recrystallization. In the commercial production of wrought magnesium alloys, dynamic recrystallization phenomena during various forming processes have been studied comprehensively [104–106]. The study concerning the static recrystallization of cold deformed magnesium alloys was rather limited.

Sarker *et al.* [107] evaluated the recrystallization kinetics of a pre-compressed and annealed AM30 magnesium alloy based on the microstructure and texture change. After annealing the twins in the pre-compressed samples were observed to disappear which was reflected by a weakened texture. The recrystallized grains initiating from the grain boundaries exhibited different orientations which caused the pre-existing strong texture to split and weaken.

Levinson *et al.* [108] reported the microstructure evolution of an AZ31 magnesium alloy during isothermal static annealing to evaluate the contribution of extension and contraction twins to the recrystallized microstructure. Their results showed that contraction and double twins were potent sites for recrystallization nuclei, as they exerted a strong influence on the recrystallized texture but no significant impact on the final annealed texture was observed.

Yang *et al.* [109] investigated the effect of prior strain on the static recrystallization of a hot-deformed AZ31 magnesium alloy. Ultrafine grains appeared to evolve due to continuous dynamic recrystallization during hot deformation and grain coarsening accompanied with static recovery i.e., continuous static recrystallization took place during subsequent annealing, while the deformation texture hardly changed even after longer times.

Li *et al*. [110] has determined the macrotextures and microstructures of a hot extruded AZ31 magnesium plate during static recrystallization using the EBSD technique. At favorable orientations, both extension and contraction twins were formed by rolling and a comparison was made between their recrystallization characteristics. The results again showed that contraction twins are more effective as nucleation sites than extension twins, and the orientation characteristics in local regions during nucleation are similar to those of sub-grains within contraction twins or shear bands. During annealing the growth of grains are easier in wider twins, and resulted in the weakening of deformation texture.

2.6 Improvement of Magnesium Alloys by Alloying with Rare Earth Elements

In recent years, magnesium alloys with rare earth (RE) elements have been widely investigated which led to numerous publications in this field [17,111–117]. By now many findings are reported for the improved properties of this class of alloys including grain refinement, better formability at low temperatures, and enhanced strength and creep resistance at elevated temperatures [18,118–120]. Wrought Mg-RE alloys have particularly attracted increasing scientific attention based on the fact that their deformation and recrystallization textures were found to be much weaker than typical textures observed in conventional extruded magnesium alloy. Ball and Prangnell [121] were the first to report that a commercial WE43 alloy containing additions of Y and RE elements can develop more random-type textures during extrusion, as opposed to conventional Mg alloys. At that time, the randomized texture in WE43 was attributed to particle stimulated nucleation (PSN) of recrystallization. Not only was the texture weaker, but the typical character of the sheet texture was also altered, which had positive implications for sheet formability. However, different RE elements can form different intermetallic compounds [122,123] that contribute to distinct

properties. Additionally, in the form of solutes, individual RE elements may interact differently with dislocations and grain boundaries. In single RE alloying studies, individual RE elements that are readily soluble (e.g. Gd, Nd and Y) or insoluble (e.g. Ce and La) in Mg are usually chosen to study the role of RE in the form of both solute solutions and two phase alloys. Investigations were mainly concerned about (a) examining the potential of individual elements as texture modifiers, and (b) determining the amount of RE elements required to modify the texture. While the addition of RE elements to thermo-mechanically processed magnesium primarily was aimed at weakening the texture, the desired engineering outcome is the improved deformation behavior and enhanced property mix of strength and room temperature ductility.

2.7 Recent Research on Mg-Zn-Y System Alloys

The Mg-Zn-Y alloy system is rich in intermetallic phases and several stable ternary intermetallic compounds (icosahedral quasicrystal phase, cubic W phase and long period stacking ordered X phase) exist near the Mg-Zn edge, making the system particularly promising for developing Mg-based light metallic alloys with a large variety of candidates of intermetallic reinforcement phases [124]. It has been reported that the phase constituency in Mg-Zn-Y alloys are largely dependent on the Zn/Y ratio.

2.7.1 The role of Zn/Y ratio

The effect of Zn/Y ratio of Mg-Zn-Y system alloys have been investigated in detail by using X-ray diffraction, thermal analysis and microstructural observations by a few researchers. Huang *et al.* [125] aimed to investigate the solidification pathways of Mg-Zn-Y-Zr alloys in the Mg-rich

corner in detail by the cooling curve method, basically, on the research of characteristic temperatures (liquidus and solidus temperatures), transformation during solidification, solid fraction variation via time (or temperature). The analyzed chemical composition of the as-cast Mg-Zn-Y-Zr alloys and the transformation sequences during solidification of these investigated alloys are listed in Table 2.2 and Table 2.3, respectively.

Table 2.2: The analyzed chemical composition of the as-cast Mg-Zn-Y-Zr alloys [125].

Nominal alloys	Composition (wt.%)				Zn/Y ratio (wt.%)
	Mg	Zn	Y	Zr	
ZW22	Bal	2.00	2.48	0.55	0.88
ZW24	Bal	2.04	4.08	0.58	0.50
ZW26	Bal	2.07	5.93	0.48	0.35
ZW42	Bal	3.72	2.19	0.58	1.70
ZW44	Bal	3.85	3.79	0.67	1.02
ZW46	Bal	3.92	6.96	0.63	0.56
ZW62	Bal	6.36	1.91	0.68	3.33
ZW64	Bal	5.67	4.12	0.65	1.38
ZW66	Bal	5.52	6.48	0.68	0.85

Table 2.3: List of reactions identified by thermal analysis during solidification [125].

1. Start of α-Mg nucleation (liquidus): L → α-Mg + L
2. End of nucleation and the growth of dendrite α-Mg
3. W-phase formation by pseudobinary eutectic reaction: L → α-Mg + W
4. X-phase formation by pseudobinary eutectic reaction: L → α-Mg + X
5. I-phase formation by invariant equilibrious reaction: L + W → α-Mg + I
6. Mg-Zn phase formation by eutectic reaction: L → α-Mg + Mg-Zn phase
7. End of solidification (solidus)

The results reveal that with increasing Zn/Y ratio, two pseudobinary eutectic reactions will appear one after the other during solidification. They are:

L→ α-Mg + X ($Mg_{12}YZn$),

L→ α-Mg + W.

The dominating secondary phases change from X-phase to W-phase and to I-phase based on the increasing Zn and Y level. With low Zn and high Y content, the alloys (ZW24, ZW26, ZW46 alloys) contain α-Mg and X-phase; with high Zn and high Y content, the alloy (ZW66 alloy) contains α-Mg, W-phase and X-phase; with high Zn and low Y content, the alloy (ZW62 alloy) contains α-Mg, W-phase and I-phase; with comparative Zn and Y content, the alloys (ZW22, ZW42, ZW44, ZW64 alloys) contain α-Mg and W-phase. It is seen that the second phases in the as-cast structure are different basically depending on the Zn/Y ratio, where the amount of Zn and Y is in wt.%. The phases identified in the as-cast microstructure are found to vary with Zn/Y ratio, i.e., it consists of α-Mg + X-phase when Zn/Y ratio is 0.35, 0.50, 0.56; whereas α-Mg + W-phase + X-phase exist when Zn/Y ratio is 0.85; and α-Mg + W-phase appears when Zn/Y ratio is 0.88, 1.02, 1.38, 1.70; finally, α-Mg + I-phase + W-phase are formed when Zn/Y ratio is 3.33.

2.7.2 Structural investigations by TEM

A stable ternary phase of composition Mg_3Zn_6Y occurs in Mg-Zn-Y alloys which is quasi-crystalline with icosahedral symmetry. The I-phase in Mg-Zn-Y system alloys can form many kinds of orientation relationships with the hexagonal matrix [126]. The most common of these has an icosahedral two-fold symmetry axis parallel to the hexagonal axis of the matrix (2f ||[0001]), with two possible common symmetrical variants and two other occasional variants [127–129]. In

these orientation relationships, the I-phase exhibits a plate-like morphology on the basal plane of the hexagonal matrix, such as in Fig. 2.4(a) because the matching icosahedral twofold and the hexagonal planes make a low energy interface. In another orientation relationship, a five-fold plane matches with the hexagonal plane of the matrix. In this case, the morphology of the I-phase is more rounded, such as shown in Fig. 2.4(b).

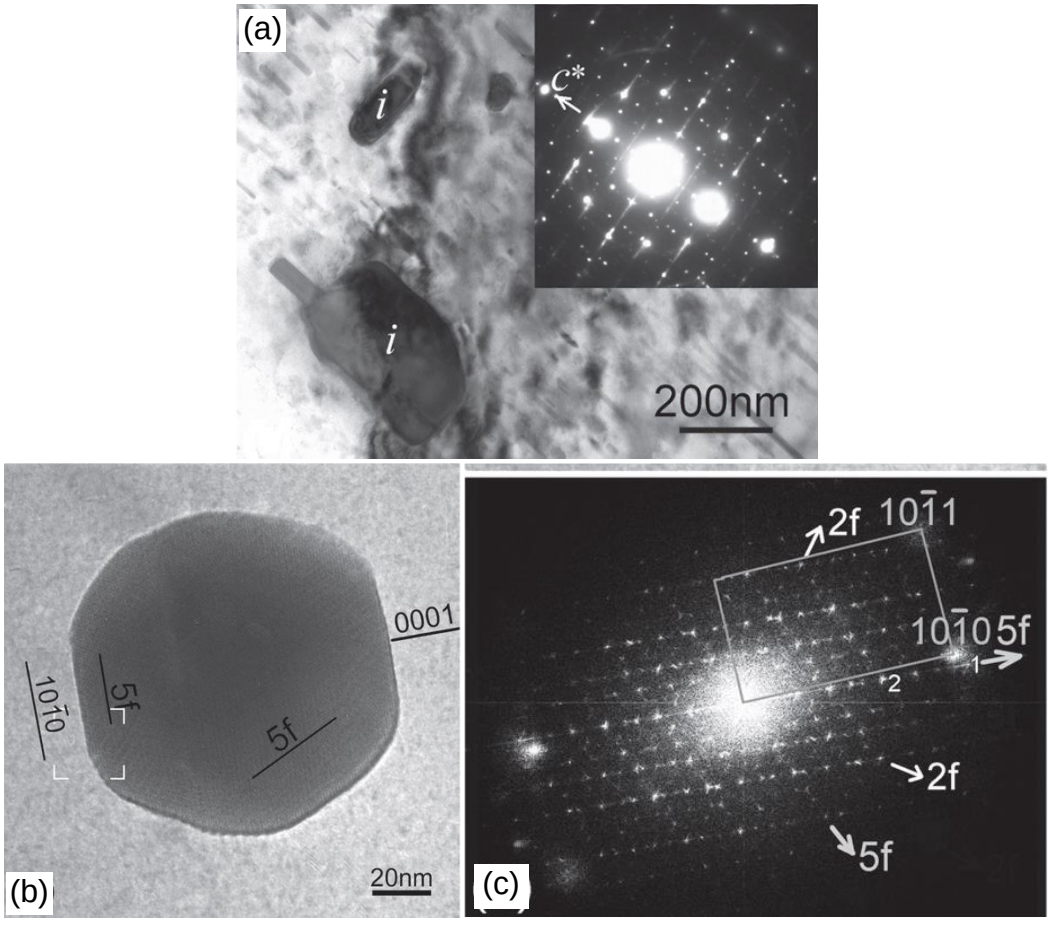

Figure 2.4: (a) Plate-like I-phase particle in a heat treated Mg-2.5Zn-0.5Y alloy. (b) A rounded I-phase particle in a Mg-4.2Zn-0.8Y alloy and an FFT pattern from the particle is shown in (c)[126].

The structure of the W-phase ($Mg_3Y_2Zn_3$), as determined by Padezhnova *et al*. [129] using XRD, possesses a partially ordered *fcc* structure with a = 0.6848 nm. The TEM image of the W-phase

and its corresponding SAED pattern in an as-extruded Mg-Zn-Y-Zr alloy, revealing the orientation between the W-phase and the Mg matrix is shown in Fig. 2.5(a) and (b) [130].

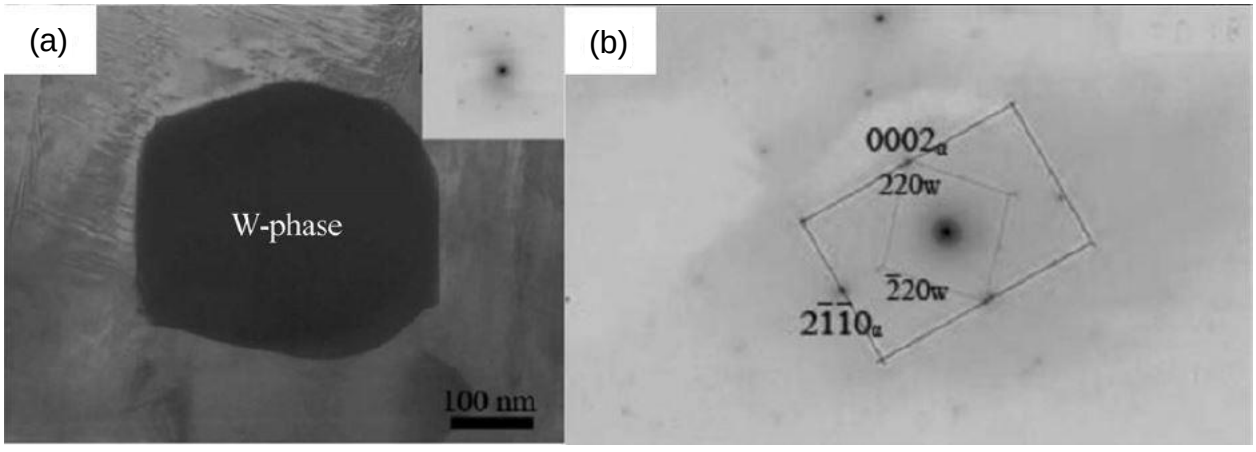

Figure 2.5: TEM images of the (a) W-phase, (b) and its corresponding SAED pattern recorded along the $\langle 01\bar{1}0 \rangle_\alpha$ direction in Mg-Zn-Y-Zr alloy [130].

The diffraction spots in the SAED pattern of the matrix and the W-phase indicate the existence of a rational orientation between the W-phase and the matrix, that is, the zonal axis $[001]_W$ is parallel to the zonal axis $[01\bar{1}0]_\alpha$, and $(220)_W$ is parallel to $(0002)_\alpha$. Therefore, the orientation between the W-phase and the matrix can be expressed as $[001]_W \parallel [01\bar{1}0]_\alpha$ and $(110)_W \parallel (0001)_\alpha$ [130]. Since the morphology of the second phase is dependent not only on the interfacial energy during solidification, only multiple interfaces with curved features exist between the matrix and the W-phase along the zonal axis $[01\bar{1}0]_\alpha$ of the matrix, not straight ones. Therefore, the atomic bonding between the W-phase and the Mg matrix is very weak due to the limited symmetry of the crystal lattice of the W-phase structure and the incoherence of the interface between them [130,131].

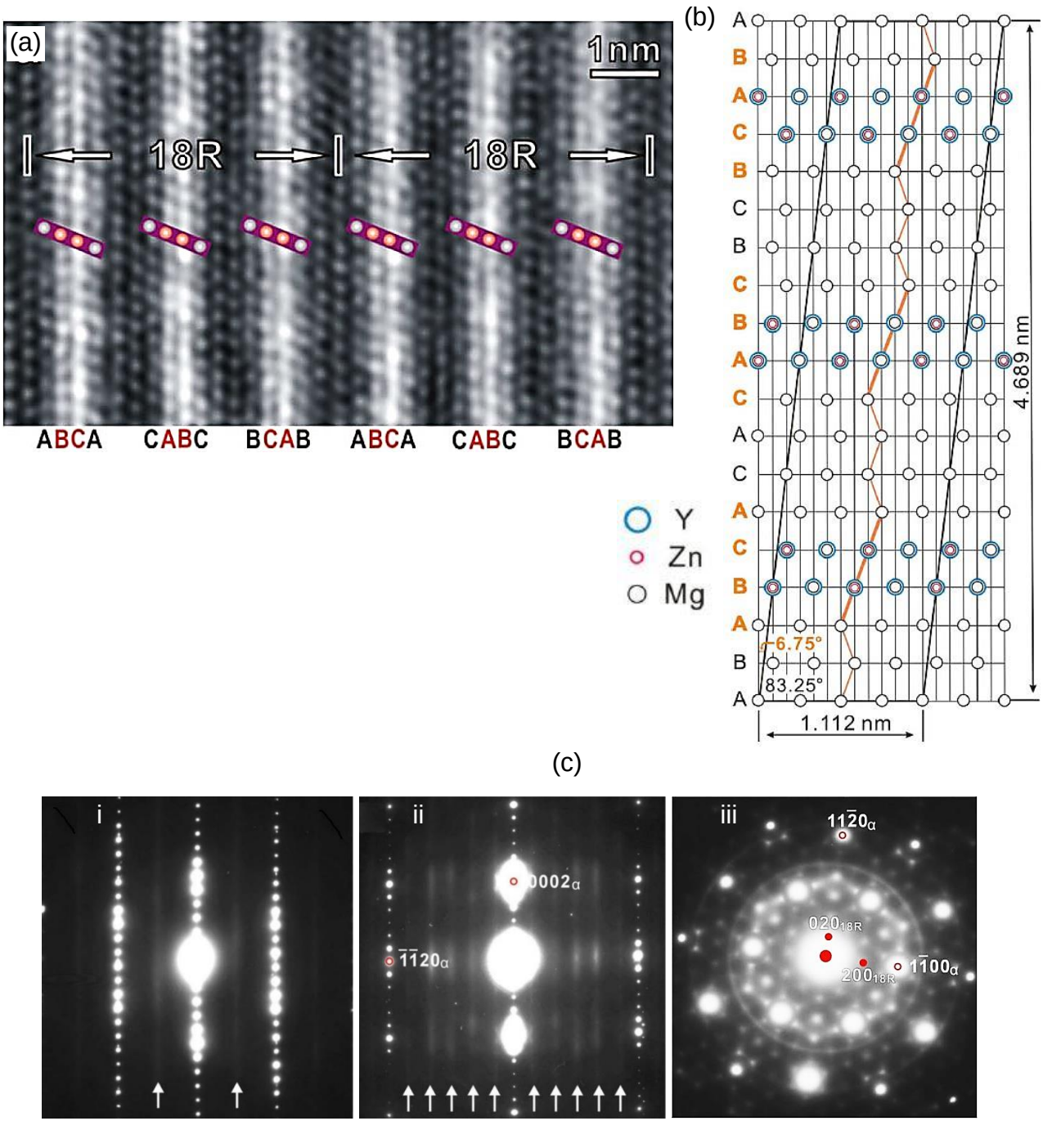

Figure 2.6: (a) The stacking sequence and the segregation layers of 18R in as-cast Mg-Zn-Y-Zr alloy. Electron beam is parallel to $\langle 11\bar{2}0 \rangle_{\alpha}$; (b) 18R unit cell viewed along $[01\bar{1}0]_{18R}$; and (c) SAED patterns recorded from local regions of 18R intermetallic particles. The electron beam is parallel to (i) $\langle 11\bar{2}0 \rangle_{\alpha}$, (ii) $\langle 1\bar{1}00 \rangle_{\alpha}$ and (iii) $[0001]_{\alpha}$ directions [132].

In Mg-Zn-Y alloys, LPSO phases are long period stacking derivatives of the hcp-Mg structure [133]. The novel phase with LPSO structure consists of structural blocks with close-packed atomic planes, forming various polytypes with different numbers of the close-packed atomic planes with different stacking of structural blocks [47,48,134–139]. The phase is not only composed of a simple polymorphic structure with periodically intruded layered defects; it is composed of solute elements that are enriched in two atom layers adjacent to the layered defect, resulting in a chemically ordered structure as well [140]. In the absence of the in-plane long-range ordering of the constituent atoms, polytypes expressed as 10*H*, 14*H*, 18*R* and 24*R* (according to the Ramsdell notation) form among which 14*H* and 18*R* polytypes are the most dominantly observed ones [141]. Zhu *et al.* [142] studied the structure of 18R LPSO by HAADF-STEM (Fig. 2.6(a)). The 18*R* unit cell contains six building blocks and each building block has two adjacent bright atomic columns. These two bright atomic layers are enriched in Y and/or Zn atoms, since the intensity in the HAADF-STEM image is proportional to the square of the atomic number (atomic number is 39 for Y, 30 for Zn, and 12 for Mg) [143,144]. Each building block has an ABCA-type stacking sequence of the closely-packed planes, where B and C layers are rich in Y and/or Zn atoms. All of these building blocks are arranged in the same shear direction, with two α-Mg atomic layers between the two adjacent building blocks. The stacking of three successive building blocks, together with the α-Mg layers between them, make up an 18R structure. The SAED patterns from 18R structure are shown in Fig. 2.6c(i-iii). The $\langle 11\bar{2}0 \rangle_\alpha$ patterns in Fig. 2.6c(i) clearly show some extra diffraction spots occurring at the $\pm 1/3 (0001)_\alpha$ and $\pm 2/3 (0001)_\alpha$ positions, which is the evidence commonly used to prove the existence of the 18*R* structure [47,135,136].

2.7.3 Tensile properties of Mg-Zn-Y alloys

In an earlier research work Bae *et al.* [145] reported the successful application of I-phase particles as a strengthening agent in Mg-Zn-Y system. Chae *et al.* [146] prepared rapidly solidified $Mg_{95}Zn_{4.3}Y_{0.7}$ alloy powder reinforced by quasicrystals followed by the warm extrusion. I-phase on the order of 0.5 μm was formed along the grain boundaries. The tensile strength and elongation increased with increasing extrusion ratio, reaching a maximum value of 347 MPa and 22%, respectively, at an extrusion ratio of 20:1 due to uniform distribution of icosahedral particles. Singh et *al.* [37] have employed extrusion to obtain a fine microstructure containing I-phase. Very fine grain size and tensile strengths of similar level as reported by Bae *et al.* [145,147] were obtained in the as-extruded alloys. By altering the microstructure of the Mg-Zn-Y alloys, YS of over 350 MPa could be achieved in a range of grain sizes, from over 20 μm down to submicron level [38,126].

Xu *et al.* [39] clarified the role of W-phase on the microstructure and the mechanical properties though investigating four Mg-Zn-Y-Zr alloys (with Zn/Y ratio lower than 1.10). When the volume fraction of W-phase increased from 11.2% to 13.8%, the YS and UTS improved from 127 and 189 MPa to 168 and 215 MPa, respectively. However, with the further increase of the volume fraction (>21.3%) of W-phase, the strength of alloys degraded greatly. It is recognized that the distributed second phase at grain boundaries can effectively retard the dislocation movement [148] but with increasing size of phase particles, a higher stress concentration occur more easily around the particles. Therefore, when the volume fraction of W-phase reached a certain value, the grain size of alloys remained same but the distributed W-phase particles at grain boundaries gradually

coarsened with increasing Zn and Y contents and the higher stress concentration easily induced early brittle fracture [39].

In 2001, Kawamura *et al.* [46] first reported that a $Mg_{97}Zn_1Y_2$ (at%) alloy, with a Mg phase of about 200 nm in grain size produced by the rapidly solidified powder metallurgy method exhibited a YS above 600 MPa and an elongation of 5% at ambient temperature. These excellent properties were considered to originate from the fine grain size and the presence of a novel 18*R* LPSO phase. Later, LPSO-containing Mg alloys with superior mechanical properties have been reported to be available by conventional thermo-mechanical processing such as extrusion, rolling, etc. [140,149–153]. Most notably, the formation of LPSO structure in Mg alloys was found to maintain the YS and UTS at 200ºC being essentially the same level at room temperature [154,155], which was exceptional in Mg alloys consisting of any other kinds of precipitates. Therefore, Mg alloys containing an LPSO phase can be one potential high-performance structural material for elevated temperature applications [156]. Itoi *et al.* [140] investigated the high temperature performance of $Mg_{90.5}Zn_{3.25}Y_{6.25}$ alloy sheet where high value of YS was maintained up to very high temperatures.

The interface between the LPSO phase and bulk Mg grains is one of the important factors influencing the mechanical properties of the materials. Shao *et al.* [156] observed the LPSO phase-Mg matrix interface of $Mg_{97}Zn_1Y_2$ alloy in the as-cast state and in a sample with an applied strain of 60% at 300ºC. The as-cast interface exhibited coherency along both the basal and prismatic planes. Any debonding or nanoscale defect at the LPSO phase-Mg matrix interface region could not be detected even at the atomic level. Therefore, it was concluded that the very stable LPSO phase-bulk Mg grain interface play a vital role in improving the strength and ductility of the $Mg_{97}Zn_1Y_2$ alloy.

2.8 Summary

The remarkable properties in Mg-Zn-Mn-Y alloys are reported to originate from the formation of different ternary stable phases known as I, W and LPSO. The current status of research field indicates that the potential strengthening effects of these beneficial phases have not been fully explored yet. Only tensile data is available in the literature. Therefore, it is essential to investigate the behavior of Mg-Zn-Mn-Y alloys under compressive loading condition. To date, the parameters related to hot processing/formability of the alloys are largely unknown which can be explored through hot deformation. Moreover, the research of Mg-Zn-Mn-Y alloys should also focus on the important aspects such as texture evolution, recrystallization, and relative activity which are closely related to plastic deformation. Furthermore, an in-depth understanding of the strengthening contribution due to Y addition and second phase formation would be highly beneficial to ascertain the impact of Y alloying. An overall comprehensive study will ensure safe and successful lightweight structural applications of Mg-Zn-Y alloys in the automotive and aerospace industry.

CHAPTER 3

3.MATERIALS AND EXPERIMENTAL DETAILS

3.1 Experimental Materials

The materials used in this study were an as-extruded ZM31 magnesium alloy with a nominal composition of 3 wt.% Zn, 1 wt.% Mn, and different amounts of Y contents, as indicated by ZM31, ZM31+0.3Y, ZM31+3.2Y and ZM31+6Y, where the value stands for the amount of Y element (in wt.% as well). It should be noted that Mg-Zn-Mn alloys were a series of magnesium alloys that were developed to be hardened by precipitation due to the substantial decrease of the solubility of Zn in Mg with decreasing temperature. The addition of Mn could improve the thermal stability of magnesium alloys and refine the grain size. Mn also played a role in transforming Fe and other impurities into relatively harmless intermetallic compounds. The alloys in the form of extruded bars with a diameter of 15 mm were received from “College of Materials Science and Engineering, Chongqing University, Chongqing, China.” The materials were extruded at 360-380°C with an extrusion ratio of 25:1.

3.2 Materials Characterization

3.2.1 Metallography

For microstructural observation, the metallographic samples were cut and cold mounted using LECO 7007 epoxy resin (1 part of liquid resin added to 2 parts of hardener). Hot mounting was avoided to prevent any possible microstructural change due to the effect of temperature during sample preparation. The mounted samples were ground with SiC sand papers with a grit number of up to 1200. Polishing was carried out with 6 μm, 3 μm, and 1 μm diamond paste using diamond extender (a mixture of rust inhibiting solution with distilled water - 10% solution by volume) as lubricant. Cleaning of the mount after polishing involved dipping in and spraying ethanol, ultrasonic cleaning, followed by drying with compressed air. After final polishing with 0.05 μm colloidal silica, the polished samples were etched using an acetic picral solution containing 4.2-g picric acid, 10-ml acetic acid, 10-ml H_2O, and 70-ml ethanol to reveal the macroscopic structure. The samples for electron backscatter diffraction (EBSD) examinations were electrochemically polished using an electrolyte consisting of 60 ml ethanol, 15 ml acetic acid, 5 ml nitric acid and 20 ml water at 15V for 10-15 s at room temperature.

3.2.2 Quantitative image analysis

Microstructural examinations were performed using an optical microscope (OM) equipped with CLEMEX quantitative image analysis software, scanning electron microscope (SEM) JSM-6380LV equipped with Oxford energy dispersive X-ray spectroscopy (EDS) system and three-dimensional (3D) surface/fractographic analysis capacity. The Clemex image analysis system was

comprised of a Clemex CMT software adaptable to ASTM standards, a Nikon optical microscope (10× eye piece, five different object lenses with magnifications of 5×, 10×, 20×, 40×, and 100×), a high-resolution digital camera, and a computer to carry out the detailed analysis. The average grain size was measured via linear intercept method. The volume fraction and size of particles were estimated on the basis of the analysis of at least 10 images.

3.2.3 Phase identification by X-ray diffraction

The phases in the materials were identified using a Panalytical X'Pert PRO X-ray diffractometer using CuK_α radiation (wavelength λ=0.15406 nm) at 45 kV and 40 mA. The diffraction angle (2θ) at which the X-rays hit the sample varied from 20° to 110° with a step size of 0.05° and 2 s in each step. *In situ* high temperature X-ray diffraction was performed at 45 kV and 40 mA. Diffraction angles were selected based on the peak analysis indicating a unique peak related to one specific phase. Diffraction patterns were recorded at 30, 100, 200, 300, 400, 450, 500, 550 and 580°C with a step size of 0.01° and 5 s in each step. In order to stabilize the temperature, the samples were maintained at each temperature 600 seconds before the acquisition of diffraction patterns.

3.2.4 Texture measurement by X-ray diffraction

The crystallographic texture of the materials was determined by measuring incomplete pole figures between ψ =0 to 75° in the back reflection mode using a PANalytical X'Pert PRO X-ray diffractometer with Cu $K\alpha$ radiation at 45 kV and 40 mA. The texture measurements were

designed to determine the intensity variation of a certain diffraction peak, indexed $\boldsymbol{h} = (hkl)$, as a function of the measurement direction (y) relative to the sample-reference frame. After corrections and normalizations, the probability maps, $P(\boldsymbol{h},\boldsymbol{y})$, or pole figures were constructed to describe the distribution of different crystal directions in the sample space using MTEX software. A set of five pole figures ($\{0001\}$, $\{10\bar{1}0\}$, $\{10\bar{1}1\}$, $\{11\bar{2}0\}$, $\{10\bar{1}3\}$) were used to calculate the orientation distribution function (ODF) and to represent ODF, Bunge notations of the Euler angles ($\varphi_1\ \Phi\ \varphi_2$) were implemented throughout. Euler angles represent a crystal orientation with respect to sample axes (normal direction, transverse direction, rolling direction) where φ_1 denotes crystal rotation about normal direction, Φ denotes crystal rotation about rotated rolling direction and φ_2 denotes crystal rotation about rotated normal direction. Defocusing due to the rotation of XRD sample holder was corrected using experimentally determined data obtained from the diffraction of Mg powders received from Magnesium Elektron.

3.2.5 EBSD analysis

The Electron Backscatter Diffraction (EBSD) works were performed at Ryerson University using a scanning electron microscope (SEM, JSM-6380LV) equipped with Oxford instrument EBSD detector HKL-Nordlys. An acceleration voltage of 20 kV, a working distance of 15 mm and a sample tilt of 70° were selected to maximize the indexing of Kikuchi diffraction patterns. The Kikuchi patterns were collected with an ultra-sensitive CCD camera and the acquired patterns were indexed and processed using post-processing software AztechHKL. Microstructure imaging, orientation imaging and coloring, inverse pole figures, misorientation profiles, grain boundary characterization, deformed/recrystallized fraction component mapping, and Schimid factor

mapping were obtained from EBSD measurement. The EBSD scan was carried out with a step size of 0.1~0.5 μm.

3.3 Uniaxial Compression Tests

The samples for compression tests were machined from the as-received bars according to the ASTM E9-09 standard [157]. All samples were machined with the cylinder axis parallel to the extrusion direction (ED) using a center lathe machine turned down to cylindrical samples. A schematic of the samples is shown in Fig. 3.1(b). Compression tests were performed along the ED until failure using a computerized United tensile/compressive test machine equipped with an environmental chamber having a temperature accuracy of ±5°C.

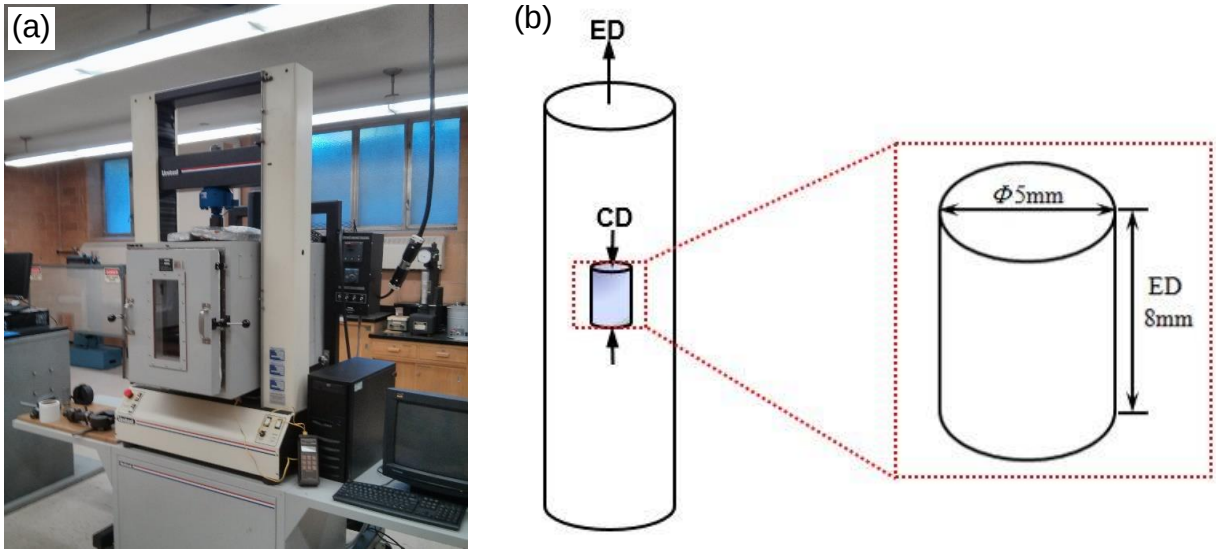

Figure 3.1: (a) Experimental set-up and (b) schematic diagram illustrating the cylindrical compression sample machined from the as-extruded rod and sample dimensions according to ASTM E9-09 standards.

The displacements and load were converted into true strain and true stresses in the standard way while neglecting the elastic strains. The tests were carried out at temperatures ranging from 25°C to 400°C and at strain rates of 0.001, 0.01, 0.1 and 1 s^{-1}. The samples were first heated to the desired test temperature and held isothermally for 300 s prior to compression to ensure homogenous temperature distribution throughout the sample. To minimize the friction between the sample and compression plates, the paste of tungsten disulfide powders mixed with ethanol was applied on both top and bottom surfaces of cylindrical samples as a lubricant. In evaluating the true stress-true strain curves, the deformation of test machine frame was eliminated using a calibration curve obtained at each temperature to obtain the actual deformation amount of test samples. Some samples were deformed up to a certain strain amount, and after deformation the samples were taken out of environmental chamber and put it into water immediately to preserve the deformed microstructures. The flow stress properties were attained based on the average values of two tests in each case. After each compression test, the deformed samples were cut along the compression axis using slow diamond cutter and prepared for microstructure and texture analysis.

3.4 Heat Treatment

The nature of the heat treatments, their duration and temperatures are summarized in Table 3.1. All the heat treatments were carried out in a radiation furnace at Ryerson University. The furnace was calibrated using Madgetech Data Logger prior to heat treatment. Solution treatment was performed to investigate phase dissolution followed by immediate cooling in water. Annealing was implemented to study static recrystallization phenomenon where one set of cylindrical

samples were annealed at 450°C for 1h and the other set of samples were annealed at 450°C for 2h. After annealing, all the samples were cooled in air.

Table 3.1: Temperature and time selected during heat treatment.

Type of heat treatment	Annealing temperature, °C	Holding time, hour
Solution treatment	525	1
Aging	225	10
Annealing	450	1, 2

3.5 Hardness Test

Vickers hardness was measured with a computerized Buehler hardness tester on the ED-RD plane of the alloys. A load of 300 g and dwell time of 15 s were applied during the hardness testing. The average of ten indentations was used for accuracy in hardness test of as-extruded and heat treated Mg-Zn-Mn-Y alloys. All the indentations were adequately spaced to avoid any potential effect of strain fields caused by adjacent indentations.

CHAPTER 4

4. MICROSTRUCTURE, PHASE FORMATION AND COMPRESSIVE DEFORMATION†

4.1 Introduction

The role of yttrium in texture weakening and the connection between texture and formability are well established [116,117,158–160]. Since ductility improvement in magnesium could also benefit from additional factors other than texture weakening such as grain refinement and increased strain hardening rate, it is important to ascertain the impact of Y on these parameters [17]. Also, an understanding of strain hardening behavior is crucial in optimizing the parameters for industrial deformation processing (or metal forming) as the strain hardening behavior is closely related to cold workability [161]. To date there is a lack of information on the influence of Y content, i.e., the existence form of secondary phases on the strain hardening behavior of Mg-Zn-Mn-Y alloy. The high-temperature work hardening behavior of extruded Mg-Zn-Mn-Y alloys is largely unknown. Besides, there are disagreements over the optimal Y addition. It is necessary to

†This chapter is based on the following publications of the author:

1. N. Tahreen, D.F. Zhang, F.S. Pan, X.Q. Jiang, C. Li, D.Y. Li, D.L. Chen, 'Influence of yttrium content on phase formation and strain hardening behavior of Mg-Zn-Mn magnesium alloy', *Journal of Alloys and Compounds*, 2014, Vol. 615, 424-432.
2. N. Tahreen, D.F. Zhang, F.S. Pan, X.Q. Jiang, D.Y. Li, D.L. Chen, 'Hot deformation and work hardening behavior of an extruded Mg-Zn-Mn-Y alloy', *Journal of Materials Science and Technology*, 2015, Vol. 31, 1161-1170.

identify the effects of Y content on the phase configuration and strain hardening behavior of magnesium alloys. This Chapter is, therefore, aimed to study the effect of Y addition on the work-hardening behavior of a ZM31 magnesium alloy by means of compression testing.

4.2 Initial Microstructure

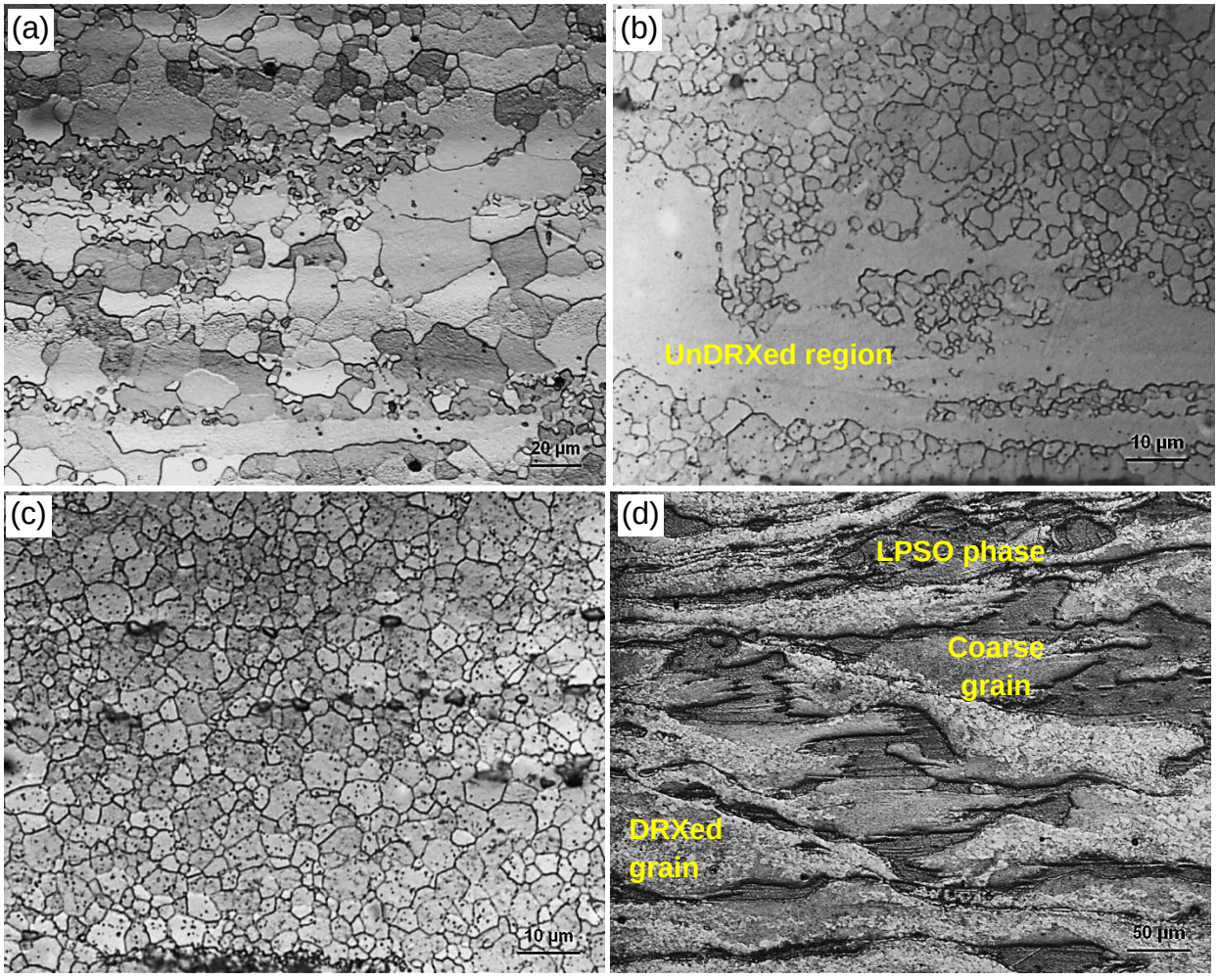

Figure 4.1: Typical optical microstructures of magnesium alloys in the as-extruded condition (a) ZM31, (b) ZM31+0.3Y, (c) ZM31+3.2Y, and (d) ZM31+6Y.

Figs 4.1(a)-(d) show optical micrographs of as-extruded alloys ZM31, ZM31+0.3Y, ZM31+3.2Y and ZM31+6Y, respectively. It is seen that the grain size generally decreased with increasing Y content. The average grain size of ZM31, ZM31+0.3Y, ZM31+3.2Y and ZM31+6Y was about 17.5, 4.3, 3.3 and 5.1 μm as measured by the linear intercept method, indicating that the addition of Y could effectively refine the grain size but the refinement efficiency was not significantly increased with a further addition of Y from 3.2% to 6%. Alloys ZM31 and ZM31+0.3Y showed a bimodal grain structure consisting of fine grains along with large elongated grains laying along the ED. The elongated grains indicated the presence of un-dynamically recrystallized (unDRXed) regions in the alloy. In contrast, a finer microstructure with a uniform grain size distribution was observed in alloy ZM31+3.2Y. The presence of more dynamically recrystallized (DRXed) regions in alloy ZM31+3.2Y compared to alloys ZM31 and ZM31+0.3Y, suggested that the dynamic recrystallization (DRX) occurred more comprehensively with increasing amount of Y. Besides, alloys ZM31+0.3Y and ZM31+3.2Y contained a distribution of broken second phase particles as streamline along the ED. Furthermore, many nano-scale precipitates appeared in the matrix. Alloy ZM31+6Y which contains the highest content of Y showed a distinctively changed multimodal microstructure with larger precipitates of the second phases than the other two alloys. As shown in Fig. 4.1(d) different regions could be observed: the DRXed α-Mg fine-grained region; the α-Mg coarse-grained region; and the LPSO X-phase region. The three different kinds of regions were indicated in Fig. 4.1(d). Two kinds of matrices were observed, that is, the DRXed fine-grain region where recrystallization took place and the coarse-grain region where recrystallization did not occur. It is of special interest to note that dynamic recrystallization mostly happened in the α-Mg matrix near the LPSO phase.

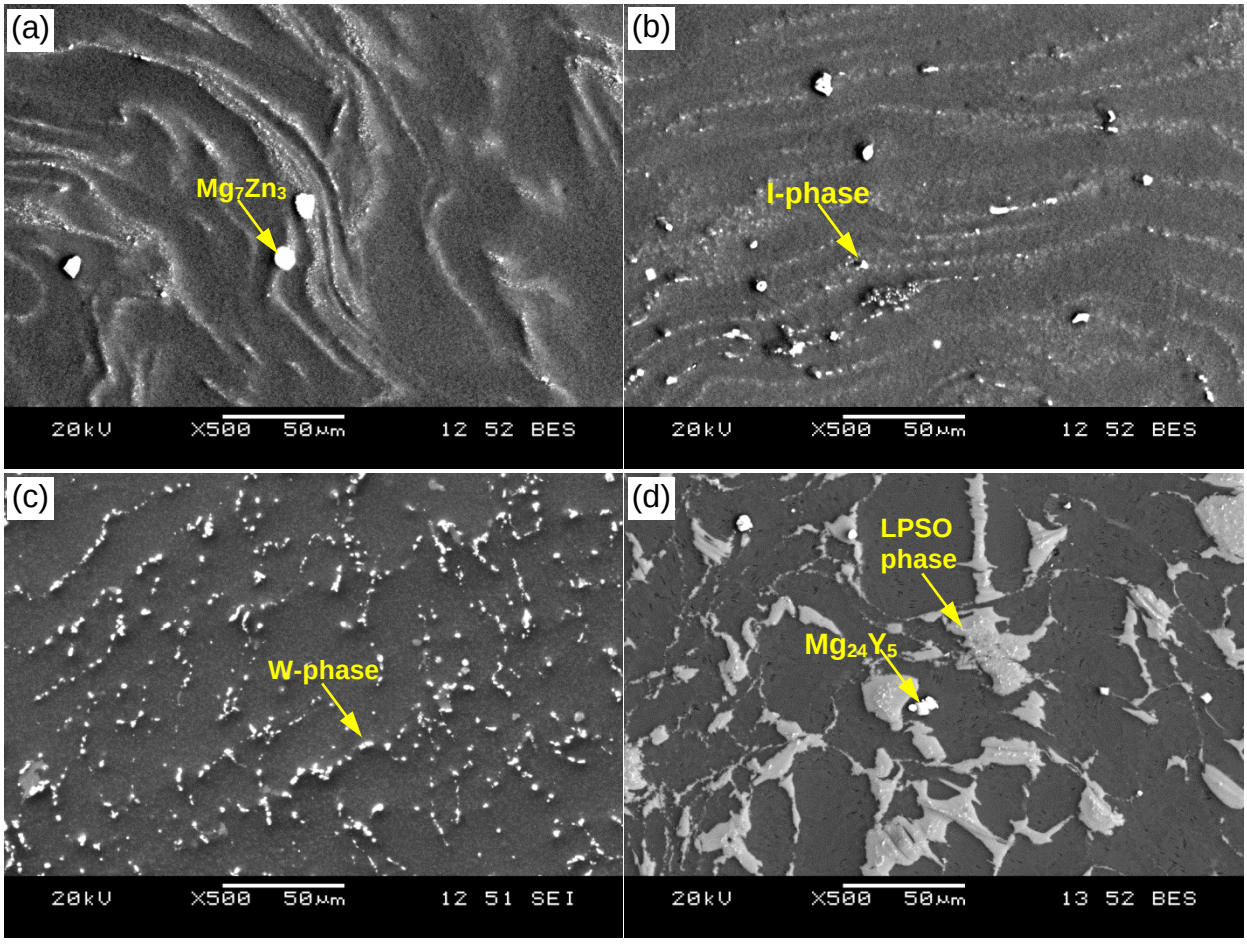

Figure 4.2: Typical SEM micrographs showing detailed microstructural features of (a) ZM31, (b) ZM31+0.3Y, (c) ZM31+3.2Y, and (d) ZM31+6Y.

Figs. 4.2(a)-(d) display representative SEM images of the as-extruded alloys. The images suggest that there were some second phases in all of the alloys, and the amount of the second phases increased with increasing amount of Y. In alloys ZM31+0.3Y and ZM31+3.2Y many fine homogenously precipitated particles were observed across the matrix. Regularly shaped second phase particles containing Mg, Zn and Y with a configuration of Mg_3YZn_6 (I-phase) were identified by EDS in alloy ZM31+0.3Y. Besides I-phase, alloy ZM31+3.2Y included ternary second phase particles with a configuration of $Mg_3Y_2Zn_3$ (W-phase). Few precipitates of the equilibrium phase MgZn in a facetted form also occurred in both the matrices. Furthermore, alloy

ZM31+6Y seemed to have large plate-like precipitates of LPSO phase with a stoichiometry of $Mg_{12}YZn$ and some rectangular particles of $Mg_{24}Y_5$. The X-phase ($Mg_{12}YZn$) which has a long period stacking ordered structure, is observed in Mg-Zn-Y system alloys by other researchers as well [49,156,162,163].

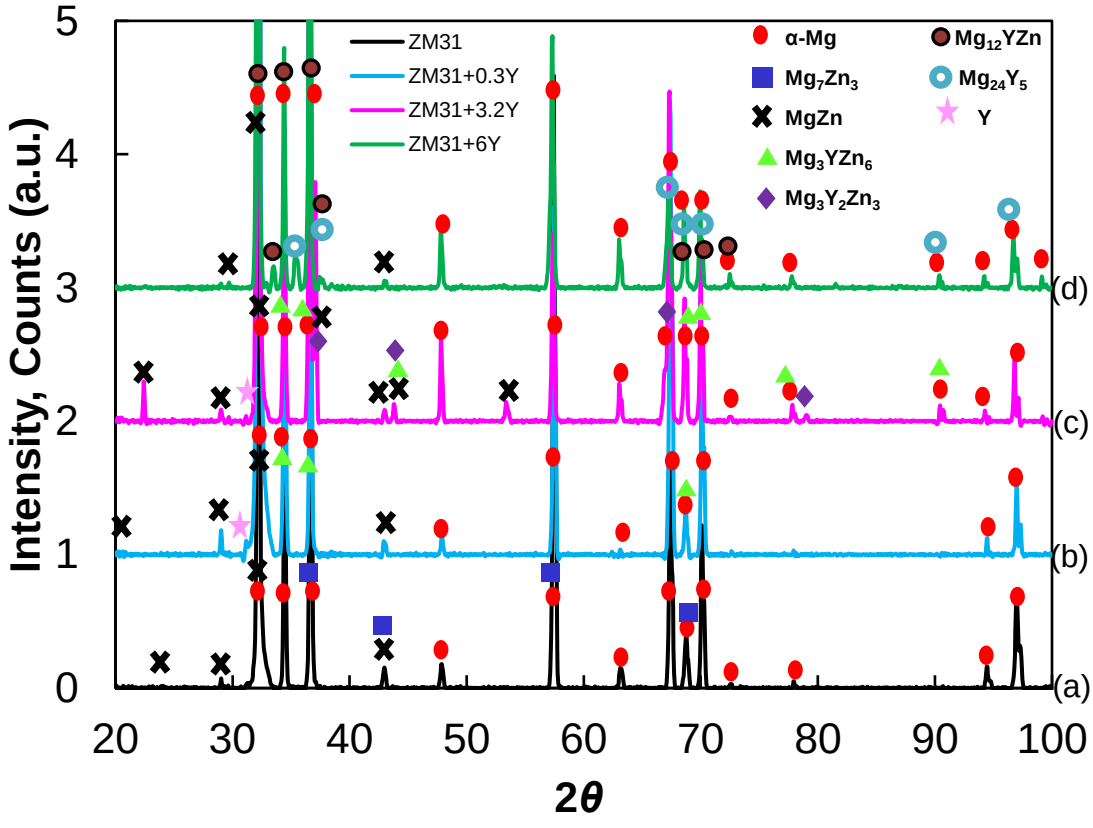

Figure 4.3: XRD patterns of (a) ZM31, (b) ZM31+0.3Y, (c) ZM31+3.2Y, and (d) ZM31+6Y magnesium alloys, where Mg_3YZn_6 is I-phase, $Mg_3Y_2Zn_3$ is W-phase, and $Mg_{12}YZn$ is LPSO X-phase.

XRD analysis revealed that the major secondary phases varied with Y content as shown in Fig 4.3. It is seen that in alloy ZM31 (without any Y content) the phases included α-Mg, MgZn and Mg_7Zn_3. However, with an addition of element Y, Mg_7Zn_3 phase was no longer detected and Mg-Zn-Y phases became the major secondary phases for alloys ZM31+0.3Y and ZM31+3.2Y. When

Y content was 0.3% the phases were α-Mg, MgZn and I-phase (Mg_3YZn_6). With increasing Y content to 3.2% the main phases of the alloy included W-phase ($Mg_3Y_2Zn_3$) as well. With a further increase in the Y content to 6%, phases of $Mg_{24}Y_5$ and LPSO X-phase ($Mg_{12}YZn$) were detected. It has been reported that a Zn/Y ratio of over 4.38 met the requirements to completely form I-phase, and with decreasing Zn/Y ratio W-phase would increasingly form since the quantity of Zn will no longer be sufficient to completely form I-phase [27]. Since the Zn/Y ratio for alloy ZM31+0.3Y and ZM31+3.2Y are about 10 and 0.94, respectively, the phases present in the alloys are in good agreement with those reported in the literature [27,28]. In addition, the present study shows that, as the Zn/Y ratio went down to 0.5 with a further addition of Y to 6%, element Y no longer fully existed in the form of I- and W-phases. Instead, LPSO X-phase and eutectic phase like $Mg_{24}Y_5$ started to develop. This is also consistent with the results reported in [25,162,164]. Addition of Mn to Mg-Zn-Y system did not contribute to phase formation but improved strength and plasticity through grain refinement.

Table 4.1: Constituent phases in the as-extruded ZM31 samples containing different amounts of Y, identified by X-ray diffraction.

Alloys	Y, wt.%	Phases
ZM31	0	α-Mg, MgZn, Mg_7Zn_3
ZM31+0.3Y	0.3	α-Mg, MgZn, I-phase
ZM31+3.2Y	3.2	α-Mg, MgZn, I-phase, W-phase
ZM31+6Y	6	α-Mg, MgZn, LPSO X-phase, $Mg_{24}Y_5$

Note: I-phase is Mg_3YZn_6, W-phase is $Mg_3Y_2Zn_3$, and LPSO X-phase is $Mg_{12}YZn$.

4.3 Strain Hardening

Fig. 4.4(a) shows the plot of strain hardening rate ($\theta = \frac{d\sigma}{d\varepsilon}$) as a function of true strain ε for the alloys ZM31, ZM31+0.3Y, ZM31+3.2Y and ZM31+6Y, respectively, where σ is true stress. Alloy ZM31+6Y showed a nearly normal (*fcc*- or *bcc*-like) strain hardening behavior where the strain hardening rate continuously decreased from the onset of plastic deformation. The strain hardening rate of alloys ZM31, ZM31+0.3Y and ZM31+3.2Y showed three distinct stages. The first, Stage A, is characterized by a rapidly decreasing strain hardening rate; the second, Stage B has an increasing strain hardening rate; and the third, Stage C, has a decreasing strain hardening rate again until failure. Similar trend in the strain hardening rate has also been observed in α-Ti [165], AM30 [166] and AZ31 magnesium alloys [161,167]. It is now generally recognized that when deformation is dominated by slip, the true stress-true strain curve is characterized by a higher yield point and a falling strain hardening rate [161,168,169]. On the other hand, when deformation is governed by $\{10\bar{1}2\}$ extension twinning, the true stress-true strain curve is characterized by a lower yield point and the strain hardening rate exhibits three distinguishable stages [120,166,168–173]. Fig 4.4(b) shows a portion of the true stress-true strain response of alloys ZM31, ZM31+0.3Y, ZM31+3.2Y and ZM31+6Y during compression along the ED. A considerably higher compressive yield strength of alloy ZM31+6Y (~265 MPa) was observed, compared to that of alloys ZM31 (~150 MPa), ZM31+0.3Y (~192 MPa) and ZM31+3.2Y (~191 MPa), as shown in Fig. 4.4(b) and the corresponding strain hardening curves (Fig. 4.4(a)), which pointed towards the slip-dictated deformation in alloy ZM31+6Y and twin dictated-deformation in alloys ZM31, ZM31+0.3Y and ZM31+3.2Y, respectively. The result suggested that an addition of rare-earth element Y altered the deformation mode from twinning to slip. Similar enhancement in the slip

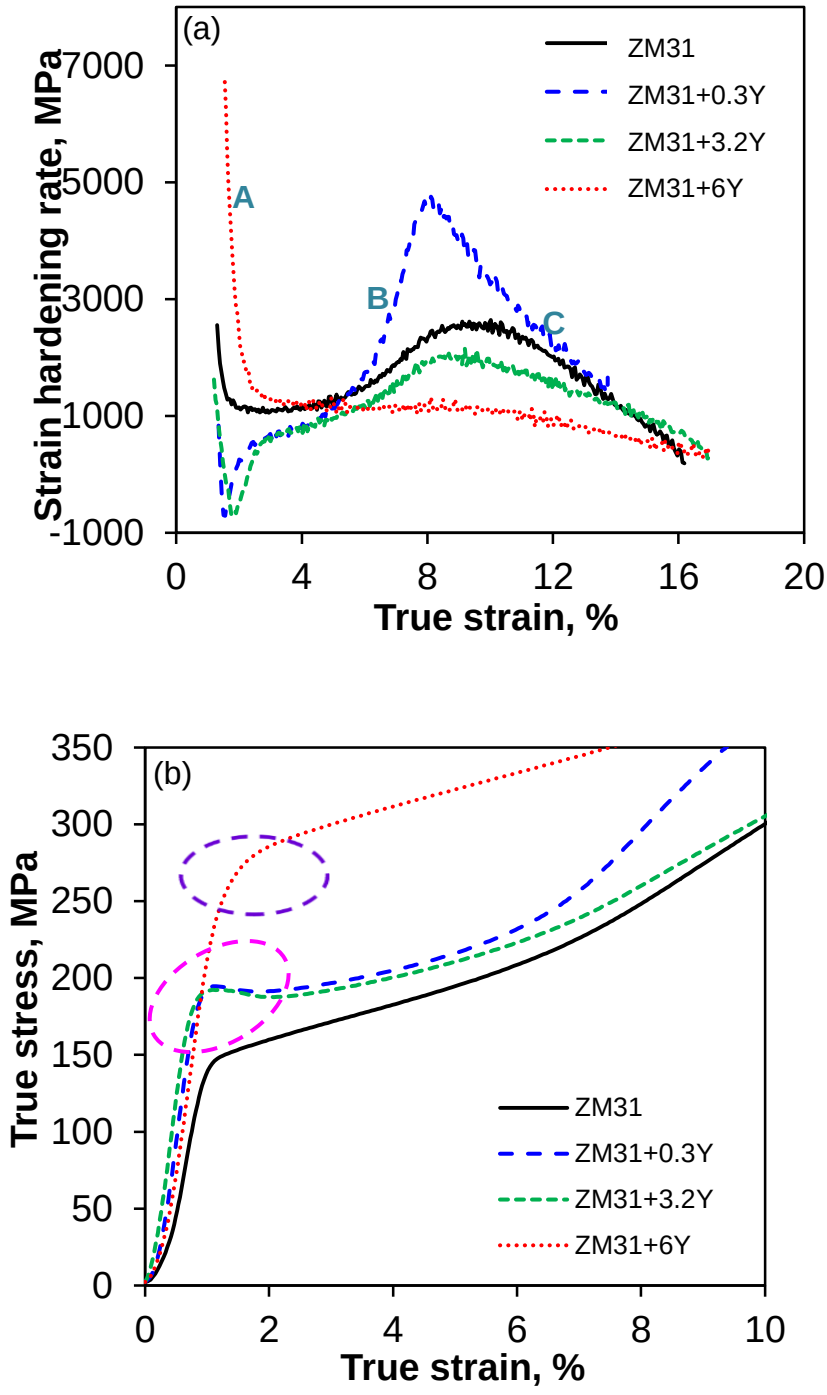

Figure 4.4: (a) Variations in the strain hardening rate with true strain, and (b) compressive true stress-true strain curve of extruded alloys ZM31, ZM31+0.3Y, ZM31+3.2Y and ZM31+6Y during compression along the ED.

activity was also observed in the Mg-Ce and Mg-Al-Y alloys due to favorable grain rotation [19,174]. It is of special interest to note that, compared to alloy ZM31, the value of peak strain hardening rate between Stages B and C increased in alloy ZM31+0.3Y and decreased in alloy ZM31+3.2Y, and indeed the ascending Stage B disappeared in alloy ZM31+6Y. That happened because when the added Y content reached 6%, Stage C emerged immediately after the rapidly falling Stage A in the absence of Stage B. While Stage A was related to the formation of $\{10\bar{1}2\}$ extension twins during compression along the ED, the appearance of Stage B was mainly attributed to the twin-dislocation interactions and the resulting twin growth [166,173,175]. The effect of twinning on strain hardening could be explained as follows: a large number of twin boundaries act as barriers to dislocation movement and thus increasing strain hardening rate [171,176]. As the addition of rare earth elements such as Y is known to suppress twin formation [19,175], it is expected that the value of peak strain hardening rate between Stages B and C would gradually decrease with increasing alloying content Y. The highest strain hardening rate of Stage B in alloy ZM31+0.3Y could be ascribed to the presence of I-phase. The highly dispersed I-phase particles in alloy ZM31+0.3Y greatly increased the strain hardening rate through interacting strongly with dislocations and pinning them.

A special or seemingly unusual observation is that alloys ZM31+0.3Y and ZM31+3.2Y produced negative strain hardening rate which was associated with the concave region of the true stress-true strain curve where the true stress decreased with increasing true strain (Fig. 4.4(b)), as indicated by the inclined pink dashed oval. This is known as yield point phenomenon and is commonly observed in some steels. The presence of yield point phenomenon in alloys ZM31+0.3Y and ZM31+3.2Y is considered to be associated with the segregation of tiny I-phase particles. It was

likely that the I-phase particles pinned down or anchored dislocations and hence deformation of the alloys required an added stress to break free the dislocations from their anchored atmosphere. Once dislocations have been freed from their atmospheres the stress needed for their motion dropped to a certain degree. It is the decreased stress that accounted for the presence of negative strain hardening rate in the alloys ZM31+0.3Y and ZM31+3.2Y (Fig. 4.4(a)). To obtain a better understanding about how the strain hardening is affected by the Y content, the strain hardening exponents are evaluated using Hollomon's equation [73] and are plotted as a function of Y content in Fig. 4.5(a). The strain hardening exponents generally decreased with increasing Y content. To characterize the varying degrees of Stage B, the change range of strain hardening rate in Stage B ($\Delta\theta_B$) was determined and is plotted in Fig. 4.5(b) for all the ZM31, ZM31+0.3Y, ZM31+3.2Y and ZM31+6Y compressed samples, where $\Delta\theta_B$ is defined as the peak/maximum strain hardening rate between Stages B and C ($\theta_{B,max}$) minus the valley/minimum strain hardening rate between Stages A and B ($\theta_{B,min}$), as shown in the insert of Fig. 4.5(b). It is seen from Fig. 4.5(b) that when the Y content increased from 0 to 0.3%, the value of $\Delta\theta_B$ increased from ~1600 MPa to ~4000 MPa, followed by a sharp drop with increasing Y content and reached zero at a Y concentration of 6%. A decreasing trend of $\Delta\theta_B$ was obvious with increasing Y content, corresponding well to the decreasing strain hardening exponent (Fig. 4.5(a)). It is also seen from Fig. 4.5 that a small addition of Y to just about 0.3% led to a fairly high value of both the strain hardening exponent and $\Delta\theta_B$. This was mainly attributed to the presence of quasicrystalline I-phase in the alloy ZM31+0.3Y, as shown in Fig. 4.3.

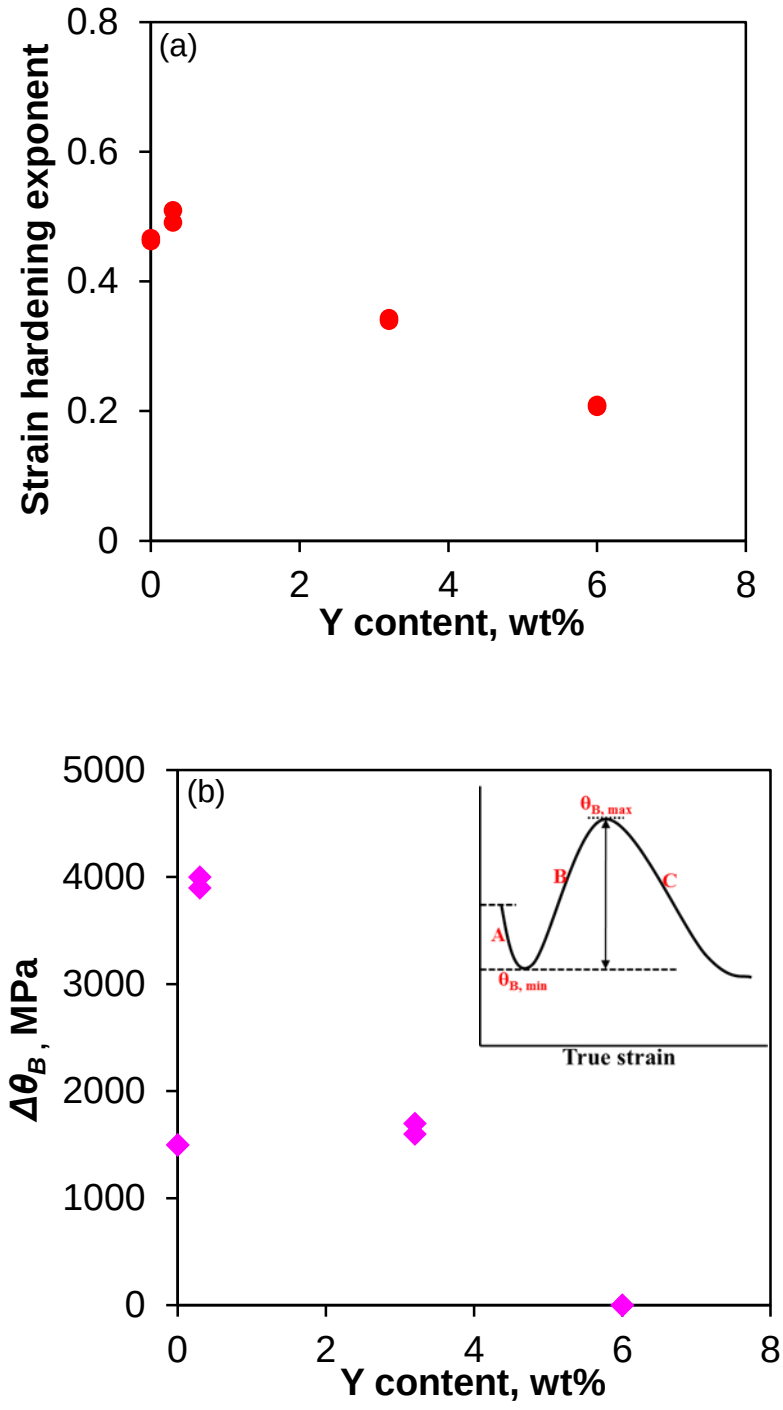

Figure 4.5: Effect of Y content on (a) strain hardening exponent evaluated using Hollomon's equation, and (b) $\Delta\theta_B$ value (=$\theta_{B,max}$ - $\theta_{B,min}$ in the inset).

4.4 Hardness

Fig. 4.6 shows a plot of hardness value as a function of Y content. An increasing trend of hardness with increasing Y content (from 0 to 0.3% Y) was observed with a sharp jump in the hardness value. This could be ascribed to the presence of a large amount of icosahedral I-phase in alloy ZM31+0.3Y containing 0.3% Y. Hard I-phase particles could effectively obstruct the slip of dislocations due to the low I-phase/matrix interfacial energy that resulted from almost coherent I-

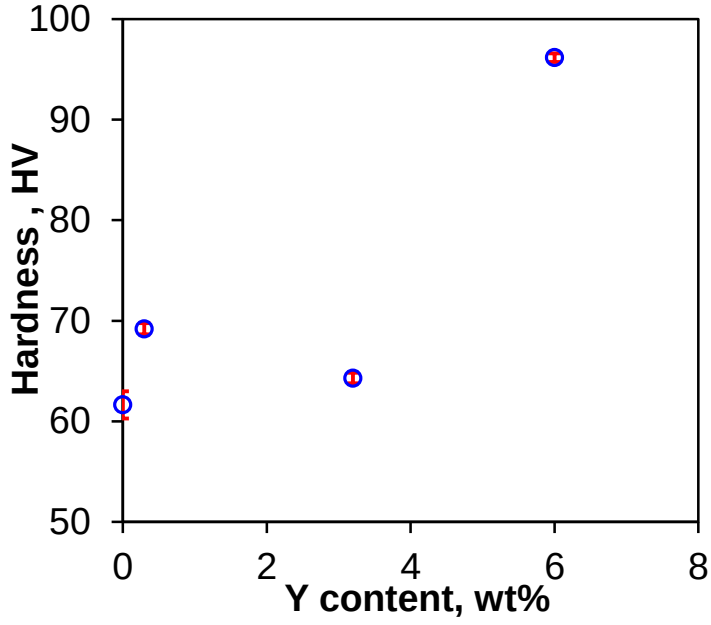

Figure 4.6: Hardness as a function of Y content.

phase/matrix interface [26,177]. As a result, negligible cavity formed at the interface during deformation which gave rise to a high hardness value. Conversely, the formation of W-phase besides I-phase in alloy ZM31+3.2Y caused a drop in the hardness value due to the weak bonding in W-phase/matrix interfaces [27,43]. The maximum hardness was observed in alloy ZM31+6Y which was mainly credited to the presence of hard $Mg_{24}Y_5$ (218 HV) and LPSO X-phase, as shown in Figs 4.1(d), 4.2(d) and 4.3. This corresponded well to the highest compressive yield strength

shown in Fig. 4.4(b). Similar results on the significant strengthening effect of LPSO X-phase in magnesium alloys have also been reported in [142,156,162,178]. The results suggest that the variation of phases arising from varying amounts of Y content significantly influenced the hardness of the alloys in the as-extruded state.

4.5 Effect of Heat Treatment

4.5.1 Heat treated microstructure

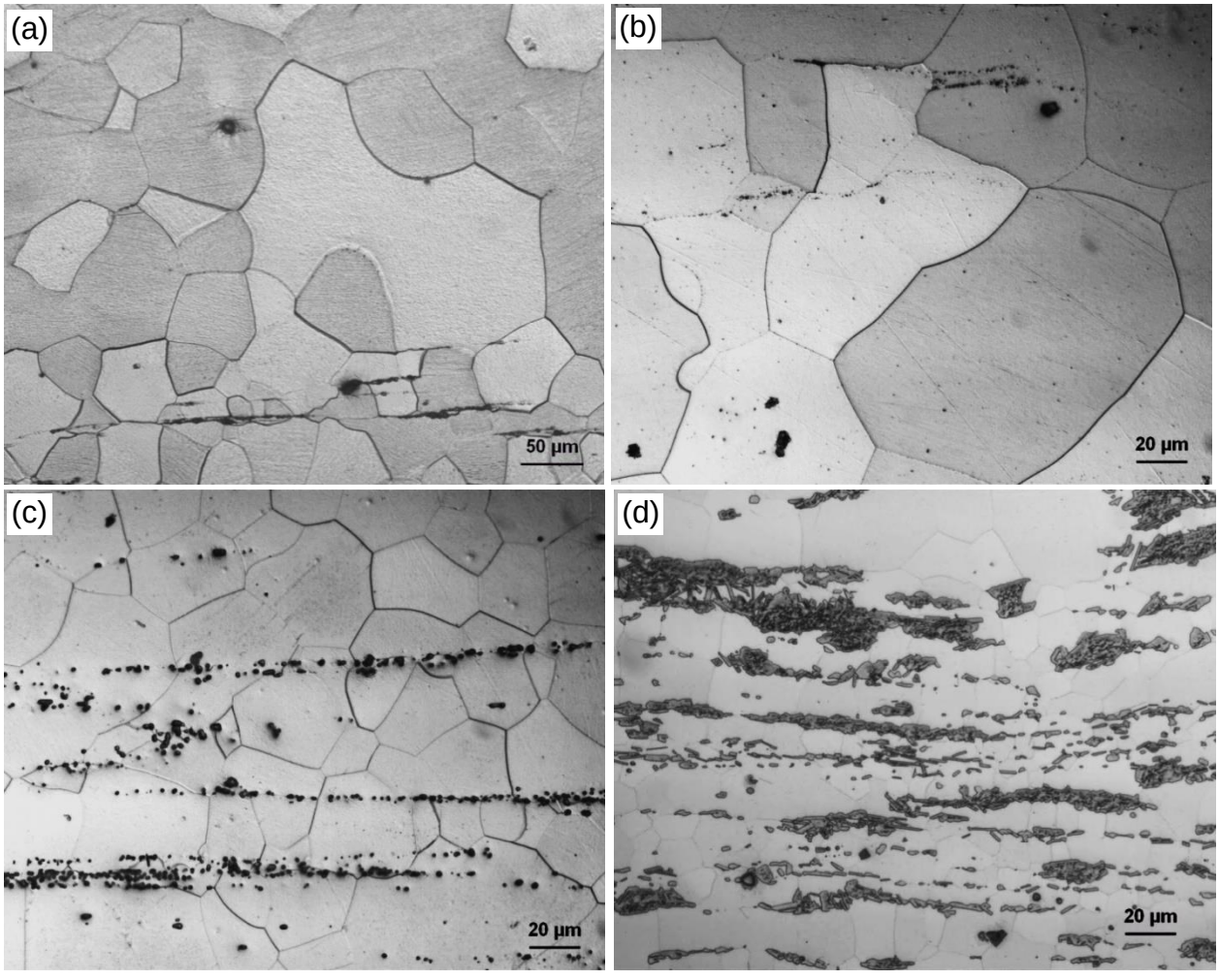

Figure 4.7: Typical microstructures of extruded Mg alloys in the solution treated and aged condition, (a) ZM31, (b) ZM31+0.3Y, (c) ZM31+3.2Y, and (d) ZM31+6Y.

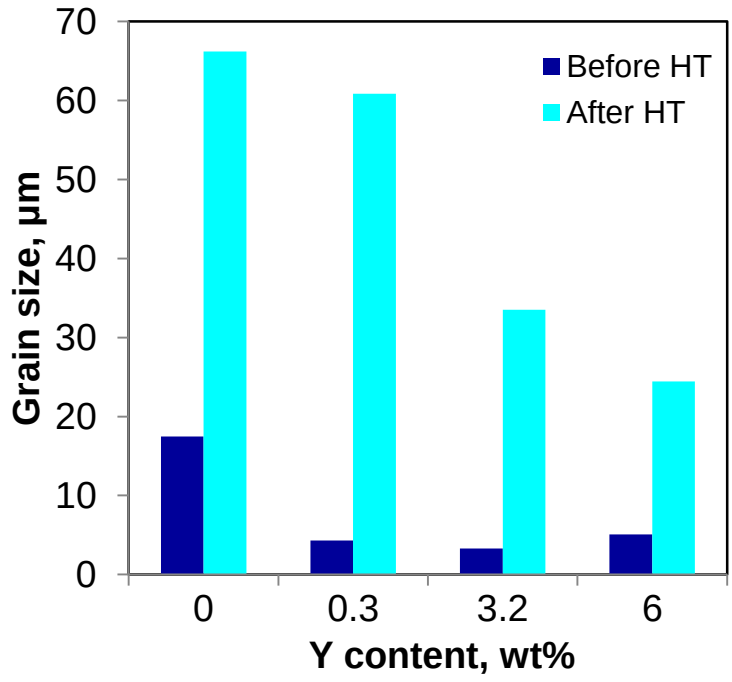

Figure 4.8: Grain size as a function of yttrium content before and after the heat treatment.

In order to better understand the roles of the phases, the studied alloys were solution treated for 1 hour at 525°C, followed by an immediate aging treatment at 225°C for 10 hours. Figs 4.7(a)-(d) show the optical micrographs of the solution treated and aged alloys ZM31, ZM31+0.3Y, ZM31+3.2Y and ZM31+6Y, respectively. It is evident that the quantities of second phase decreased considerably and the grain size increased significantly as a result of the solution treatment. Fig. 4.8 shows the change in grain size as a function of Y content before and after the heat treatment. Alloy ZM31+0.3Y exhibited the maximum grain growth owing to heat treatment, followed by ZM31, ZM31+3.2Y and ZM31+6Y. It has been reported that element Y can effectively refine grains of magnesium alloys by forming Mg-Zn-Y phases, especially I-phase which can restrain the grain growth during dynamic recrystallization process [26]. It follows that a greater extent of grain growth in alloys ZM31, ZM31+0.3Y and ZM31+3.2Y would indicate the absence of Mg-Zn-Y phases in the alloys, which needs further verification by XRD. It is also seen

that the overall grain size after heat treatment decreased consistently with increasing Y content, suggesting that Y acted as an effective inhibitor to suppress the grain growth during recrystallization. Similar grain refining effect of yttrium was also reported in Mg-Zn-Y-Zr alloys during annealing owing to the pinning effect of Y-containing particles [179].

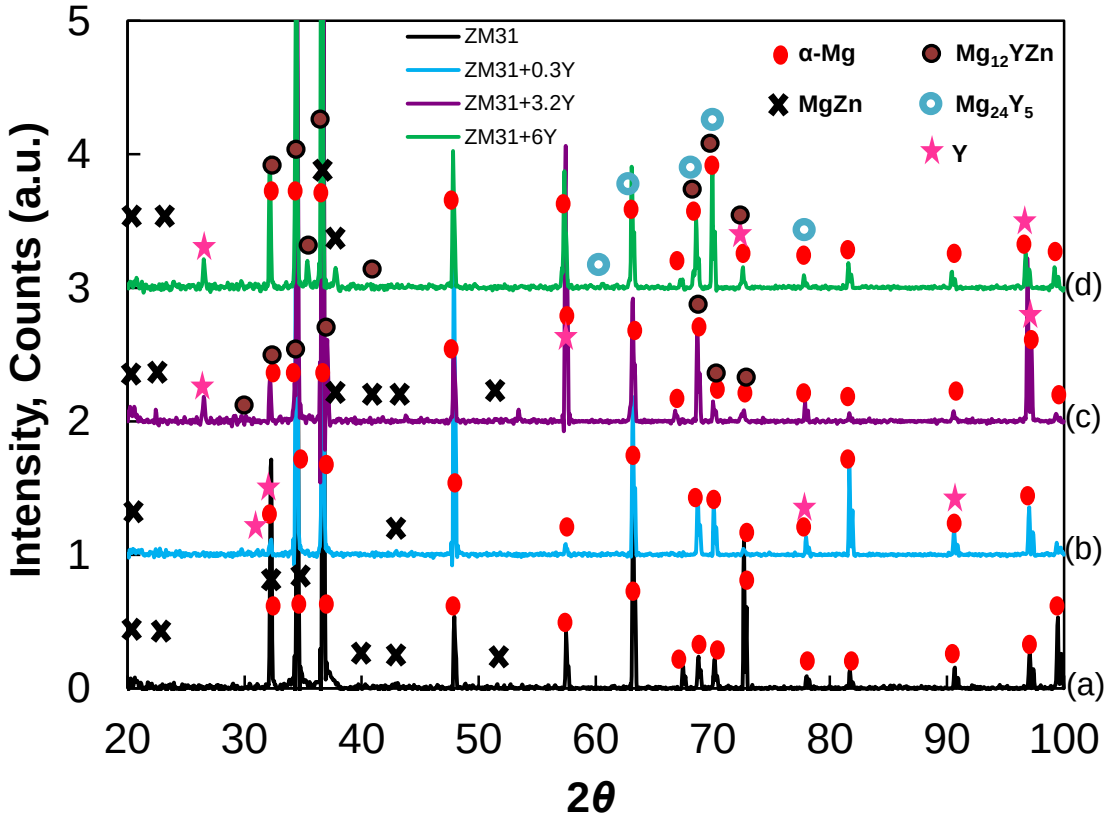

Figure 4.9: XRD patterns of solution treated and aged (a) ZM31, (b) ZM31+0.3Y, (c) ZM31+3.2Y, and (d) ZM31+6Y magnesium alloys where $Mg_{12}YZn$ is LPSO X-phase.

An XRD measurement was performed on the solution treated and aged alloys ZM31, ZM31+0.3Y, ZM31+3.2Y and ZM31+6Y. As shown in Fig. 4.9, only main peaks corresponding to α-Mg and MgZn phase were present in the XRD pattern of alloys ZM31 and ZM31+0.3Y, and peaks corresponding to α-Mg, MgZn and X-phases were observed in the XRD pattern of alloy

ZM31+3.2Y. Thus, the applied solution treatment and aging brought about the precipitation of LPSO X-phase in alloy ZM31+3.2Y. However, as seen from Figs 4.9 and 4.3, no major phase change could be observed in alloy ZM31+6Y. The constituent phases in the alloys under study after the solution and aging treatment are listed in Table 4.2.

Table 4.2: Constituent phases in the heat treated samples containing different amounts of Y, identified by X-ray diffraction.

Alloys	Y, wt.%	Phases
ZM31	0	α-Mg, MgZn
ZM31+0.3Y	0.3	α-Mg, MgZn
ZM31+3.2Y	3.2	α-Mg, MgZn, LPSO X-phase
ZM31+6Y	6	α-Mg, MgZn, LPSO X-phase, $Mg_{24}Y_5$

Note: LPSO X-phase is $Mg_{12}YZn$.

The results suggested that the following second phases were dissolved: Mg_7Zn_3 in alloy ZM31, I-phase in alloy ZM31+0.3Y, both I- and W-phases in alloy ZM31+3.2Y, as a result of the solution and aging treatment. Again, all of the major phases ($Mg_{24}Y_5$ and X-phase) in alloy ZM31+6Y still remained under the current solution and aging treatment condition (525°C for 1h + 225°C for 10 hrs), suggesting a high degree of thermal stability of $Mg_{24}Y_5$ and LPSO X-phase, which was also reported in the literature [154,180,181].

4.5.2 Strain hardening after heat treatment

Fig. 4.10(a) shows the true stress-true strain curves of the heat treated alloys, which were compressed along the ED as well. All of them apart from alloy ZM31+6Y showed a noticeable curve shape change after the heat treatment (Fig. 4.10(a) versus Fig. 4.4(b)), and now became

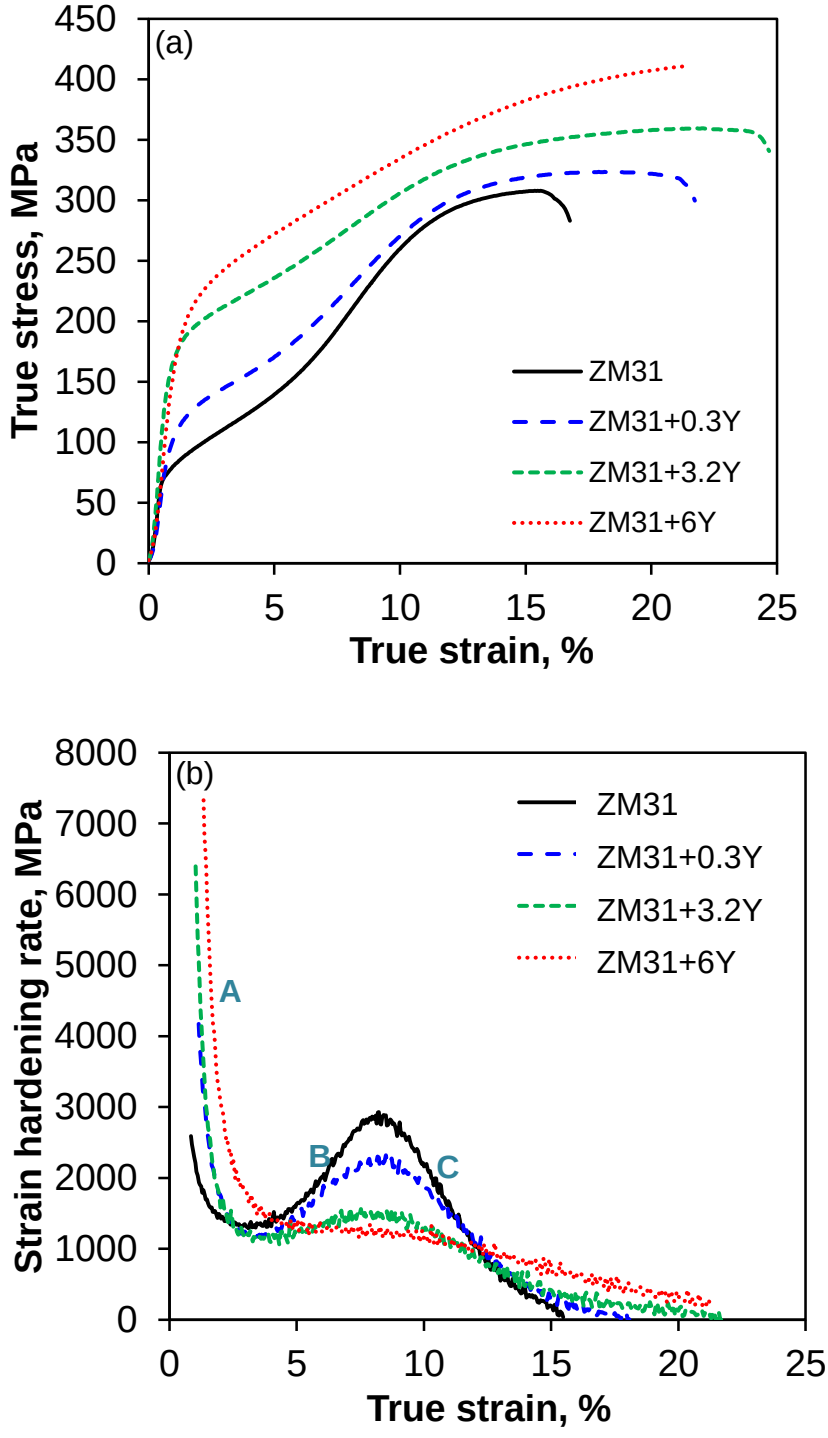

Figure 4.10: (a) True stress-true strain curves, and (b) strain hardening rate θ as a function of true strain for the solution treated and aged ZM31, ZM31+0.3Y, ZM31+3.2Y, and ZM31+6Y magnesium alloys.

sigmoidal shaped stress-strain curve, being indicative of the activation of deformation twinning. However, with increasing Y content the extent of the skewed sigmoidal shape on the true stress-true strain curve gradually decreased and the compressive yield stress regularly increased. This clearly indicates the beneficial role of Y addition in enhancing the resistance of magnesium alloys to extension twinning in the heat treatment state. The strain hardening rate $d\sigma/d\varepsilon$ of solution treated and aged alloys ZM31, ZM31+0.3Y, ZM31+3.2Y and ZM31+6Y compressed along the ED as a function of true strain is plotted in Fig. 4.10(b). In comparison with Fig. 4.4(a), the negative strain hardening reflecting the yield point phenomenon was no longer present and a visible difference was observed in Stage B hardening of the heat treated alloys, i.e., the value of peak strain hardening rate of Stage B consistently decreased with increasing Y content and ultimately reached to extinction when the Y content was 6%. This was mainly related to the reduction of Stage B hardening in the alloy ZM31+0.3Y after heat treatment (Figs 4.4(a) versus Fig. 4.10(b)) due to the absence of I-phase particles (Fig. 4.9 and Table 4.2), since I-phase particles had a strong pinning effect on the dislocation movement and thus contributed greatly to the strain hardening. In other words, the lack of I-phase resulted in a lower strain hardening rate in the heat treated alloy ZM31+0.3Y, as well as the absence of negative strain hardening rate in the heat treated alloys ZM31+0.3Y and ZM31+3.2Y.

Fig. 4.11(a) illustrates the evaluated strain hardening exponent of the heat treated alloys using Hollomon's equation [73] as a function of Y content. As shown, the strain hardening exponent decreased with increasing Y content. Unlike the extruded alloys, a consistently decreasing trend was observed with no exception occurring at 0.3%Y content any more. Since the quasicrystalline I-phase was dissolved during the solution treatment, the strain hardening exponent value

corresponding to the extruded alloy ZM31+0.3Y dropped. Fig. 4.11(b) shows the change range of strain hardening rate in Stage B ($\Delta\theta_B$) evaluated for the solution treated and aged ZM31, ZM31+0.3Y, ZM31+3.2Y and ZM31+6Y compressed samples. Similar to the strain hardening

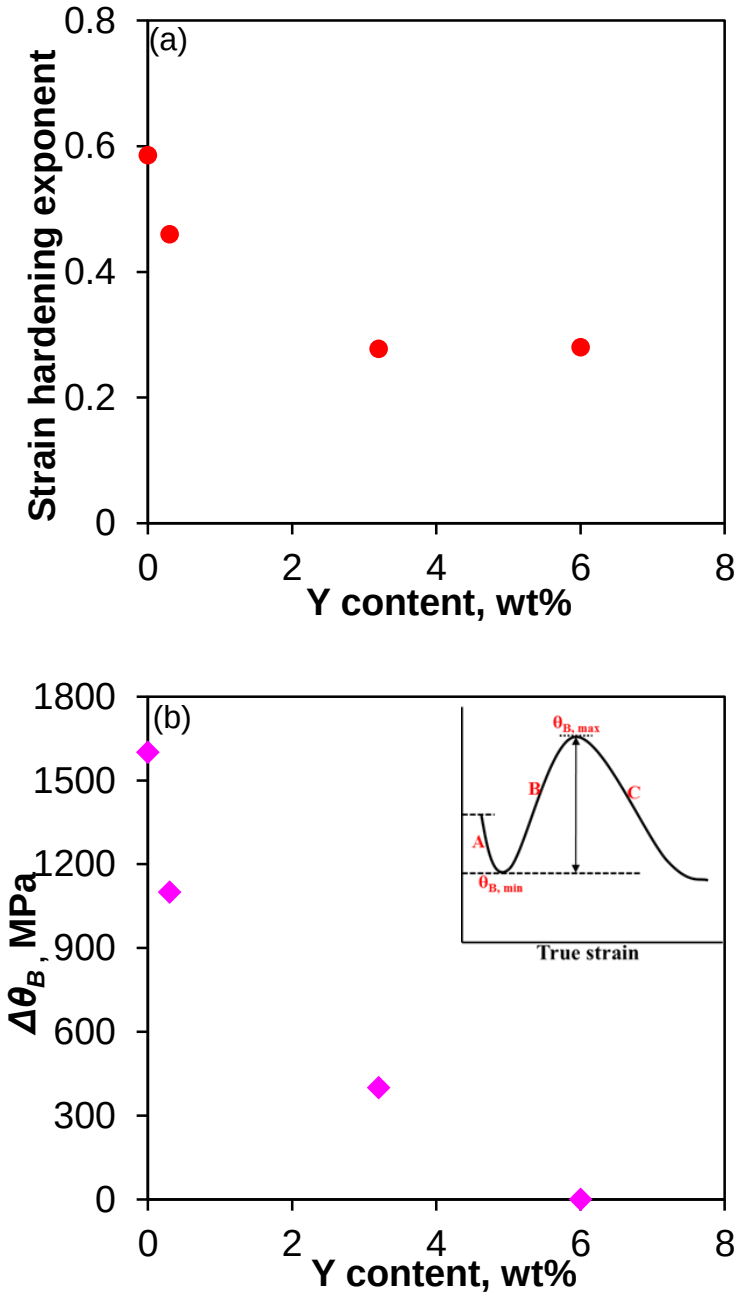

Figure 4.11: Effect of Y content on (a) strain hardening exponent evaluated using Hollomon's equation, and (b) $\Delta\theta_B$ value (= $\theta_{B,max}$ - $\theta_{B,min}$ in the inset) after solution treatment and aging.

exponent given in Fig. 4.11(a), $\Delta\theta_B$ decreased evenly with increasing Y amount as well. Unlike the extruded alloy ZM31+0.3Y, the heat treated alloy did not exhibit any sharp elevation in the value of $\Delta\theta_B$ (Fig. 4.11(b) versus Fig. 4.5(b)). Again, this was mainly associated with the absence of I-phase particles after the heat treatment.

4.5.3 Hardness after heat treatment

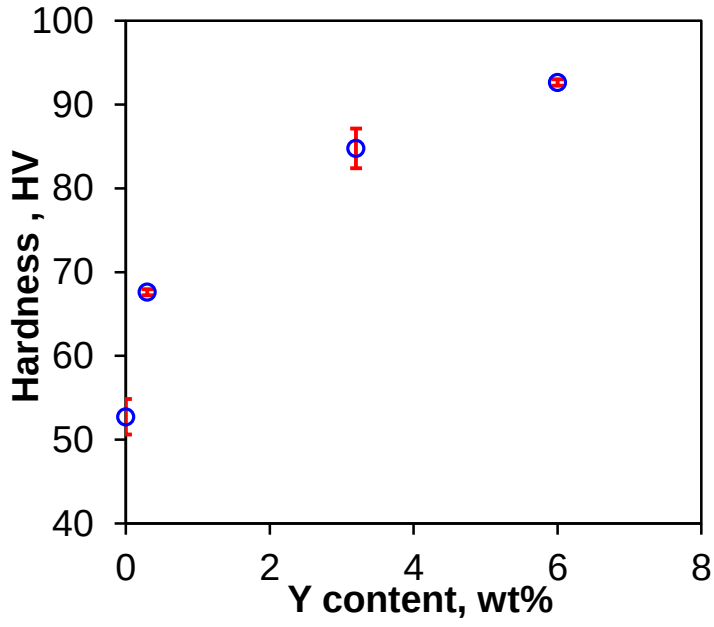

Figure 4.12: Changes of hardness with Y content after solution and aging treatment.

Fig. 4.12 shows a plot of hardness as a function of yttrium content. As shown, the hardness value (HV) increased with increasing Y content. Due to the presence of thermally stable LPSO X-phase and $Mg_{24}Y_5$ (Table 4.2 and Fig. 4.9) alloy ZM31+6Y retained much of its hardness, showing a slight decrease in hardness as a result of grain growth after heat treatment. Alloys ZM31 and ZM31+0.3Y became somewhat softer due to grain growth and the dissolution of Mg_7Zn_3 and I-

phase, and alloy ZM31+3.2Y became much harder (as shown in Fig. 4.12 versus Fig. 4.6) due to the precipitation of LPSO X-phase in spite of the dissolution of MgZn, I-phase, W-phase (Tables 4.1 and 4.2) and grain growth. Similar increase in hardness was also observed, as reported in Ref. [182], when up to 4% Y content was added to a Mg-Al-Y alloy.

4.6 Compressive Behavior at Elevated Temperatures

The true stress-true strain response of alloys ZM31+0.3Y, ZM31+3.2Y and ZM31+6Y during compression at 200°C and a constant strain rate of 1×10^{-3} s^{-1} is shown in Fig. 4.13.

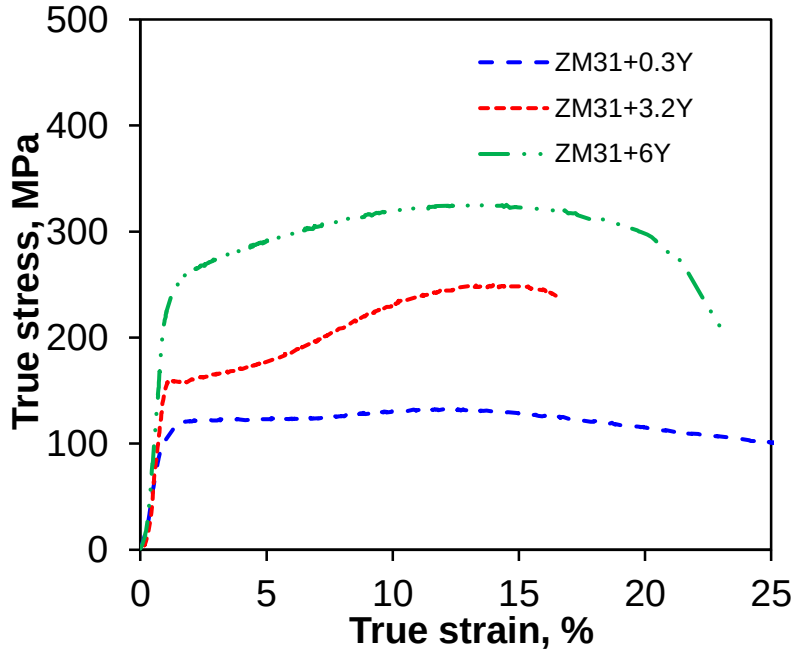

Figure 4.13: Compressive true stress-true strain curves of extruded alloys ZM31+0.3Y, ZM31+3.2Y and ZM31+6Y during compression along the ED at 200°C and at a strain rate of 1×10^{-3} s^{-1}.

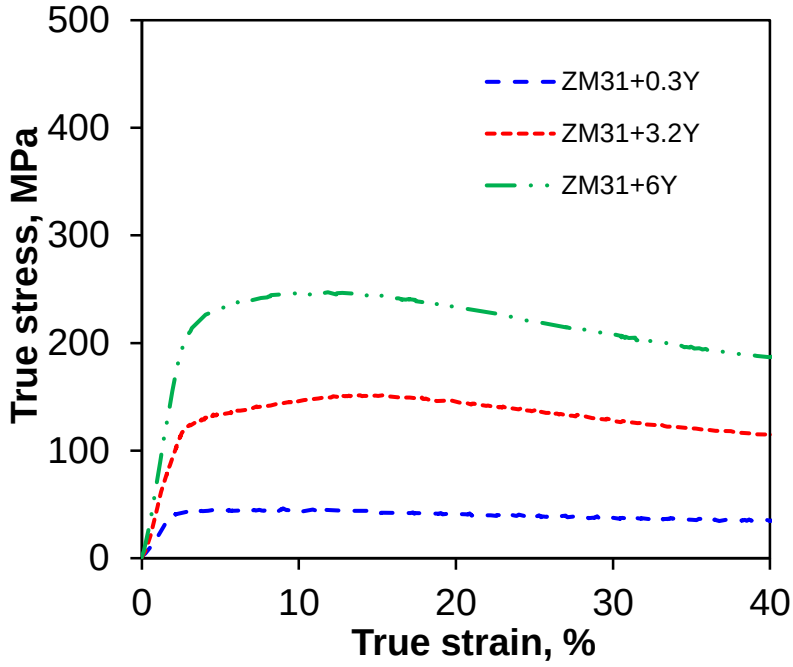

Figure 4.14: Compressive true stress-true strain curves of extruded alloys ZM31+0.3Y, ZM31+3.2Y and ZM31+6Y during compression along the ED at 300°C and at a strain rate of 1×10^{-3} s^{-1}.

The flow curve data at strains beyond -0.25 were excluded due to increased friction effects, which would cause a false increase of stress at higher strains. It is seen from Fig. 4.13 that at 200°C, the CYS of the alloys showed an increasing trend with increasing Y content. For alloy ZM31+3.2Y deformed at 200°C, the flow curve still exhibited a skewed hardening response typical for twinning-dictated deformation similar to that observed during compressive deformation at RT [166,173]. On the other hand, the flow curve of alloy ZM31+0.3Y exhibited a nearly parabolic hardening response as typical for slip assisted deformation [13,183,184]. The characteristic nature of the flow curve of alloy ZM31+6Y indicated that the deformation mode remained the same. The deformation mode discussed here needs further verification by microstructure examinations. A considerable decrease in the CYS and hardening was also observed in alloy ZM31+0.3Y and the

alloy demonstrated a more or less steady-state flow behavior at ~132 MPa. However, the yield strength and hardening rate for alloys with higher Y contents (ZM31+3.2Y and ZM31+6Y) in this test condition were slightly lower than those obtained at RT.

Fig. 4.14 shows the true stress-true strain behavior of the studied alloys subjected to compression along the ED at 300°C and a strain rate of 1×10^{-3} s^{-1}. At 300°C, all the materials seemed to reach steady-state without the presence of skewed curve shape as seen in Figs 4.13 and 4.14. The big difference, however, lies in the yield stress and peak stress of the materials. The quasi-steady-state was attained until the peak stress, followed by a little softening. The steady-state flow stress of the materials ZM31+0.3Y, ZM31+3.2Y and ZM31+6Y were 51, 177 and 271 MPa, respectively. It is clear that, with increasing Y content, the flow stress of the extruded magnesium alloy remarkably increased at 300°C. This suggested that the addition of Y to the magnesium alloys could effectively increase the difficulty of hot deformation.

At both temperatures of 200°C and 300°C, the shape of stress-strain curves reflected the mechanism of hot deformation to some extent. For example, the flow stress increased with increasing strain in the initial stage of deformation due to strain hardening, and then the increasing trend decreased gradually due to the occurrence of recovery or dynamic recrystallization (DRX). Since the presence of rare-earth elements is known to increase the recrystallization temperature, it is likely that the alloys with higher Y contents would experience a much less extent of DRX and therefore did not undergo significant softening at elevated temperatures, as compared with the low Y-containing alloy.

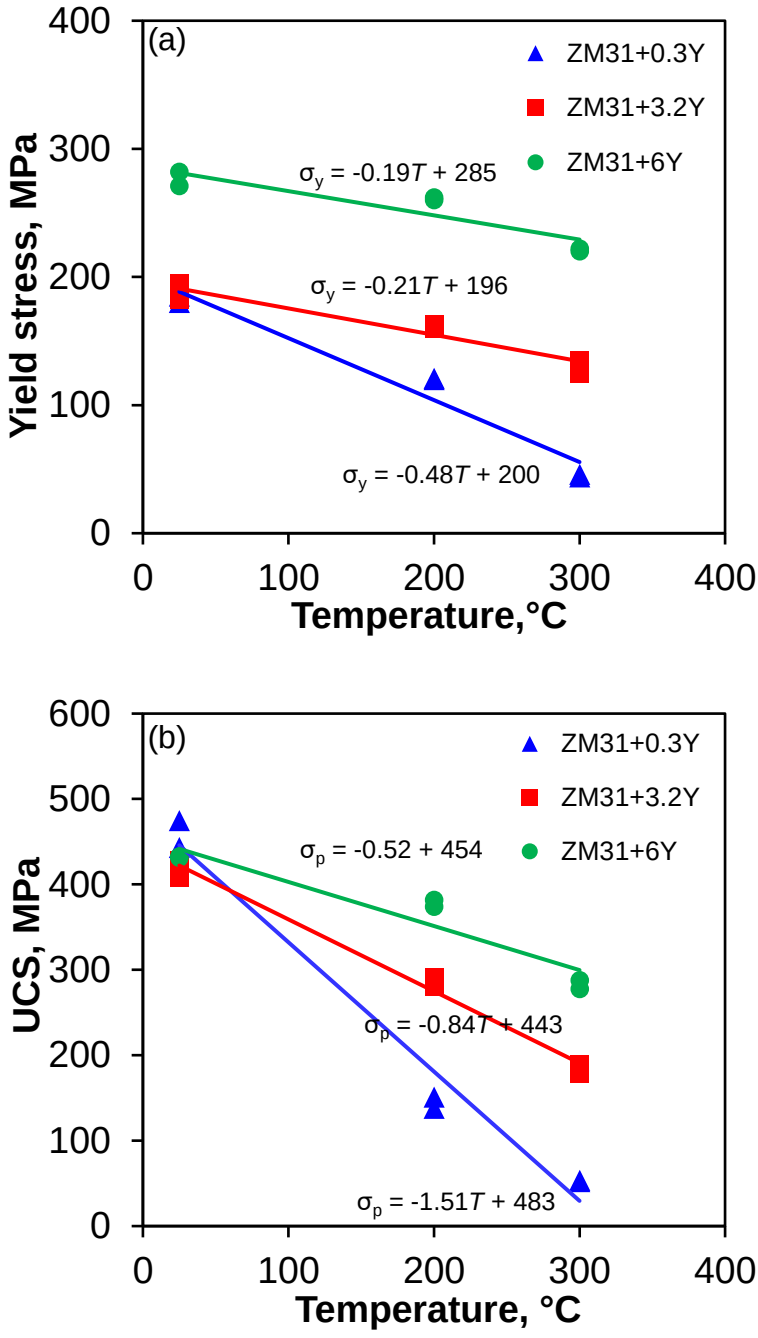

Figure 4.15: Variation of (a) yield strength and (b) UCS with test temperature.

To obtain a better understanding about how mechanical properties are related to Y content and temperature, the CYS and UCS of the alloys ZM31+0.3Y, ZM31+3.2Y and ZM31+6Y were plotted as a function of temperature in Fig. 4.15(a) and (b). It is seen that the CYS almost linearly

decreased with increasing temperature. The slope in the CYS vs. temperature followed a declining trend (0.48>0.21>0.19) with increasing Y content (0.3<3.2<6.0). Similar results were also observed in the case of UCS. This indicated that the extent of loss of strength owing to increasing temperature decreased with increasing Y content. The improved strength at high temperatures could be credited to the presence of various phases arising from varying amounts of Y content. At RT, the presence of I-phase significantly strengthened ZM31+0.3Y alloy due to the low I-phase/matrix interfacial energy that resulted from almost coherent I phase/matrix interface [35], and the formation of W-phase along with I-phase in alloy ZM31+3.2Y caused a drop in the UCS due to the weak bonding in W-phase/matrix interfaces [42]. However, at elevated temperatures I-phase was reported to be not an important strengthening phase; indeed the thermal stability of the ternary Mg-Zn-Y phases followed a sequence of I-phase<W-phase<LPSO X-phase [25,185]. Due to the presence of thermally-stable LPSO X-phase and $Mg_{24}Y_5$ [40], alloy ZM31+6Y retained much of its strength even at high temperatures.

4.7 High Temperature Strain Hardening

Fig. 4.16(a and b) show the plot of strain hardening rate ($\theta = \frac{d\sigma}{d\varepsilon}$) during compression at 200°C and 300°C as a function of true strain ε for the studied alloys where σ is true stress. At both 200°C and 300°C, alloy ZM31+6Y showed a nearly normal strain hardening behavior where the strain hardening rate continuously decreased from the commencement of plastic deformation.

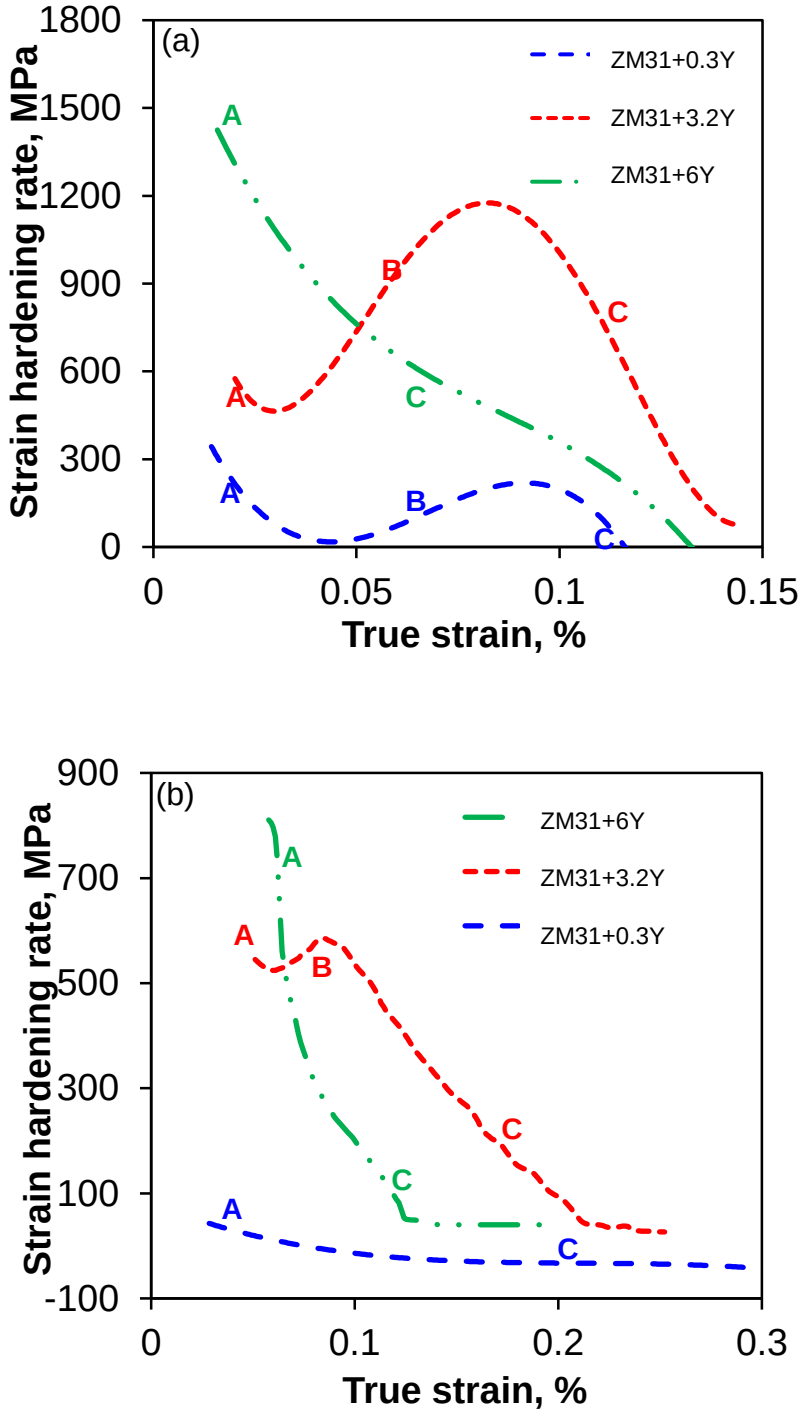

Figure 4.16: Variation of the strain hardening rate θ with true strain along the ED during compression at (a) 200°C and (b) 300°C.

At 200°C the strain hardening rate of alloys ZM31+0.3Y and ZM31+3.2Y showed three distinct stages, where Stage A was characterized by a decreasing strain hardening rate, followed by Stage B with an increasing strain hardening rate and then Stage C with a decreasing strain hardening rate again. Similar trend in the strain hardening rate has also been observed during compressive deformation at RT [40]. In contrast, at 300°C alloys ZM31+0.3Y and ZM31+3.2Y demonstrated nearly falling strain hardening rate with the presence of a very short Stage B hardening in alloy ZM31+3.2Y (Fig. 4.16(b)). As mentioned previously, when deformation was dominated by slip, the true stress-true strain curve was characterized by a higher yield point and a falling strain hardening rate [161,168,169]. On the other hand, when deformation was governed by $\{10\bar{1}2\}$ extension twinning, the true stress-true strain curve was reflected by a lower yield point and the strain hardening rate exhibited three distinguishable stages [168–171,173,186]. A considerably higher CYS of alloy ZM31+6Y, at 200°C as shown in Fig. 4.13 and the corresponding strain hardening curves (Fig.4.16(a)), pointed towards the slip-dictated deformation in alloy ZM31+6Y and twinning-dictated deformation in alloys ZM31+0.3Y and ZM31+3.2Y. In contrast, the true stress-true strain curve at 300°C (Fig. 4.14) and the corresponding strain hardening curves (Fig. 4.16(b)) indicated slip-dictated deformation in all the three alloys. This suggested that the increase in temperature altered the deformation mode from twinning to slip. Similar enhancement in the slip activity through the activation of prismatic and pyramidal slip systems was also reported in a ME20 magnesium alloy at high temperatures [50]. It is noteworthy that, with increasing temperature (300°C) the value of peak strain hardening rate between Stages B and C significantly declined in alloy ZM31+3.2Y, and indeed the ascending Stage B completely disappeared in alloy ZM31+0.3Y. While Stage A was related to the formation of $\{10\bar{1}2\}$ extension twins, the appearance of Stage B was mainly attributed to the twin-dislocation interactions and the resulting

twin growth [166,173,187]. The effect of twinning on strain hardening could be explained as follows [171,176]: (i) a large number of twin boundaries acting as barriers to dislocation movement; (ii) twin lamellae dividing grains and impeding dislocations movement by grain refinement; (iii) dislocations trapped inside twin boundaries changing from glissile to sessile; and thus increasing the strain hardening rate. Since the addition of rare-earth elements such as Y is recognized to suppress twin growth [19,119,183], no stage B hardening was ever observed in alloy ZM31+6Y. As high temperatures are known to promote dislocation movement by diffusion and discourage twin formation [50], thus the likelihood of interactions between the dislocations and twins in Stage B became lower, leading to a decreased value of peak strain hardening rate between stages B and C with increasing test temperature. The presence of trivial Stage B hardening in alloy ZM31+0.3Y at 200°C and in alloy ZM31+3.2Y at 300°C could be ascribed to the formation of some twins. The highly dispersed I-phase particles in alloy ZM31+0.3Y which was highly effective in improving strain hardening at RT through pinning dislocations as discussed in [40], could no longer impede dislocation movement as dislocations started to move by climb at high temperatures.

In order to obtain a better understanding about how the strain hardening parameters are related to Y content at high temperatures, the strain hardening exponents are evaluated using Hollomon's equation [73] and are plotted as a function of temperature in Fig. 4.17. At RT the strain hardening exponents generally decreased with increasing Y content. Also, a decreasing trend of strain hardening exponents was obvious with increasing temperature in all the materials. Furthermore, alloy ZM31+0.3Y exhibited a stronger drop in the value of strain hardening exponent at 200°C and reached nearly zero at 300°C, which pointed towards the significant strain softening of the alloy at high temperatures. This suggested that the presence of distinct phases particularly the

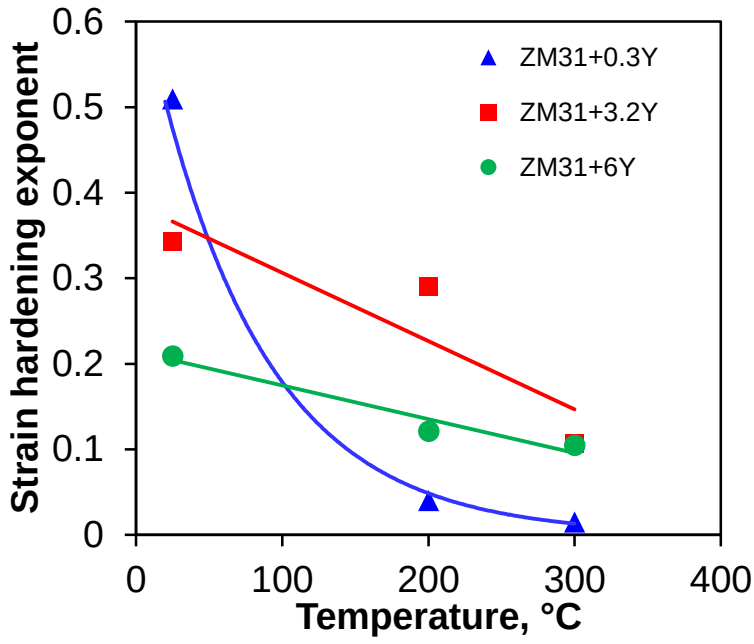

Figure 4.17: Effect of temperature on strain hardening exponent evaluated using Hollomon's equation.

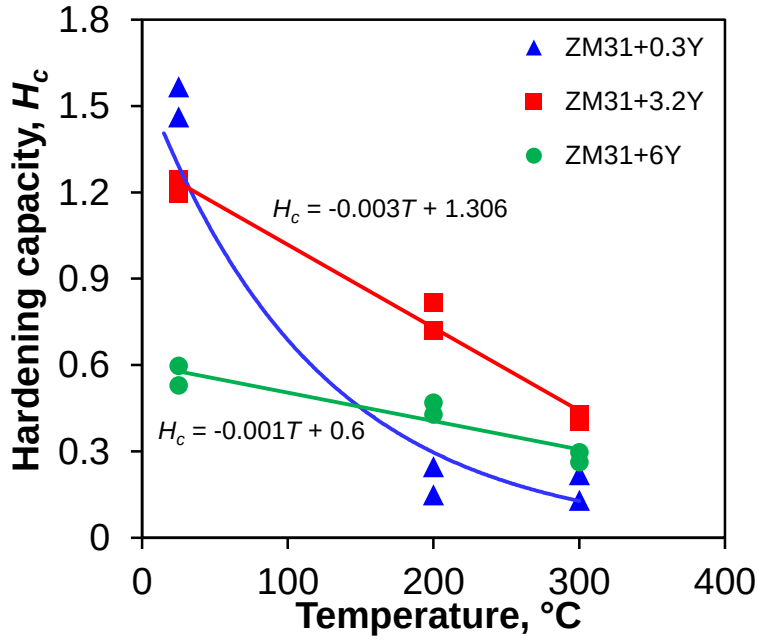

Figure 4.18: Variation of the hardening capacity (H_c) with temperature.

thermally-stable LPSO X-phase and $Mg_{24}Y_5$ in alloy ZM31+6Y and W-phase in alloy ZM31+3.2Y resisted strain softening at elevated temperatures.

Fig. 4.18 presents the plot of hardening capacity of the alloys ZM31+0.3Y, ZM31+3.2Y and ZM31+6Y evaluated using the following equation [74]:

$$H_c = \frac{\sigma_{ucs} - \sigma_{ys}}{\sigma_{ys}} \quad . \tag{4.1}$$

Similar to the strain hardening exponents in Fig. 4.17, alloy ZM31+0.3Y showed the highest hardening capacity, followed by alloys ZM31+3.2Y and ZM31+6Y at RT. The hardening capacity of all the materials decreased with increasing temperature, but had a different varying trend. The hardening capacity of alloy ZM31+0.3Y reflected a parabolic decrease, while a linear decrease was observed in the ZM31+3.2Y and ZM31+6Y alloys, which could be expressed as,

$$H_c = a + bT \, , \tag{4.2}$$

where a and b are two empirical constants (a = 1.3 and b = -0.003 obtained for ZM31+3.2Y alloy and a = 0.6 and b = -0.001 obtained for ZM31+6Y alloy in the present study). A parabolic change in the hardening capacity of alloy ZM31+0.3Y was expected since the alloy went through significant softening at 200°C, corresponding well to the change of the strain hardening exponent with test temperature.

4.8 Summary

In this Chapter, the strain hardening and deformation behavior of as-extruded ZM31 magnesium alloy with varying Y contents up to 6 wt.% was studied via compression testing both at RT and

elevated temperatures. The addition of Y significantly influenced the as-extruded microstructure in terms of grain morphology and second phase particles. When a Y content of 0.3% was added, the alloy showed a bimodal grain microstructure consisting of fine DRXed and elongated Un-DRXed grains and I-phase. When the Y content increased to 3.2%, the volume fraction of uniform DRXed grains increased, containing both I-phase and W-phase. With a further increase in Y content to 6%, multimodal microstructure was observed consisting of coarse grains, fine DRXed grains, LPSO X-phase and $Mg_{24}Y_5$ particles. The presence of quasicrystalline I-phase in the extruded alloy ZM31+0.3Y increased compressive yield strength, hardness, and Stage B strain hardening rate due to its resistance to the motion of dislocations and twinning. The extruded alloy ZM31+3.2Y exhibited lower hardness and Stage B hardening rate due to the co-existence of I- and W-phases. Both alloys ZM31+0.3Y and ZM31+3.2Y displayed a yield-point-like phenomenon or initial negative strain hardening rate. At 200°C alloys ZM31+0.3Y and ZM31+3.2Y still displayed three-stage strain hardening characteristic. With increasing Y content and temperature, Stage B strain hardening gradually disappeared. Strain hardening exponent and hardening capacity also showed a decreasing trend with increasing Y content and temperature. In comparison with alloys ZM31+0.3Y and ZM31+3.2Y, while the strain hardening exponent and hardening capacity were lower in alloy ZM31+6Y, the decrease of these values with increasing temperature was relatively small, mainly due to the presence of thermally-stable LPSO X-phase.

CHAPTER 5

5. RECRYSTALLIZATION AND RELATIVE ACTIVITY‡

5.1 Introduction

Micro-alloying with RE elements can weaken the extrusion texture and thus improve the formability [188,189]. The extent of texture weakening via alloying depends on the RE element and its solid solubility in Mg [158,190]. Alloying elements are known to alter the deformation mechanisms through hardening or softening of different slip modes and twinning response [64,116]. Twinning can be activated and lead to a rapid texture evolution even at elevated temperatures [98,99] when RE is added depending on the choice of RE and its content [191]. It is therefore essential to ascertain the impact of individual RE element on deformation activity which is linked to texture evolution. It is also known that the processing of magnesium alloys at elevated temperatures is predominantly accompanied by recovery and recrystallization (DRX) [91]. The present Chapter focuses on the Y content and temperature-dependence of slip and twinning interplay in relation to recrystallization.

‡ This chapter is based on the following publications of the author:

1. N. Tahreen, D.F. Zhang, F.S. Pan, X.Q. Jiang, D.Y. Li, D.L. Chen, Microstructure and texture evolution in a yttrium-containing ZM31 alloy: Effect of pre- and post-deformation annealing, *Metallurgical and Materials Transactions B*, (2015) 1-8.
2. N. Tahreen, D.F. Zhang, F.S. Pan, X.Q. Jiang, D.Y. Li, D.L. Chen, Texture evolution and deformation activity of an extruded magnesium alloy: Effect of yttrium and deformation temperature, *Journal of Alloys and Compounds* 688 (2016) 270-284.

5.2 Study of Static Recrystallization

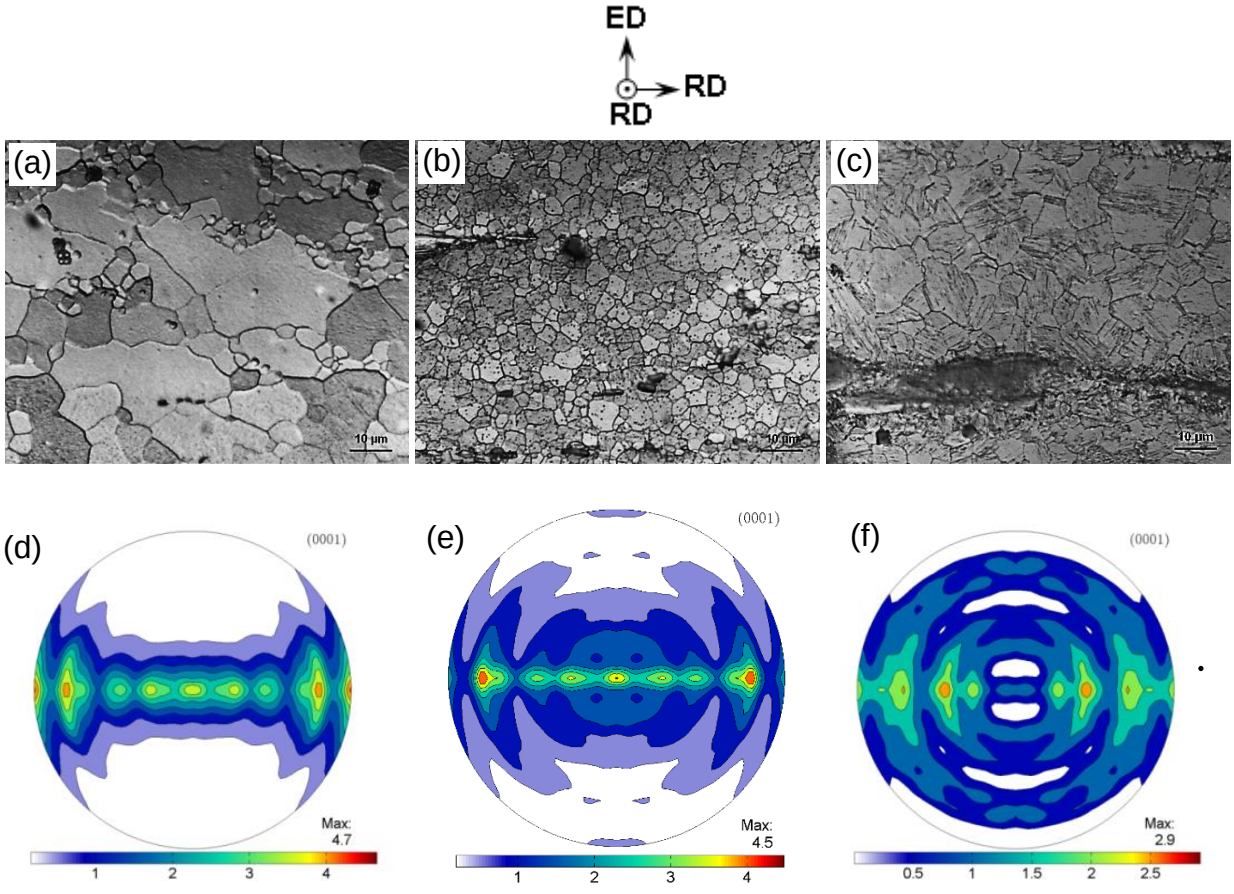

Figure 5.1: Typical microstructures and the corresponding (0001) pole figures of as-extruded alloys of (a, d) ZM31, (b, e) ZM31+3.2Y and (c, f) ZM31+6Y, respectively, where ED indicates the extrusion direction and RD stands for the radial direction.

Fig. 5.1(a)-(c) shows the optical micrographs of as-extruded alloys ZM31, ZM31+3.2Y and ZM31+6Y, respectively. The microstructures of the alloys under study exhibited a significant change in terms of grain morphology and second phase particles due to Y addition. Fig. 5.1(d)-(f) shows the (0001) pole figures of the as-extruded alloys ZM31, ZM31+3.2Y and ZM31+6Y, respectively. It is seen that alloy ZM31 exhibited a typical strong basal texture along the radial direction (RD) with a maximum texture intensity value of 4.7 MRD (multiples of random

distribution). It indicated that the basal planes of most grains were approximately aligned with the ED or the *c*-axes of most grains were perpendicular to the ED. With increasing Y content especially from 3.2% to 6% the maximum texture intensity values became significantly lower and the qualitative characters of the texture depicted a more scattered distribution of basal poles. The role of RE elements on the texture weakening of magnesium alloys during deformation processing is well recognized [41,117,160,192]. The promotion of nonbasal slip and suppression of grain boundary mobility are known as solid solution-based mechanisms responsible for the observed texture weakening phenomenon in Mg rare earth alloys [192]. As a result, the maximum texture intensity values in the as-extruded alloys decreased with increasing Y content.

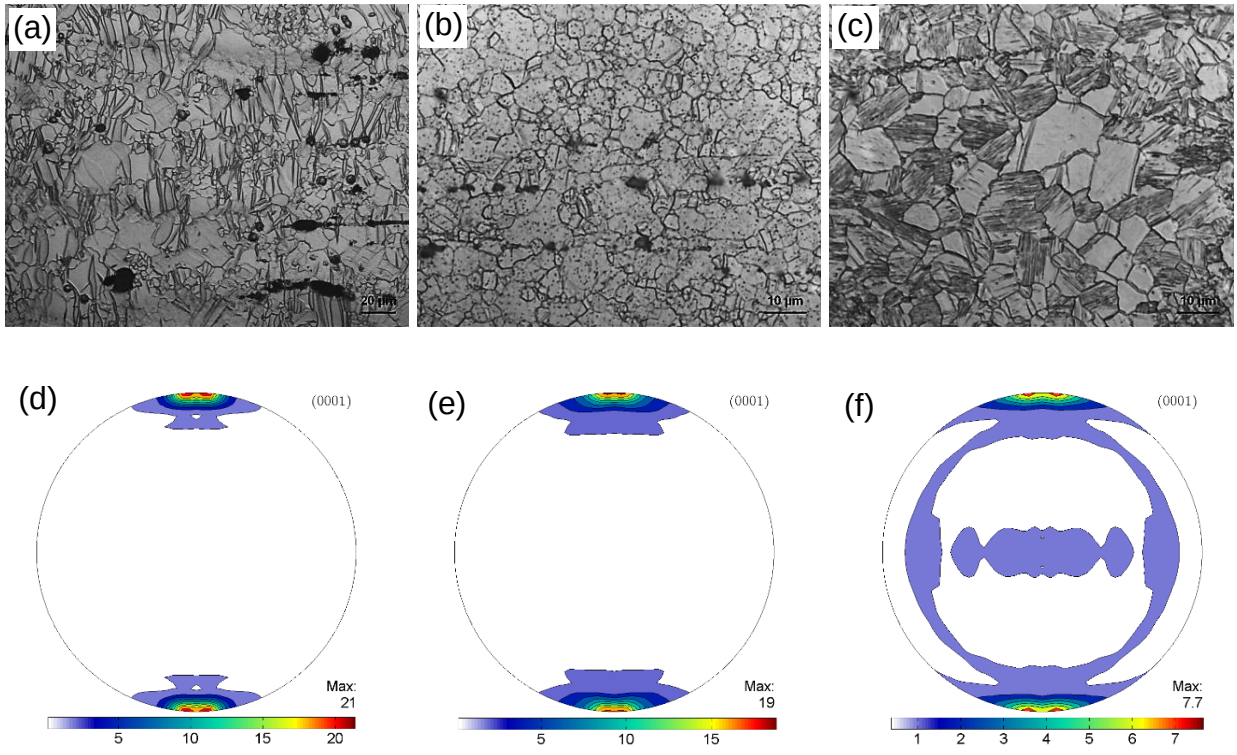

Figure 5.2: Typical microstructures and the corresponding (0001) pole figures of 10% compressed alloys of (a, d) ZM31, (b, e) ZM31+3.2Y and (c, f) ZM31+6Y, respectively.

The optical micrographs of the deformed microstructure after 10% compression are shown in Fig. 5.2(a)-(c), respectively, to examine the occurrence of deformation twins. The presence of extensive deformation twins (extension twins $\{10\bar{1}2\}$) could be seen in most grains in the ZM31 alloy, whereas fewer deformation twins occurred in some grains in the ZM31+3.2Y alloy. The microstructure of compressed ZM31+6Y alloy barely demonstrated any twin. Therefore this alloy appeared to exhibit a mixed mode of deformation involving both dislocation slip and twinning. The increase in the slip activity was attributed to an increase in the Y content. Similar enhancement in the slip activity was also observed in the Mg-RE alloy due to favorable grain rotations [174]. The changes of texture after compression are shown in Fig. 5.2(d)-(f). After compressive deformation to 10%, the basal (0001) pole of alloy ZM31 presented a maximum intensity of 21 MRD towards the compression direction (CD) or ED. This implies that the *c*-axes of hcp unit cells in nearly all grains rotated towards anti-compression direction. In alloy ZM31+3.2Y, the maximum intensity in that direction became lower (19 MRD) and in alloy ZM31+6Y such intensity towards the CD was much lower (7.7 MRD), again with a fairly scattered distribution. This clearly reflected the beneficial role of adding Y in the Mg alloy.

Fig. 5.3(a)-(c) shows the optical micrographs of the investigated alloys subjected to annealing followed by compression. The as-extruded alloys were annealed at 723 K (450°C) for 60 minutes and then compressed up to a strain amount of 10% as well. The alloys exhibited a lesser extent of deformation twinning in the pre-annealed and compressed condition relative to solely compressed condition (Fig. 5.2). As shown in Fig. 5.3(a)-(c), there were fewer twins, as compared with Fig. 5.2(a)-(c). Moreover, the pre-annealed and compressed materials showed an obvious decrease in the twin volume fraction with increasing Y content. No twin was noticeable in pre-annealed

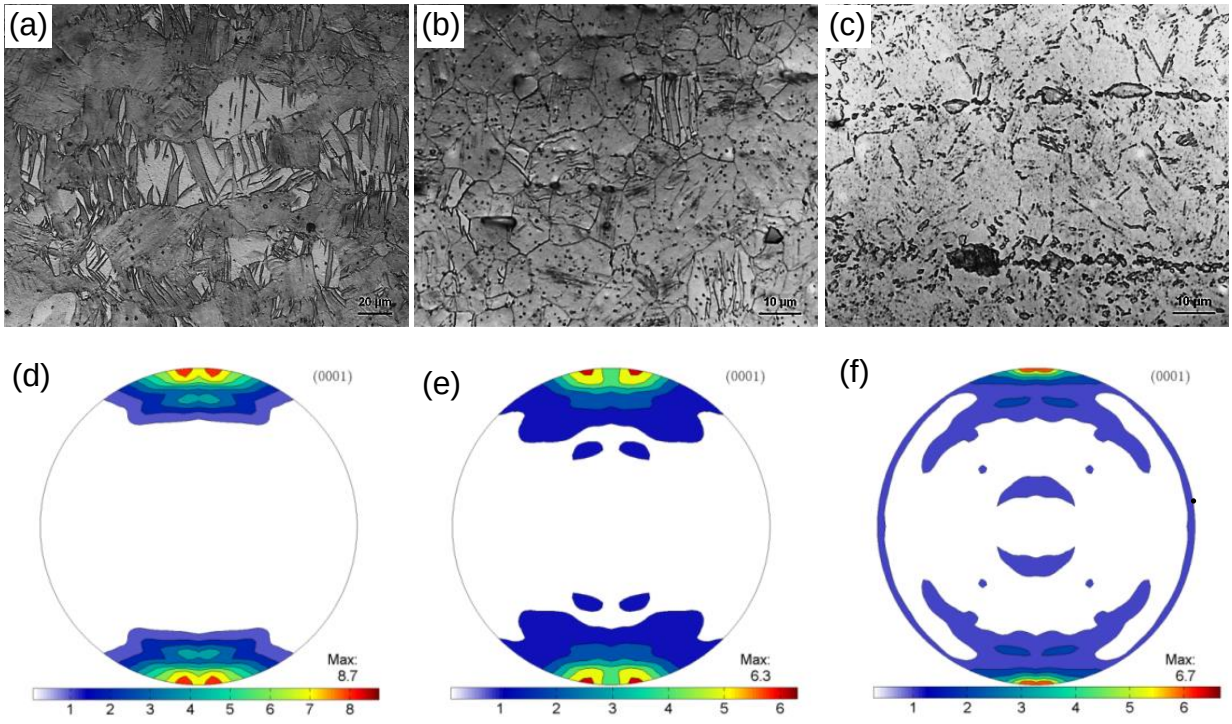

Figure 5.3: Typical microstructures and the corresponding (0001) pole figures of pre-annealed (450°C, 1 hour) and compressed (10%) alloys of (a, d) ZM31, (b, e) ZM31+3.2Y and (c, f) ZM31+6Y, respectively.

ZM31+6Y alloy after compression to 10%. The evolved microstructures as shown in Fig. 5.3(a)-(c) were also consistent with the texture data shown in Fig. 5.3(d)-(f) which indicated relatively weaker textures. This was reflected by the considerable decrease in the intensity of (0001) poles for alloys ZM31 and ZM31+3.2Y upon compression of pre-annealed samples relative to just compressed samples. There was only a moderate decrease from 7.7 to 6.7 in the intensity of (0001) poles for ZM31+6Y alloy. While the same rotation of the *c*-axes of grains towards the anti-compression direction was observed during the compression (Fig. 5.3(d-f)), it had a less intense rotation of basal (0001) poles, compared with those after a compression to the same total strain amount of 10% without any annealing (Fig. 5.2(d-f)). This suggested that an annealing

substantially altered the microstructure, grain size and texture formation. This might be due to unfavorable *c*-axis orientation for twinning as a consequence of annealing.

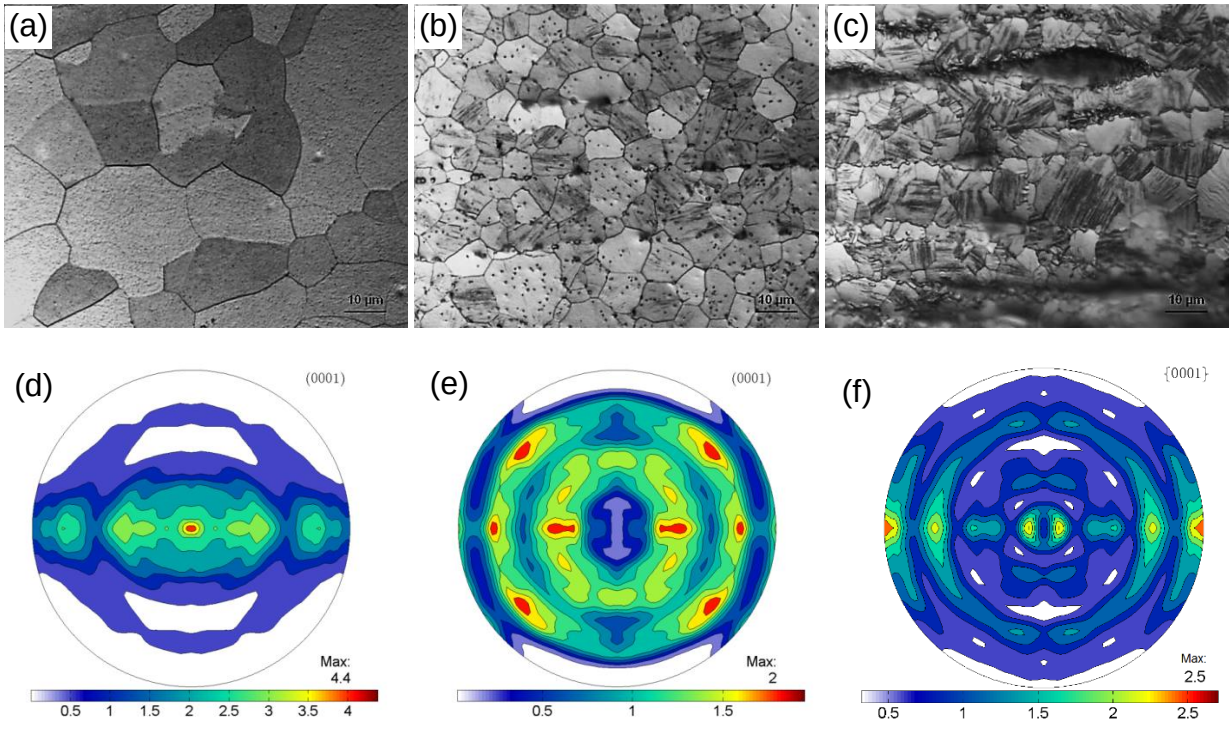

Figure 5.4: Typical microstructures and the corresponding (0001) pole figures of annealed (450°C, 1 hour) Mg alloys of (a, d) ZM31, (b, e) ZM31+3.2Y, and (c, f) ZM31+6Y, respectively.

To further understand the role of annealing, the microstructure and texture of samples solely annealed at 723 K (450°C) for 60 minutes (without pre- or post-compression) were examined, as shown in Fig. 5.4. It is seen from Fig. 5.4(a-c) that the grain size increased as a result of annealing. The average grain size of annealed ZM31, ZM31+3.2Y and ZM31+6Y became about 22.5, 6.2 and 5.9 µm. Alloy ZM31 exhibited the largest grain growth followed by ZM31+3.2Y and ZM31+6Y, which was expected as the presence of Y containing particles restrained grain growth by pinning grain boundaries [40]. Although no drastic change was noted, the texture of the

annealed samples was weakened to some extent in the annealing process as seen from Fig. 5.4(d-f).

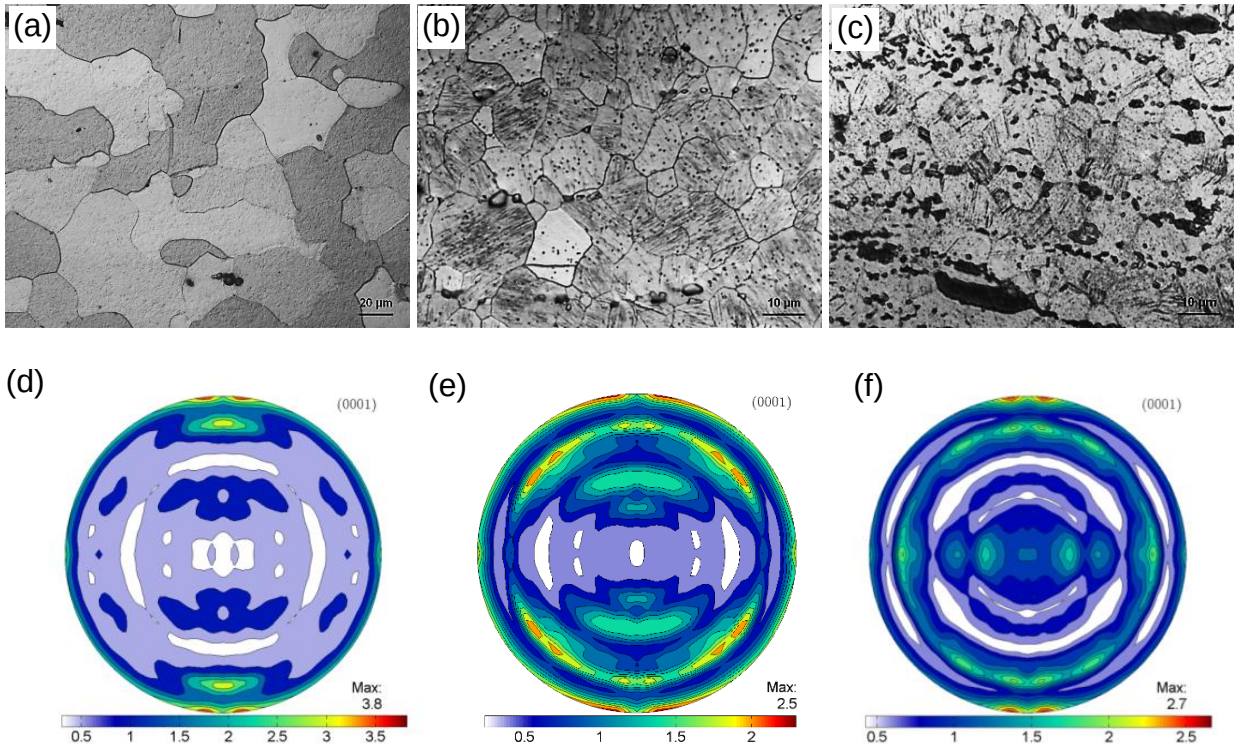

Figure 5.5: Typical microstructures and the corresponding (0001) pole figures of pre-compressed (10%) and annealed (450°C, 1 hour) alloys of (a, d) ZM31, (b, e) ZM31+3.2Y and (c, f) ZM31+6Y, respectively.

Fig. 5.5(a)-(c) shows the optical micrographs of the studied alloys subjected to pre-compression followed by annealing, which was reverse to the situation shown in Fig. 5.3. In this case the as-extruded alloys were compressed up to a strain amount of 10% and subsequently annealed at 723 K (450°C) for 60 minutes. The microstructural examinations of pre-compressed and annealed alloys revealed extensive thermally activated recovery which was reflected by the disappearance of twins. The result was also supported by the lower texture intensity as shown in Fig. 5.5(d)-(f). Since the overall texture has changed and weakened, there must have been recrystallized grains

that formed from twinned grains. Therefore, the vanishing of twins was attributed to extensive recovery and the occurrence of static recrystallizations. This was corroborated by the orientation maps via EBSD analysis since recrystallization is generally complemented by a change in grain structure and orientations. To warrant sufficient increase in recrystallization progression, the samples were further annealed at 723 K (450°C) for additional one hour for EBSD analysis. The recrystallized, substructured and deformed grains with blue, green and red color in alloys ZM31, ZM31+3.2Y and ZM31+6Y were screened and partitioned using HKL Channel 5 software, as shown in Fig. 5.6(a)-(c). It is seen that recrystallization was not complete even after extended annealing. In particular, the alloys with a higher Y content showed lesser complete proceedings of recrystallization. Fig 5.7 compares the recrystallized fraction of the 10% pre-compressed alloys after annealing at 723 K (450°C) for 2 hours. At this point, 82.5%, 66.3% and 46.4% of grains were fully recrystallized in alloys ZM31, ZM31+3.2Y and ZM31+6Y, respectively. The reduced extent of static recrystallization in the higher Y-containing alloys could possibly be due to the presence of lower deformation twinning and more Y enriched second-phase particles. According to Levinson *et al.* [108] twinning significantly contributed to the recrystallization as twinned regions contained a high level of stored energy that provided a driving force for recrystallization. As there were more twins in the pre-compressed alloy ZM31 than alloys ZM31+3.2Y and ZM31+6Y, static recrystallization could occur more comprehensively in alloy ZM31 compared with alloys ZM31+3.2Y and ZM31+6Y. In other words, the lowest tendency of twinning in alloy ZM31+6Y offered the minimum potentiality for the nucleation sites of recrystallization and therefore led to only 46.4% partially recrystallized microstructure. Furthermore, the presence of Y element could influence the static recrystallization behavior in two possible ways. Firstly, solute Y would segregate strongly to grain boundaries due to the large atomic size misfit with magnesium which was predicted to produce a solute drag pressure on migrating boundaries [193–195]. It is

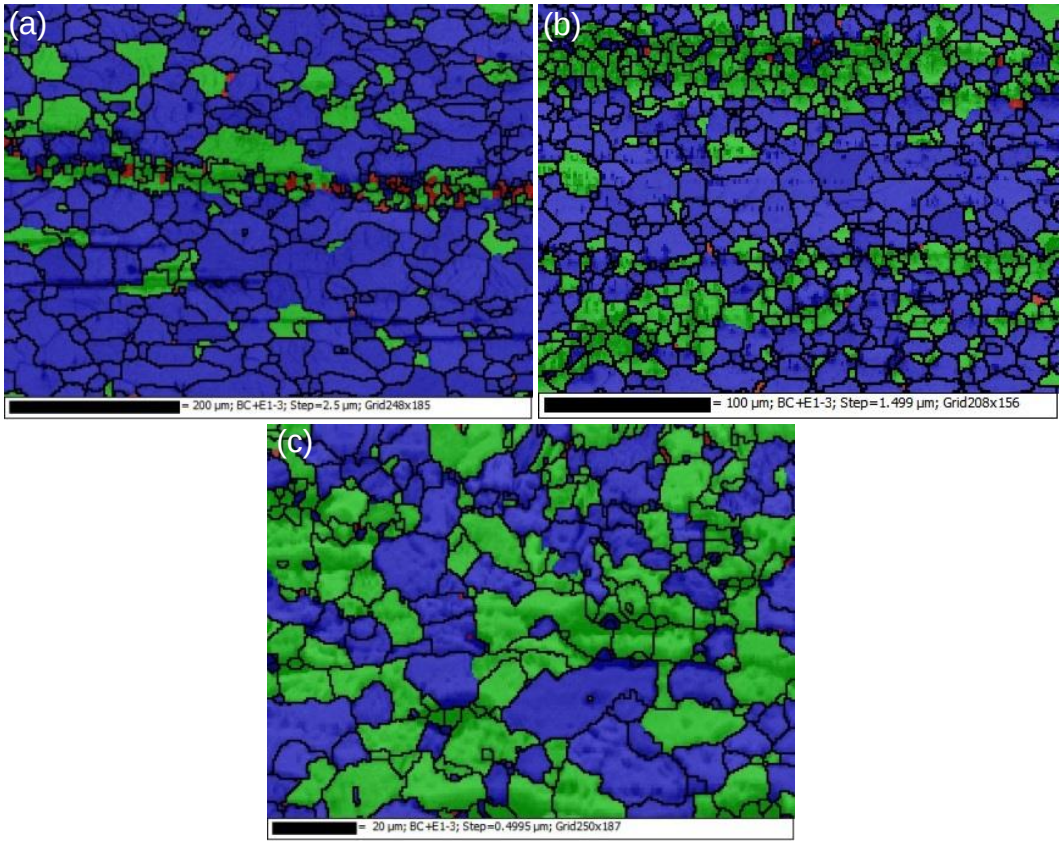

Figure 5.6: Orientation maps of pre-compressed (10%) and annealed (450°C, 2 hour) alloys of (a) ZM31, (b) ZM31+3.2Y, and (c) ZM31+6Y, respectively.

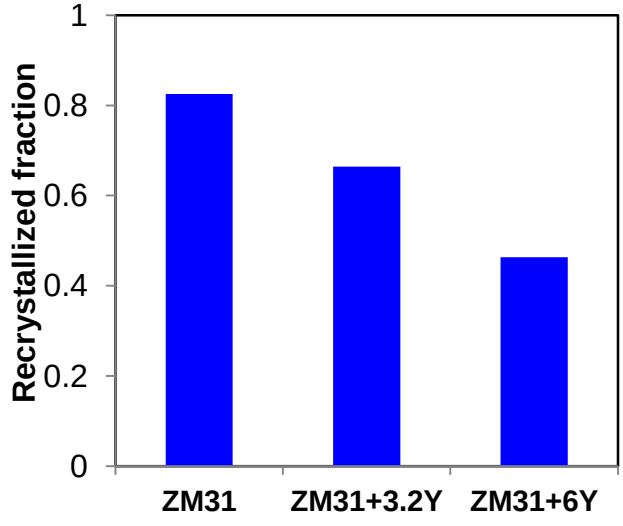

Figure 5.7: A comparison of the recrystallized fraction of pre-compressed (10%) and annealed (450°C, 2 hour) alloys of ZM31, ZM31+3.2Y, and ZM31+6Y, respectively.

possible that this drag was sufficient to strongly retard static recrystallization under static annealing conditions. Moreover, Y as a solute in the substitutional solid solution [196] would also increase the recrystallization temperature of the Mg alloys [197]. It is likely that the temperature required for initiation and continuation of recrystallization was high enough for alloys having a higher Y content such as ZM31+3.2Y and ZM31+6Y, giving rise to a partial completion of recrystallization at 723 K (450°C) for 2 hours (Figs. 5.6 and 5.7). Secondly, the homogenously distributed I- and W-phases in alloy ZM31+3.2Y and especially LPSO X-phase in alloy ZM31+6Y could conceivably suppress static recrystallization by restricting grain and twin boundary migration mainly via the effect of Zener pinning (or Zener drag) [112].

Fig. 5.8(a) shows the yield strength (YS) of alloys ZM31, ZM31+3.2Y and ZM31+6Y compressed along the ED in as-extruded, annealed and pre-compressed annealing [723 K (450°C), 1 hour] conditions. Since grain coarsening occurred during static annealing, the YS of the investigated alloys decreased considerably compared to as-extruded state. In particular, the pre-compressed annealing samples experienced a greater decrease in YS due to static recrystallization marked by recovery, nucleation and larger grain growth as compared to solely annealing condition. Fig. 5.8(b) presents the compressive fracture strain of the studied alloys in as-extruded, annealed and pre-compressed annealing [723 K (450°C), 1 hour] conditions. It is seen that the strain to failure of the as-extruded alloys increased with increasing Y content in a sequence of ZM31, ZM31+3.2Y and ZM31+6Y, which corresponded well to the initial texture information (Fig. 5.1(d-f)).

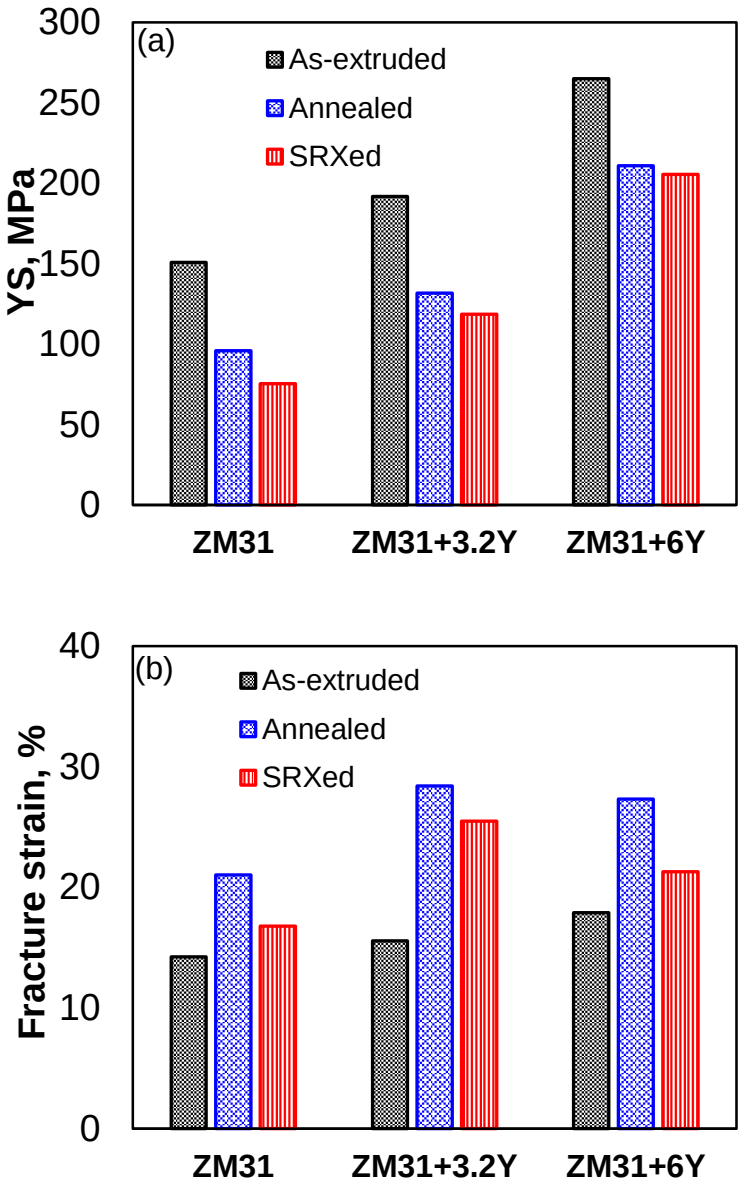

Figure 5.8: A comparison of the (a) YS and (b) fracture strain of as-extruded, annealed (450°C, 1 hour) and pre-compressed (10%) and annealed (450°C, 1 hour) alloys of ZM31, ZM31+3.2Y, and ZM31+6Y, respectively.

Moreover, annealing and pre-deformation annealing led to an improvement in the fracture strain along with texture weakening.

5.3 Study of Dynamic Recrystallization and Relative Activity

5.3.1 Initial EBSD texture

Fig. 5.9 shows the initial EBSD maps (both grain orientation maps (a-c) and the corresponding inverse pole figures (IPFs) (d-f)) of as-extruded alloys ZM31+0.3Y, ZM31+3.2Y and ZM31+6Y, respectively, where the grain orientations in Fig. 5.9(a-c) can be seen by referring to the map color legend. The microstructures of the alloys revealed a significant difference in terms of grain size and its distribution. Alloy ZM31+0.3Y exhibited a partially recrystallized bimodal microstructure in the presence of both elongated and fine uniform grains, whereas alloy ZM31+3.2Y exhibited fully recrystallized microstructure with a uniform grain size distribution. The presence of more dynamically recrystallized (DRXed) regions in alloy ZM31+3.2Y, compared with alloy ZM31+0.3Y, suggested that the DRX during hot extrusion occurred more comprehensively with increasing amount of Y from 0.3% to 3.2%. It should be noted that, when Y content is 0.3% the phase present is I-phase (Mg_3YZn_6); with Y increasing to 3.2% the main phases in the alloy include both I-phase and W-phase ($Mg_3Y_2Zn_3$) [40,41]. The EBSD map of alloy ZM31+6Y presented a distinctive multi-modal grain structure containing LPSO X-phase ($Mg_{12}YZn$). As shown in Fig. 5.9(c), a few coarse un-DRXed grains were embedded inside the fine DRXed grains. Because the AztecHKL EBSD system was unable to analyze the Kikuchi diffraction patterns from the LPSO phase owing to the large amount of residual strain, the LPSO phase appeared in white color in Fig. 5.9(c), indicating an area with a low confidence index [151,198].

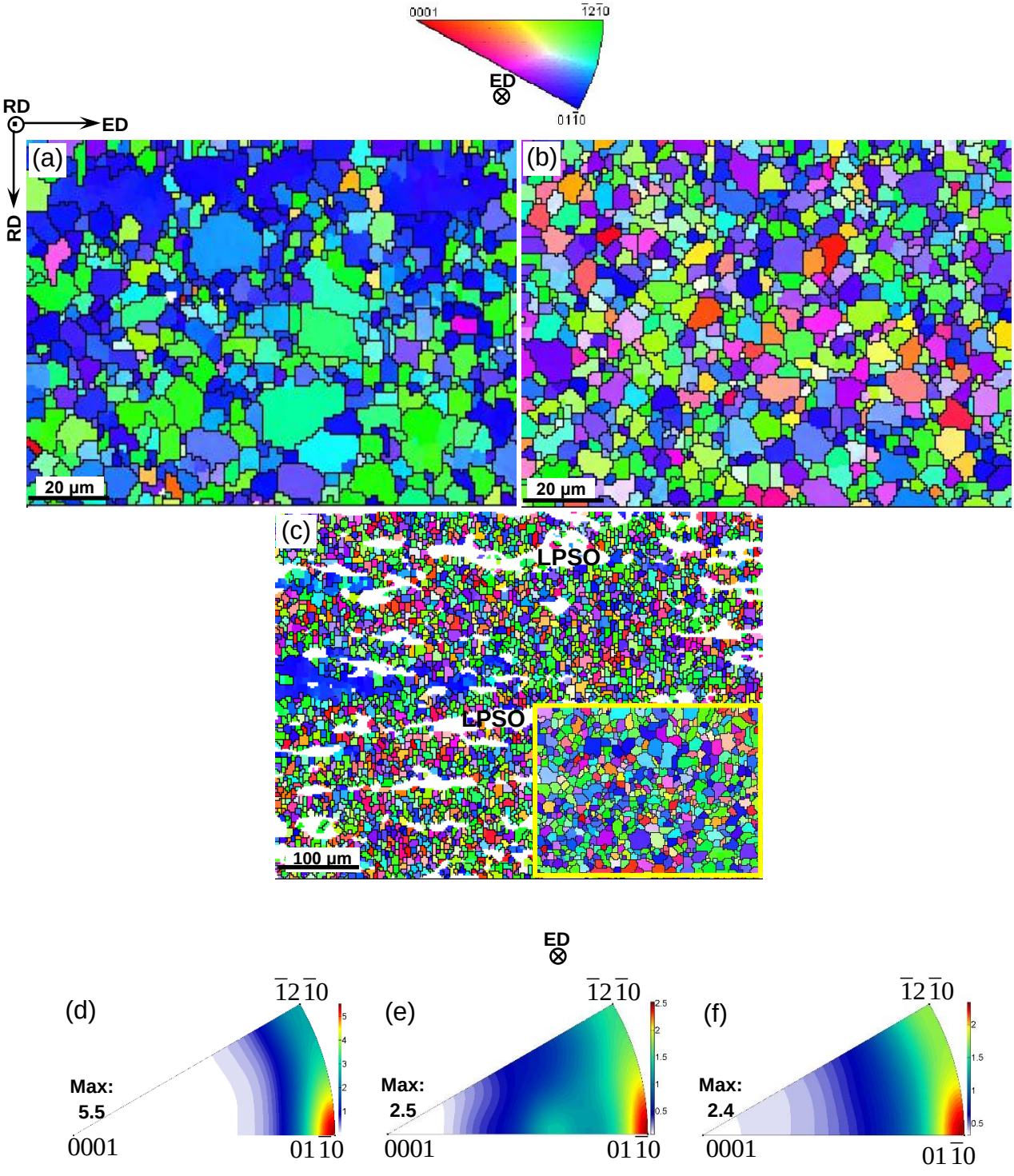

Figure 5.9: Orientation maps and the corresponding inverse pole figures (IPFs) of (a, d) ZM31+0.3Y, (b, e) ZM31+3.2Y, and (c, f) ZM31+6Y, respectively, where both map color legend and IPF project the direction parallel to both the ED and the surface of observation.

The coarse un-DRXed grains were observed to have a strong basal texture with (0001) plane and <01$\bar{1}$0> direction parallel to the ED. On a closer examination, a magnified narrow-scan region of alloy ZM31+6Y selected from a fine DRXed zone is shown as an inset of Fig. 5.9(c), which revealed almost randomized crystallographic orientations with more assorted colors. The more color distribution in the microstructure of the alloys with increasing Y content indicated more diverse alignments of grains with respect to the ED. The crystallographic directions of the alloys could be better seen in the form of IPF (Fig. 5.9(d-f)). A continuous orientation spread between prismatic poles <01$\bar{1}$0> and <$\bar{1}$2$\bar{1}$0> is observed, with a more intense concentration towards the <01$\bar{1}$0> pole. This suggested most grains with their <01$\bar{1}$0> directions being oriented towards the ED. With increasing Y content, the maximum intensity decreased from 5.5 MRD (multiple of a random distribution) for ZM31+0.3Y to 2.5 MRD for ZM31+3.2Y to 2.4 MRD for ZM31+6Y, and a broader spread towards <0001> pole could be seen as well.

5.3.2 Texture evolution

The macrotextures of the as-extruded alloys ZM31+0.3Y, ZM31+3.2Y and ZM31+6Y are shown in Fig. 5.10(a-c) in the form of (0001) pole figures. Alloy ZM31+0.3Y exhibited a typical strong (0001) basal texture with a maximum texture intensity value of 8.1 MRD. It indicated that most grains had their basal planes parallel to the ED or *c*-axes perpendicular to the ED of the extruded round bar. Similar to the IPF intensity determined via EBSD (Fig. 5.9(d-f)), with increasing Y content the texture intensity determined via XRD decreased and the qualitative character of the pole figures also depicted a more scattered distribution of basal poles (Fig. 5.10(a-c)).

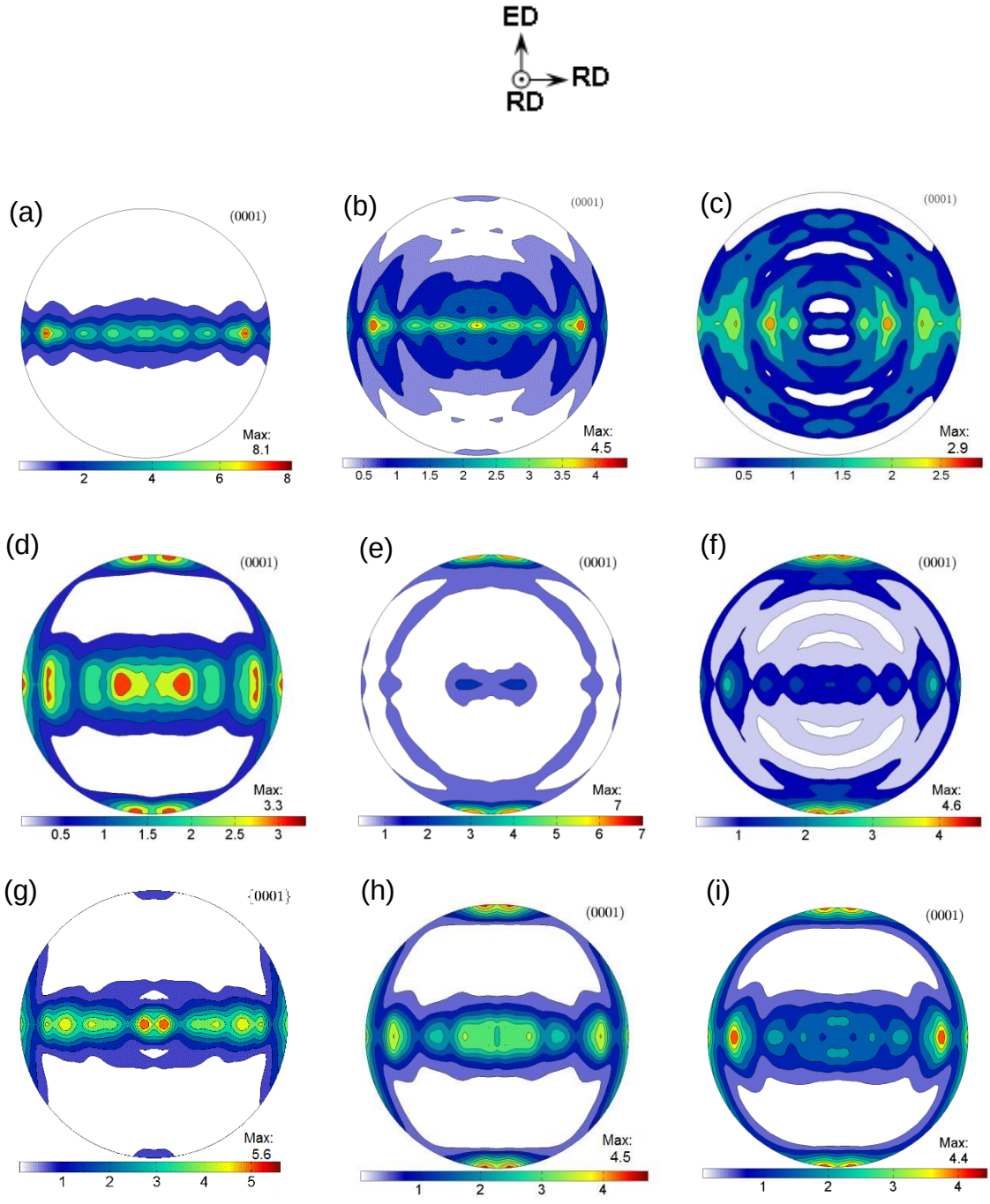

Figure 5.10: (0002) pole figures of ZM31+0.3Y (left), ZM31+3.2Y (middle) and ZM31+6Y (right), respectively, obtained from the samples (a-c) as-extruded, (d-f) compressed to 10% along the ED at 200°C, (g-i) compressed to 10% along the ED at 300°C, where ED stands for the extrusion direction and RD indicates the radial direction of extruded round bars.

Fig. 5.10(d-f) shows the (0001) pole figures of ZM31+0.3Y, ZM31+3.2Y and ZM31+6Y alloys, respectively, which were obtained from the samples compressed to 10% along the ED at 200°C.

For alloy ZM31+0.3Y, the initial texture was preserved to some extent and the texture intensity decreased significantly (from 8.1 MRD to 3.3 MRD after compression), with some rotations of *c*-axes from the orientation perpendicular to the ED towards the ED (i.e., compression axis). Since the compression axis perpendicular to the basal pole was favorable for the $\{10\bar{1}2\}\langle 10\bar{1}\bar{1}\rangle$ extension twinning with a *c*-axis rotation of 86.3°, such a texture evolution during compression was expected. The developed texture suggested a mixed mode of deformation involving both twinning and slip. When Y content increased to 3.2%, the texture component corresponding to extension twinning intensified substantially with a maximum intensity of 7 MRD (i.e., the *c*-axes of most grains were rotated towards the ED direction, Fig. 5.10(e)), suggesting much more extensive twinning than slip. But with a further increase of Y content to 6%, the texture intensity lay in-between those of ZM31+0.3Y and ZM31+3.2Y. In comparison with ZM31+3.2Y, alloy ZM31+6Y exhibited a less extensive twinning or rotation of *c*-axes towards the anti-compression direction at 200°C. The observed changes in the texture were associated with the microstructures and especially the presence of solute and second phases in these alloys due to the Y addition, which will be verified further and discussed in the later section.

Fig. 5.10(g-i) shows the macrotextures of alloys ZM31+0.3Y, ZM31+3.2Y and ZM31+6Y after compression to a strain amount of 10% along the ED at 300°C in terms of (0001) pole figures. With increasing deformation temperature, the texture showed significant deviations from that of alloys compressed at 200°C (Fig. 5.10(d-f)). This implies that deformation temperature had a significant influence on texture formation. The texture in the alloy ZM31+0.3Y was close to that in the as-extruded state, but was slightly more diffused (Fig. 5.10(g)). This was because very few extension twins occurred during hot deformation at the higher temperature of 300°C, which was reflected by negligible rotations of *c*-axes towards the anti-compression direction. The main

deformation mechanisms at 300°C involved different slip modes which could scarcely modify the initial texture. In contrast, in the case of alloys ZM31+3.2Y and ZM31+6Y, the compression texture exhibited rotations of basal poles towards the ED to some extent (Fig. 5.10(h and i)). However, the extent of the *c*-axes rotation towards the ED due to twinning at 300°C was less pronounced than that at 200°C. Therefore, the final textures of ZM31+3.2Y and ZM31+6Y alloys compressed at 300°C pointed towards a mixed mode of deformation comprising mainly slip and less twinning.

It is clear that a significant change in textures occurred arising from the variation in both Y content and deformation temperature (Fig. 5.10). This directly reflected the underlying deformation mechanisms during hot compression. Increasing deformation temperature led to a decreasing critical resolved shear stress (CRSS) for different non-basal slip modes and thereby increasing the number of activated slip systems. It follows that the increase of deformation temperature endorsed the operation of different slip systems which contributed considerably to the deformation at higher temperatures. Also, the weakened texture owing to Y addition altered the grains from hard to soft orientations for favorable slip deformation. However, at a higher temperature of 300°C ZM31+0.3Y alloy exhibited enhanced slip activity compared with ZM31+3.2Y and ZM31+6Y alloys. This could be attributed to the lower CRSS value of the slip modes of the alloy. It is realized that apart from texture weakening, Y as a solute increased the CRSS value of individual slip systems known as solid solution strengthening. As Y content increased (Fig.5.10(g and i)), the solute strengthening of slip systems (i.e., the increase of slip resistance) instead contributed to a higher twinning incidence [191]. It is likely that in the ZM31+0.3Y alloy slip systems got activated abundantly due to a lower extent of solute strengthening, and thus led to mainly slip-dominated texture (Fig. 5.10(g)) during the hot deformation at 300°C. Further verification and analysis about

this point based on the EBSD study and polycrystal plasticity modeling will be presented in the subsequent sections.

5.3.3 Twinning

The results shown in Fig. 5.10 suggested that magnesium alloys with different amounts of Y did not go through the same activation scenario of slip and twinning even though the deformation conditions (temperature and strain amount) were kept identical. When an extruded sample was compressed along the ED, deformation was mainly governed by extension twinning at room temperature, but dislocation slip tended to take over at elevated temperatures. An active competition occurred between twinning and dislocation slip at the initial stage of hot compression. However, at the later stage of deformation, DRX occurred and consumed the twinned grains, thus weakening the texture and dominating the deformation microstructure. Therefore, an early stage of deformation was also chosen for EBSD analysis to capture the competitive nature between the twinning and slip. The representative EBSD orientation maps of alloy ZM31+0.3Y compressed at 200°C and 300°C at a strain level of 10% are shown in Fig. 5.11(a,b). The microstructure of ZM31+0.3Y deformed at 200°C exhibited fine DRX grains together with some large parent grains (Fig. 5.11(a)). The nucleated “necklace grains” due to DRX were clustered typically along the boundaries of parent grains. The presence of larger parent grains in the microstructure suggested incomplete proceedings of DRX. Since the samples were deformed only to a strain amount of 10%, DRX grains could not grow and overtake the parent grains.

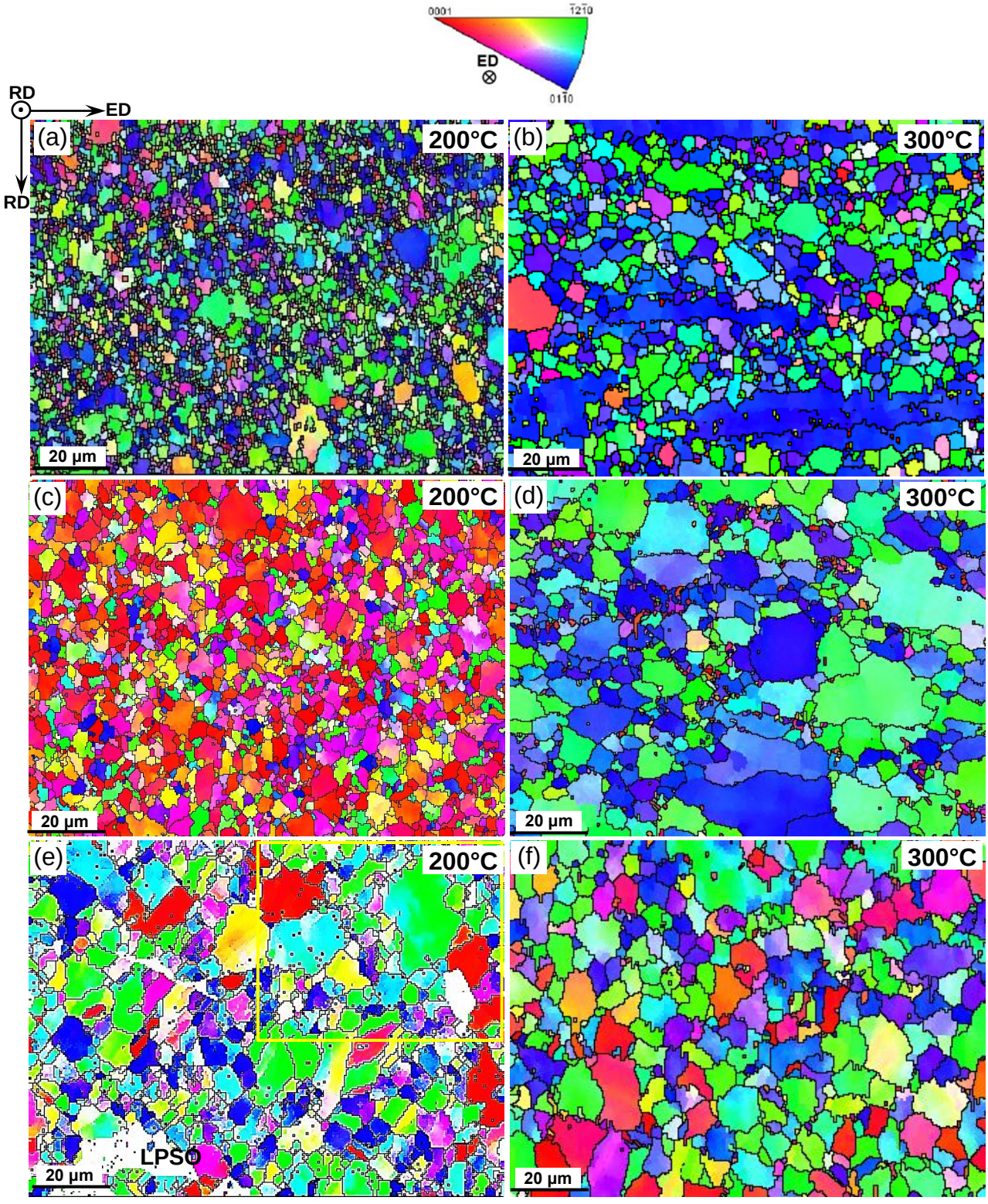

Figure 5.11: Orientation maps of alloys (a, b) ZM31+0.3Y, (c, d) ZM31+3.2Y, and (e, f) ZM31+6Y compressed at a strain amount of 10% at 200°C (left) and 300°C (right), respectively. Maps project the direction parallel to both the ED and the surface of observation.

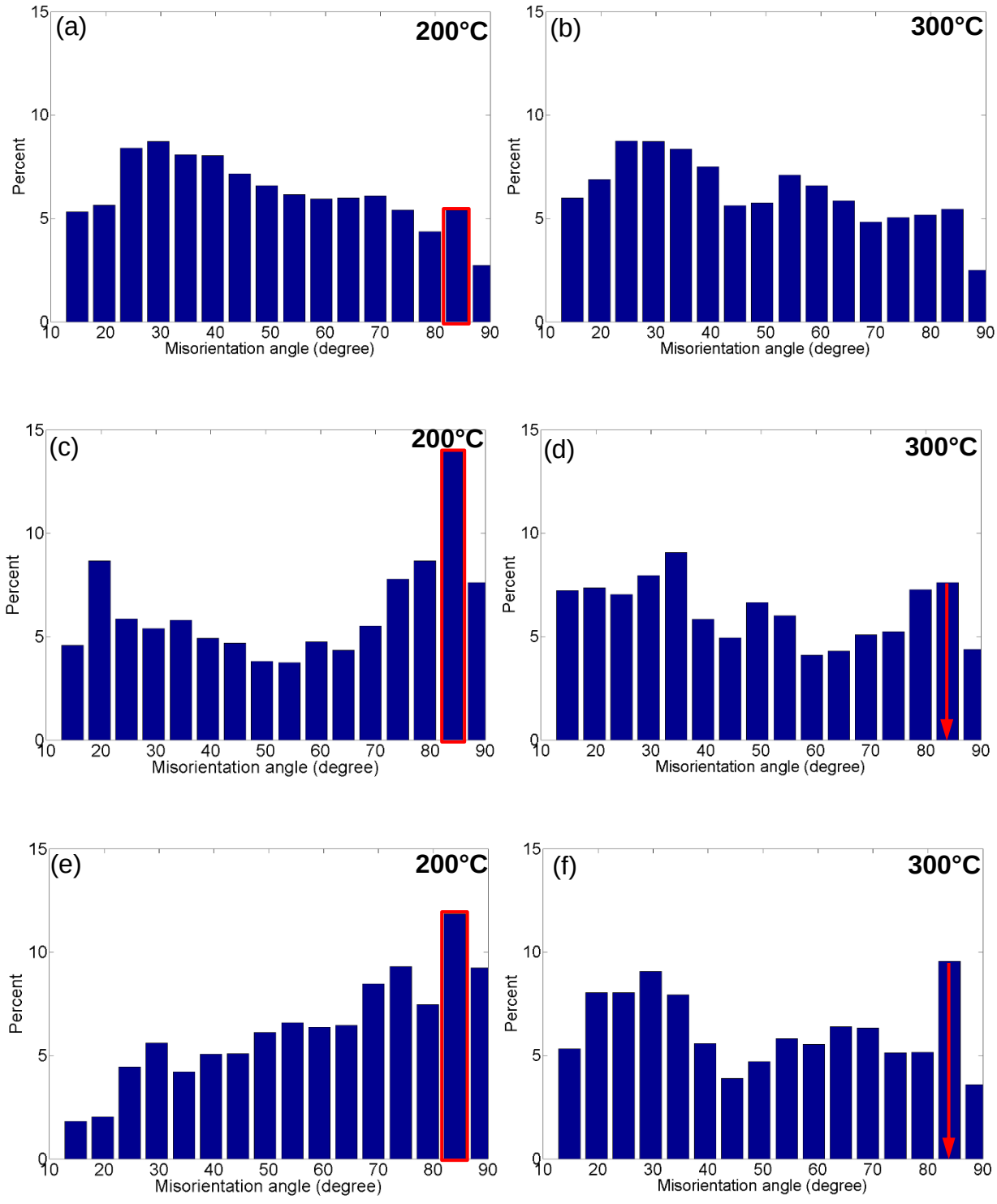

Figure 5.12: Misorientation angle distribution of alloys (a, b) ZM31+0.3Y, (c, d) ZM31+3.2Y, and (e, f) ZM31+6Y compressed at a strain amount of 10% at 200°C and 300°C, respectively.

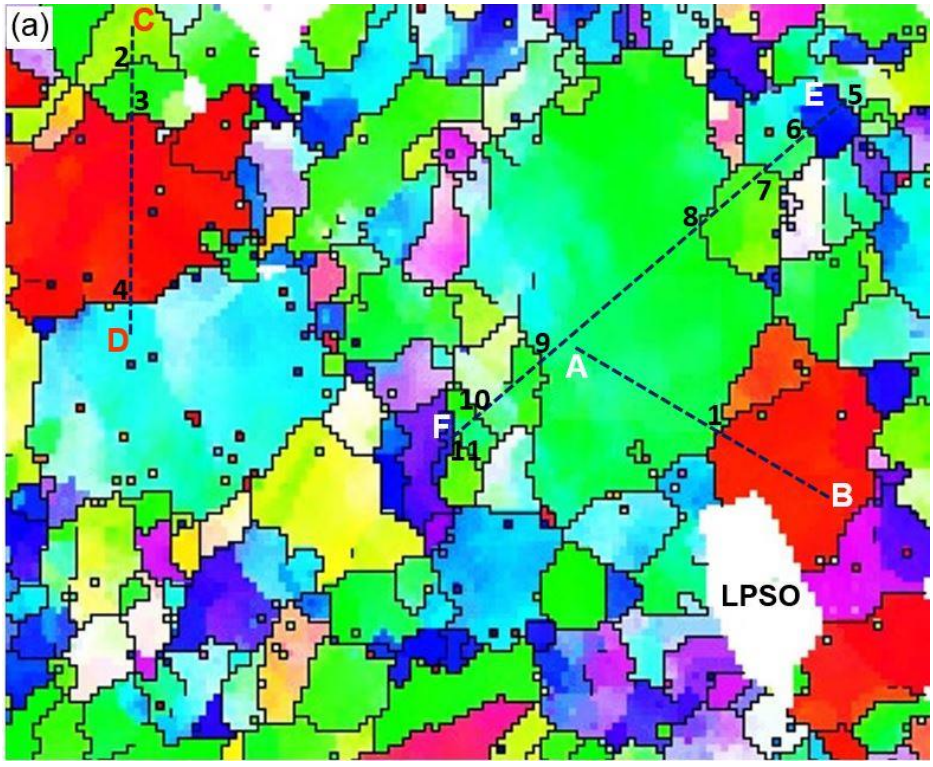
(a)
C
2
3
4
D
E
5
6
7
8
9
A
10
F
11
1
B
LPSO

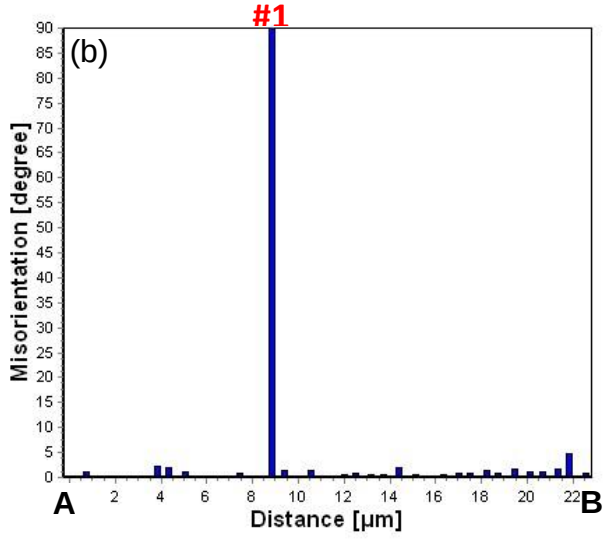
(b)
#1
Misorientation [degree]
Distance [μm]
A
B

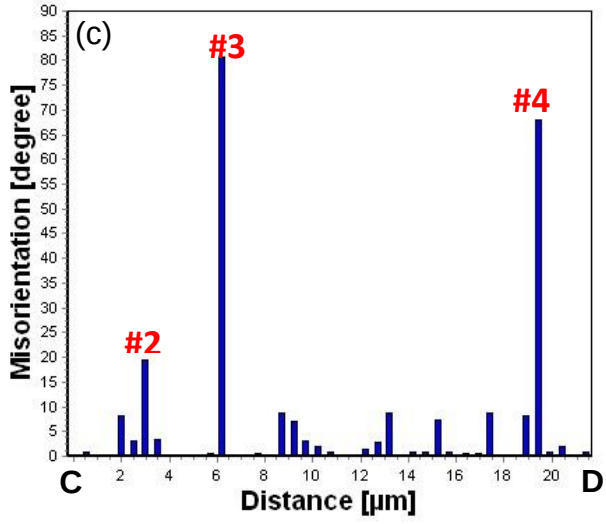
(c)
#2
#3
#4
Misorientation [degree]
Distance [μm]
C
D

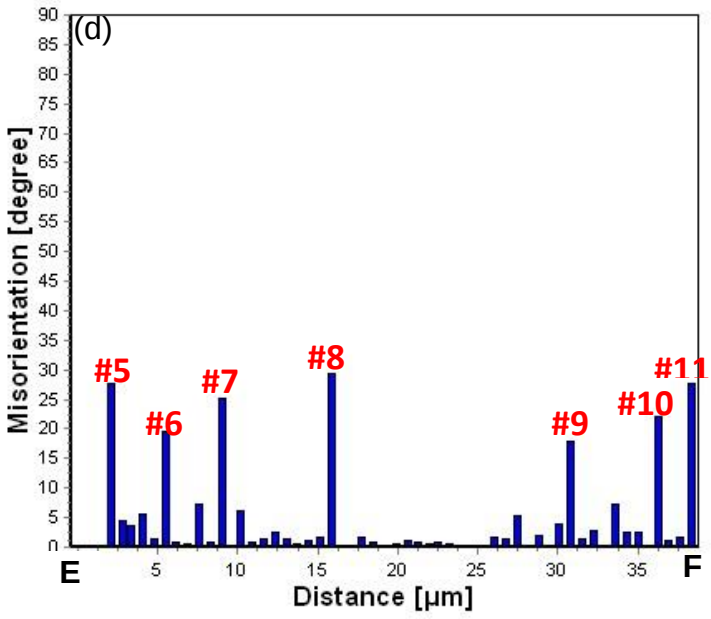

Figure 5.13: (a) A magnified orientation map of alloy ZM31+6Y compressed at a strain amount of 10% at 200°C, showing the misorientation profiles across various boundaries. (b, c, d) The corresponding misorientation profiles along lines AB, CD and EF as indicated in the map.

However, deformation twins provided enough room to modify the orientation of parent grains as extension twinning nucleated at a fairly low strain value and saturated quickly [171,184,187]. When the deformation temperature reached 300°C, grain growth occurred and the initially fine DRX grains grew and matured into an equiaxed morphology (Fig. 5.11(b)). The corresponding misorientation angle distribution also exhibited only a small peak around 86° which satisfied the condition of extension twin boundary misorientation (Fig. 5.12(a-b)). Therefore, in the low rare-earth alloy ZM31+0.3Y with increasing temperature an enhanced slip activity was apparent from the EBSD study, which was also confirmed by the XRD pole figures (Fig. 5.10(a,d,g)).

Fig. 5.11(c,d) shows the EBSD orientation maps of alloy ZM31+3.2Y compressed to a strain amount of 10% at 200°C and 300°C, respectively. When the deformation temperature was 200°C

(Fig. 5.11(c)), profuse extension twinning occurred, as indicated by the predominantly red-colored grains (i.e., the grains with their [0001] directions oriented toward ED by referring to the color legend), which overtook the majority of grains (Fig. 5.9(b)). The red grains in the orientation map (Fig. 5.11(c)) indeed revealed that the *c*-axes of most grains were rotated towards the ED direction, corresponding well to the pronounced texture with a maximum intensity of 7 MRD in Fig. 5.10(e) and a strong peak around 86° in the misorientation angle distribution shown in Fig. 5.12(c). All of these observations suggested the occurrence of substantial extension twinning in the ZM31+3.2Y alloy compressed along the ED at 200°C. As the deformation temperature increased to 300°C, dislocation slip activity increased and became a major contributor to the microstructure and texture. Consequently, the role of twinning was less significant (Fig. 5.11(d)) and the evolved texture revealed a less noticeable rotation of *c*-axes towards the ED with a reduced maximum density of 4.5 MRD (Fig. 5.10(h)). The misorientation angle of ~86° for extension twin-parent boundaries also corroborated such a reduction when the deformation temperature increased from 200°C to 300°C in the ZM31+3.2Y alloy (Fig. 5.12(c,d)). During hot deformation at 300°C DRX and grain coarsening dominated the overall microstructural evolution in this alloy, as seen from Fig. 5.11(d).

The EBSD orientation maps of alloy ZM31+6Y after compression at 200°C and 300°C are presented in Fig. 5.11(e,f). When compressed at 200°C, some grains were completely twinned, as indicated by the red grains in Fig. 5.11(e). Also, at a higher deformation temperature at 300°C a few red grains were observed (Fig. 5.11(f)). These results were also in agreement with the texture evolution (Fig. 5.10(f,i)) and the change in the misorientation angle of ~86° indicated in Fig. 5.12(e,f). This was related to the presence of LPSO phase in the ZM31+6Y alloy which strongly

hindered the formation of twins [164,198,199]. A magnified view of the region enclosed by a box in Fig. 5.11(e) is shown in Fig. 5.13(a), where non-indexed areas are shown in white color. To verify that the red grains were the twinned grains, the misorientation profiles were measured across a few typical lines (AB, CD and EF) and are presented in Fig. 5.13(b-d), respectively. Since the activation of an extension twin provokes a misorientation of ~86° between the twinned and untwinned lattice, a characteristic misorientation peak (peak #1) present at the grain boundary crossed by line AB from the $[\bar{1}2\bar{1}0]$-oriented green-colored grain to the [0001]-oriented red-colored grain confirmed the detection of extension twin. Similar characteristic peaks appeared along line CD when the boundary of the red grain was intersected (peaks #3 and #4). Besides, one additional peak (peak #2) was detected at a misorientation of about 20° which represented the original grain boundary with a typical misorientation of less than 30°. For the sake of further verification, a line EF was drawn traversing several non-red untwinned grains. It is clear that several peaks (peak #5-11) with a misfit of 10°-30° were present along line EF which corresponded to the untwinned grain boundaries, while several sub-grain boundaries with misorientations lower than 10° were also detected in the grain interior. It should be noted that the grain orientations of ZM31+6Y alloy after compression at 300°C (Fig. 5.11(f)) were similar to those in the initial extruded state (Fig. 5.9(c)), with fairly assorted grain colors, indicating that the slip was the underlying mechanism in the hot deformation.

To quantify the influence of Y content and deformation temperature on twinning extent, a further analysis using orientation distribution function (ODF) is presented in Fig. 5.14.

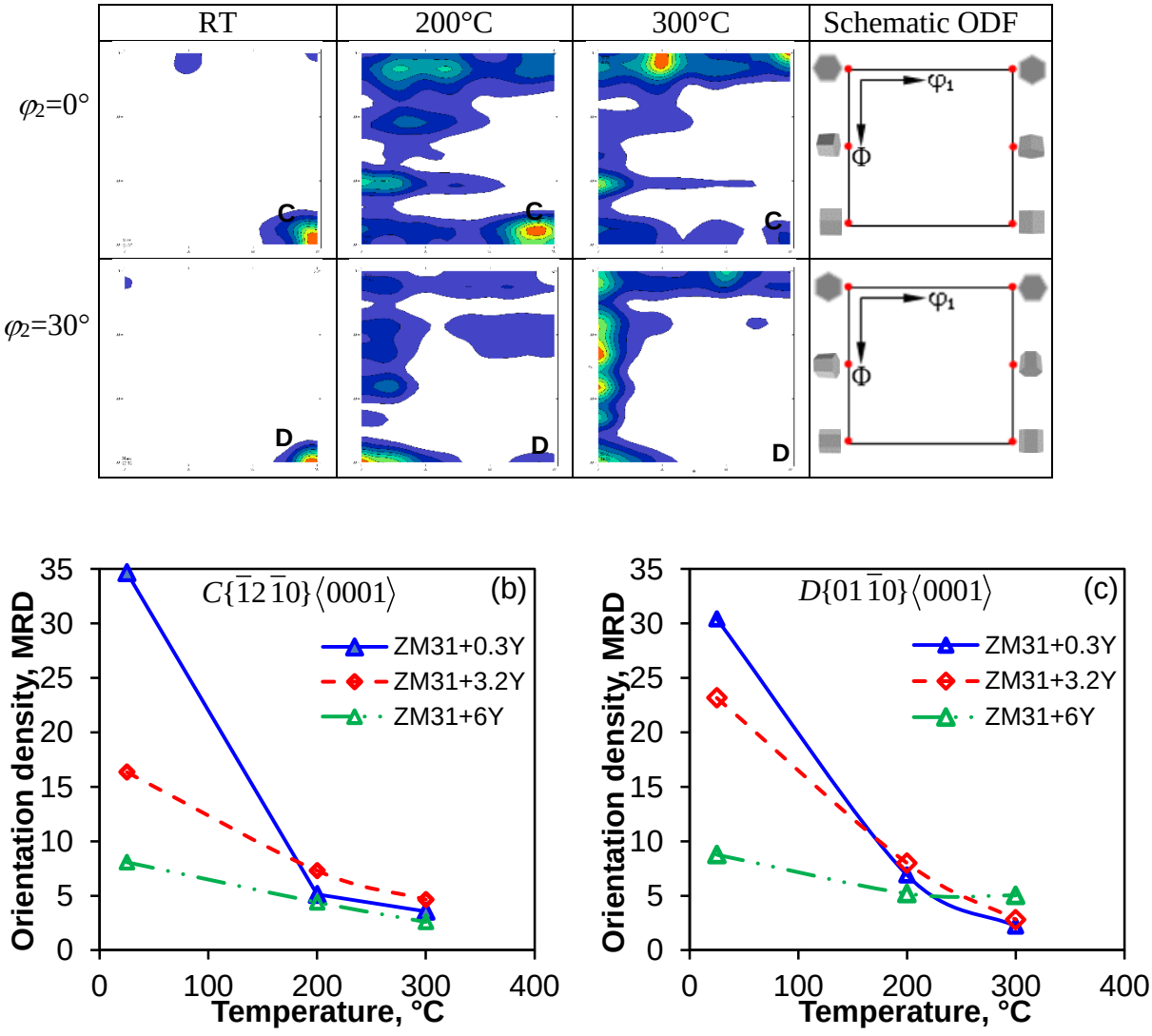

Figure 5.14: (a) ODF sections at φ_2=0° and φ_2=30° for the ZM31+0.3Y sample compressed to a strain of 10% at RT, 200°C and 300°C, and the change of orientation intensity of two main deformation texture components of (b) C$\{\bar{1}2\bar{1}0\}\langle 0001\rangle$ and (c) D$\{01\bar{1}0\}\langle 0001\rangle$ with deformation temperature.

Two major components of deformation texture, namely C{$\bar{1}$2$\bar{1}$0}<0001> and D{01$\bar{1}$0}<0001>, could be identified from the ODF sections at φ_2=0° and φ_2=30° (Fig.5.14(a)), due to the rotation of *c*-axes towards the anti-compression direction during deformation to a strain of 10%. The same components of deformation textures in magnesium alloys were reported by

[19,184,200]. The orientation intensity of the two components as a function of Y content and temperature is shown in Fig. 5.14(b) and (c), respectively. It is seen that at room temperature the orientation intensity of both components of deformation texture decreased with increasing Y content, indicating the beneficial role of the addition of element Y. While the intensity of all three alloys decreased with increasing deformation temperature, alloy ZM31+6Y exhibited the least decrease followed by alloy ZM31+3.2Y and then ZM31+0.3Y. This suggested that with a higher content of Y, the deformation mechanisms of magnesium alloys at elevated temperatures were more similar to those at room temperature, reflecting a better thermal resistance. The increase of deformation temperature promoted slip-dictated deformation by activating non-basal slip systems, thus reducing overall twinning activity and retarding the formation of strong texture. Although the addition of Y to magnesium alloys, being present in both forms of solutes and Y-containing second phase particles, was able to randomize texture which made some grains less favorable for twinning, a complete elimination of twinning even at elevated temperatures was difficult. Therefore, both mechanisms of twinning and dislocation slip were co-existent during hot compression, depending on the Y amount and temperature. However, the exact contribution of each individual deformation mode is a topic of further discussion.

5.3.4 Dynamic recrystallization

The grain maps screening the recrystallized, substructured and deformed grains with blue, green and red color in alloys ZM31+0.3Y, ZM31+3.2Y and ZM31+6Y which were deformed to a strain of 10% at 300°C are shown in Fig. 5.15(a-c).

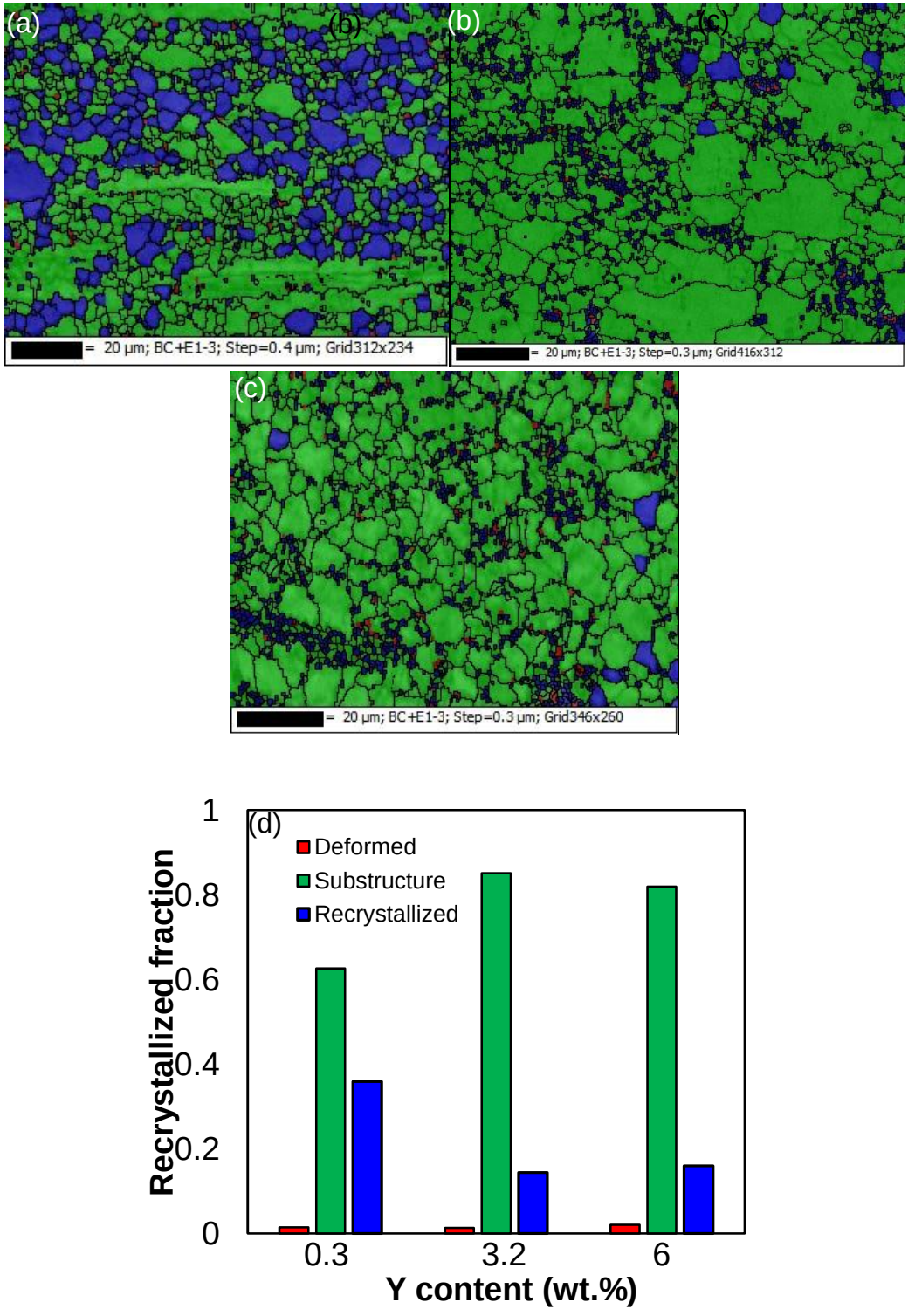

Figure 5.15: Mapping of recrystallization analysis of (a) ZM31+0.3Y, (b) ZM31+3.2Y and (c) ZM31+6Y compressed to a strain of 10% at 300°C, and (d) a quantitative comparison of the recrystallized fraction among the alloys containing different amounts of Y.

A GAM (grain average misorientation) approach based on EBSD data could be used to separate recrystallized grains from the deformed ones and to assess the recrystallized grain fraction, which was based on the grain internal statistics [201,202]. In general, the dislocation density in the deformed grains is high and these dislocations are arranged in special dislocation structures, which result in local misorientations of several degrees within grains [202]. In contrast, recrystallized grains have much lower dislocation densities and exhibit minor local misorientations. GAM is a measure of misorientation within a grain calculated by the Tango software by finding an average misorientation between all neighboring pairs of points inside a grain [203] based on point-to-point misorientations. The GAM values for recrystallized grains are lower than those of deformed or substructured grains [201,204]. Two threshold values of GAM were used to distinguish among recrystallized, substructured and deformed grains. In the present work, the threshold values of 2º and 7º have been used. The grains with GAM less than 2º were considered as recrystallized grains [202,205], whereas the grains consisting of subgrains with misorientations from 2º to 7º were classified as "substructured". All other remaining grains were classified as “deformed”. During hot deformation, incomplete DRX occurred along with the formation of substructures (or subgrains) and the deformed parent grains. Therefore, the recrystallization mechanism occurred in the alloys could be inferred as CDRX. As seen from Fig. 5.15(d), only about 36%, 14% and 16% of grains were fully recrystallized in alloys ZM31+0.3Y, ZM31+3.2Y and ZM31+6Y, respectively. That is, the recrystallization fraction decreased when Y content increased from 0.3% to 3.2% and then slightly increased when Y content further increased to 6%. It was likely that the kinetics of recrystallization was different in the three alloys. Alloy ZM31+0.3Y exhibited rapid recrystallization followed by ZM31+6Y and ZM31+3.2Y. The reduced kinetics of DRX in the higher Y-containing alloys was directly related to the role of Y. According to Basu and Al-Samman [205] Y with an atomic radius larger than magnesium was expected to exert a stronger

solute-dislocation interaction which retarded recrystallization kinetics. Besides, the drag effects on grain boundaries by second phase particles and solute segregation [195] were considered to be another underlying reason for the delay in recrystallization in Mg-Y alloys, as reported by [101,206]. Compared with alloy ZM31+3.2Y, a slightly greater recrystallized fraction in alloy ZM31+6Y could be accredited to the formation of LPSO phase. It has been reported that the presence of LPSO phase induced a high strain concentration at the phase/matrix interface which would stimulate DRX during hot deformation [198].

5.3.5 Slip deformation

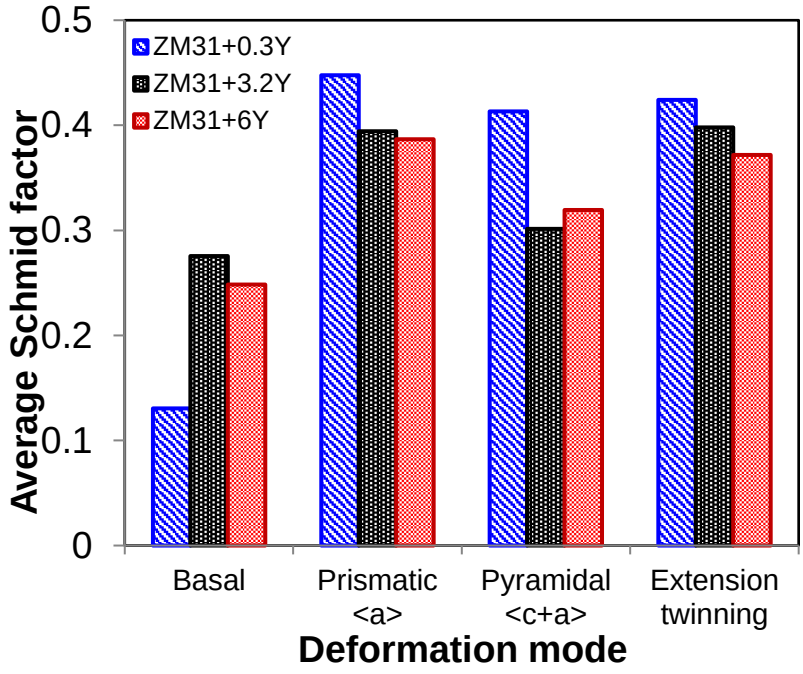

Figure 5.16: Average Schmid factor for the basal, prismatic <*a*>, pyramidal <*c*+*a*> slip and extension twinning in the as-extruded/non-deformed alloys ZM31+0.3Y, ZM31+3.2Y and ZM31+6Y.

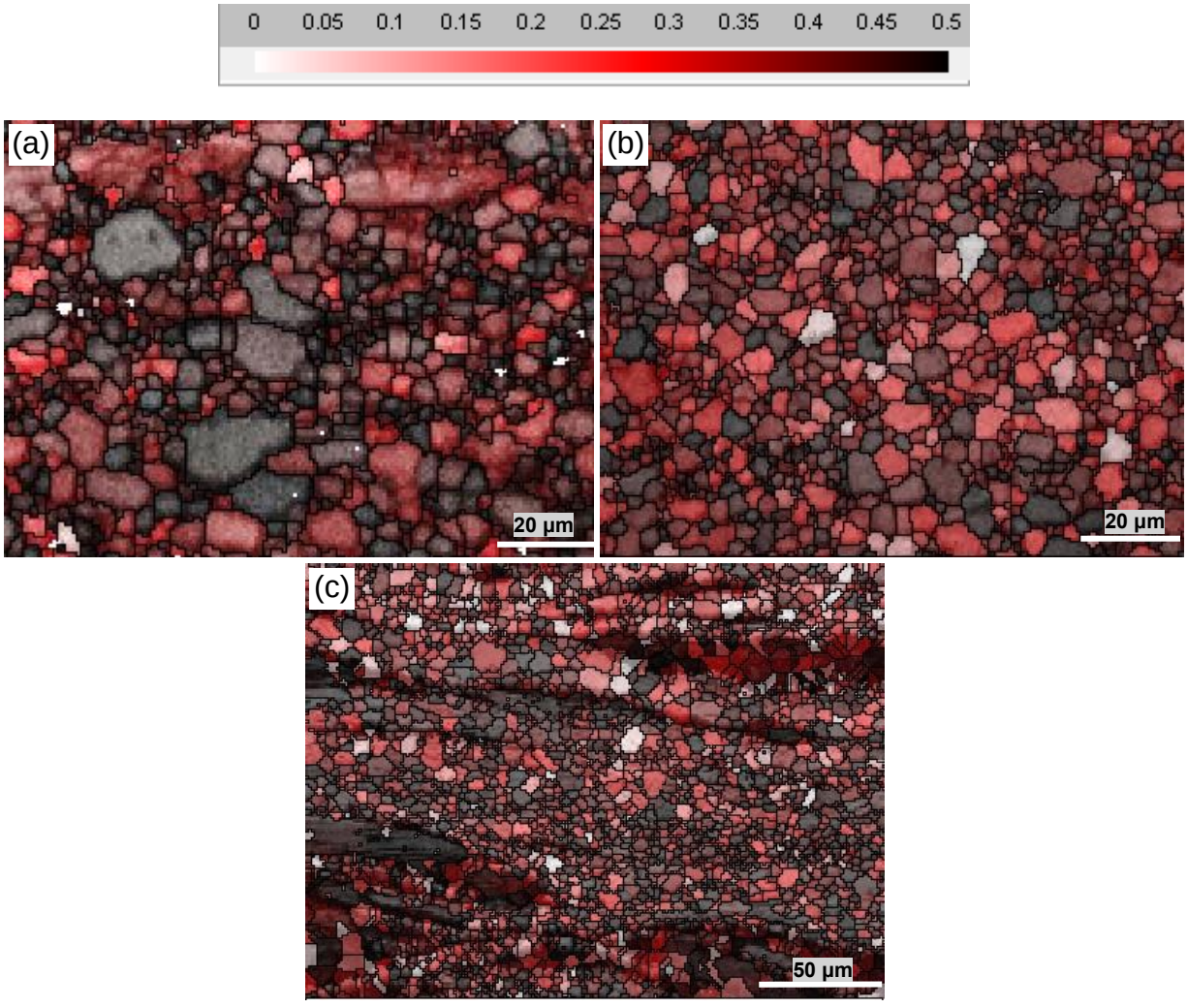

Figure 5.17: Schmid factor mapping for the prismatic slip in the as-extruded/non-deformed alloys (a) ZM31+0.3Y, (b) ZM31+3.2Y and (c) ZM31+6Y, respectively.

To quantify the activation of twinning and slip in the alloys studied, an average Schmid factor (SF) of each possible deformation mode are obtained from the EBSD analysis and presented in Fig. 5.16. It is seen that most grains were initially oriented favorable for extension twinning and non-basal slip. It should be pointed out that the average SF of ZM31+0.3Y was the maximum followed by ZM31+3.2Y and ZM31+6Y for extension twinning. This provided a direct corroboration that extension twinning occurred more profusely at low RE containing alloys at ambient temperature when non-basal slip systems were restricted. With an addition of element Y,

the main deformation mode changed from mainly extension twinning to a combined mode of slip with twinning accompanied by texture weakening. For additional clarification, a comparison of SF maps for prismatic slip of the three alloys are presented in Fig. 5.17. It is seen that the starting orientations for prismatic slip appeared more favorable in the sequence of ZM31+0.3Y, ZM31+3.2Y, and ZM31+6Y in terms of SF, as also shown in Fig.8. Again, the presence of Y in the magnesium alloys in the form of both second phase precipitates and solute atoms was most likely to endorse activation of non-basal slip during compression [205].

5.3.6 Visco-plastic self-consistent (VPSC) simulation

Polycrystal plasticity and texture modeling are a useful tool to gain an insight of the operating deformation mechanisms. VPSC model developed by Tome *et al*. [80,207–210] has been widely used to predict the texture evolution and the relative activity of deformation modes. The model could capture the transition from twin-dominated to slip-dominated deformation as temperature increased and incorporate twin-slip and twin-twin interactions as well. Twinning was treated using the predominant twin reorientation (PTR) scheme [80] and hardening was treated with the extended Voce law. According to the extended Voce hardening law, the threshold resolved shear stress of each deformation mode within a grain can be described as,

$$\tau^s(T) = \tau_0^s(T) + \left(\tau_1^s(T) + \theta_1^s(T)\Gamma\right)\left(1 - \exp\left(-\frac{\theta_0^s(T)\Gamma}{\tau_1^s}\right)\right), \tag{5.1}$$

where $\Gamma = \sum_s \Delta\gamma^s$ is the accumulated shear strain which is representative of the total dislocation density stored in the grain; τ_0, θ_0, θ_1, $(\tau_0 + \tau_1)$ are the initial threshold resolved shear stress, the initial hardening rate, the asymptotic hardening rate, and the back-extrapolated CRSS. The four

Voce parameters, τ_0, θ_0, θ_1, $(\tau_0+\tau_1)$ are dependent on deformation temperature. The hardening of each deformation mode is accounted for using the following equation at the end of each straining step, which allows for the incorporation of latent hardening effects [64,208],

$$\dot{\tau}^s = \frac{\partial \tau^s}{\partial \Gamma}(\Gamma, T)\sum_r h^{sr}\dot{\gamma}^r, \tag{5.2}$$

where h^{sr} measures the hardening of system *s* due to the shear rate $\dot{\gamma}^r$ taking place in system *r*. In this case, the associated h^{sr} values reflect the strength of the twin-dislocation interaction in an empirical way because they indirectly represent the barrier effect posed by evolving twin interfaces to dislocation or twin propagation. More details about the model were given in [64,79,208].

The initial texture measured by XRD was used to generate the input texture based on initial 4000 orientations for the simulations. The allowed deformation modes for the investigated magnesium alloys were basal, prismatic, second-order pyramidal and extension twinning (Fig. 5.16). The hardening parameters were adjusted by fitting the predicted stress-strain curves and textures to the experimentally measured data, and the results for deformation at 300°C are tabulated in Table 5.1. The latent hardening parameter in Table 5.1 suggested that twin boundaries will introduce potent barriers to subsequent slip and twinning [211]. It is generally recognized that basal slip and extension twinning (ETW) are the preferred deformation mechanisms in randomly oriented pure Mg polycrystals due to their low CRSS value at RT. However, as the temperature increases, the CRSS of non-basal systems decreases and the activity of these deformation modes increases considerably [212,213]. Moreover, the activity of non-basal slip in Mg-RE alloys was observed to be effectively enhanced even at low temperatures, as compared with the conventional Mg

alloys, because the CRSS values of prismatic and pyramidal slip systems became closer to those of extension twinning and basal slip [212,214].

Table 5.1: Hardening parameters for VPSC modelling (300°C).

ZM31+3.2Y	τ_0 (MPa)	τ_1 (MPa)	θ_0 (MPa)	θ_1 (MPa)	h_{sr}
Basal	9	7	1200	0	1
Prismatic	12	11	750	0	1
Pyramidal	20	32	1200	0	1
ETW	20	25	500	0	5
ZM31+3.2Y	τ_0 (MPa)	τ_1 (MPa)	θ_0 (MPa)	θ_1 (MPa)	h_{sr}
Basal	15	17	1000	0	1
Prismatic	45	70	1450	0	1
Pyramidal	35	38	1200	0	1
ETW	35	33	500	0	5
ZM31+6Y	τ_0 (MPa)	τ_1 (MPa)	θ_0 (MPa)	θ_1 (MPa)	h_{sr}
Basal	30	29	1000	0	1
Prismatic	70	90	1450	0	1
Pyramidal	60	60	1200	0	1
ETW	55	65	500	0	5

In particular, Y-alloyed Mg exhibited significantly higher activation of pyramidal slip leading to an increased ductility [215,216]. In the case of higher Y containing alloys (ZM31+3.2Y and ZM31+6Y) during compression at 300°C, if prismatic slip is considered to be similar in strength or weaker than pyramidal <*c*+*a*> slip, the role of prismatic slip becomes significant, which leads to the features in the simulated texture not observed experimentally. Therefore except for ZM31+0.3Y alloy, a higher activation stress was chosen for prismatic slip compared to pyramidal <*c*+*a*> slip during simulation. A similar consideration of prismatic slip has also been reported by other researchers [64,204]. Furthermore, unlike the non-basal slip all the hardening parameters associated with the basal slip and extension twinning modes are regarded as temperature-

independent [208,213,214]. This assumption entails that overcoming of the twin barriers and basal slip is not a thermally-activated process and is basically independent of deformation temperature.

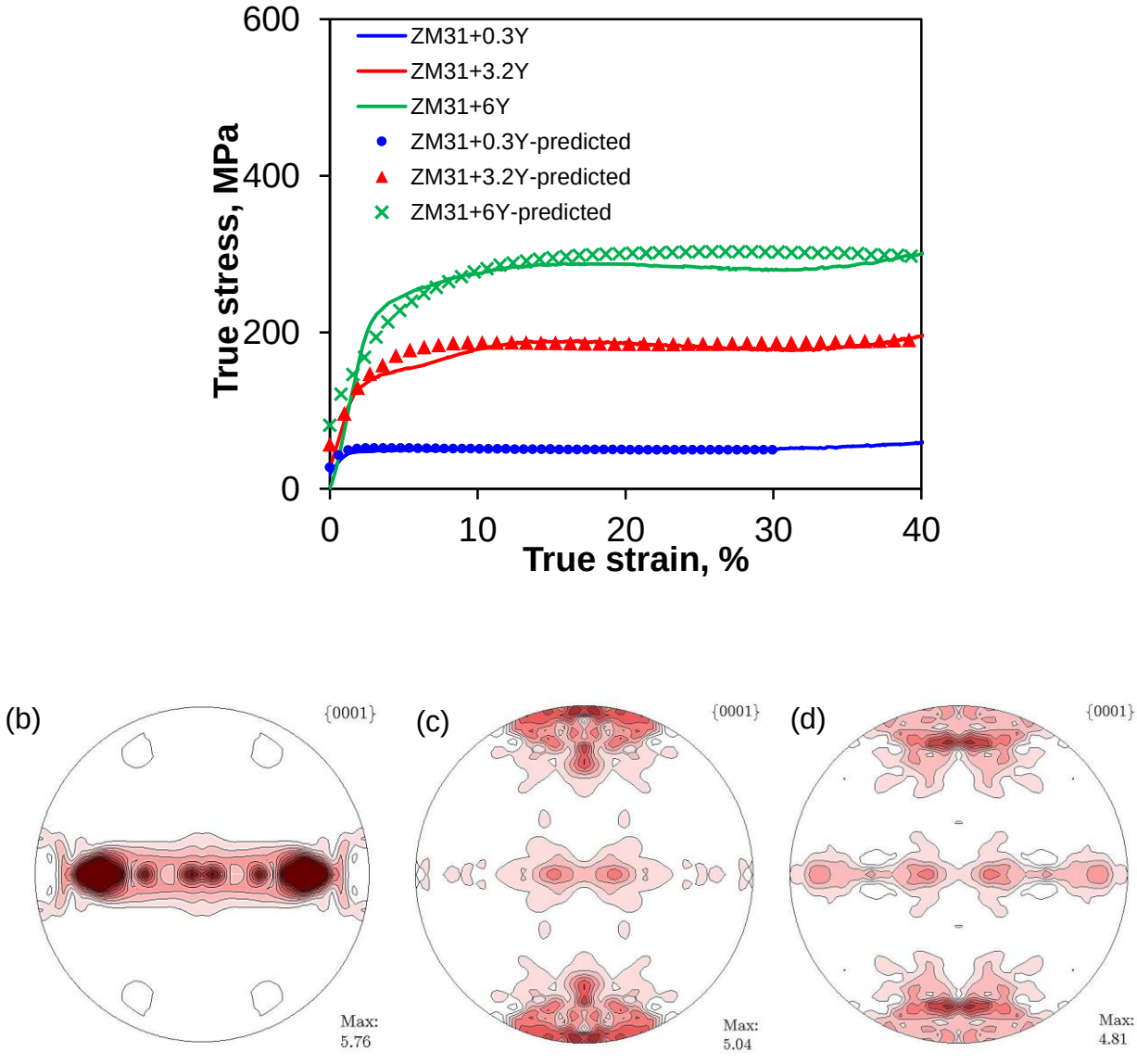

Figure 5.18: (a) The experimental and predicted stress-strain curves, and simulated texture of (b) ZM31+0.3Y, (c) ZM31+3.2Y and (d) ZM31+6Y during compression to a strain amount of 10% along the ED at 300°C.

It should be noted that contraction twinning and double twinning were excluded in the VPSC simulation as these twins were not observed during EBSD analysis. The first order pyramidal slip was not considered since the second order pyramidal slip was widely used in the literature [99,190]. Based on the above considerations, the model was capable of reproducing the experimental data of the three alloys in reasonable agreement. Fig. 5.18(a) demonstrates the mechanical response of alloys ZM31+0.3Y, ZM31+3.2Y, and ZM31+6Y, where the solid lines represent the measured stress-strain curves and the dotted lines represent the VPSC predictions at 300°C. It is seen that the measured and predicted stress-strain curves were in fairly good agreement in all the three alloys. The corresponding simulated texture (at a compressive strain of 10% along the ED) of the materials are presented in Fig. 5.18(b-d). Again, a reasonable agreement between the simulated texture and measured texture (Fig. 5.10(g-i)) was obtained. It should be noted that DRX was not considered in the simulation. Consequently, the influence of DRX could be considered as the deviations between the experimental and simulated textures.

5.3.7 Active deformation modes

The relative activity of slip and twinning modes of alloys ZM31+0.3Y, ZM31+3.2Y, and ZM31+6Y deformed up to a strain amount of 50% at 200°C and 300°C based on the above polycrystal plasticity simulation is presented in Fig. 5.19(a-f). As seen from Fig. 5.19(a,c,e), while the applied large strain at later stage of deformation was mostly accommodated by basal slip at 200°C for all the three alloys, the earlier deformation up to a strain of ~10% was mainly accommodated by both extension twinning and basal slip. With increasing Y content the relative activity of pyramidal slip increased, whereas the relative activity of basal slip decreased. For example, for ZM31+6Y alloy deformed at 200°C (Fig. 5.19(e)), the relative activity of both

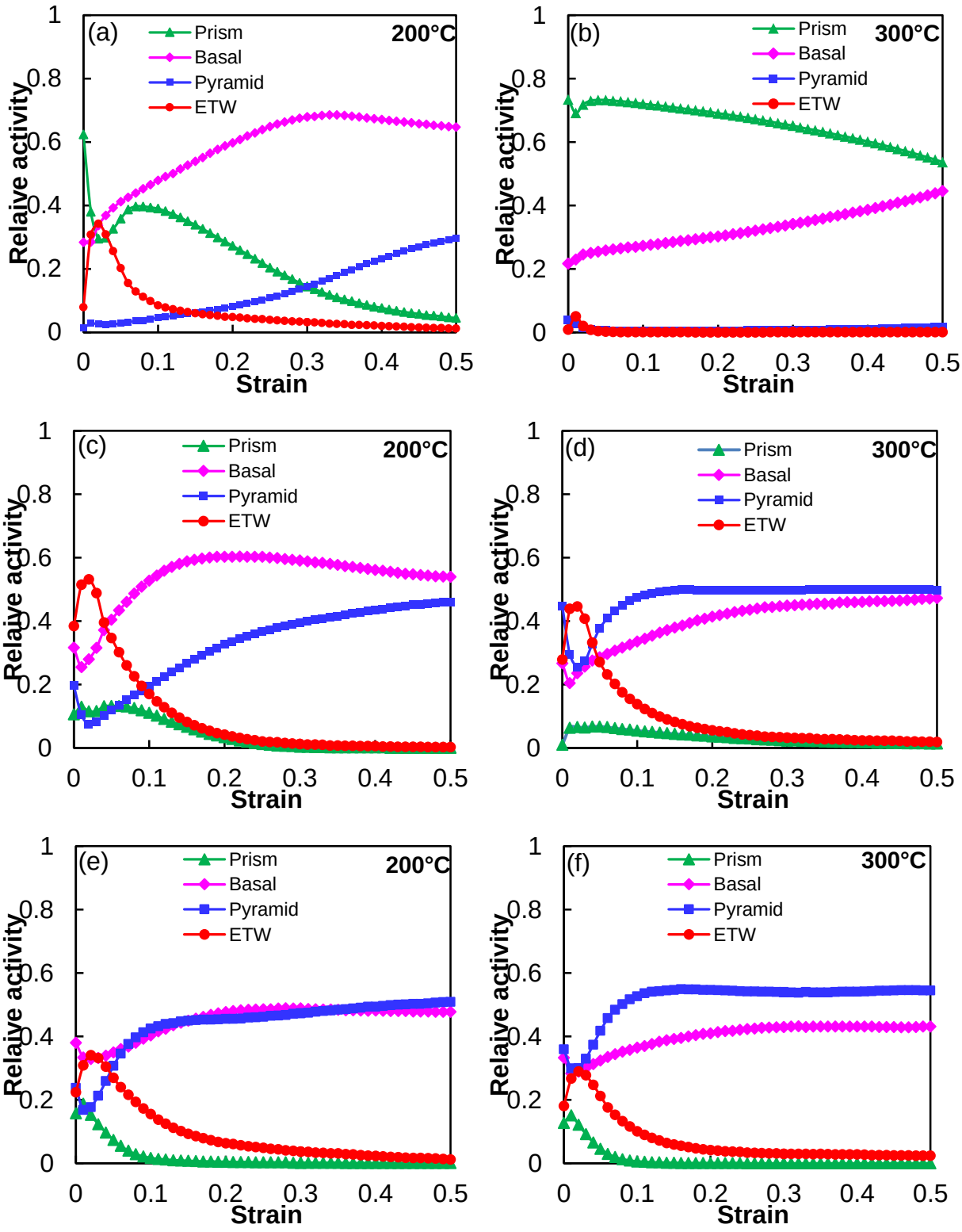

Figure 5.19: Relative activities of specific deformation modes of (a, b) ZM31+0.3Y, (c, d) ZM31+3.2Y, and (e, f) ZM31+6Y at 200°C and 300°C, respectively.

pyramidal slip and basal slip was nearly the same. The superior activation of non-basal slip in Mg alloy during hot compression was also observed by other researchers [63,99]. Tsuru and Chrzan [217] recently reported that the addition of Y solutes increased the stress required for slip on the basal plane, and enabled cross-slip to prismatic and pyramidal planes. As seen from Fig. 5.19(b,d,f), the relative activity of non-basal slip further increased with increasing deformation temperature. At 300°C, the predominant deformation mechanism was prismatic slip along with some basal slip for the low RE-containing ZM31+0.3Y alloy (Fig. 5.19(b)), while it was pyramidal slip coupled with some basal slip for the intermediate and high RE-containing ZM31+3.2Y and ZM31+6Y alloys (Fig. 5.19(d,f)). This was basically in agreement with the prediction based on Schmid factors (Fig. 5.16), where SF values for prismatic slip decreased with increasing Y content. Besides, the relative contribution from extension twinning (ETW) decreased significantly with increasing deformation temperature and deformation amount. In particular, in the hot deformation of alloy ZM31+0.3Y at 300°C the relative contribution from extension twinning was nearly absent (Fig. 5.19(b)), corresponding well to the EBSD results in Fig. 5.11(b). Thus, the activity of twinning and slip deformation shown in Fig. 5.19 could be used to understand the outcome at elevated temperatures as discussed above. As seen from Fig. 5.19(c), alloy ZM31+3.2Y compressed at 200°C exhibited the highest activity of extension twinning (~55%) compared with alloys ZM31+0.3Y and ZM31+6Y in the initial deformation stage, which was also consistent with the above analyses via XRD pole figure in Fig. 5.10(e) and EBSD orientation map in Fig. 5.11(c). Generous activation of prismatic slip since the onset of plastic deformation at 300°C moderated the significance of twinning in alloy ZM31+0.3Y (Fig. 5.19(b)). Correspondingly, deferred activation of pyramidal slip mode in alloys ZM31+3.2Y and ZM31+6Y at 300°C preserved the deformation mechanism reliant on twinning to some extent (Fig. 5.19(d,f)).

It appeared as if extension twinning facilitated the activation of pyramidal slip by favorable lattice rotations in subsequent slip deformation. Most importantly, in all cases pyramidal slip activity was observed to increase with increasing Y content. The fact that the addition of Y makes <*c*+*a*> pyramidal slip system active in Mg has also been experimentally corroborated by TEM [215,216,218]. This was related to Y solute enhanced pyramidal slip activity as a result of the increased stability of easy-glide $\langle c+a \rangle$ dislocations produced by the solutes [219]. At a lower temperature of 200°C, the thermally activated $\langle c+a \rangle$ pyramidal slip system might not be able to contribute to large *c*-axis compression, leading to an earlier fracture (<50%). According to Wu and Curtin [219], this is because $\langle c+a \rangle$ dislocation is metastable on easy-glide pyramidal plane and undergoes a thermally activated, stress-dependant transition to lower-energy immobile dislocations which no longer can contribute to plastic straining. By shifting the transition to higher temperatures, longer times or slower strain rates, the easy-glide $\langle c+a \rangle$ core can be energetically stabilized which can avoid undesirable transition. It was likely that the added Y solute atoms pinned the easy-glide $\langle c+a \rangle$ core and lowered its energy. Therefore, a higher temperature and solute Y are favourable for the stability of $\langle c+a \rangle$ edge dislocations on pyramidal plane to achieve high ductility. A decrease in alloy ZM31+6Y compared with alloy ZM31+3.2Y at elevated temperatures in terms of twinning activity would be attributed to the formation of LPSO phase. The presence of LPSO phase strongly impeded twinning activity and promoted nucleation of non-basal slip modes in addition to improving the thermal resistance [164,198,199].

5.4 Summary

In this Chapter, microstructure and texture evolution of as-extruded ZM31 magnesium alloys with different amounts of yttrium (Y) during pre- and post-deformation annealing were examined, with special attention to the effect of Y on static recrystallization. With increasing Y content, both the extent of extension twinning during compression and the fraction of recrystallization during annealing decreased due to the role of Y present in the substitutional solid solution and in the second phase particles. Also, texture evolution and deformation activity of an extruded Mg-Zn-Mn (ZM31) alloy containing different amounts of yttrium subjected to hot compression along the extrusion direction at 200°C and 300°C were studied via electron backscatter diffraction (EBSD) and X-ray diffraction (XRD). Visco-plastic self-consistent simulation, along with EBSD and XRD analyses, revealed that with increasing deformation temperature the relative contribution of non-basal slip increased and the relative contribution of extension twinning decreased. With increasing Y content the relative contribution of pyramidal slip increased, while the relative contribution of basal slip decreased.

CHAPTER 6

6. INFLUENCE OF Y ON HOT CHARACTERIZATION[§]

6.1 Introduction

The microstructures and mechanical properties of the as-extruded Mg-Zn-Mn-Y alloys with I-, W-and LPSO phases at RT have been studied in Chapter 4. The notable influence of Y addition on phase formation and the resulting compressive behavior have been investigated comprehensively. The results revealed that the strength of the Mg-Zn-Mn-Y alloys increased significantly due to the occurrences of ternary Mg-Zn-Y second phases [40]. Hence, the investigation of the hot deformation behavior of these alloys appear to be important. However, to the authors' knowledge no information about the hot deformation parameters of the as-extruded Mg-Zn-Y-Mn alloys is available in the open literature. Therefore, the present Chapter was aimed to identify the hot deformation behavior of the as-extruded Mg-Zn-Y-Mn alloys based on isothermal compression tests. The processing maps of the alloys are constructed with a view to

[§]This chapter is based on the following publications of the author:

1. N. Tahreen, D.F. Zhang, F.S. Pan, X.Q .Jiang, C. Li, D.Y. Li, D.L. Chen, Characterization of hot deformation behavior of an extruded Mg-Zn-Mn-Y alloy containing LPSO phase, *Journal of Alloys and Compounds*, 2015, 644, 814-823.
2. N. Tahreen, D.F. Zhang, F.S. Pan, X.Q. Jiang, D.Y. Li, D.L. Chen, Hot deformation and processing map of an as-extruded Mg-Zn-Mn-Y alloy containing I and W phases, *Materials and Design*, 2015, 87, 245-255.
3. N. Tahreen, D.F. Zhang, F.S. Pan, X.Q. Jiang, D.Y. Li, D.L. Chen, Hot deformation and processing map in an Mg-Zn-Mn-Y alloy, Magnesium Technology 2016, edited by A. Singh, K. Solanki, M.V. Manuel, and N.R. Neelameggham, TMS (The Minerals, Metals & Materials Society), 2016, pp.183-186.

analyze and optimize the hot working parameters. Moreover, the deformation mechanisms of Mg-Zn-Y-Mn alloys are validated by microstructural examinations.

6.2 Base Alloy (ZM31) and Modified Alloy (ZM31+0.3Y)

6.2.1 Flow behavior

The true stress-true strain compression curves of the ZM31 and ZM31+0.3Y alloys, obtained at different temperatures and strain rates, are shown in Fig. 6.1. It is clear that the flow behavior of both alloys are largely reliant on the deformation temperature and strain rate. The flow stress decreased with increasing temperature in the range of 300-400°C at a constant strain rate (Fig. 6.1a). Decreasing the strain rate in the range of 1.0-0.001 s^{-1} exhibited a similar influence on the strength characteristics as the material became softer and more ductile with increasing temperature (Fig. 6.1b). For all testing conditions, the flow stress increased with increasing true strain during the initial stages of deformation. In all cases, after reaching the peak value, the flow stress decreased slightly and finally reached a steady-state with further increases in the strain. It is seen that the peak stress of the base ZM31 alloy decreased from 121 MPa to 60 MPa with increasing temperature from 300 to 400°C at a strain rate of 1 s^{-1}. Similarly, the change of peak stress from 121 MPa to 46 MPa at 300°C occurred with decreasing strain rate from 1 s^{-1} to 0.001 s^{-1}. The ZM31+0.3Y alloy showed higher strength compared to the base alloy; i.e. a reduction of the peak stress occurred from 147 MPa to 67 MPa with increasing temperature from 300 to 400°C at a constant strain rate of 1 s^{-1} and from 147 MPa to 51 MPa with decreasing strain rate from 1 s^{-1} to 0.001 s^{-1} at a constant temperature of 300°C.

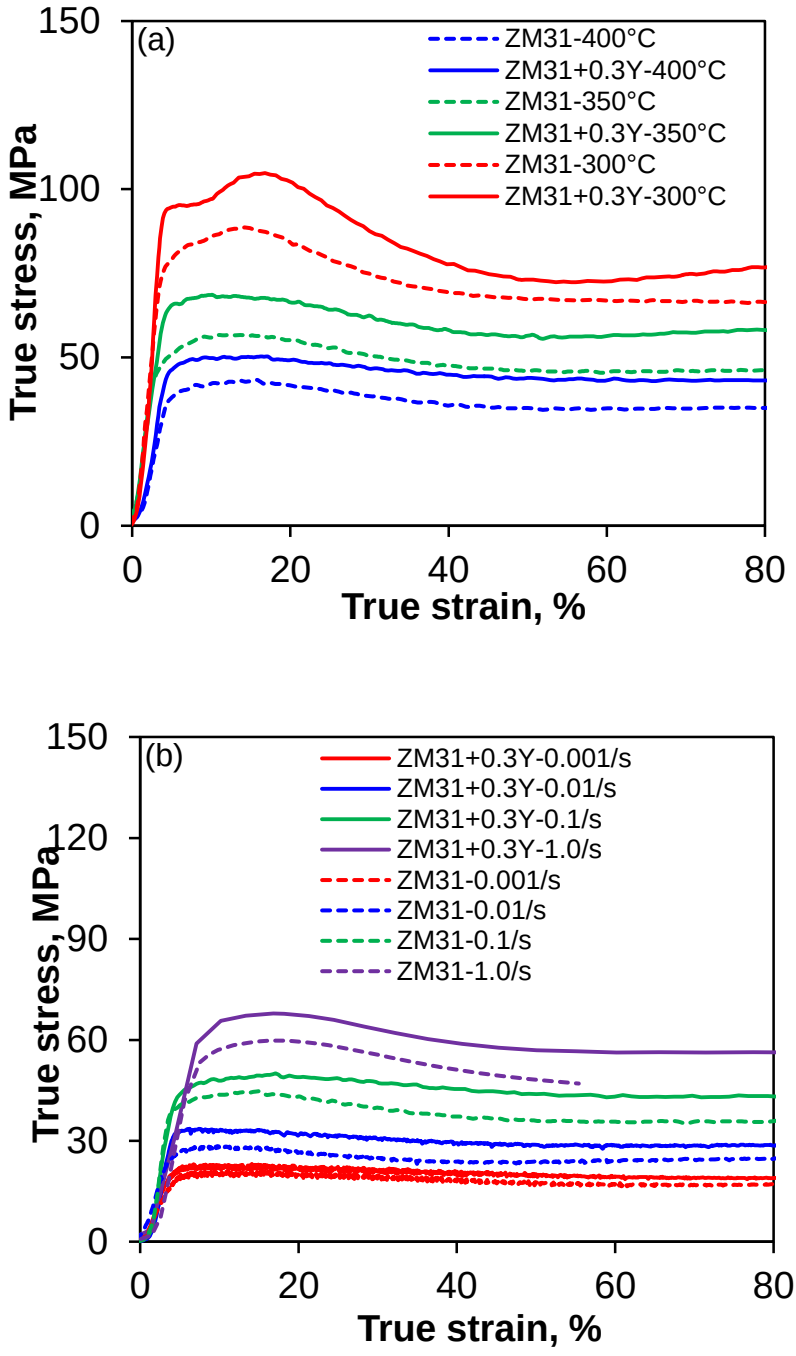

Figure 6.1: Typical true stress strain behavior of the studied alloys under uniaxial compression (a) at different temperatures and constant strain rate of 0.1 s^{-1}, and (b) at constant temperature of 400°C and different strain rates.

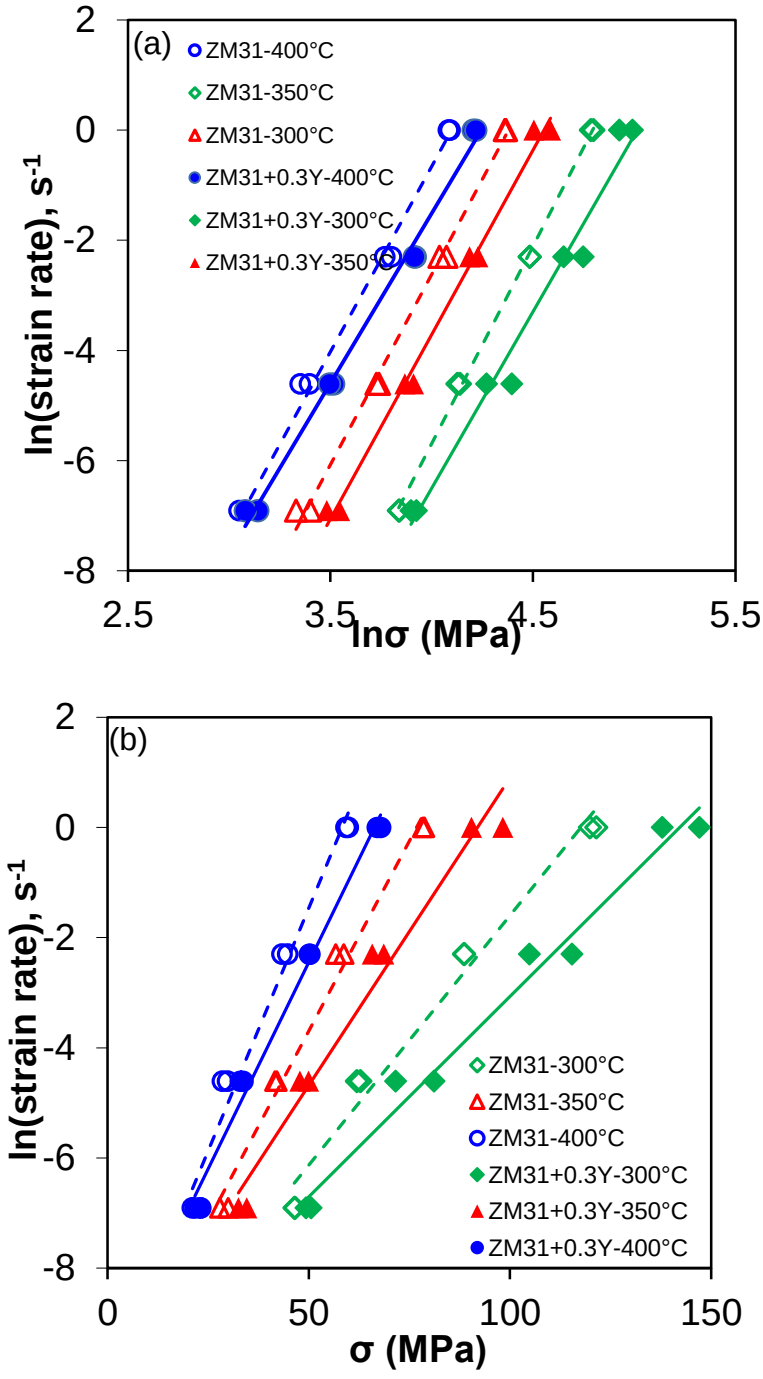

Figure 6.2: Relationships between (a) $\ln \dot{\varepsilon}$ and $\ln\sigma$ and (b) $\ln \dot{\varepsilon}$ and σ.

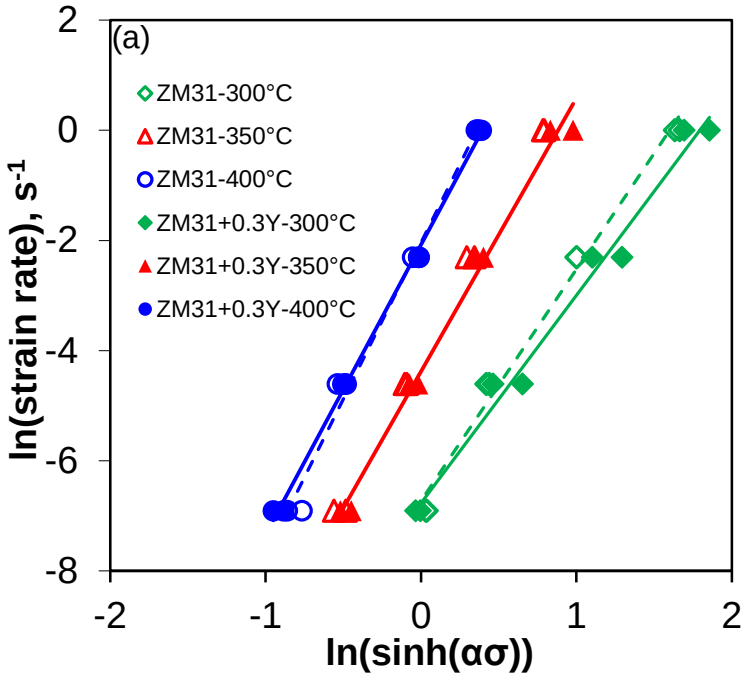
(a)
ZM31-300°C
ZM31-350°C
ZM31-400°C
ZM31+0.3Y-300°C
ZM31+0.3Y-350°C
ZM31+0.3Y-400°C
ln(strain rate), s-1
ln(sinh(ασ))
2
0
-2
-4
-6
-8
-2
-1
0
1
2

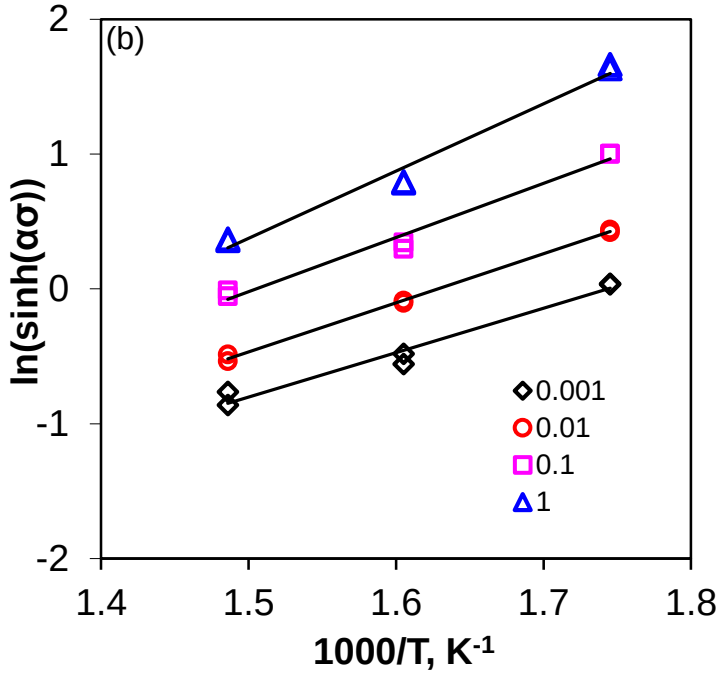
(b)
0.001
0.01
0.1
1
ln(sinh(ασ))
1000/T, K-1
2
1
0
-1
-2
1.4
1.5
1.6
1.7
1.8

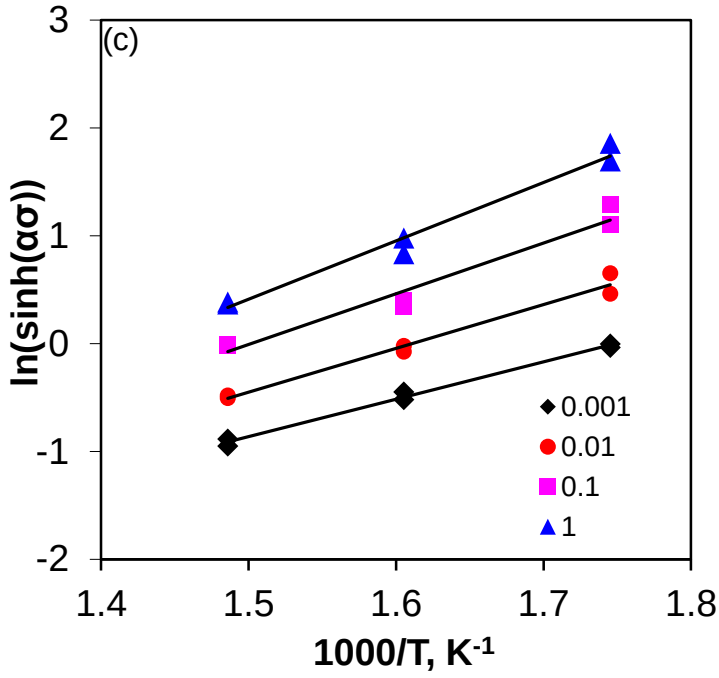

Figure 6.3: Relationships between (a) $\ln\dot{\varepsilon}$ and $\ln[\sinh(\alpha\sigma)]$ of alloys ZM31 and ZM31+0.3Y, (b) $\ln[\sinh(\alpha\sigma)]$ and $1000/T$ of ZM31, and (c) $\ln[\sinh(\alpha\sigma)]$ and $1000/T$ of ZM31+0.3Y.

6.2.2 Constitutive equation

The constitutive equation, proposed by Sellars and McTegart [220], is widely used to describe the relationship between the strain rate, deformation temperature, and flow stress in the process of hot deformation. It can be expressed as follows:

$$\dot{\varepsilon} = A[\sinh(\alpha\sigma)]^n \exp(-\frac{Q}{RT}), \tag{6.1}$$

where n and A are material constants, α is a stress multiplier, σ is the flow stress (MPa), Q is the activation energy for hot deformation (kJ/mol), R is the universal gas constant (8.314 J/mol-K),and T is the deformation temperature (K). For high and low stress levels, the relationship between the flow stress and strain rate could be described by the following equations [221,222]:

$$\dot{\varepsilon} = A_1 \sigma^{n_1} \exp(-\frac{Q}{RT}), \tag{6.2}$$

$$\dot{\varepsilon} = A_2 \exp(\beta\sigma) \exp(-\frac{Q}{RT}), \tag{6.3}$$

where A_1 and A_2 are the material constants. Taking logarithm on both sides of Eqs. (6.2) and (6.3) gives to,

$$\ln \dot{\varepsilon} = \ln A_1 + n_1 \ln \sigma - \frac{Q}{RT}, \tag{6.4}$$

$$\ln \dot{\varepsilon} = \ln A_2 + \beta\sigma - \frac{Q}{RT}. \tag{6.5}$$

In the present study, the peak stress σ_p is used as the σ term. The plots of relationships between $\ln \dot{\varepsilon}$ and $\ln \sigma$ and $\ln \dot{\varepsilon}$ and σ are shown in Fig. 6.2(a) and 6.2(b), respectively, where the stress is the peak flow stress. Then the slope in Fig. 6.2(a) and 6.2(b) represents the value of n_1 and β. The mean values of the slopes are taken to obtain the n_1 and β values. Finally the stress multiplier α could be calculated as $\alpha = \beta / n_1$. The obtained material constants for both alloys are listed in Table 6.1.

Table 6.1: Material constants of the hot deformed alloys, evaluated from the constitutive equation.

	n_1	β	α	n	Q (kJ/mol)
ZM31	6.9	0.1350	0.0195	5	164
ZM31+0.3Y	6.4	0.1116	0.0174	4.67	172

Taking natural logarithm on both sides of Eq. (6.1), it can be expressed as,

$$\ln \dot{\varepsilon} = \ln A + n \ln[\sinh(\alpha\sigma)] - \frac{Q}{RT}. \tag{6.6}$$

6.2.3 Activation energy

Activation energy is the measure of the minimum energy required to initiate dislocation movement by diffusion. It is considered to be an important physical parameter indicating the degree of difficulty to deform a material plastically under specific deformation condition. Taking partial differential equation of Eq. (6.6) into consideration yields:

$$Q = R\left[\frac{\partial \ln \dot{\varepsilon}}{\partial \ln[\sinh(\alpha\sigma)]}\right]_T \cdot \left[\frac{\partial \ln[\sinh(\alpha\sigma)]}{\partial(1/T)}\right]_{\dot{\varepsilon}} = RnS\,, \tag{6.7}$$

where n is the average slope of plots of $\ln\dot{\varepsilon} - \ln[\sinh(\alpha\sigma)]$ at different temperatures and S is the average slope of plots of $\ln[\sinh(\alpha\sigma)] - 1/T$ at varying strain rates. The relationship between $\ln\dot{\varepsilon} - \ln[\sinh(\alpha\sigma)]$ is shown in Fig. 6.3(a), while the relationship between $\ln[\sinh(\alpha\sigma)] - 1/T$ for alloys ZM31 and ZM31+0.3Y are plotted as shown in Fig. 6.3(b) and Fig. 6.3(c) respectively. The mean value of the slopes at different deformation temperatures (n) and the mean value of the slopes at various strain rates (S) were then determined. Therefore, the activation energy Q can be calculated from Eq. (6.7). In the present study, the activation energy was determined to be 164 and 172 kJ/mol for alloys ZM31 and ZM31+0.3Y, respectively. It should be noted that the value of Q for the 0.3 wt.% Y containing alloy (172 kJ/mol) is higher than the value of 164 kJ/mol obtained for the base alloy.

6.2.4 Zener-Hollomon parameter

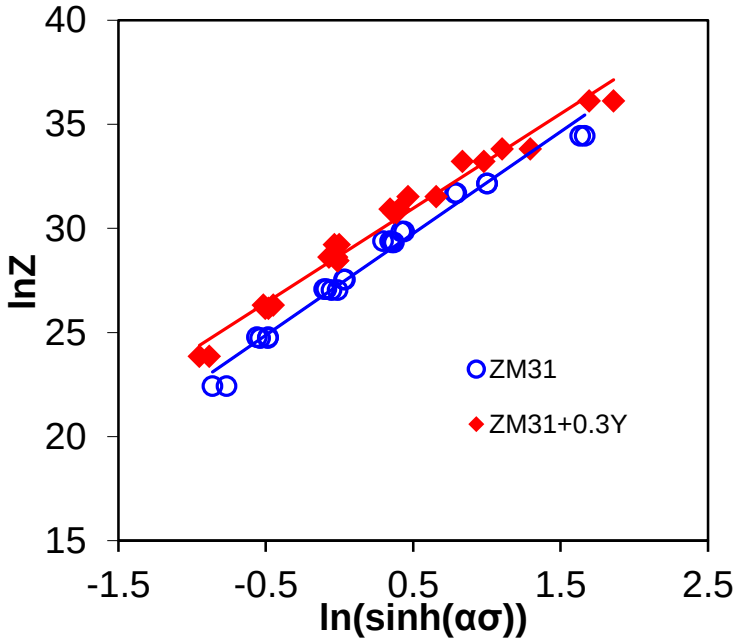

Figure 6.4: Relationship between lnZ and $\ln[\sinh(\alpha\sigma)]$.

The effects of strain rate and deformation temperature on flow stress are often incorporated into a single parameter of Zener-Hollomon (Z), $\dot{\varepsilon}\exp\left(\frac{Q}{RT}\right)$, representing a temperature-compensated strain rate, which can be calculated using Eq. (6.8), i.e.,

$$Z = \dot{\varepsilon}\exp\left(\frac{Q}{RT}\right) = A[\sinh(\alpha\sigma)]^n . \tag{6.8}$$

By substituting the values of Q and different hot deformation parameters into Eq. (6.8), Z values can be calculated subsequently. Then, a linear relationship between ln$Z$ and $\ln[\sinh(\alpha\sigma)]$ should be present based on Eq. (6.8), which is plotted in Fig. 6.4. The intercepts of the fitted curve in Fig. 6.4 are taken as the value of ln$A$ = 27.3 and 28.7, of which A value is obtained as 7.18×10^{11} and 2.91×10^{12} s^{-1}. Substituting the measured values of A, α, n and Q into the Eq. (6.1), the constitutive

equation during hot compression of the studied alloys ZM31 and ZM31+0.3Y are obtained as follows,

$$\dot{\varepsilon} = 7.18\times10^{11}\left[\sinh\left(0.0195\sigma\right)\right]^{5}\exp\left(-\frac{164152}{8.314T}\right). \quad (6.9)$$

$$\dot{\varepsilon} = 2.91\times10^{12}\left[\sinh\left(0.0174\sigma\right)\right]^{4.67}\exp\left(-\frac{171512}{8.314T}\right). \quad (6.10)$$

6.3 ZM31+3.2Y Alloy

6.3.1 Flow behavior

Fig. 6.5 shows typical true stress-true strain curves of as-extruded ZM31+3.2Y alloy compressed at different deformation temperatures in the range of 300-400°C and strain rates of 0.001-1.0 s^{-1}. The stress-strain curve obtained at 300ºC/1s^{-1} was not presented due to unavailability of sufficient data points during the test. In all deformation conditions, flow stress curves exhibited similar characteristics, i.e., the flow stress initially increased to a maximum and then decreased or remained nearly constant. At a higher temperature or lower strain rate the material exhibited almost none or very little hardening followed by slight flow softening leading to a steady-state. In contrast, at a lower temperature or higher strain rate, the alloy demonstrated significant hardening followed by moderate flow softening and shear fracture at 45° with respect to the loading axis.

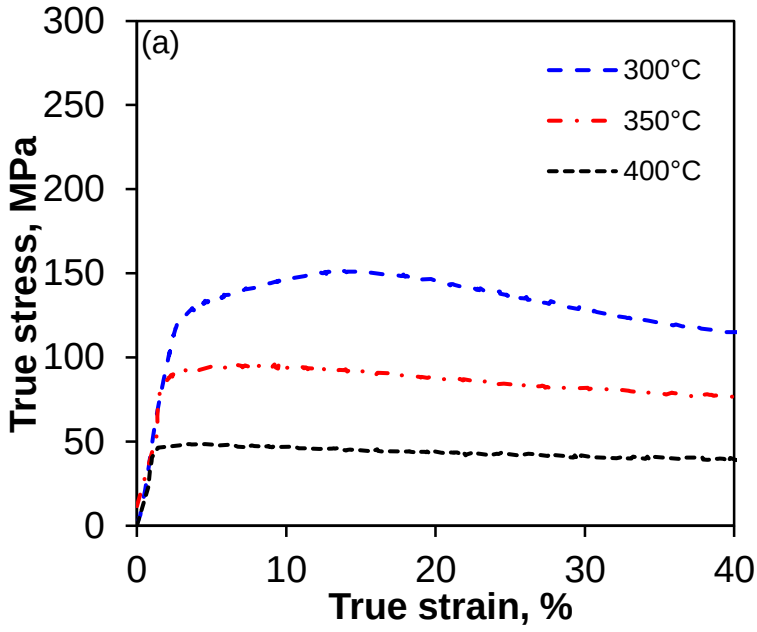
(a)
300°C
350°C
400°C
True stress, MPa
True strain, %
0
50
100
150
200
250
300
0
10
20
30
40

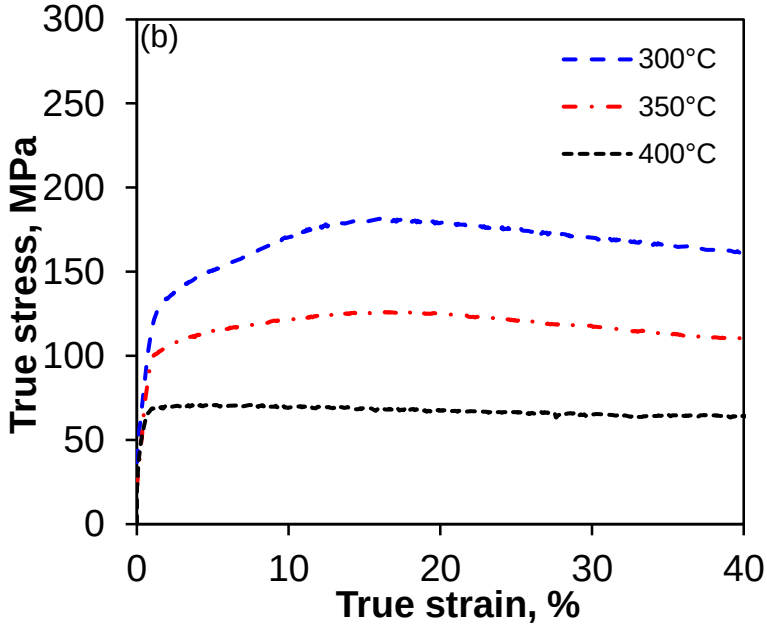
(b)
300°C
350°C
400°C
True stress, MPa
True strain, %
0
50
100
150
200
250
300
0
10
20
30
40

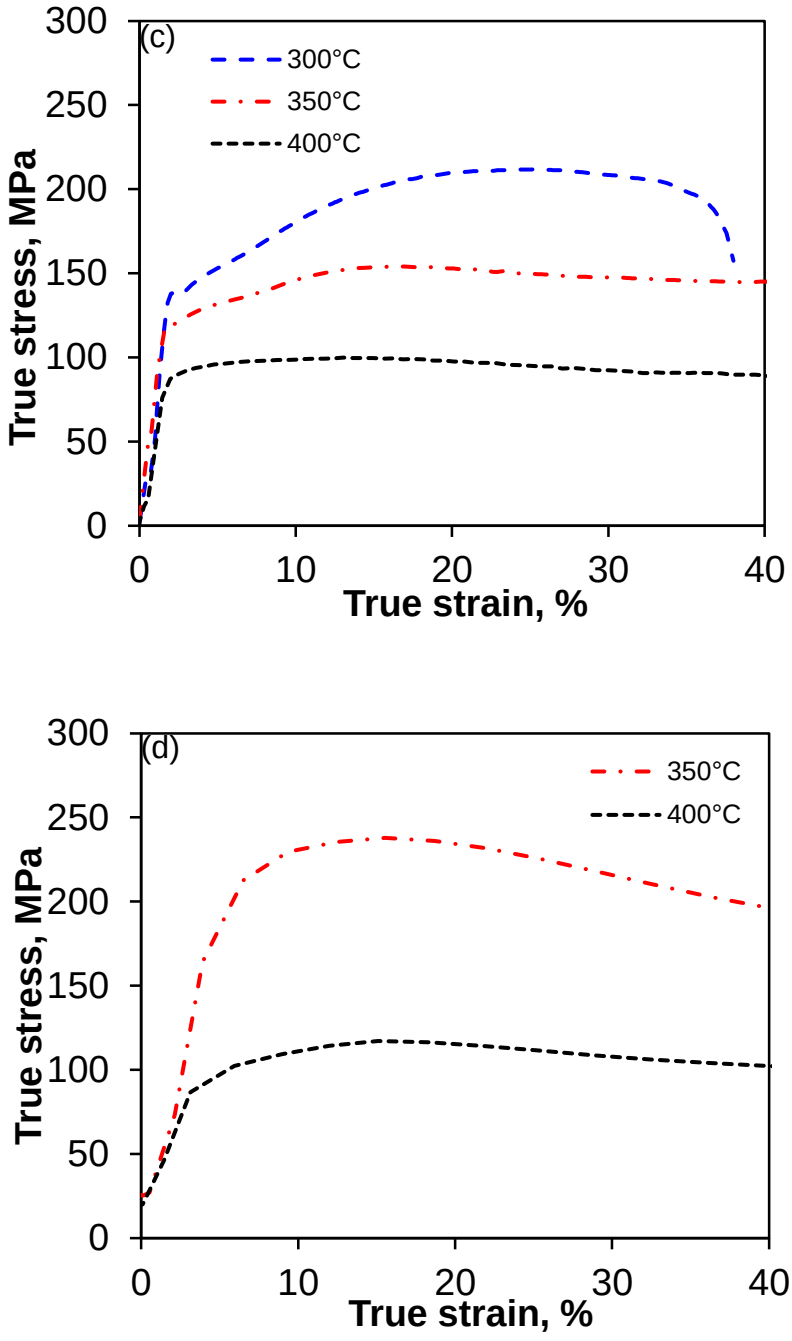

Figure 6.5: Compressive true stress-true strain curves of ZM31+3.2Y alloy deformed at different temperatures at strain rates of (a) 0.001 s^{-1}, (b) 0.01 s^{-1}, (c) 0.1 s^{-1} and (d) 1 s^{-1}.

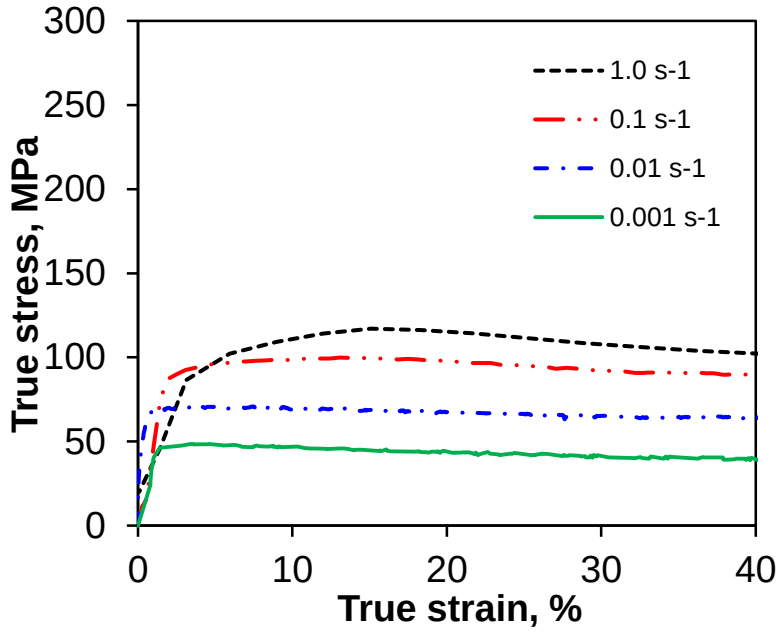

Figure 6.6: Compressive true stress-true strain curves of ZM31+3.2Y alloy deformed at strain rates of (a) 0.001 s^{-1}, (b) 0.01 s^{-1}, (c) 0.1 s^{-1} and (d) 1 s^{-1} at 400°C.

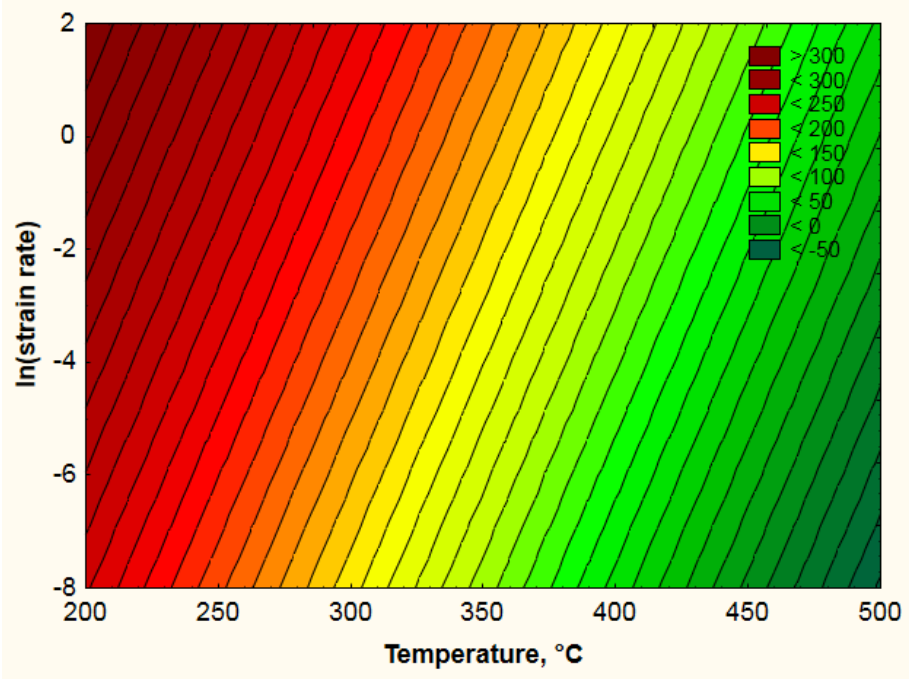

Figure 6.7: Change of peak stress with deformation temperature and strain rate of ZM31+3.2Y alloy.

It is clear that the flow behavior is largely reliant on the deformation temperature and strain rate. The flow stress decreased with increasing temperature at a constant strain rate. With increasing test temperature, the kinetic energy of metal atoms increased and accumulated, which boosted the dislocation movement, leading to a decreased flow stress. Decreasing the strain rate exhibited a similar influence on the strength characteristics as the material became softer and more ductile with increasing temperature. Fig. 6.6 clearly shows that the higher the strain rate, the greater the flow stress at a given temperature. This is because there was no sufficient time for energy accumulation and dislocation annihilation at a higher strain rate [13,16,223]. The peak stress of the alloy decreased from 157 MPa to 52 MPa with increasing temperature from 300 to 400°C at a strain rate of 0.001 s^{-1}. Similarly, the peak stress increased from 52 MPa to 119 MPa at 400°C with increasing strain rate from 0.001 s^{-1} to 1 s^{-1}. To better apprehend the results, the contour plot of peak stresses, natural logarithm of strain rates and temperatures were fitted linearly in a 2D graph and is presented in Fig. 6.7. As seen, the peak stress of the alloy increased with decreasing temperature and increasing strain rate.

6.3.2 Activation energy

The data obtained at 300ºC/1s^{-1} were excluded to compute activation energy. Fig. 6.8(a) shows the plot of $\ln\dot{\varepsilon}$ vs. $\ln\sigma$. A linear relationship appeared to exist between $\ln\dot{\varepsilon}$ and $\ln\sigma$ with a slope n_1, as described by Eq. (6.4). Similarly, Fig. 6.8(b) shows the plot of $\ln\dot{\varepsilon}$ vs. σ. A linear relationship was existent as well between $\ln\dot{\varepsilon}$ and σ with a slope β, as seen in Eq. (6.5). Substituting the value of peak flow stress and the corresponding strain rate into Eqs (6.4) and (6.5), the value of n_1 and β could be derived using a linear regression.

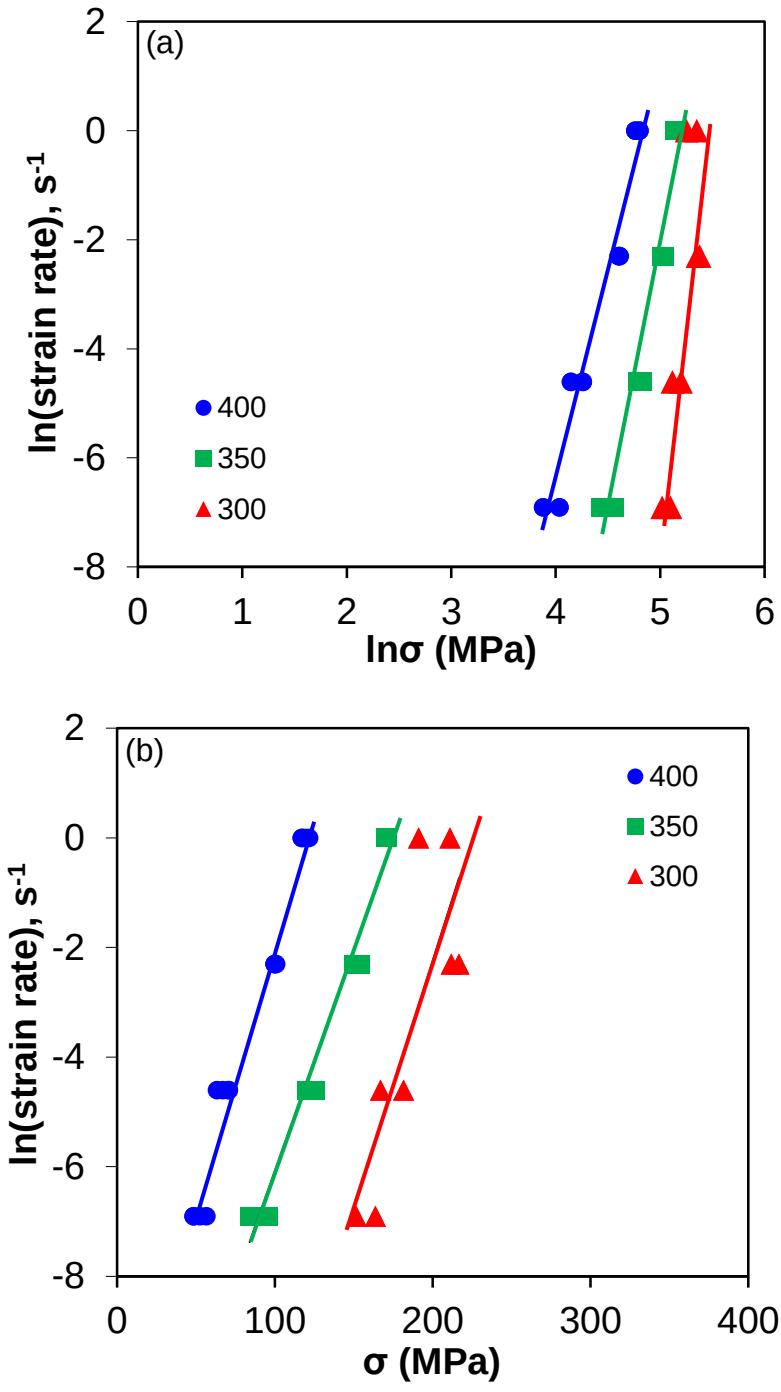

Figure 6.8: Relationships between (a) $\ln\dot{\varepsilon}$ and $\ln\sigma$ and (b) $\ln\dot{\varepsilon}$ and σ.

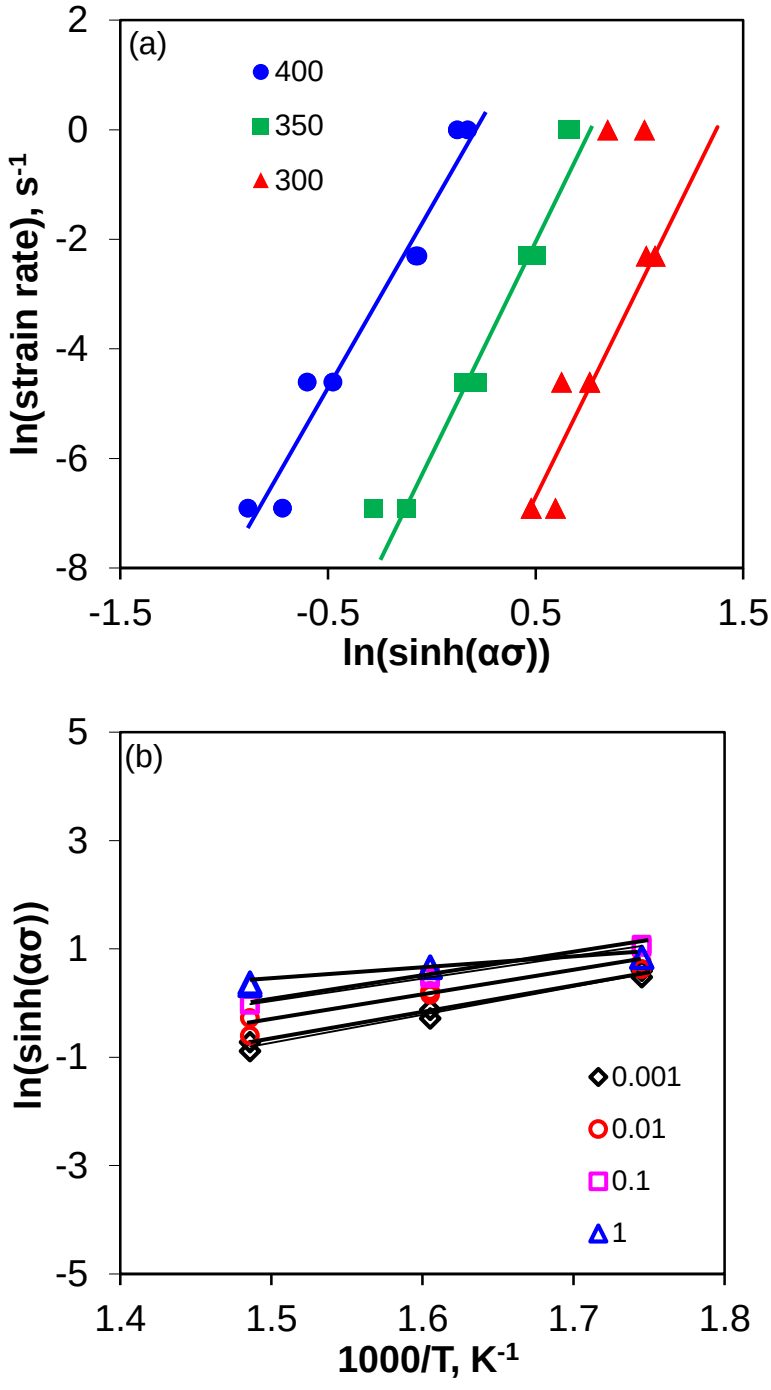

Figure 6.9: Relationships between (a) $\ln\dot{\varepsilon}$ and $\ln[\sinh(\alpha\sigma)]$ (b) $\ln[\sinh(\alpha\sigma)]$ and $1000/T$.

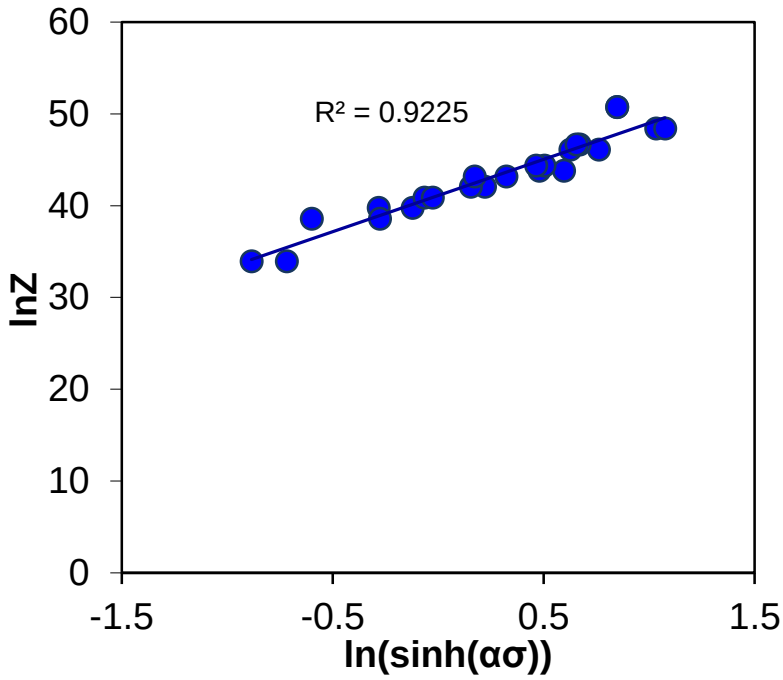

Figure 6.10: Relationship between lnZ and $\ln[\sinh(\alpha\sigma)]$.

The average values of the slopes are taken to calculate the values of n_1 and β, which are obtained to be 11.14 and 0.0897, respectively. Finally the stress multiplier α can be estimated as $\alpha = \beta / n_1 =$ 0.0081. The stress multiplier α is an adjustable constant which brings $\alpha\sigma$ into the correct range that gives linear and parallel lines in $\ln\dot{\varepsilon}$ versus $\ln\left[\sinh\left(\alpha\sigma\right)\right]$ plots [224]. It should be noted that for hot deformation of AZ magnesium alloys α values of about 0.001-0.07 MPa^{-1} have been reported [224].

The relationship between $\ln\dot{\varepsilon} - \ln[\sinh(\alpha\sigma)]$ is shown in Fig. 6.9(a). Likewise, the relationship between $\ln[\sinh(\alpha\sigma)] - 1/T$ is plotted in Fig. 6.9(b). Ignoring the difference between various temperatures and strain rates, the average value of the slopes at different deformation temperatures (n) and the mean value of the slopes at various strain rates (S) were then determined. Then the activation energy Q could be calculated from Eq. (6.7). In the present study, the activation energy

of the alloy during hot compression is obtained to be 241 kJ/mol which is higher than the lattice self-diffusion activation energy of magnesium (135 kJ/mol) or the grain boundary diffusion activation energy (92 kJ/mol) [224–227]. This can be ascribed to the presence of Y, pinpointing the importance of rare earth elements on increasing the deformation resistance at high temperatures. For instance, the activation energy of the present alloy is significantly higher than the most commercially important magnesium alloy AZ31, which was found to be about 147 kJ/mol [228]. Previously, it was reported that the rate-controlling mechanism may be identified based on the stress exponent (n) and the apparent activation energy (Q) [52,229]. At 400ºC/0.001s^{-1} the values of n and Q are estimated to be 6.58 and 282 kJ/mol, respectively. The cross-slip of screw dislocations may be the rate controlling process due to the much higher apparent activation energy than that for self-diffusion (135 kJ/mol) [52,230,231]. At 300ºC/1s^{-1}, the values of n and Q are 7.7 and 146 kJ/mol, respectively. The lower apparent activation energy (146 kJ/mol), which is close to that for self-diffusion (135 kJ/mol), and the higher stress exponent (7.7) indicate that dislocation climb controlled by self-diffusion is likely to be the rate controlling mechanism [52,229,232].

The linear relationship between ln$Z$ and $\ln[\sinh(\alpha\sigma)]$ could be plotted, as shown in Fig. 6.10. At lower temperatures and higher strain rates, the higher Z values corresponded to higher strengths. On the other hand, at higher temperatures and lower strain rates Z exhibited lower values, which reflected the occurrence of dynamic recrystallization, giving rise to a decrease in the strength of the alloy. The intercept of the fitted curve in Fig. 6.10 is taken as the value of ln$A$ = 41.1, of which A value is obtained as 7.07×10^{17} s^{-1}. Substituting the measured values of A, α, n and Q into the

Eq. (6.1), the constitutive equation during hot compression of the studied alloy is obtained as follows,

$$\dot{\varepsilon} = 7.07\times10^{17}\left[\sinh\left(0.0081\sigma\right)\right]^{7.26}\exp\left(-\frac{241740}{8.314T}\right). \quad (6.11)$$

6.3.3 Processing maps

In general, the values of efficiency of power dissipation increase with decreasing strain rate or increasing test temperature [53,233]. Therefore, a lower efficiency of power dissipation corresponds to a lower temperature region or higher strain rate region, whereas a higher efficiency of power dissipation corresponds to a higher temperature region or a lower strain rate region. At lower temperatures, the deformation mode is mostly twinning and basal slip in magnesium alloys due to its limited number of available slip systems [173,234,235]. Other slip systems become active as the deformation temperature increases [50,51]. In addition, the dynamic recrystallization (DRX) phenomenon is more likely to occur with increasing deformation temperature and decreasing strain rate owing to the activation of dislocation glide, climb and cross slip and the enhanced migration of grain boundaries [53,96,233,236]. It has been reported that the volume fraction of dynamic recrystallized (DRXed) grains increase at high temperatures and low strain rates [233,237]. It is also known that the temperature plays a more predominant role than the strain rate in promoting the DRX process during hot deformation [52]. Therefore, a more uniform grain size distribution is expected to appear in the microstructure deformed at elevated temperatures.

The 2D processing maps of as-extruded ZM31+3.2Y alloy developed at strains of 0.1, 0.2, 0.3 and 0.4 are shown in Fig. 6.11, where the contour values denote the efficiency of power dissipation

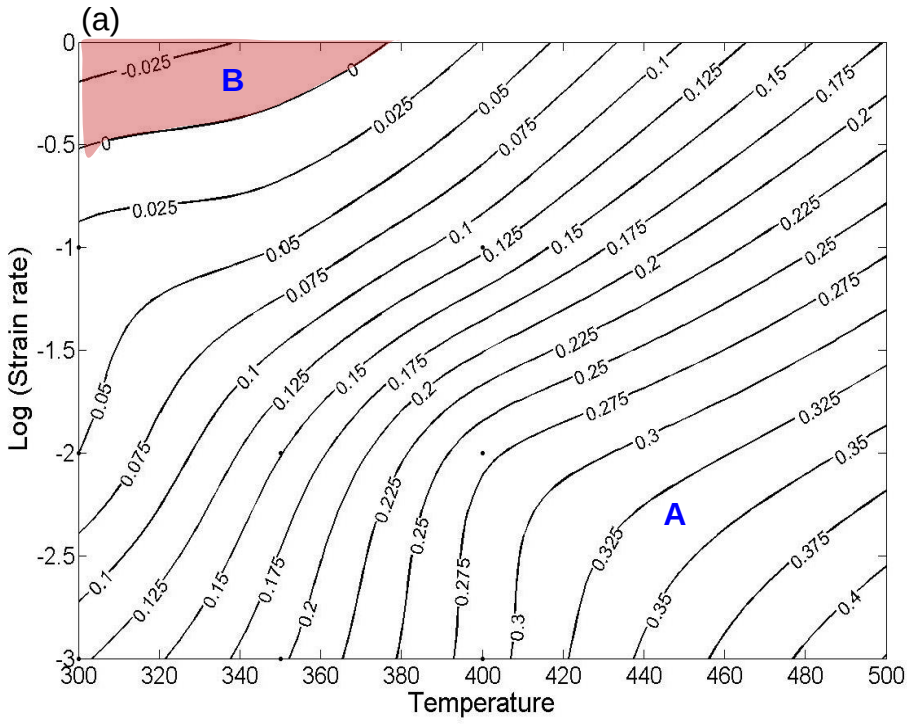
(a)
B
A
Log (Strain rate)
Temperature
0
-0.5
-1
-1.5
-2
-2.5
-3
300
320
340
360
380
400
420
440
460
480
500

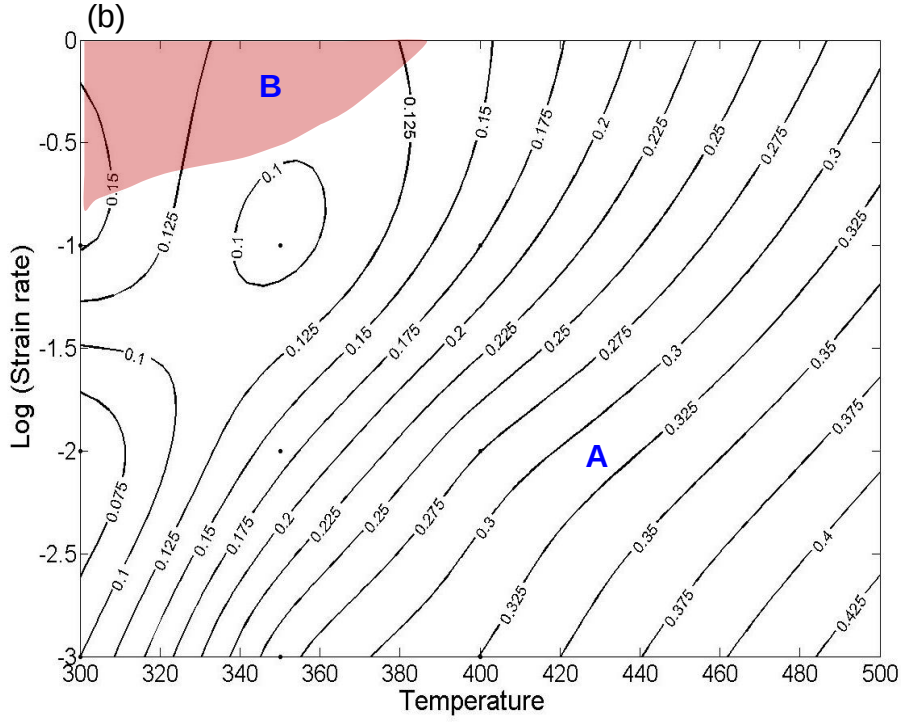
(b)
B
A
Log (Strain rate)
Temperature
0
-0.5
-1
-1.5
-2
-2.5
-3
300
320
340
360
380
400
420
440
460
480
500

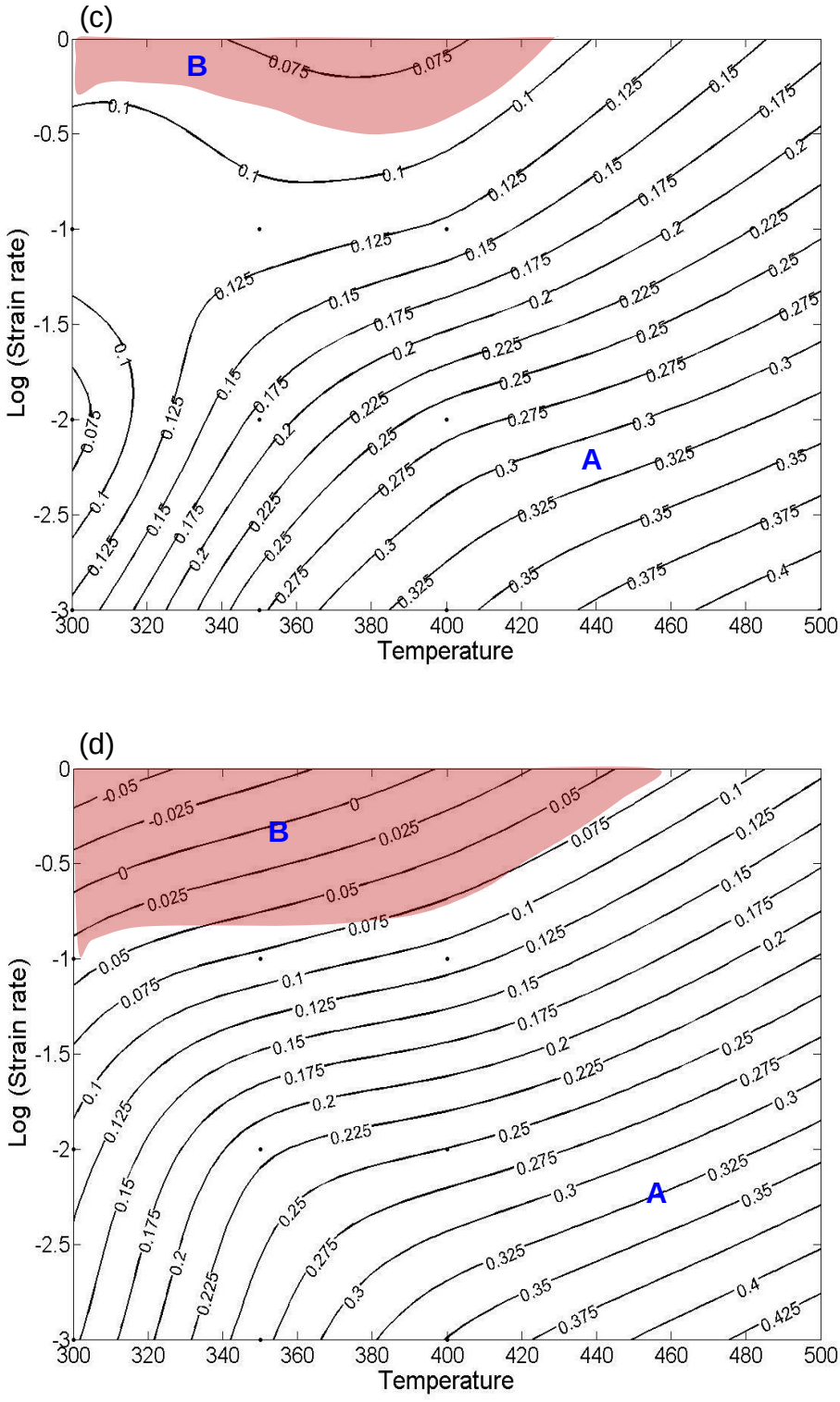

Figure 6.11: Processing maps of the studied alloy at strains of (a) ε= 0.1, (b) ε= 0.2, (c) ε= 0.3, and (d) ε= 0.4.

and the shaded areas stand for the regions of unstable flow. The processing map at varying strain amounts could be allocated into two different domains on the basis of efficiency of power dissipation and instability criterion: (1) Domain A represents a stable region where fairly high values of efficiency of power dissipation were observed, which corresponds to the samples deformed at higher temperatures and lower strain rates. It revealed a greater efficiency of power dissipation in the temperature range of 340-500°C and strain rate range of 0.001-0.03 s^{-1}, with a peak efficiency of about 42.5% at about 500°C and 0.001s^{-1}. (ii) Domain B corresponds to the samples deformed at the lower temperature and higher strain rate conditions in which very low or negative values of efficiency of power dissipation were obtained. This is often referred to as instability region.

From processing maps shown in Fig. 6.11, it is seen that the profile of power dissipation maps was different at different strain amounts, which implies that the train has a strong influence on the power dissipation maps. Since a greater efficiency was observed at a strain rate range of 0.001-0.01 s^{-1} it could be inferred that the favorable condition for hot processing of ZM31+3.2Y alloy lies in the region of lower strain rates. It is known that domains with a higher efficiency of power dissipation commonly represent optimum processing conditions [52,238]. Domain A is similar to that reported for as-cast Mg-Zn-Y-Zr alloy [53]. The characteristic microstructures of the stable domain constitute DRXed grains. Fig. 6.12(a) illustrates the associated post-deformed microstructure at 400°C and $\dot{\varepsilon} = 0.001\,s^{-1}$. The microstructure displayed a homogenous grain size distribution which indicated the occurrence of adequate DRX. The corresponding compressive true stress-strain curves in Fig. 6.6(a) showed an obvious strain softening effect induced by DRX. This suggests that higher temperatures and lower strain rates are preferred for the hot working of ZM31+3.2Y alloy. The reason for this could be attributed to the fact that at higher temperatures

and lower strain rates the DRX occurred more extensively with the progress of deformation, which helped reduce the flow localization, and therefore the material exhibited good workability in these conditions.

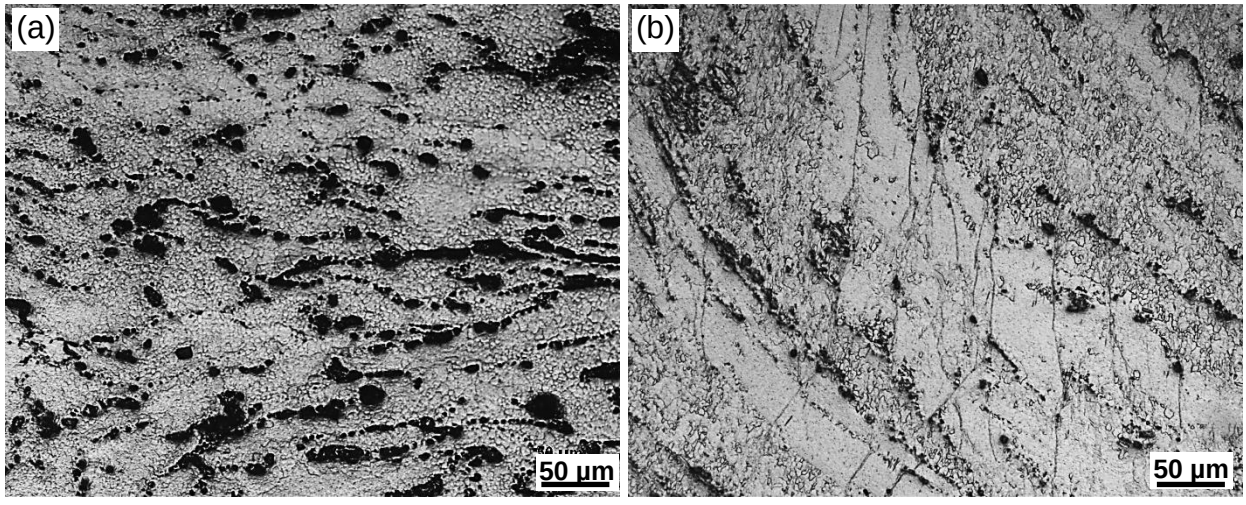

Figure 6.12: Typical microstructures of the test alloy deformed at (a) 400°C and 0.001 s^{-1}, and (b) 300°C and 1 s^{-1}.

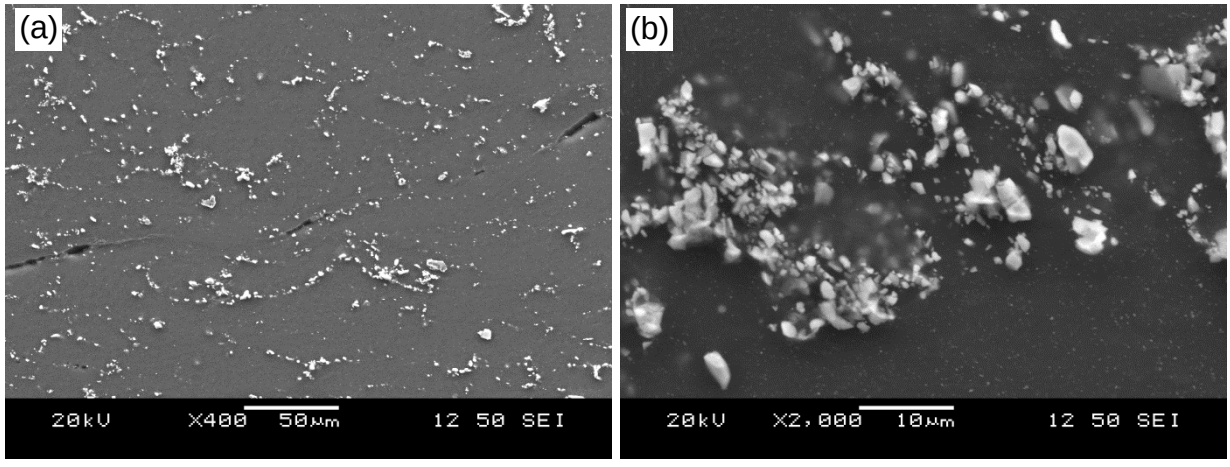

Figure 6.13: Typical microstructures of the test alloy deformed at 300°C and 1 s^{-1} at (a) lower and (b) higher magnifications.

Only one instability region subsisted in the processing maps as shown in Fig. 6.11. Microstructures within the instability regions were often characterized by fine DRX grains along the boundaries of coarse grains, local deformation bands, twins and micro-cracks [52]. The instability parameter ξ is estimated as negative in Domain B where material flow is unstable. Indeed, the negative strain rate sensitivity is directly accountable for the negative η and ξ values. As seen from the figure, Domain B or instability region occurred at higher strain rates (>0.1 s^{-1}) and lower deformation temperatures, which broadened with increasing strain. This suggests that the hot-workability of the alloy in the high strain rate region became inferior as the strain amount increased, hence it became increasingly difficult to deform the alloy at higher strain rates. It is generally accepted that flow instability is associated with the localized shear initiated by high strain rates [239]. Xu *et al*. [52] and Srinivasan *et al*. [240] also reported similar results. Fig. 6.12(b) displays the microstructure of the specimen deformed in the instability region at 300°C and $\dot{\varepsilon}$ = 1 s^{-1}. It is seen that the post-deformed microstructure demonstrated coarse grains and localized deformation bands extended inside the coarse grains along the direction perpendicular to the compressive direction. The presence of fine DRXed grains mainly at grain boundaries and elongated coarse grains indicated the inadequate occurrence of DRX. Furthermore, micro-cracks were also observed in the microstructure deformed at 300°C and 1 s^{-1} as shown in Fig. 6.13(a). The crack nucleated and propagated through second-phase particles due to the presence of stress concentration caused by nonhomogeneous deformation at higher strain rates. Fig 6.13(b) shows an SEM image of the distribution of I and W phase particles in a deformed specimen in this instability region. It is of importance to note that no particle-interface cracking or debonding was observed even at a higher magnification. Furthermore, no dynamic second-phase particle coarsening was spotted. When a material is deformed in the instability domain, it is not easy to

achieve the desired mechanical properties. Hence, it is important to avoid such processing conditions during hot deformation.

6.3.4 Microstructural evolution during hot deformation

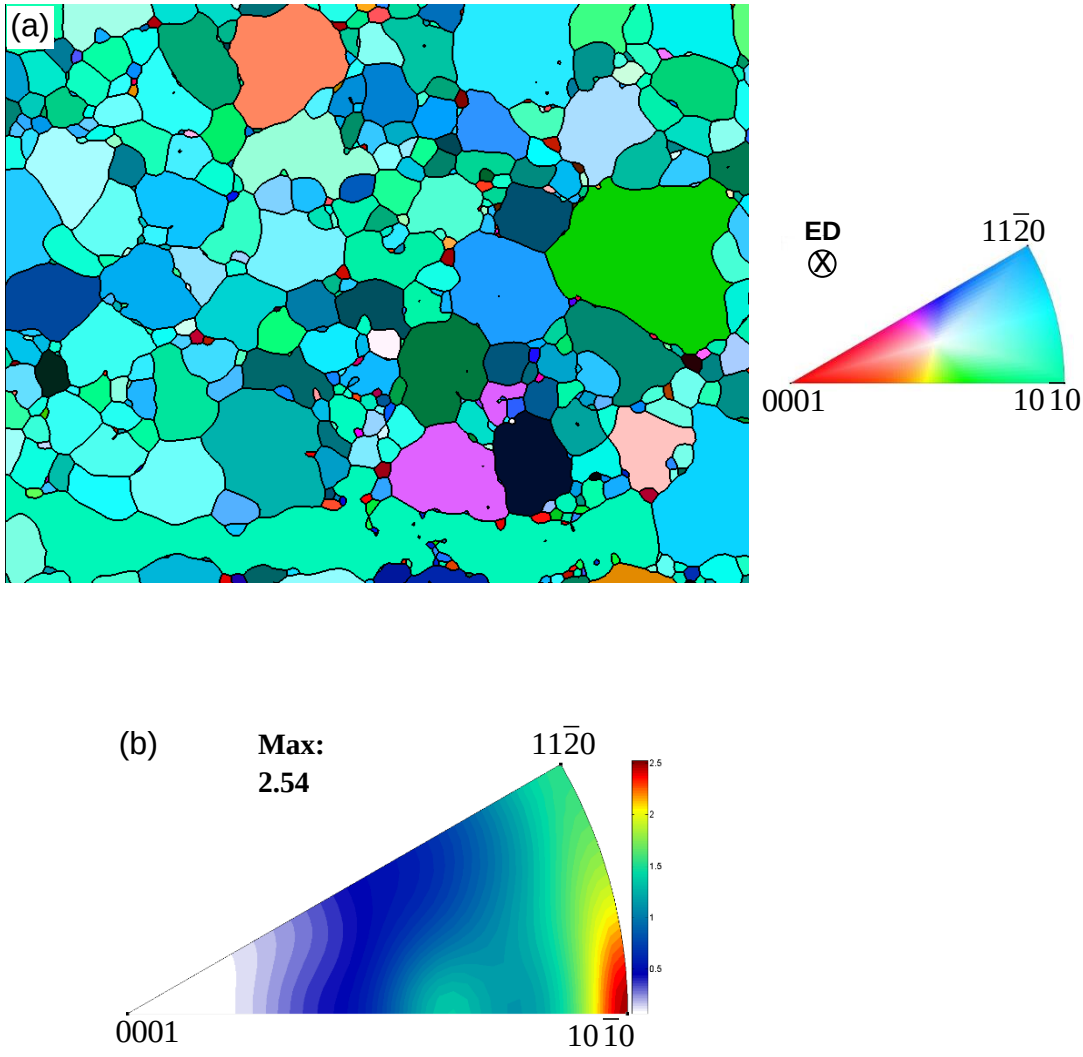

Figure 6.14: Typical (a) OIM (or IPF map), and (b) inverse pole figure (IPF) of ZM31+3.2Y magnesium alloy in the as-extruded condition, where the map color code (or legend) in (a) and IPF in (b) project the directions parallel to ED and surface of observation.

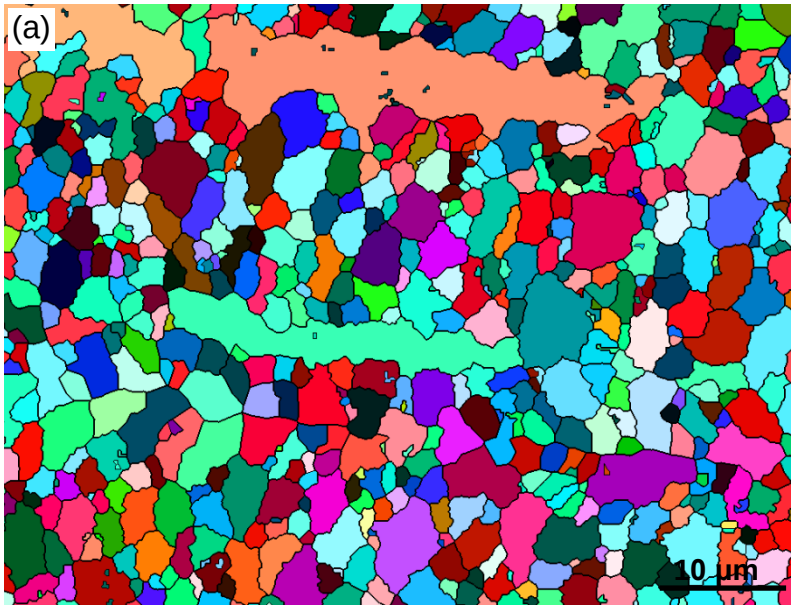
(a)
10 µm

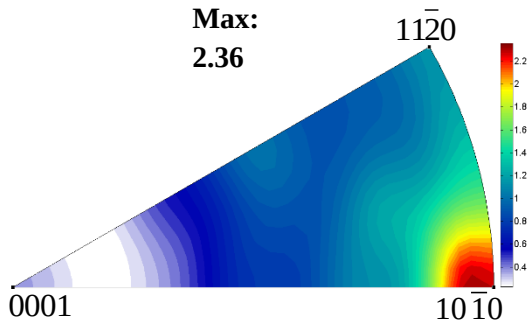
Max:
2.36
11$\bar{2}$0
0001
10$\bar{1}$0

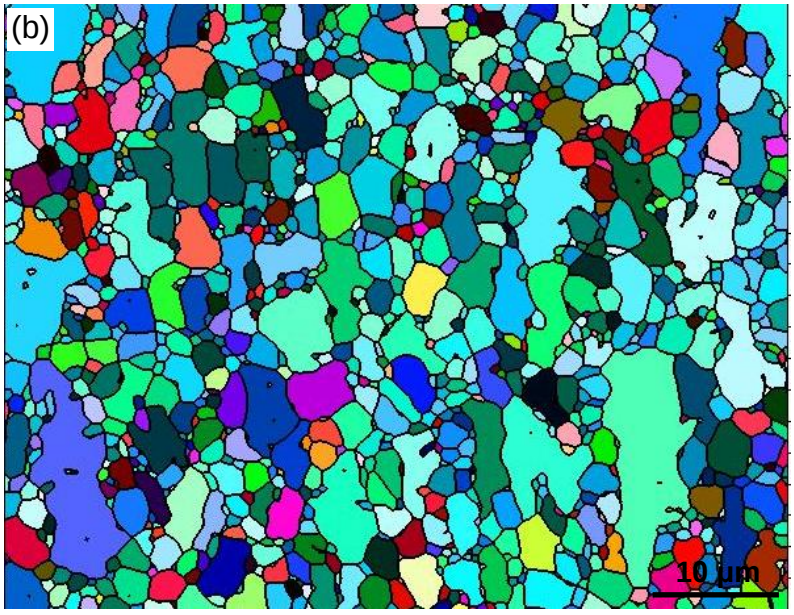
(b)
10 µm

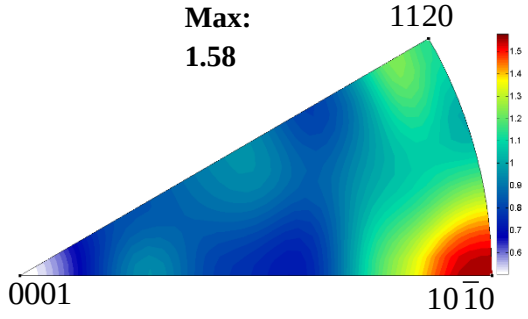
Max:
1.58
11$\bar{2}$0
0001
10$\bar{1}$0

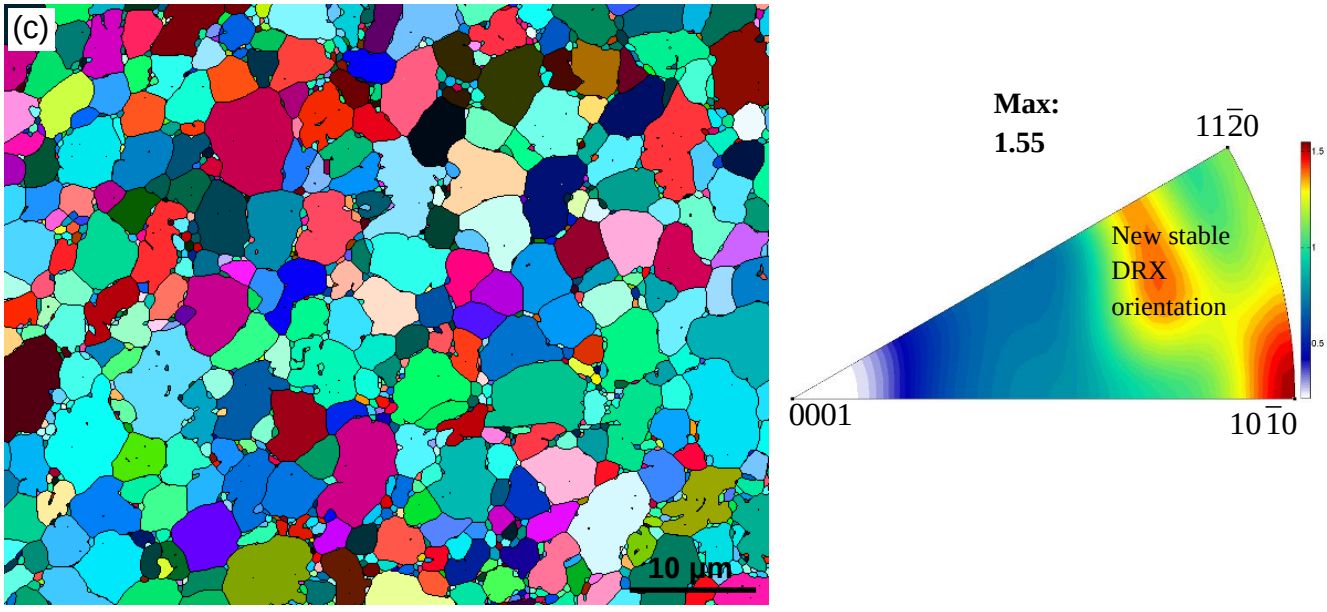

Figure 6.15: Orientation maps (left) and the corresponding inverse pole figures (right) of the specimens deformed to a strain amount of 50% at a strain rate of 0.001 s^{-1} and a temperature of (a) 300°C, (b) 350°C, and (c) 400°C.

Fig. 6.14(a) illustrates the orientation map for the as-extruded ZM31+3.2Y alloy where different colors represent different orientations and grain boundaries are outlined by black lines. The orientations associated with the color are represented in the EBSD color code (or legend). The corresponding inverse pole figure (IPF), as shown in Fig. 6.14(b), revealed a high density of grains with their $\langle 10\bar{1}0 \rangle$ directions parallel to the ED and the absence of <0001> directions parallel to the ED. The representative EBSD microstructure obtained upon compression to a strain amount of 50% at different temperatures is shown in Fig. 6.15(a, b and c) in terms of Kikuchi diffraction based orientation maps (left-hand side of images). The orientations corresponding to the deformed and dynamically recrystallized area are also presented in the form of inverse pole figures by means of contour data (right-hand side of "triangle-like" circular segments). During hot compression at 300°C new grains were developed in the form of clusters along the grain boundaries. As seen from

the color in Fig. 6.15(a), crystal orientations of new grains were almost randomly distributed. It should be noted that in the DRX of the present Mg alloy at a deformation temperature of 300°C (Fig. 6.15(a)) new grains were not fully developed throughout the material even at such a high strain of 50%. Therefore a non-homogenous microstructure was observed where the original grains were surrounded by nucleated finer grains during deformation at 300°C. The inverse pole figure revealed a faint texture component around [0001] pole, reflecting a rotation of *c*-axes (or basal planes) of some grains at about 86° relative to the original grain orientation. That is, the texture component close to [0001] pole corresponds to the grains that experienced extension twinning. When the deformation temperature increased to 350°C, EBSD microstructure showed a similar but more inhomogeneous microstructure with some non-equiaxed grains signifying the insufficient occurrence of DRX (Fig. 6.15(b)). The corresponding inverse pole figure revealed a more random orientation in the absence of [0001] pole and a lower maximum density of 1.58 MRD (multiples of a random distribution, or multiples of a random density) in the $\left[10\bar{1}0\right]$ pole, due to the occurrence of more complete DRX in comparison with the deformation at 300°C. With increasing deformation temperature to 400°C where strain softening occurred and DRX took place more completely, new equiaxed grains developed homogeneously throughout the material, as seen from Fig. 6.15(c). The corresponding inverse pole figure data showed an appreciable continuous orientation spread between both $\left[11\bar{2}0\right]$ and $\left[10\bar{1}0\right]$ poles. Again, at this deformation temperature no [0001] pole was present, and especially a DRX texture component was evidently developed between the [0001] and $\left[11\bar{2}0\right]$ poles, as noted in the IPF of Fig.6.15(c). A similar texture component in the inverse pole figure for stable new DRX grains was also reported by Al-Samman *et al.* [93]. It is generally recognized that according to the nature of the recrystallization process, continuous or discontinuous DRX could be distinguished. Continuous DRX is essentially

a one-step process, where new grains are nucleated evenly throughout the material and can hardly grow [241]. In contrast, discontinuous DRX involves a two-step process, i.e., the nucleation of new grains is followed by grain growth with a long-distance migration [241]. The above EBSD observations and discussion provided an important vision into the mechanisms of DRX in the present magnesium alloy. At 300 and 350°C, the dynamic recrystallization could be regarded to be of a "continuous" nature (CDRX), based upon microstructure where nucleated grains could not grow. However, the DRX mechanism at 400°C can be considered as discontinuous (DDRX) because of well-developed equiaxed grains, as seen from Fig.6.15(c).

6.4 ZM31+6Y Alloy

6.4.1 Flow behavior

The typical true stress-true strain curves of as-extruded ZM31+6Y alloy obtained at different deformation temperatures in the range of 200-400°C and strain rates of 0.001-1 s^{-1} are shown in Fig. 6.16. The stress-strain curve obtained at 200ºC/1s^{-1} was not presented due to unavailability of sufficient data points during the test. The general features of the flow stress curves are similar in all deformation conditions, i.e., the flow stress initially increased to a maximum and then decreased continuously. Upon a close examination, specific differences in the deformation behavior of the curves could be observed. At higher temperatures the material exhibited less significant hardening followed by mild flow softening leading to a quasi-steady state. In contrast, at lower temperatures the alloy displayed greater hardening followed by more substantial flow softening and shear fracture at 45° with respect to the compression axis (or extrusion direction).

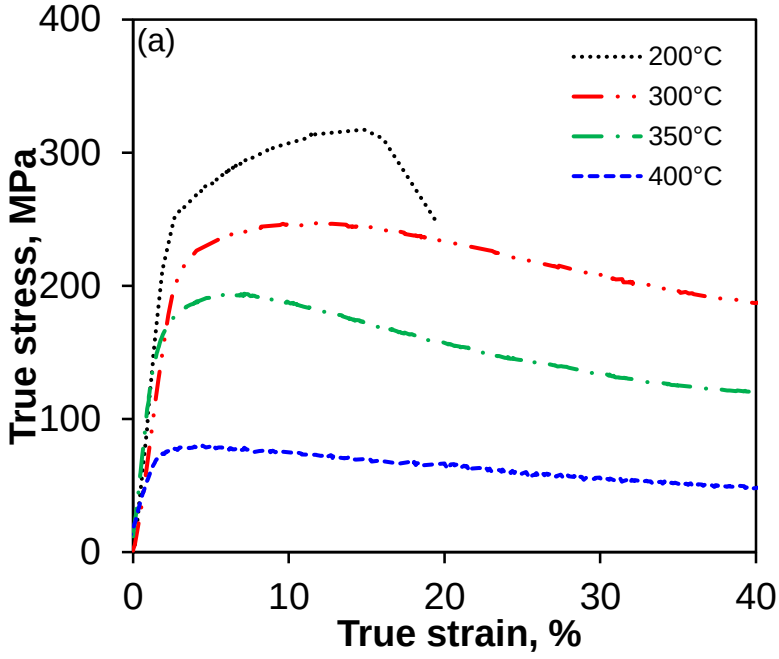
(a)
200°C
300°C
350°C
400°C
True stress, MPa
True strain, %
0
100
200
300
400
0
10
20
30
40

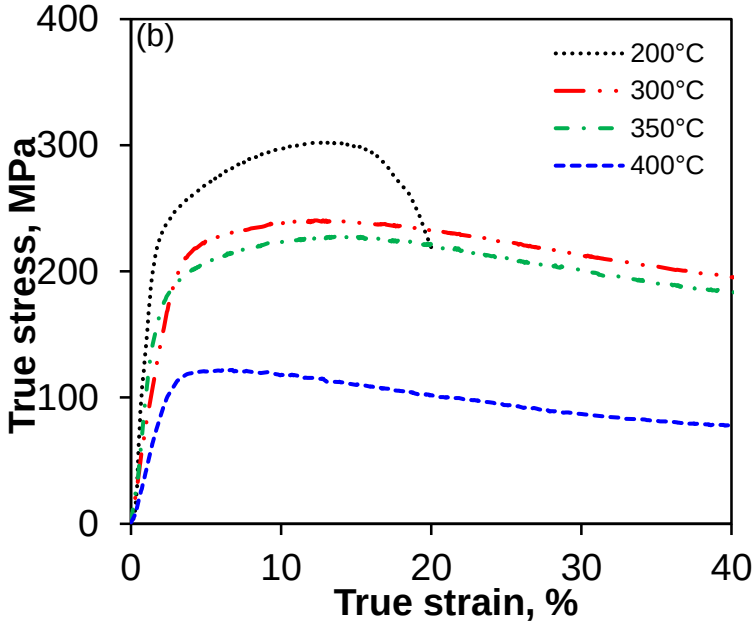
(b)
200°C
300°C
350°C
400°C
True stress, MPa
True strain, %
0
100
200
300
400
0
10
20
30
40

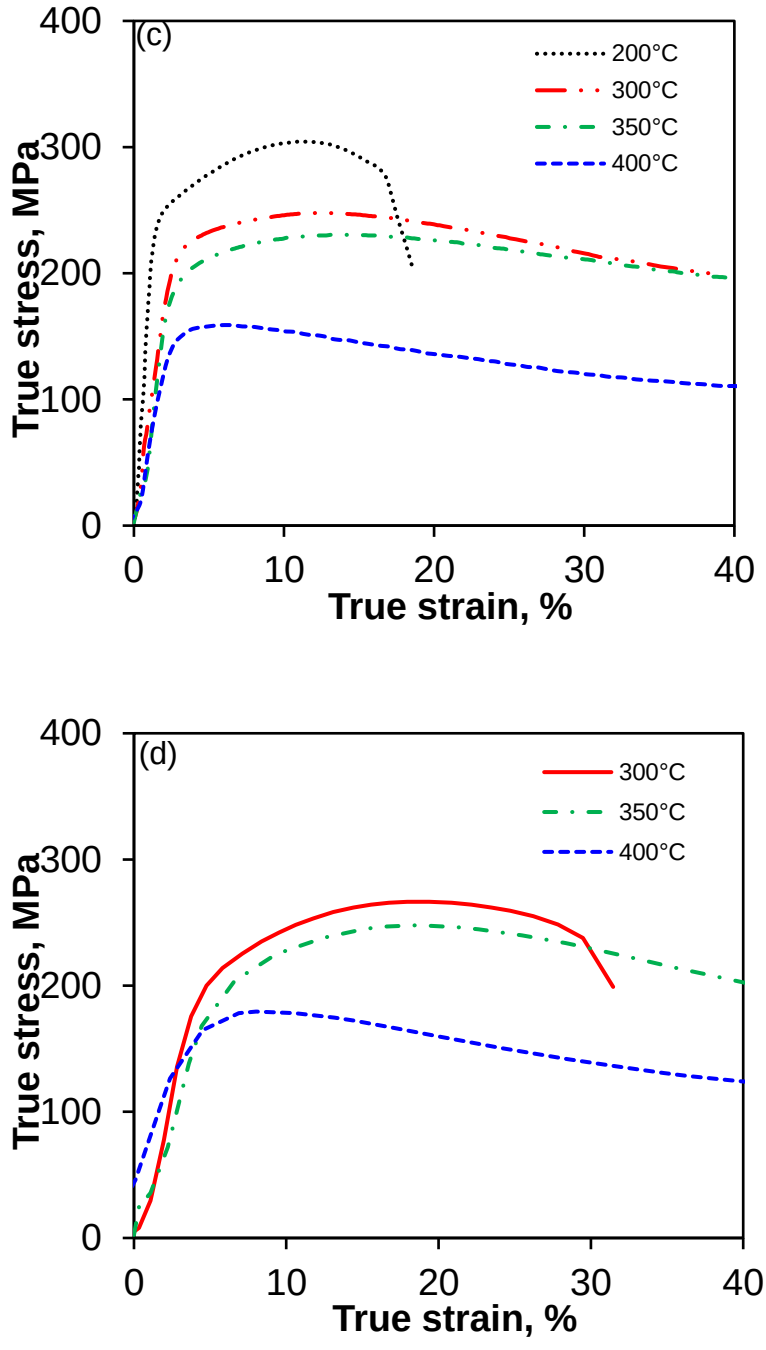

Figure 6.16: Typical compressive true stress-true strain curves of ZM31+6Y alloy deformed at different temperatures at strain rates of (a) 0.001 s^{-1}, (b) 0.01 s^{-1}, (c) 0.1 s^{-1} and (d) 1 s^{-1}.

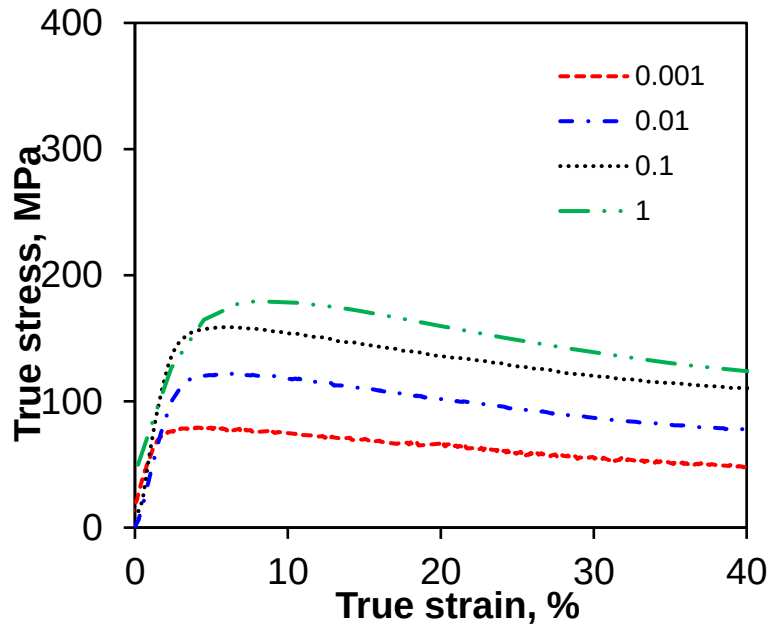

Figure 6.17: Typical compressive true stress-true strain curves of ZM31+6Y alloy deformed at varying strain rates from 0.001 s^{-1} to 1 s^{-1} at a temperature of 400°C.

It is also seen that the peak flow stress was dependent on the deformation temperature and strain rate. At a given strain rate, the flow stress decreased with increasing temperature (Fig. 6.17). For example, the peak stress of the alloy decreased from 326 MPa to 80 MPa with increasing temperature from 200 to 400°C at a strain rate of 0.001 s^{-1}. This was due to the augmented thermal activation of the alloy and the kinetic energy of metal atoms accumulated which enhanced the movement of dislocations at higher temperatures. The higher the strain rate, the greater the flow stress at a certain temperature, which can be clearly seen in Fig. 6.17 where the peak stress changed from 80 MPa to 179 MPa with increasing strain rate from 0.001 s^{-1} to 1 s^{-1} at 400°C. This is because there was an inadequate time for energy accumulation and dislocation annihilation at higher strain rates [223,242].

The temperature and strain rate sensitive behavior of flow stress of the studied alloy could be explained in terms of work hardening and dynamic recrystallization. It is known that the deformation at higher temperatures is a competing process of dynamic softening and strain hardening [233]. At the initial stage of deformation, dislocation density increased drastically. Strain hardening exceeded dynamic softening, leading to a rapid increase of flow stress. Therefore, the true stress-true strain curves exhibited a rising trend of work hardening. With increasing strain amount, the stored energy rapidly accumulated, which provided a sufficient driving force for the movement of dislocations such as dislocation climb or cross-slip. As the deformation progressed, the dynamic softening such as dynamic recrystallization occurred in hot deformation conditions, which compensated or partially compensated the effect of work hardening.

6.4.2 Activation energy

The data obtained at a test temperature of 200°C were not taken into account to compute activation energy because no substantial strain rate sensitivity was observed at that temperature. The plots of relationships between $\ln\dot{\varepsilon}$ and $\ln\sigma$ and $\ln\dot{\varepsilon}$ and σ are shown in Fig. 6.18(a) and 6.18(b), respectively, where the stress is the peak flow stress. Then the slope in Fig. 6.18(a) and 6.18(b) represents the value of n_1 and β. The mean values of the slopes are taken to obtain the n_1 and β values, which are 16.18 and 0.21, respectively. Finally the stress multiplier α could be calculated as $\alpha = \beta / n_1 = 0.013$. The relationship between $\ln\dot{\varepsilon} - \ln[\sinh(\alpha\sigma)]$ is shown in Fig. 6.19(a), while the relationship between $\ln[\sinh(\alpha\sigma)] - 1/T$ is plotted as shown in Fig. 6.19(b). The mean value of the slopes at different deformation temperatures (n) and the mean value of the slopes at various strain rates (S) were then determined. In the present study, the activation energy of the alloy during

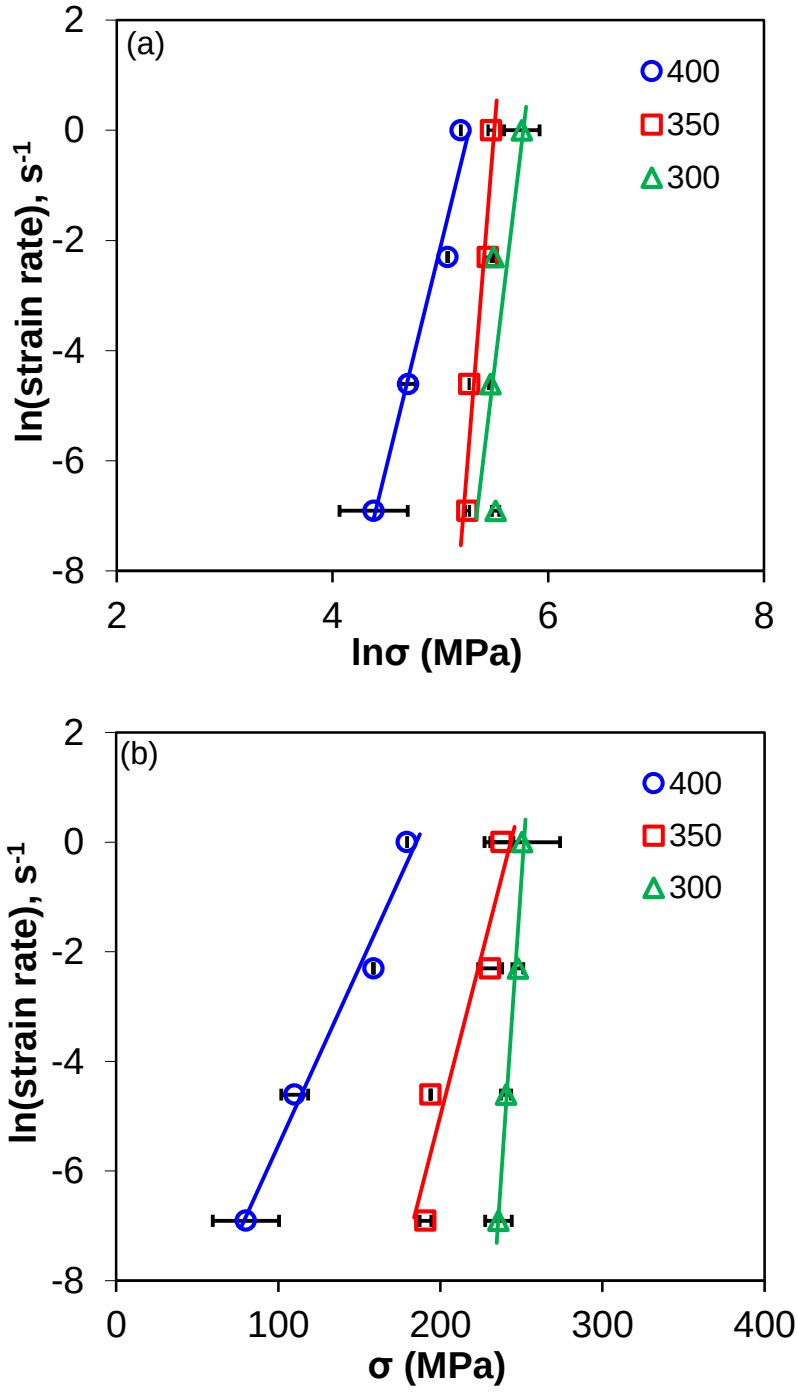

Figure 6.18: Relationships between (a) $\ln \dot{\varepsilon}$ and $\ln\sigma$ and (b) $\ln \dot{\varepsilon}$ and σ.

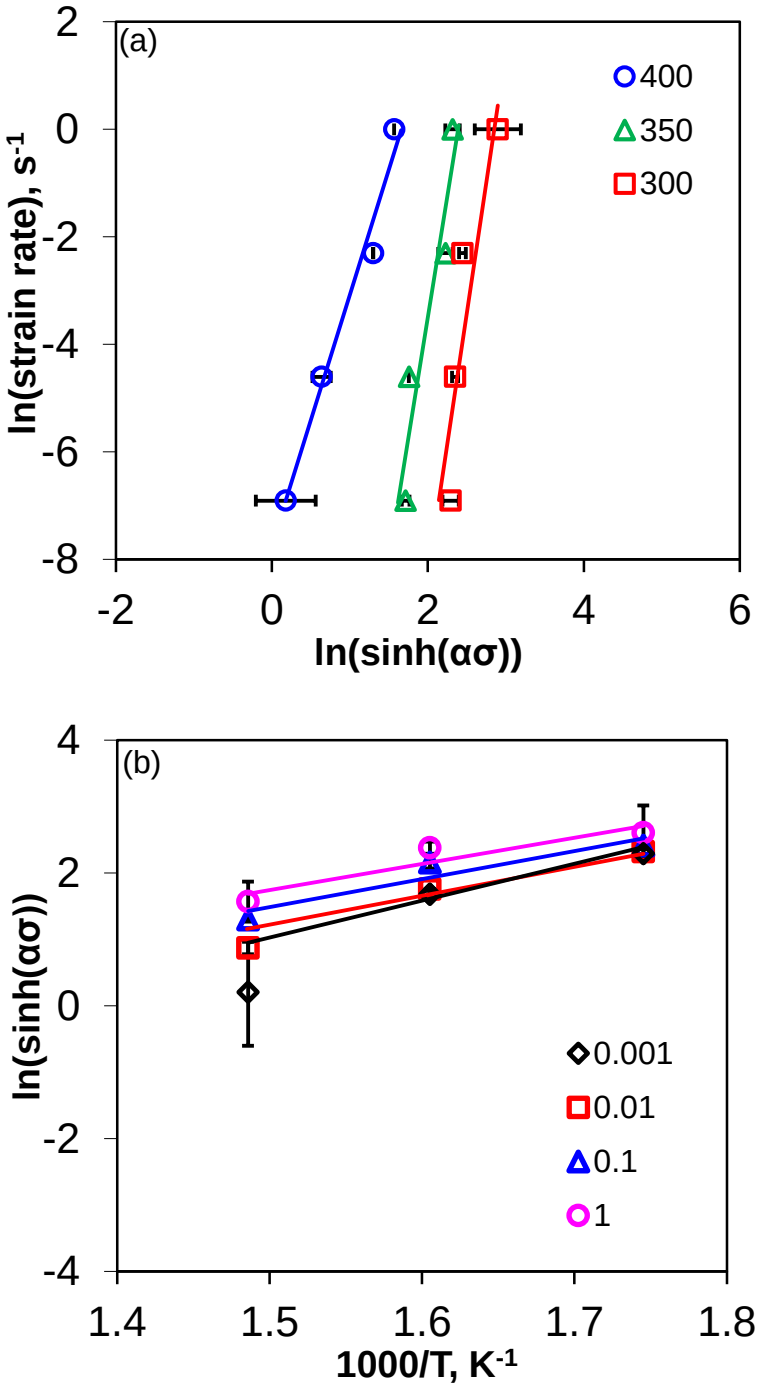

Figure 6.19: Relationships between (a) $\ln\dot{\varepsilon}$ and $\ln[\sinh(\alpha\sigma)]$, and (b) $\ln[\sinh(\alpha\sigma)]$ and $1000/T$

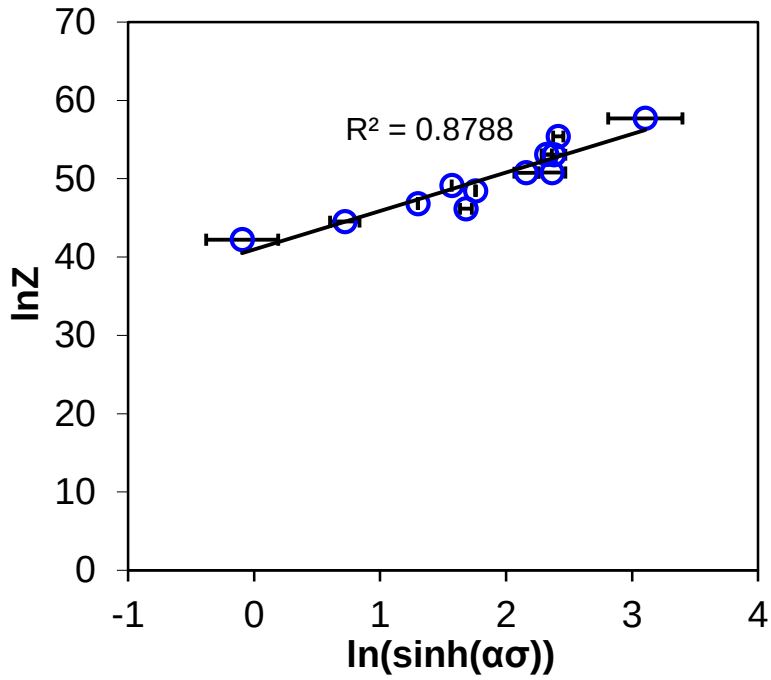

Figure 6.20: A relationship between ln*Z* and $\ln[\sinh(\alpha\sigma)]$.

hot compression is obtained to be approximately 274.8 kJ/mol which is much higher than that for self-diffusion (135 kJ/mol) in pure magnesium. For a typical as-cast AZ91D alloy the average apparent activation energy was estimated to be 181.9 kJ/mol at similar deformation condition [245]. Chen *et al.* [53] have obtained an average activation energy of 251.2 kJ/mol for an as-cast Mg-Zn-Y-Zr alloy containing W-phase. The average *Q* value of a cast Mg-Gd-Y-Zr alloy without having LPSO phase was determined to be 209 kJ/mol by Li and Zhang [51]. It is worth mentioning that the activation energy of the present ZM31+6Y alloy was higher than that of these alloys. This was obviously ascribed to the presence of LPSO phase, which was thermally stable and could be effective barriers to the motion of dislocations, resulting in a higher *Q* value.

A linear relationship between ln*Z* and $\ln[\sinh(\alpha\sigma)]$ is plotted in Fig. 6.20. The values of *Z* at different test temperatures and strain rates are also listed in Table 6.2, showing that the values of

Z increased with decreasing temperature and increasing strain rate. At lower temperatures and higher strain rates, *Z* exhibited higher values pointing towards the larger flow stress. On the other hand, at higher temperatures and lower strain rates, *Z* exhibited lower values, which indicated that dynamic recrystallization occurred causing a decrease in the flow stress.

Table 6.2: The calculated Zener-Hollomon parameter of the ZM31+6Y alloy at different strain rates and temperatures.

Strain rate, s^{-1}	**Zener-Hollomon parameter (*Z*) Temperature, °C**		
	300	**350**	**400**
0.001	1.15×10^{22}	1.12×10^{20}	2.17×10^{18}
0.01	1.15×10^{23}	1.12×10^{21}	2.17×10^{19}
0.1	1.15×10^{24}	1.12×10^{22}	2.17×10^{20}
1.0	1.15×10^{25}	1.12×10^{23}	2.17×10^{21}

6.4.3 Processing maps

The 2D processing maps of as-extruded ZM31+6Y alloy developed at strains of 0.1 and 0.4 are shown in Fig. 6.21, where the contour values denote the efficiency of power dissipation and the shaded brown areas stand for the regions of unstable flow. The processing map at strain amounts of 10% and 40% could be allotted into two different domains: (1) Domain A indicates a stable region where fairly high values of efficiency of power dissipation were seen, which corresponds

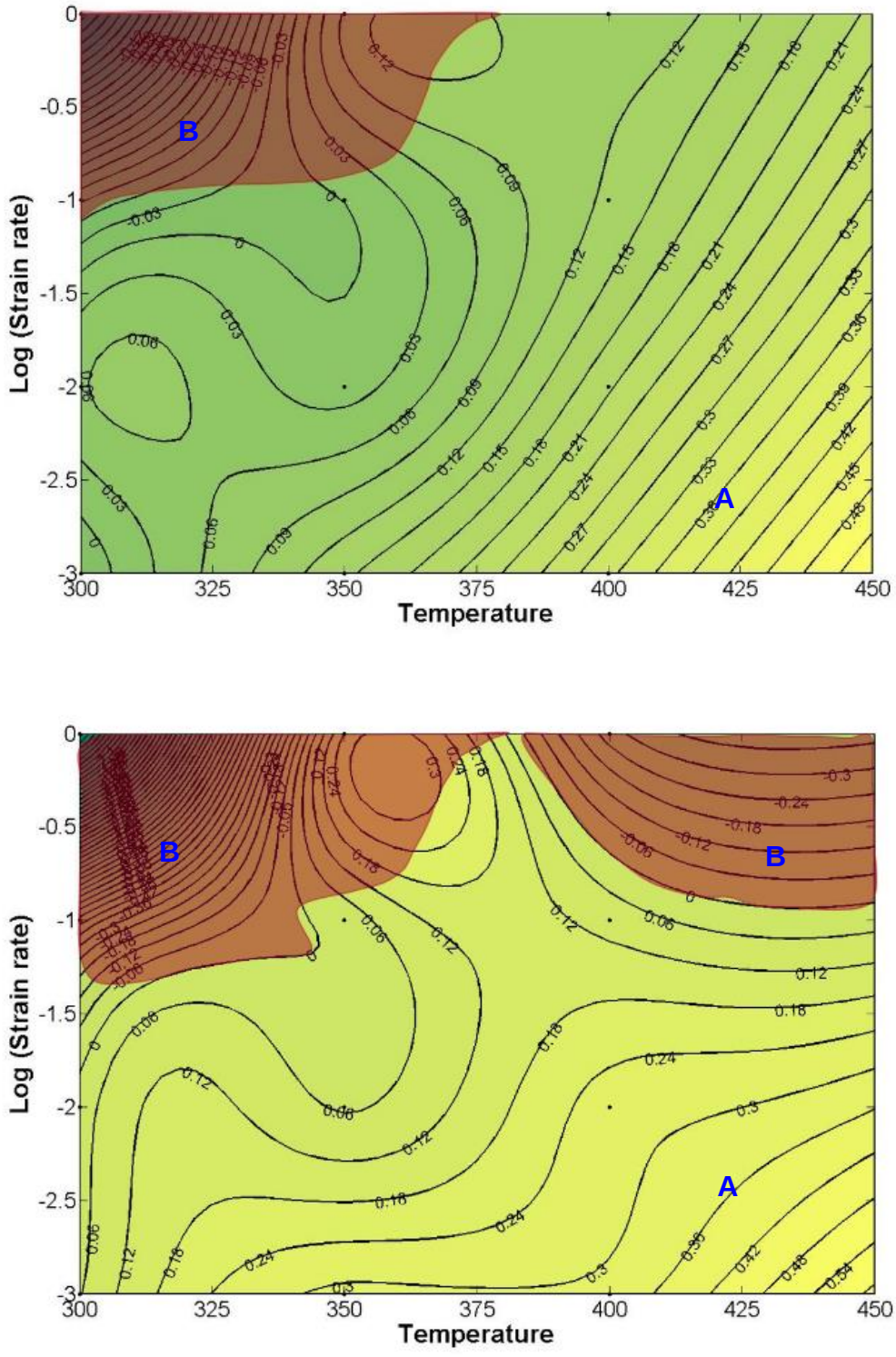

Figure 6.21: Processing maps of the ZM31+6Y alloy at strains of (a) ε= 0.1 and (b) ε= 0.4.

to the samples deformed at relatively higher temperatures and lower strain rates. It lay in a temperature range of 325-450°C and a strain rate range of 0.001-0.1 s^{-1}, with a peak efficiency of ~48% occurring at 425°C and 0.003 s^{-1}. (ii) Domain B corresponds to the samples deformed in the lower temperature and higher strain rate conditions in which very low or negative values of efficiency of power dissipation were obtained. This is often referred to as instability region. As can be seen from Fig. 6.21 the contour of power efficiency varies with increasing strain. Generally, dissipation efficiency is connected with microstructure evolution mechanisms where higher values represent DRX and relatively lower values represent DRV [90,246]. DRX is a desired beneficial phenomenon in hot deformation since it gives good workability to the material by reducing flow localization and simultaneous softening. It is known that domains with a higher efficiency of power dissipation commonly represent optimum processing conditions. Since a higher efficiency value was observed in the ranges range of 350-450°C and 0.001-0.03 s^{-1} it could be inferred as the favorable condition for hot processing of ZM31+6Y alloy.

Domain B is characterized by unstable material flow where the instability parameter ξ is estimated as negative. Domain B is only visible in the high strain rate and low temperature region at a strain of 0.1. With increasing strain Domain B extends and also appears in the high temperature regime, which suggests that the hot-workability of the alloy in the high strain rate region became poor as the strain amount increased. Hence, it became increasingly difficult to deform the alloy at higher strain rates. Microstructures within the instability regions were often characterized by local deformation bands, twins and micro-cracks [52]. When a material is deformed in the instability domain, it is not easy to achieve the desired mechanical properties. Thus, it is important to avoid such processing conditions during hot deformation.

6.4.4 Microstructural evolution during hot deformation

Fig. 6.22 shows the optical micrographs of ZM31+6Y alloy deformed at temperature 200°C, 300°C and 400°C up to a compressive strain amount of 10%**.**

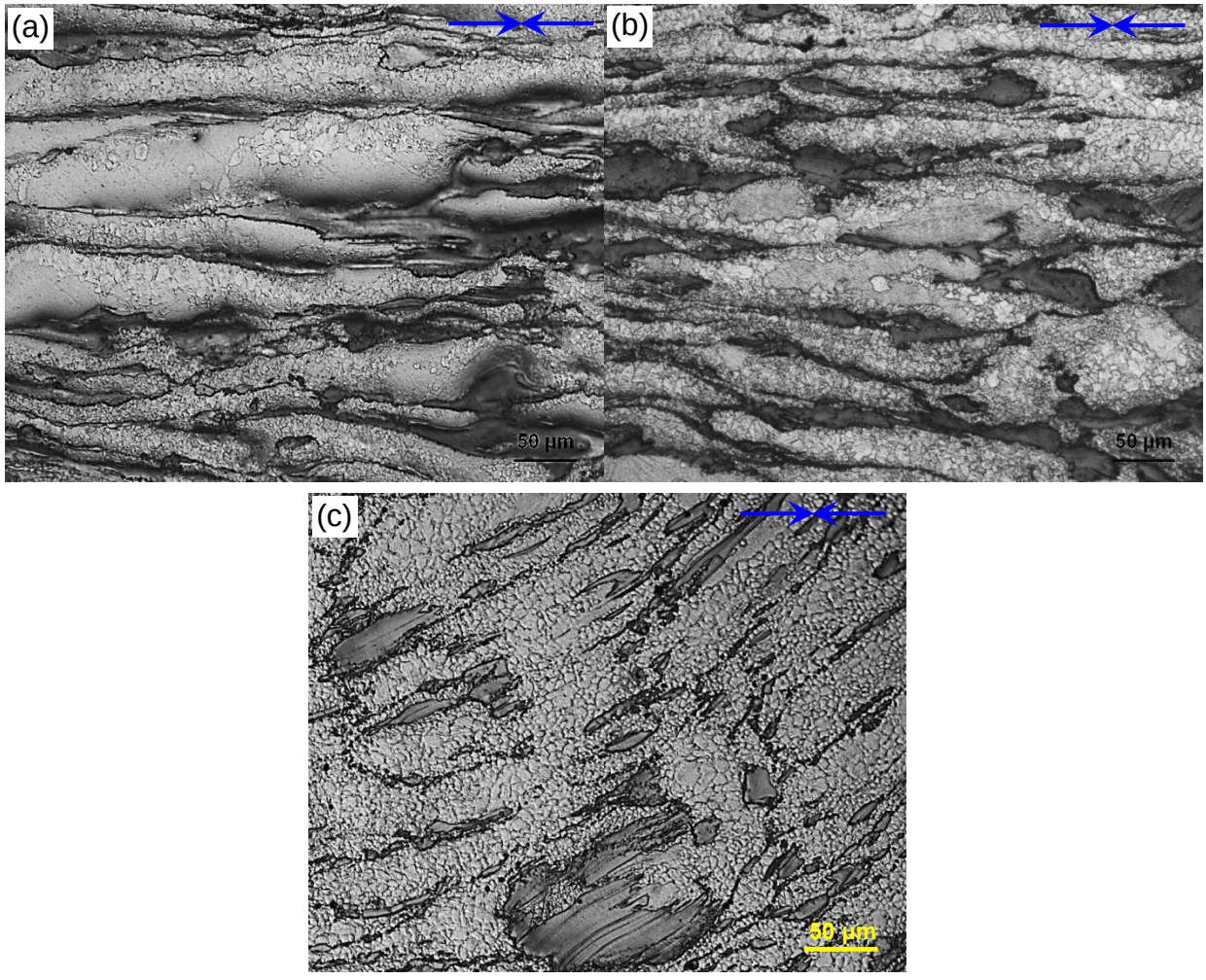

Figure 6.22: Typical optical microstructures of ZM31+6Y magnesium alloy compressed to a strain amount of 10% at (a) 200°C, (b) 300°C, and (c) 400°C (Blue arrows represent the compression direction).

It is clearly seen that deformation temperature had a significant influence on microstructure evolution. Some grain growth would occur while heating up the samples to the desired

deformation temperature and during the required holding time prior to deformation. At 200°C grain growth was insignificant, and at 300°C grain size increased from ~5.1 μm to ~7 μm. It is of interest to observe that the grain growth took place only in α-Mg fine grain region. No new grains seemed to develop in the deformed samples at 200°C or 300°C. The alloy indicated no signs of DRX and the deformed microstructure consisted of both hot worked coarse grain and recrystallized fine grains similar to as-extruded condition. In addition, LPSO phase did not exhibit any marked change in their morphology and distribution. In contrast, the microstructure deformed at 400°C exhibited recrystallized microstructure with a finer grain size of ~4.8 μm. This suggested that DRX occurred during hot compression process at 400°C. The new grains emerged mostly in the α-Mg matrix originating from the interface between the matrix and the LPSO phase [198]. This could be due to the local stress concentration which became sources for dislocation nucleation and pile-ups, and the formation of sub-grains and sub-grain boundaries. Upon further compression, low angle grain boundaries of the sub-grains developed to become high angle grain boundaries and resulted in the presence of DRXed grains. In contrast to the case at the lower deformation temperature, the LPSO phase unveiled some alteration in terms of dimension at 400°C. The average length and width of LPSO phase decreased to some extent with increasing test temperature. Such a refinement phenomenon in LPSO phase rather than coarsening at elevated temperatures due to kinking was also reported in [156,247].

The distribution of three different regions in the multimodal microstructure of the studied alloy after deformation at a strain rate of 0.001 s^{-1}, a strain amount of 10% and a temperature of 200-400°C is presented in Fig. 6.23(a). The as-extruded alloy contained 24.8% LPSO phase, 8.9% coarse elongated grains and 66.3% fine recrystallized grains. Increasing the deformation temperature from 200 to 400°C resulted in a reduction in the fraction of LPSO phase in the alloy

from 23.4% to 18%. At the same time, there was a decrease in the fraction of hot-worked coarse grain from 7% to 1%. In contrast, raising the deformation temperature from 200 to 400°C led to increased finer recrystallized grains due to more adequate happening of DRX. Correspondingly, the area of the recrystallized grains extended about 80% replacing the area of worked grains. The influence of deformation temperature on the size of LPSO phase was also observed and summarized in Fig. 6.23(b). For the as-extruded alloy, the average width of fiber-shaped LPSO phase was 28.9 ± 5.8 μm. Raising the deformation temperature from 200 to 400°C resulted in a reduction in the width of the LPSO phase from 27 ± 8.6 μm to 22 ± 4.9 μm. Such a small decrease in the width and volume fraction at 400°C suggested a high degree of thermal stability of the LPSO phase, which is also consistent with other reported studies [25,40,163].

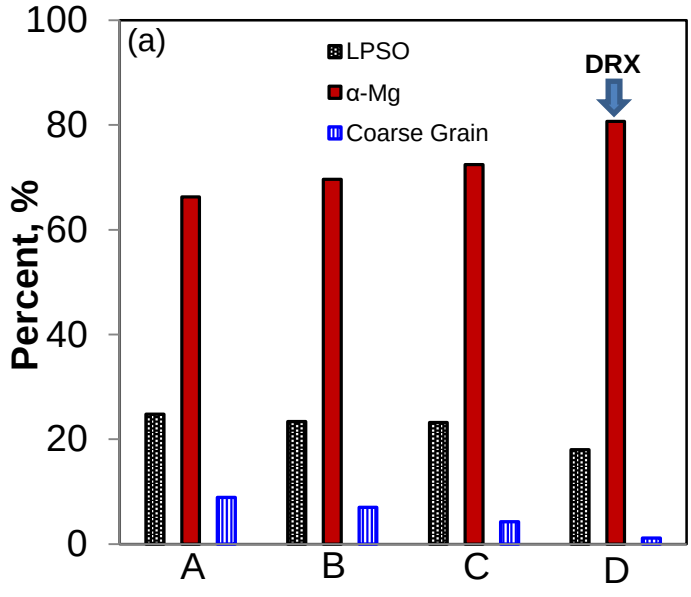

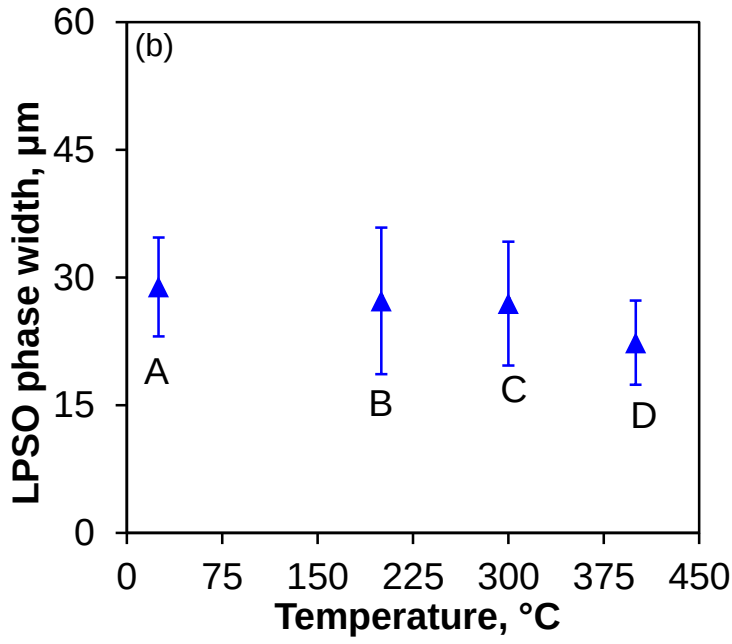

Figure 6.23: A comparative study of quantitative image analysis of (a) multimodal microstructure and (b) LPSO phase present in the studied alloys after hot compression up to a strain of 10% at a strain rate of 0.001 s^{-1} (Note: A - as-extruded ZM31+6Y alloy at RT, B - ZM31+6Y alloy deformed at 200°C, C - ZM31+6Y alloy deformed at 300°C, and D - ZM31+6Y alloy deformed at 400°C).

Also, the drop is primarily noted in the case of deformation over 300°C. From the microstructure analysis it was clear that a greater fraction of ultrafine grains and a lesser fraction of coarse grains could be achieved by increasing the deformation temperature. An increase in the volume fraction of fine grains is desirable to increase the strength of the alloy according to Hall-Petch relationship [248,249]. Moreover, the DRX grains with almost randomized crystallographic orientations could help improve the ductility in the alloy [198]. In other words, with increasing deformation temperature, the alloy kept losing its multimodal features and gaining bimodal appearances consisting mainly of fine Mg grains and LPSO phase.

6.4.5 Deformation of LPSO phase

Fig. 6.24(a) presents the SEM image of the ZM31+6Y alloy in the as-extruded condition. The changes in the microstructures of the alloy subjected up to a compressive strain amount of 50% at 300°C, 350°C and 400°C are shown in Fig. 6.24(b, c and d).

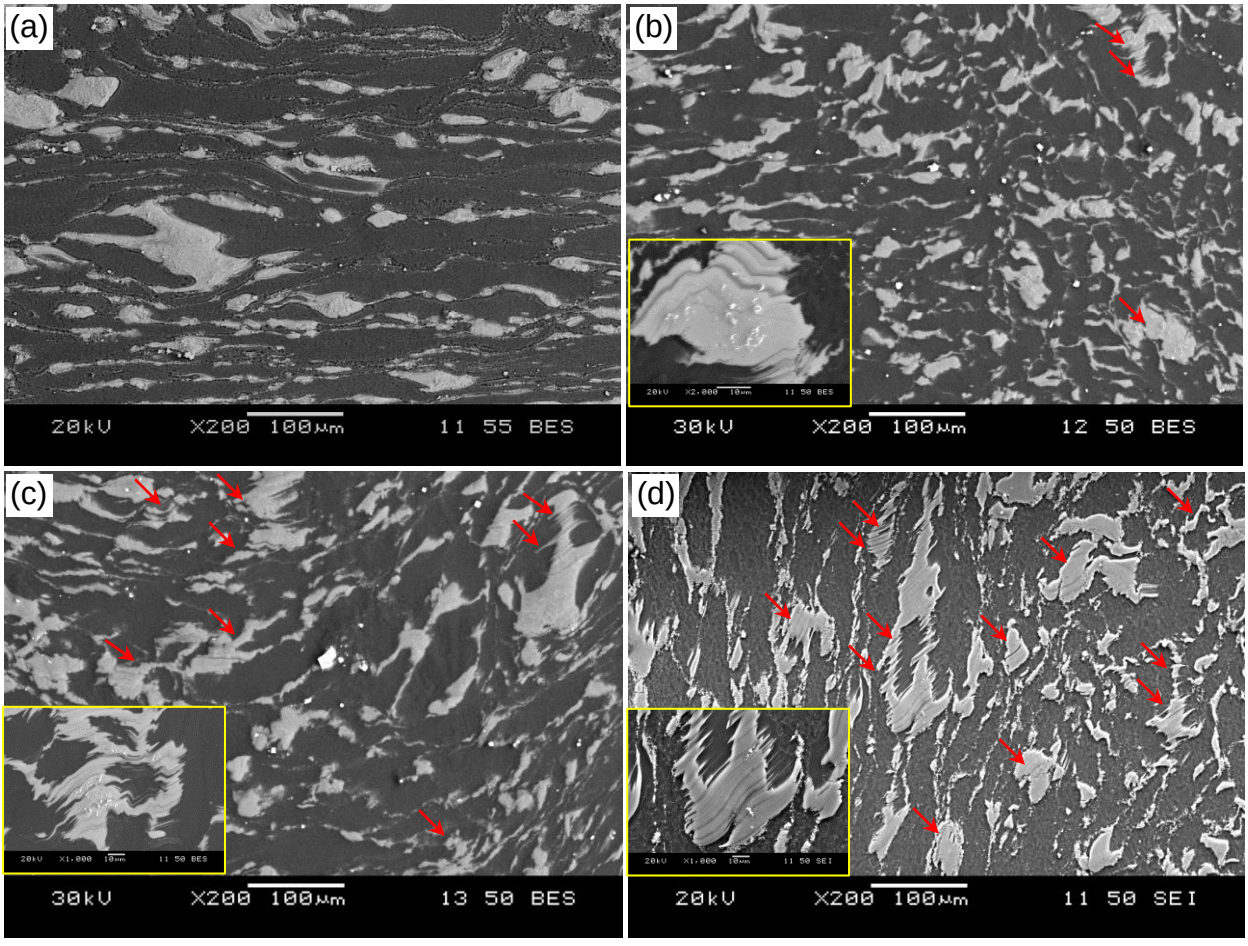

Figure 6.24: Typical optical microstructures obtained for the ZM31+6Y magnesium alloy in (a) as-extruded condition, and compressed up to a compressive amount of 50% at (a) 300°C, (b) 350°C, and (c) 400°C (Red arrows represent kink band deformation, and the higher magnification images are shown as an inset).

As seen from Fig. 6.24(a), the LPSO phase in the as-extruded ZM31+6Y alloy exhibited a typical elongated fiber shape oriented parallel to the extrusion direction, and no evidence of additional deformation within the LPSO phase was visible in this case. However, during hot compressive deformation, the LPSO phase appeared to experience a high degree of amendment. The change of orientation and distortion occurred in the LPSO phase were dependent on the localized material flow. The alignment of the LPSO phase was significantly disturbed and extensive deformation marks were noticed after compression. Consequently, the fiber-shaped LPSO phase with nearly-continuous network arrangement was transformed into a clustered and irregularly-shaped semi-continuous network arrangement, which reflected a superior deformability of the LPSO phase at elevated temperatures. In particular, no debonding or micro-cracking within the LPSO phase or at the interface in-between the LPSO phase and matrix could be observed even at higher magnifications during SEM examinations. This could be attributed to the presence of coherent interface between Mg matrix and the LPSO phase along both the basal and prismatic planes. Furthermore, the LPSO phase itself amazingly accommodated a significant amount of compressive strain (as high as 50% compressive strain in the present case, Fig. 6.24) without causing crack nucleation. This beneficial role of LPSO phase significantly contributing to the plastic deformability or ductility improvement of magnesium alloys was consistent with the observations by others [156,178,198,250].

The formation of deformation kinks in the LPSO phase (Fig. 6.24) was considered to be an underlying mechanism working behind the enhanced ductility and strength of the alloy compared with other conventional magnesium alloys. Kinking, first observed by Orawan [251], is an essential deformation mechanism to generate homogenous strain in crystal which substantially contributes to ductility. It has been reported that deformation kinks within the LPSO phase took

in the compressive strain to a certain extent when the stress was applied parallel to the basal plane [156,250]. Kinking in the phase absorbed the confined strains leading to relatively uniform plastic deformation which was important for the ductility of the alloy. Based on our SEM observations, wave-like deformation bands within the LPSO phase indicative of the kink deformation was confirmed, as shown in Fig. 6.24, with arrows designating the kinked LPSO phase in the alloy. From the SEM examinations it was apparent that multiple kink bands in the LPSO phase were associated with a higher deformation temperature: the higher the test temperature, the greater the number of kink bands in the LPSO phase. According to Shao *et al*. [156], the kinking of the LPSO phase was closely related to the generation and synchronized slip of dislocation pairs of opposite sign on the basal planes during compression. Since slip is the predominant deformation mechanism at higher temperatures, increasing the deformation temperature will boost the slip activity, facilitating the synchronized slip of dislocations. As a result, increasing the deformation temperature is likely to make the LPSO phase more susceptible to deformation kinking. To better understand the phenomena of kink band formation, a schematic illustration is presented in Fig. 6.25. Upon compressive deformation at an elevated temperature, LPSO phase would undergo progressive rotation and shape reformation. The flood of dislocations having opposite signs moves along the basal plane of the LPSO phase and introduces deformation kink. The mechanism is well documented and explained in the literature by other researchers based on HR-TEM observations [133,156,250,252].

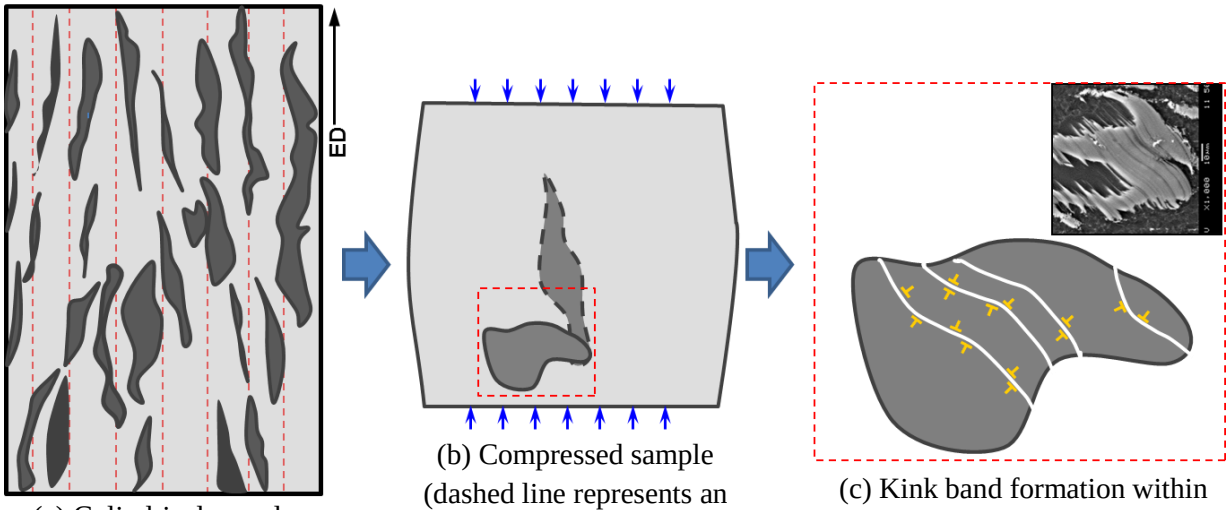

(a) Cylindrical sample (microstructure drawn inside at a larger magnification)

(b) Compressed sample (dashed line represents an initial LPSO phase before compression)

(c) Kink band formation within a LPSO phase

Figure 6.25: Schematic illustration showing the formation of deformation kinks by the motion of dislocation pairs having opposite signs.

It is well known that there is an active competition between work hardening due to twinning and work softening due to DRX in magnesium grains during deformation at elevated temperatures. In the present study, alloy ZM31+6Y demonstrated hardening behavior due to the refinement of the LPSO phase by kinking, as well as work hardening in the magnesium matrix and softening behavior due to DRX. In contrast to other magnesium alloys, hardening due to twinning would be limited since twinning was largely absent in this alloy. Based on the above experimental results and discussion, it could be stated that the present ZM31+6Y alloy is a potential candidate for elevated temperature applications which would not experience disastrous failure for the following reasons: (i) the refinement of LPSO phase due to kinking, and (ii) reduced nucleation sites for micro-cracks due to coherent interface between magnesium matrix and LPSO phase.

6.5 Summary

In this Chapter, the hot deformation behavior of as-extruded alloys ZM31, ZM31+0.3Y, ZM31+3.2Y and ZM31+6Y was studied via uniaxial compression testing in the temperature and strain ranges of 300-400°C and 0.001-1.0 s^{-1}, respectively. A constitutive model based on hyperbolic-sine equation was used to describe the dependence of flow stress on the strain, strain rate, and deformation temperature. The flow stress was observed to decrease with increasing deformation temperature and decreasing strain rate. The apparent activation energy of plastic deformation of as-extruded alloys ZM31, ZM31+0.3Y, ZM31+3.2Y and ZM31+6Y were derived to be 164, 172, 241 and 275.9 kJ/mol, respectively. The processing maps at different strain level were generated to determine the region of hot workability of alloys ZM31+3.2Y and ZM31+6Y. The processing map of as-extruded ZM31+3.2 alloy revealed a maximum efficiency of power dissipation of 42.5% and the optimum processing parameters were identified to be 340-500°C and 0.001-0.03 s^{-1}. A characteristic DRX texture component was observed to develop between the [0001] and [$11\bar{2}0$] poles at higher deformation temperatures. It is believed that at lower temperatures the CDRX occurred, whereas the DDRX was active during deformation at elevated temperatures. The processing map of as-extruded ZM31+6Y alloy showed a maximum efficiency of power dissipation of 48% and the optimum processing parameters of 350-450°C and 0.001-0.03 s^{-1}. During compression at elevated temperatures the LPSO phase exhibited a high degree of deformability, thus accommodating a large compressive strain without cracking suggesting superior formality of the phase at elevated temperatures.

CHAPTER 7

7. STRENGTHENING CONTRIBUTIONS

7.1 Introduction

Although experimental research work in Chapter 4 revealed that the addition of Y improves the strength of Mg-Zn-Mn-Y system alloys, precise determination of the underlying strengthening mechanisms has not been accomplished yet. Therefore, it is necessary to develop a theoretical understanding of how the various potential strengthening mechanisms collectively determine the strength of these alloys. Accordingly, the goal of the present study is to formulate a quantitative insight into strengthening mechanisms by providing a direct comparison among three Y containing alloys with dissimilar Mg-Zn-Y phases.

7.2 Microstructural Characterization

Figs. 4.2(b)-(d) show the SEM micrograph of studied alloys ZM31+0.3Y, ZM31+3.2Y and ZM31+6Y. The images reveal that there are second phases in all of the alloys, and the amount of these second phases increased with increasing amount of yttrium. However, the morphology and size of the particles appeared to be different in these alloys. The dominant second phases identified using SEM/EDX along with chemical formulas (calculated and as reported in the literature) are

listed in Table 7.1. The metallographic analysis reveals that alloy ZM31+0.3Y possesses I-phase particles with an average volume fraction of 0.5%. Regularly shaped I-phase particles are frequently observed with an average diameter of 0.5 μm. Similar analysis of alloy ZM31+3.2Y demonstrates spherical W-phase particles located along ED with an average grain diameter of 1.2 μm. The volume fraction for W-phase particles is measured as 11%. In contrast to the other two alloys, alloy ZM31+6Y exhibits a relatively large volume fraction (24.8%) of plate-like LPSO precipitates. The length of plate-like LPSO precipitates are ranged from 5 ~ 65 μm along the extrusion direction. The average length and width of the LPSO precipitates are measured as 25 and 5 μm respectively. Averaging the mean length and mean width of the precipitate yields an estimate for the mean precipitate diameter of 15 μm. It should be pointed out that the mean diameter are estimated by averaging the diameter of all particles regardless of their morphology. The values are estimated from 10 measurements on several high resolution SEM images and are found to be consistent with reported literature.

Table 7.1: Main ternary phase in the as-extruded Mg-Zn-Y samples containing different amounts of Y, identified by EDS.

Alloys	Points	Calculated phases	Suggested phases based on literature
ZM31+0.3Y	A	$Mg_{2.8}YZn_6$	I-phase
ZM31+3.2Y	B	$Mg_{2.88}Zn_{2.95}Y_2$	W-phase
ZM31+6Y	C	$Mg_{12}YZn$	LPSO phase

Note: I-phase is Mg_3YZn_6, W-phase is $Mg_3Y_2Zn_3$, and LPSO phase is $Mg_{12}YZn$.

7.3 X-ray Diffraction Studies

To incorporate the descriptive information concerning the second phase particle into the strengthening mechanism estimates it is essential to know the co-efficient of thermal expansion (CTE) of each phase. The linear CTE of W and LPSO phases are estimated considering the evolution of their lattice parameters with temperature from diffraction patterns. Fig. 7.1(a) shows the X-ray measurements of alloys ZM31+3.2Y and ZM31+6Y at room temperature revealing W and LPSO phase, respectively. Two unique peaks corresponding to W and LPSO phase, are directly recognized in the X-ray pattern (Fig. 7.1(b)). Due to high fraction of the phases, overlapping of diffraction peaks with peaks from the base magnesium matrix did not complicate the identification. As shown in Fig. 7.2, a shift in diffraction peak positions to lower 2θ values are observed with increasing testing temperature and is related to alloy thermal expansion. For W-phase, the evolution of lattice spacing '*d*' with temperature has been calculated using Bragg's law of diffraction from RT to 580°C as shown in Fig. 7.3(a)). Likewise, the evolution of lattice spacing '*d*' with temperature has been calculated using Bragg's law of diffraction from RT to 550°C for LPSO phase (Fig. 7.3(b)). Therefore, the linear CTE for lattice parameter, $\alpha_{lattice}$, can be calculated from Eq. 7.1 [253,254]:

$$\alpha_{lattice} = \frac{1}{d_0}\left(\frac{\Delta d}{\Delta T}\right), \tag{7.1}$$

where d_0 is the lattice spacing at room temperature. Fig. 7.4 shows the thermal elastic expansion $\frac{\Delta d}{d_0}$, as a function of temperature increment. The slope of the curve gives directly the linear CTE for each phase. CTE values of 1.376×10^{-5} and 2.351×10^{-5} K^{-1} are calculated for W and LPSO phase respectively. The CTE value of LPSO phase is in close agreement with the value reported

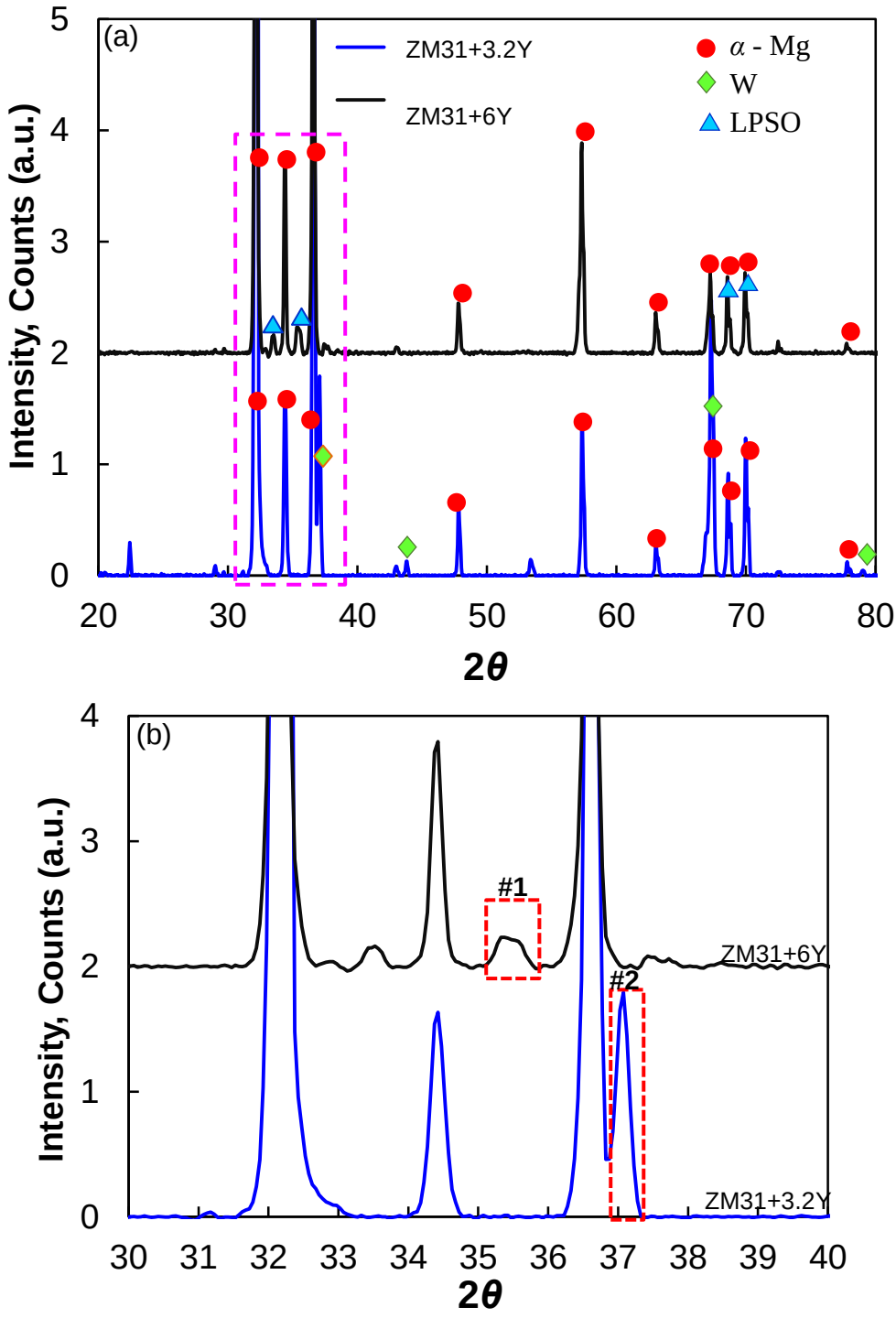

Figure 7.1: (a) XRD patterns showing the major phases present in the as-extruded alloys ZM31+3.2Y and ZM31+6Y. (b) The patterns obtained at diffraction angles in the range of 30-40º.

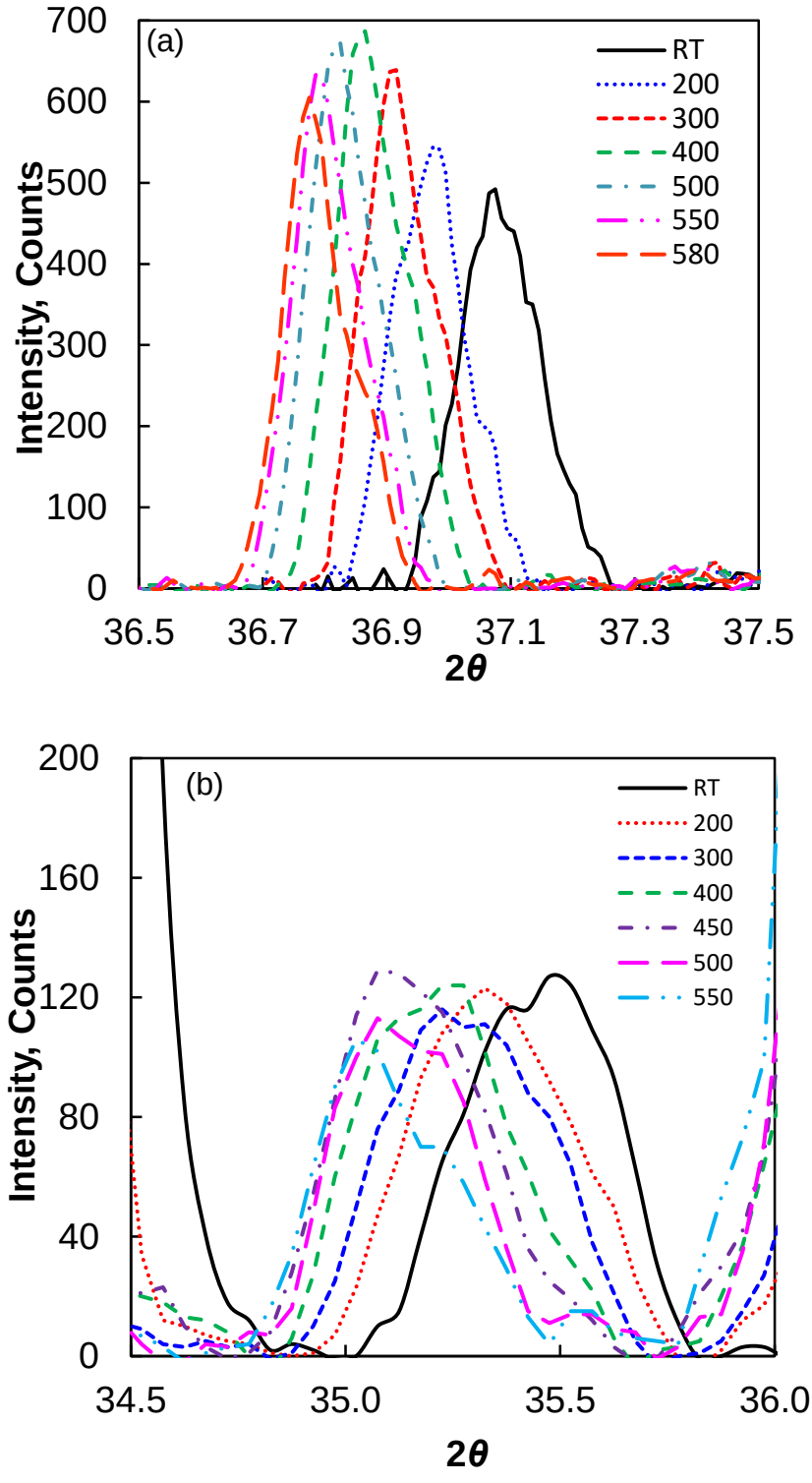

Figure 7.2: The diffraction patterns of selected peaks at different temperatures obtained during heating cycle from alloys (a) ZM31+3.2Y (#1 as marked in Figure 7.1(b)), and (b) ZM31+6Y (#2 as marked in Figure 7.1(b)).

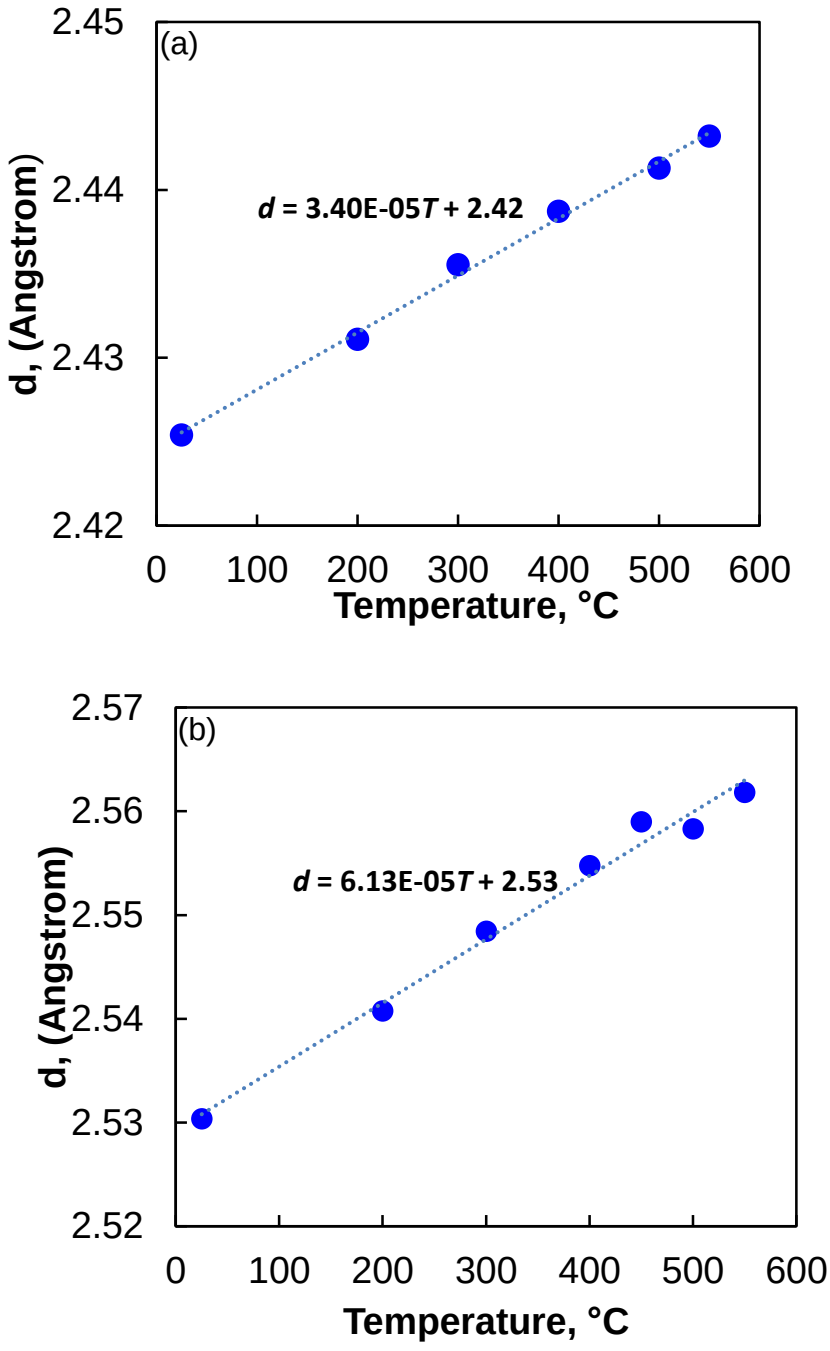

Figure 7.3: (a) Evolution of lattice spacing as a function of temperature for (a) W phase and (b) LPSO phase.

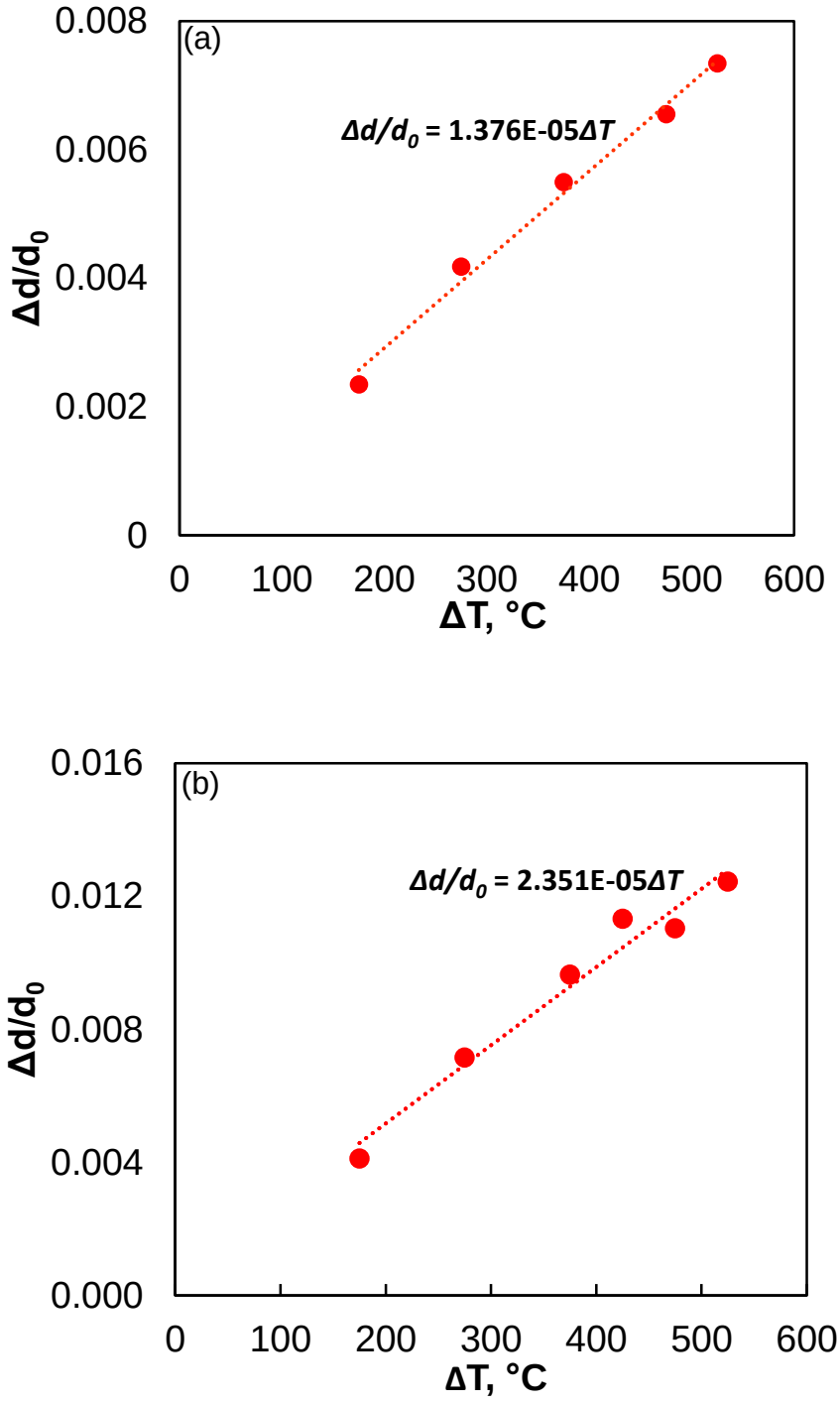

Figure 7.4: Changes of lattice distance of (a) W phase, and (b) LPSO phase with increasing temperature.

by *Garces et al.* which was measured using dilatometry and synchrotron radiation diffraction [253]. The CTE value of W phase could not be matched as no data is available in the literature. It is of important to note that, the authors were unable to determine the CTE of I phase experimentally since no unique peak associated with I-phase could be detected in the XRD pattern.

7.4 Mechanical Testing

The measured compressive true stress-strain curves of the as-extruded alloys ZM31+0.3Y, ZM31+3.2Y and ZM31+6Y were shown in Fig. 4.4(b). For comparison, the stress-strain curve corresponding to base ZM31 alloy is also included. Since the present study deals with contributions of various strengthening mechanisms towards the YS of the materials, no reference to UCS and fracture elongation has been made. The as-extruded ZM31, ZM31+0.3Y, ZM31+3.2Y and ZM31+6Y alloys have a yield strength of 150, 192, 191 and 265 MPa in compression, respectively.

7.5 Strengthening Mechanisms

Mg-Zn-Y series alloys are particularly recognized for their excellent mechanical properties [8,40,41,255]. The addition of Y to the Mg-Zn alloy leads to the formation of unique ternary phases which are assumed to play a key role in strengthening the alloys. To provide an insight into the underlying strengthening mechanisms and the measured difference in the yield strength among these materials it is important to establish the operative deformation mechanisms. Considering all the microstructural features and parameters obtained by OM, SEM and XRD the following strengthening mechanisms are presumed to be active in the Mg-Zn-Mn-Y alloys: grain

refinement strengthening, dislocation strengthening, CTE strengthening, load bearing strengthening and particle strengthening. For ZM31+0.3Y, ZM31+3.2Y and ZM31+6Y alloys having I, W and LPSO individually, the respective quantitative contributions of the different strengthening mechanisms are calculated, total strengths are estimated and compared.

7.5.1 Grain refinement strengthening

Grain boundaries act as barriers towards dislocation movement and dislocation propagation to adjacent grains, thereby strengthening the materials [256,257]. The grain boundary strengthening mechanism is traditionally described by the empirical Hall-Petch relation [248,249,258]:

$$\sigma_y = \sigma_0 + \frac{k_y}{\sqrt{D}}, \tag{7.2}$$

where D is the average grain size, σ_0 is the friction stress and k_y is the Hall-Petch slope. In cases where the addition of an alloy reduces the size of the grains compared to the base alloy processed under the same conditions, an improvement to yield strength due to grain refinement, $\Delta\sigma_{GR}$ can be estimated from [259]:

$$\Delta\sigma_{GR} = k_y\left(\frac{1}{\sqrt{D}} - \frac{1}{\sqrt{D_0}}\right), \tag{7.3}$$

where D and D_0 are average grain diameters of alloyed alloy and base alloy respectively. Several publications including our earlier research work mentioned about one of the most significant influence of Y addition, which is grain refinement indicating that the addition of Y (upto 3.2%) can effectively refine grain size but the refinement efficiency breaks down with further addition of Y from 3.2% to 6% [40,114,260]. In the present analysis, Hall-Petch coefficient k_y = 0.08

MPa√m was used based on ref [259]. Assuming the values of σ_0 are the same for all the alloys the strength enhancement from grain-boundary strengthening is assessed using Eq. 7.3. Therefore, the increase in yield strength due to grain-boundary strengthening is calculated to be 19.5, 24.9 and 16.3 MPa for samples ZM31+0.3Y, ZM31+3.2Y and ZM31+6Y, respectively.

7.5.2 CTE strengthening

During post-processing cooling, residual plastic strain develops due to the difference in the co-efficient of thermal expansion (CTE) between the reinforcement phase and the matrix which will consequently produce dislocations around the particles to accommodate the CTE difference. The CTE mismatch strengthening can be estimated by the following expression [261,262]:

$$\Delta\sigma_{CTE} = kG_m b\sqrt{\rho_{CTE}}\,, \tag{7.4}$$

$$\rho_{CTE} = \frac{12\Delta\alpha\Delta T V_p}{bd_p\left(1-V_p\right)}, \tag{7.4a}$$

where ρ_{CTE} is the density of dislocations generated from the CTE mismatch, G_m is the shear modulus of the matrix, b is the Burgers vector of the matrix, k is a constant, approximately equal to 1.25 [262], d_p is the particle size, V_p is the volume fraction of the particles, $\Delta\alpha$ is the CTE difference between the matrix and the reinforcement phase particles, ΔT is the difference between the processing and test temperatures. The Burgers vector and the shear modulus are taken as b = 0.32 nm and G_m = 16.6 GPa [263], respectively. The average thermal expansion coefficients of pure magnesium is 28.4 $\times 10^{-6}$ K^{-1} [262]. A linear CTE value of 8.5×10^{-5} K^{-1} is approximated for the quasicrystalline I phase in the present study based on literature survey [254]. The experimentally measured linear CTE of both I and W phase are lower than that of magnesium and,

therefore, thermal mismatch stresses will develop at the phase-Mg matrix interface during thermal transients. On the other hand, only small thermal mismatch stresses due to differences in CTE will be generated at the Mg/LPSO interface [253]. This evidence together with the perfect epitaxy between the magnesium and LPSO phase describe the coherent interface observed during deformation of extruded Mg-Zn-Y alloys compared to other magnesium alloys [156,264]. Taking $T_{extrusion}$ = 380°C and $T_{tes\ t}$= 25°C, the increase in yield strength due to CTE strengthening is computed as 34.3, 29.7 and 7.8 MPa for samples ZM31+0.3Y, ZM31+3.2Y and ZM31+6Y, respectively.

7.5.3 Dislocation strengthening

The dislocation strengthening describes the generation of dislocations when an alloy is subjected to a compressive loading processing such as hot extrusion [259]. In order to accommodate the moduli differentials between the matrix and particles, dislocations are formed during plastic deformation [259]. As, dislocations interact with themselves and impede their own motion, increasing the dislocation density in a metal increases the yield strength of the material [256]. The strength improvement by modulus mismatch is approximated by [259,265,266]:

$$\Delta\sigma_D = \sqrt{3}\beta G_m b\sqrt{\rho_{Modulus}}\,, \tag{7.5}$$

$$\rho_{Modulus} = \frac{6V_p\varepsilon}{bd_p}, \tag{7.5a}$$

Where β is the material specific coefficient, equal to 0.33 [263], $\rho_{Modulus}$ is the dislocation density generated by the modulus mismatch and ε is the microstrain. A bulk strain value of 0.001 is used

[259]. Dislocation strengthening contributed an increase of 4.2, 3.9 and 1.7 MPa for alloys ZM31+0.3Y, ZM31+3.2Y and ZM31+6Y, respectively.

7.5.4 Load bearing strengthening

The load-bearing strengthening mechanism explains the direct strengthening contribution from the presence of reinforcement phases. According to the shear-lag theory, the load transfer occurs at the particle/matrix interface by shear stresses and can be expressed as [267,268],

$$\sigma_{Load} = \sigma_m \left[\frac{V_p (s+2)}{2} + V_m \right], \tag{7.6}$$

where V_p and V_m are volume fraction of particles and matrix, respectively and s is the aspect ratio. For equiaxed particles such as I and W phase $s \approx 1$, for plate-like LPSO precipitate $s \approx 5$, and considering $V_p + V_m = 1$, the strength increment caused by the load bearing mechanism is expressed as:

$$\Delta\sigma_{Load} = \frac{1}{2} V_p \sigma_m \text{ ; (I and W phase)} \tag{7.6a}$$

$$\Delta\sigma_{Load} = 2.5 V_p \sigma_m \text{; (LPSO phase)} \tag{7.6b}$$

The yield strength improvement owing to load bearing strengthening is configured as 0.4, 8 and 91 MPa for samples ZM31+0.3Y, ZM31+3.2Y and ZM31+6Y, respectively.

7.5.5 Particle strengthening

The interaction between particles and dislocations occur either by (i) shearing of the particles or (ii) dislocation looping around the non-penetrable particles. If particles get sheared by dislocations

the contribution to strengthening come from either one or a combination of the following mechanisms [256,257,269–271]: (a) coherency strengthening, (b) modulus strengthening and (c) order strengthening. The dislocation looping phenomenon is described by the Orowan model and is commonly known as Orowan strengthening.

(i) Dislocation looping around particles

The Orowan strengthening describes the increase in strength caused by the resistance of closely spaced hard particles to the passing of dislocations [261,262,272]. The dislocation movement bypass particles by bowing, leaving behind dislocation loops around the vicinity of the particles. The strength improvement related to Orowan strengthening is given as follows [261,262]:

$$\Delta\sigma_{Orowan} = \frac{0.13 G_m b}{\lambda} \ln \frac{d_p}{2b}, \tag{7.7}$$

where λ *i*s the interparticle spacing, expressed as,

$$\lambda \approx d_p \left[\left(\frac{1}{2V_p} \right)^{\frac{1}{3}} - 1 \right]. \tag{7.7a}$$

The Orowan bypass mechanism is the operative strengthening mechanisms which leads to strength increments of 16.5, 6.6, 1.7 MPa for samples ZM31+0.3Y, ZM31+3.2Y and ZM31+6Y respectively. It should be noted that, a volume fraction of 24.3% has been used to calculate $\Delta\sigma_{Orowan}$ for the LPSO phase, as precipitate shearing mechanism is predicted to be functioning at few places within the phase as confirmed by TEM observation by other researchers [156,164].

(ii) Shearing of particles

For the shearing mechanism, the increase in yield strength from the contributions of order strengthening, coherency strengthening and modulus strengthening are expressed as [256,257,269–271]:

$$\Delta\sigma_{Order} = 0.81M\,\frac{\gamma_{apb}}{2b}\left(\frac{3\pi f}{8}\right)^{\frac{1}{2}}, \tag{7.8}$$

$$\Delta\sigma_{Coherency} = M\alpha_{\varepsilon}\left(G\varepsilon_c\right)^{\frac{3}{2}}\left(\frac{rf}{0.5Gb}\right)^{\frac{1}{2}}, \tag{7.9}$$

$$\Delta\sigma_{\text{Modulus}} = 0.0055M\left(\Delta G\right)^{\frac{3}{2}}\left(\frac{2f}{G}\right)^{\frac{1}{2}}\left(\frac{r}{b}\right)^{\frac{3m}{2}-1}, \tag{7.10}$$

where M = 6.5 is the mean matrix orientation factor for magnesium [263], f is the volume fraction of the thin Mg nano-slice within LPSO phase where shearing takes place, γ_{apb} =0.09 J/m^2 is an average value of antiphase boundary energy for LPSO phase [273], ε_c is the constrained lattice parameter mismatch and ΔG is the shear modulus mismatch between the matrix and LPSO phase. In order to fully comprehend the strengthening mechanism due to shearing of LPSO precipitate it is necessary to explain its unique crystal structure in relation to the deformation mechanism kinking. LPSO phase in Mg-Zn-Y ternary systems is reported to consist of structural blocks with close-packed atomic planes, along with thin Mg nano-slices embedded or sandwiched in between the LPSO blocks [141,156,274]. The softer Mg-nano slice could be sheared along the kinking direction via slip of dislocations [156]. The kinking of the LPSO phase is closely related to the abundant generation of dislocation pairs of opposite signs during compression [16,164]. Synchronized slip of dislocation pairs in the LPSO phase outcomes in kinking [16,164] or

shearing. It has been informed that kinking of the LPSO structure contributes significantly to the strengthening of the alloy [156,164,275]. The volume fraction of Mg-nano slices within the LPSO block is approximated as $f = 0.5\%$ from microstructure examination. The calculation for coherency and modulus strengthening are redundant since shear modulus mismatch (ΔG) and constrained lattice parameter misfit (ε_c) will be zero leading to no contribution in strengthening. Therefore the strengthening contribution due to shearing of LPSO phase or order strengthening is calculated as 56.8 MPa. It should be noted that no strengthening improvement results from the shearing of I and W phase particles as shearing does not take place within these particles.

7.6 Strength Prediction and Comparisons with Corresponding Experimental Values

7.6.1 Linear summation

Linear summation method simply sums up the contribution of individual strengthening mechanisms assuming that different mechanisms do not influence each other and therefore independently pays to the yield strength of the material [259,276]. This method is not commonly used as it often predicts yield strength much higher than the experimental measurement [277].

$$\Delta\sigma_y = \Delta\sigma_{GR} + \Delta\sigma_{CTE} + \Delta\sigma_D + \Delta\sigma_{Load} + \Delta\sigma_{Orowan} + \Delta\sigma_{Order}\,. \tag{7.11}$$

7.6.2 Quadrature summation

Clyne and Withers [278] proposed quadratic summation method where the individual strengthening mechanisms interact with each other and the summation of the squares of individual strengthening contribution is proportional to the square of the total yield strength improvement.

$$\Delta\sigma_y = \sqrt{\left(\Delta\sigma_{GR}\right)^2 + \left(\Delta\sigma_{CTE}\right)^2 + \left(\Delta\sigma_D\right)^2 + \left(\Delta\sigma_{Load}\right)^2 + \left(\Delta\sigma_{Orowan}\right)^2 + \left(\Delta\sigma_{Order}\right)^2}\,. \quad (7.12)$$

Quite a few researchers calculated the yield strength using this method which shows better agreement between prediction and experimental observation than other methods [266,277–279].

7.6.3 Compounding summation

Compounding method, originated by Ramakrishnan [280], later adapted and modified by Zhang and Chen [261,262], have been demonstrated to predict yield strength very close to the experimental values. This method assumes that strengthening mechanisms influence each other and are continually counted as multiplication factors as follows [259]:

$$\Delta\sigma_y = \sigma_{ym}\left(\Delta\sigma_f - 1\right), \quad (7.13)$$

where

$$\Delta\sigma_f = \left(1+\frac{\Delta\sigma_{GR}}{\sigma_{ym}}\right)\left(1+\frac{\Delta\sigma_{CTE}}{\sigma_{ym}}\right)\left(1+\frac{\Delta\sigma_d}{\sigma_{ym}}\right)\left(1+\frac{\Delta\sigma_{Load}}{\sigma_{ym}}\right)\left(1+\frac{\Delta\sigma_{Orowan}}{\sigma_{ym}}\right)\left(1+\frac{\Delta\sigma_{Order}}{\sigma_{ym}}\right). \quad (13a)$$

This approach diverges from the other two approaches in a way that the strengthening contributions are not added, rather multiplied with the original base material yield strength.

7.6.4 Yield strength prediction

The overall yield strength of the reinforced alloys can be estimated by the following equation,

$$\sigma_y = \sigma_{ym} + \Delta\sigma_y, \tag{7.14}$$

where σ_y is the yield strength of the alloys (ZM31+0.3Y, ZM31+3.2Y, ZM31+6Y) reinforced with I, W and LPSO phases, $\Delta\sigma_y$ is the yield strength improvement due to Y addition calculated using Equation (7.11-7.13) and σ_{ym} is the yield strength of the base alloy (ZM31) without reinforcement phases. The yield strength of the three materials are predicted using Equation 7.14 and compared with experimental values as presented in Fig. 7.5. Also, the three summation approaches are experimented to determine which model best represents the reality. It is evident from Fig. 7.5 that in the present scenario, quadrature summation model best describes the experimental yield strength of the materials.

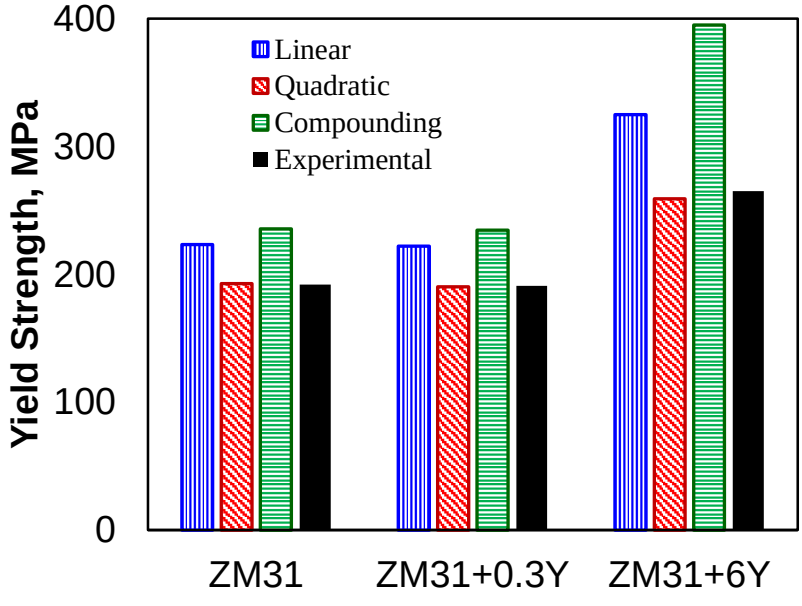

Figure 7.5: Comparative bar graph of estimated overall yield strength using different summation methods and experimental measurement.

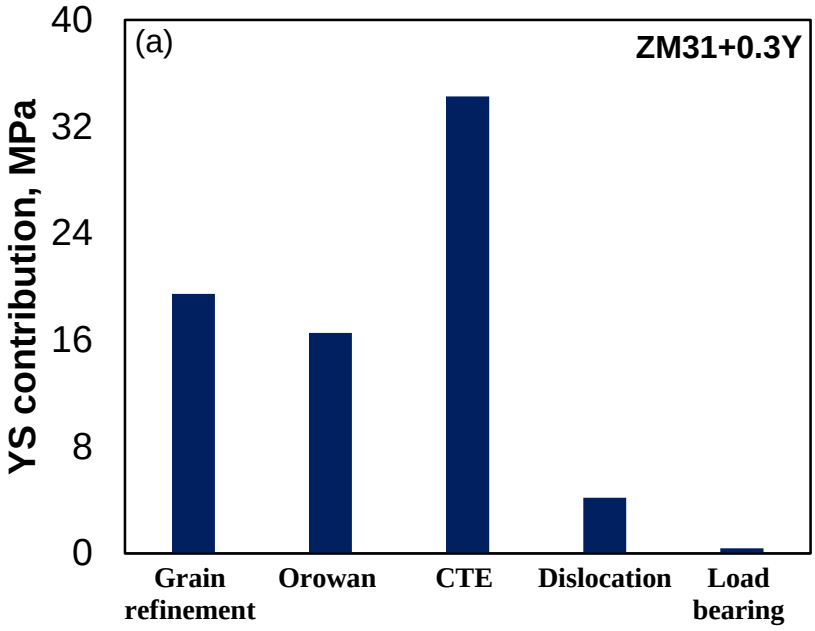
(a)
ZM31+0.3Y
YS contribution, MPa
40
32
24
16
8
0
Grain refinement
Orowan
CTE
Dislocation
Load bearing

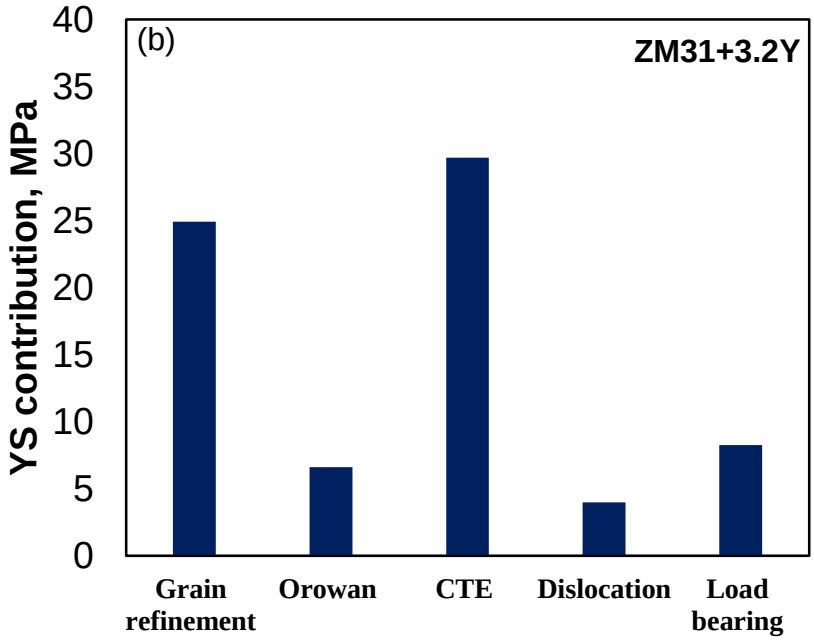
(b)
ZM31+3.2Y
YS contribution, MPa
40
35
30
25
20
15
10
5
0
Grain refinement
Orowan
CTE
Dislocation
Load bearing

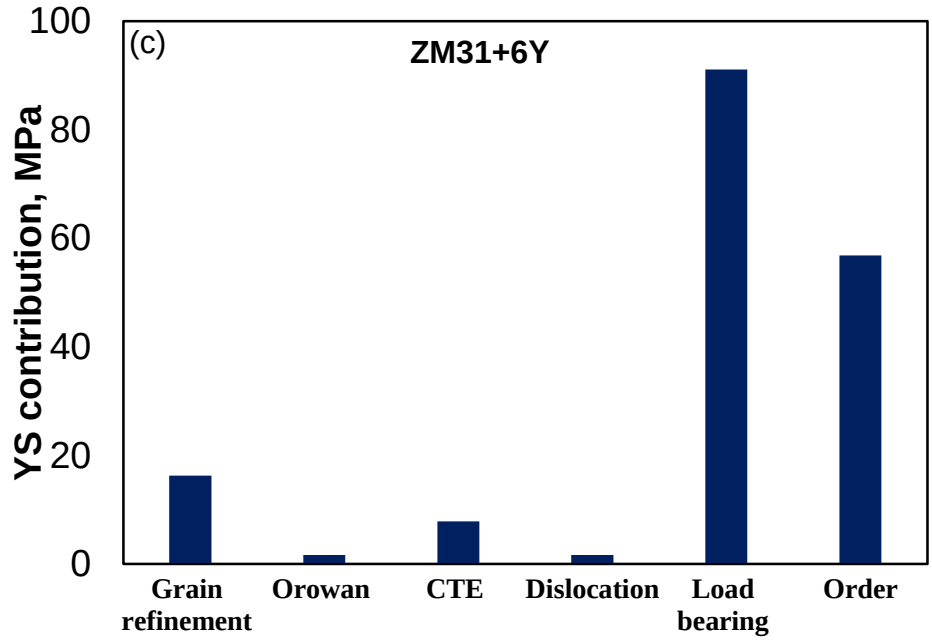

Figure 7.6: Contribution from different strengthening mechanisms to yield strength improvement in as-extruded alloys (a) ZM31, (b) ZM31+0.3Y, and (c) ZM31+6Y.

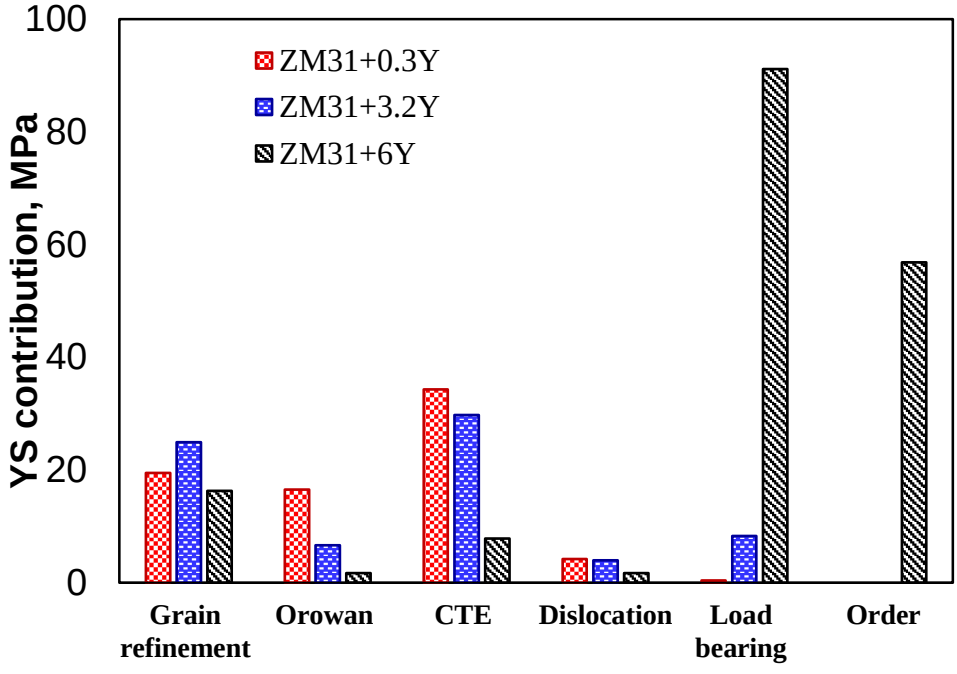

Figure 7.7: Comparative bar graph of predicted yield strength improvement from various strengthening mechanisms due to Y addition.

7.7 Contribution of Different Strengthening Mechanisms

Fig. 7.6(a-c) shows the bar chart that quantify the predicted individual strengthening contribution from grain refinement, CTE mismatch, dislocation density, Orowan bypass, load bearing and shearing of particles towards the overall yield strength enhancement in alloys ZM31+0.3Y, ZM31+3.2Y and ZM31+6Y respectively. As seen from Fig. 7.6(a), for alloy ZM31+0.3Y the potential strength improvement is caused mainly due to grain refinement, Orowan looping and particularly CTE mismatch mechanisms with a very slight contribution from load bearing and dislocation. Fig. 7.6(b) shows that the grain refinement strengthening and CTE mismatch strengthening are both predicted to be large in magnitude while the effects of other mechanisms are relatively minor in ZM31+3.2Y alloy. However, for alloy ZM31+6Y, load bearing strengthening and order strengthening are the leading strengthening mechanisms followed by grain refinement strengthening as depicted in Fig. 7.6(c). In summary, it can be comprehended that grain refinement is an effectively operating strengthening mechanism in the three studied alloys and much of the yield strength improvement can be attributed to the reduced grain size of the materials.

7.8 Relative Strengthening Contribution from Different Phases

Fig. 7.7 shows a comparison chart among the three alloys with individual strengthening contributions from different mechanisms. A comparative study reveals that contribution from I-phase by Orowan strengthening mechanism is the maximum, followed by W and LPSO phase. Since strengthening caused by dislocation bypass largely depends on particle size and becomes stronger with decreasing particle size [261,262], large LPSO precipitate results in very little

Orowan strengthening. A similar trend is anticipated for CTE strengthening since high thermal mismatch stresses is likely to develop around I phase particles due to much smaller CTE value compared to Mg matrix whereas small thermal mismatch stresses is expected to generate around LPSO phase due to compatible CTE value of the LPSO phase and the Mg matrix [253]. Load bearing strengthening makes somewhat minor contribution due to minute size and low volume fraction of I and W phase particles. On the other hand, LPSO phase plays a more significant role in load bearing as compared to other two phases. Strong plate like LPSO phase carries most of the load applied to the material via fiber strengthening mechanisms similar to composite materials thus enabling the material to withstand higher stresses. Since shearing and Orowan bypass occurs, in parallel within the LPSO phase, strengthening is also dictated by particle shearing mechanism such as order strengthening. Combined, these results suggests that LPSO reinforced alloys exhibit significantly higher yield strength compared to those of I and W phases due to strengthening mechanisms such as load bearing and order strengthening.

7.9 Summary

In this Chapter, the yield strength improvement in Mg-Zn-Y alloys due to Y addition are quantitatively predicted. The underlying strengthening mechanisms are identified and individual contribution from each mechanism are estimated and compared. In summary, grain refinement strengthening is present in all the materials irrespective of the second phase particles. Orowan dislocation bypassing and CTE strengthening are the dominant strengthening mechanisms in the ZM31+0.3Y and ZM31+3.2Y alloys possessing I and W phase respectively. Load bearing and order strengthening due to particle shearing are dominant and makes a significant contribution in the superior yield strength of the LPSO-reinforced ZM31+6Y alloy.

CHAPTER 8

8. CONCLUSIONS AND FUTURE WORK

8.1 Conclusions

Based on the studies of the mechanical behavior and the associated plastic deformation mechanisms under uniaxial compressive loading of as-extruded Mg-Zn-Mn-Y alloys containing varying Y contents, the following conclusions can be drawn:

(1) The addition of Y significantly influenced the as-extruded microstructure in terms of grain morphology and second phase particles. The extruded base ZM31 alloy contained MgZn and Mg_7Zn_3 phases. When a Y content of 0.3% was added, the alloy showed a bimodal grain microstructure consisting of fine DRXed and elongated Un-DRXed grains and I-phase. When the Y content increased to 3.2%, the volume fraction of uniform DRXed grains increased, containing both I-phase and W-phase. With a further increase in Y content to 6%, multimodal microstructure was observed consisting of coarse grains, fine DRXed grains, LPSO X-phase ($Mg_{12}YZn$) and $Mg_{24}Y_5$ particles.

(2) The presence of quasicrystalline I-phase in alloy ZM31+0.3Y increased CYS, hardness, and Stage B strain hardening rate due to its resistance to the motion of dislocations and twinning.

Alloy ZM31+3.2Y exhibited lower hardness and Stage B hardening rate due to the co-existence of I- and W-phases. Both alloys ZM31+0.3Y and ZM31+3.2Y displayed a yield-point-like phenomenon (stress-strain plateau) and initial negative strain hardening rate. An addition of Y content up to 6% resulted in a superior CYS, high hardness, and the disappearance of Stage B hardening, suggesting a change of the major deformation mode from twinning to slip as a result of the presence of LPSO X-phases.

(3) At RT while alloys ZM31+0.3Y and ZM31+3.2Y exhibited a skewed true stress-true stain curve with a three-stage strain hardening characteristic, being typical of most common extruded Mg alloys due to the occurrence of $\{10\bar{1}2\}$ extension twinning, the true stress-true stain curve of alloy ZM31+6Y became fairly normal due to the activation of dislocation slip during compression. With increasing temperature, the extent of skewness on the true stress-true stain curves decreased, and it basically disappeared at 300°C. While both CYS and UCS of all alloys decreased as the temperature increased, the high-temperature strength increased with increasing Y content. Also, the retention ability of the high-temperature strength was much higher with a higher amount of Y content, as revealed by a much slower decrease of the strength with increasing temperature.

(4) Both EBSD and XRD revealed a typical basal texture present in the extruded ZM31 Mg alloy containing different amounts of Y, where (0001) planes and mainly $<01\bar{1}0>$ directions of most grains were oriented parallel to the ED. With increasing Y content the basal texture was weakened with a decreased intensity, and grain orientations became more randomized with a wider orientation spread.

(5) Increasing Y content reduced the extent of extension twinning as a deformation mode and enhanced the slip deformation. With increasing Y content the fraction of static recrystallization decreased due to the role of Y present in the substitutional solid solution and in the second phase particles.

(6) The occurrence of extension twinning was reflected by the formation of $\{\bar{1}2\bar{1}0\}<0001>$ and $\{01\bar{1}0\}<0001>$ textures, indicating that the *c*-axes (or basal pole) in most grains were rotated towards the anti-compression direction. The intensity of twinned texture components decreased with increasing deformation temperature and the extent of decrease was more significant in alloy ZM31+0.3Y followed by ZM31+3.2Y and ZM31+6Y.

(7) VPSC simulation was able to predict the texture consistent with the experimental measurements. With increasing Y content the relative activity of pyramidal slip increased, while the relative activity of basal slip decreased. The relative activity of non-basal slip further increased with increasing deformation temperature. While extension twinning occurred at the onset of deformation facilitated <*c*+*a*> pyramidal slip, the relative contribution from extension twinning decreased significantly with increasing deformation temperature and deformation amount.

(8) The apparent activation energy of plastic deformation of as-extruded alloys ZM31, ZM31+0.3Y, ZM31+3.2Y and ZM31+6Y was derived to be 164, 172, 241 and 276 kJ/mol, respectively, suggesting that the activation energy increased significantly with increasing Y content.

(9) The processing map of as-extruded ZM31+6Y alloy showed a maximum efficiency of power dissipation of 48% and the optimum processing parameters of 350-450°C and 0.001-0.03s^{-1}. During compression at elevated temperatures, extensive deformation kink bands were observed which increased with increasing test temperature. The thickness of the LPSO phase decreased due to kinking. The LPSO phase exhibited a high degree of deformability, thus accommodating a large compressive strain without cracking suggesting superior formality and stability of the phase at elevated temperatures.

(10) The processing map of as-extruded ZM31+3.2 alloy revealed a maximum efficiency of power dissipation of 42.5% and the optimum processing parameters were identified to be 340-500°C and 0.001-0.03 s^{-1}. The instability region occurring at higher strain rates and lower temperatures was associated with an inadequate DRX and the formation of micro-cracks, which suggests that the hot working in this region must be avoided for the as-extruded ZM31+3.2Y alloy.

(11) The yield strength improvement in Mg-Zn-Mn-Y alloys due to Y addition are quantitatively predicted. The underlying strengthening mechanisms are identified and individual contribution from each mechanism is estimated. Grain refinement strengthening is present in all the alloys. Orowan dislocation bypassing and CTE strengthening are the dominant strengthening mechanisms in the ZM31+0.3Y and ZM31+3.2Y alloys possessing I and W phases, respectively. Load bearing and order strengthening are prevalent and significant contributors in the superior yield strength of the LPSO-reinforced ZM31+6Y alloy.

8.2 Recommendations for Future Work

The ternary Mg-Zn-Y system has been identified to be very promising as it exhibits a variety of thermally stable phases, such as I, W and LPSO. These phases differ widely in the structure which explains their fundamental variations in the plastic behavior and relationship with hexagonal Mg matrix. The present investigation was aimed at studying the beneficial impact of different amounts of Y alloying in the extruded Mg-Zn-Mn alloys by means of compression testing. While a number of results have been obtained in the present study, there still remained a lot of work that needs to be further done. The following future investigations could ensure safe and successful applications of Mg-Zn-Mn-Y alloys:

(1) The LPSO phase is found to be chimerically ordered as well as stacking ordered. So far, four types of LPSO structures including 10H, 18R, 14H and 24R have been reported for the Mg-Zn-Y alloys. A precise assignment of the stacking sequence of each structure has not yet been clarified. The 18R structure gradually transforms into 14H structure after appropriate heat treatment in a temperature range of 350-500°C. Therefore, further systematic study on the transformation mechanism, their mutual relationship and thermal stability of each structure is needed.

(2) The measurement of resistivity-temperature curve combined with differential scanning calorimetry (DSC) needs to be carried out to identify the solidification and melting temperature of I, W and LPSO phases.

(3) Cyclic deformation behavior, including high and low cycle fatigue, bi-axial or multi-axial fatigue, would be an interesting aspect to study the anisotropic behavior of Mg-Zn-Mn-Y alloys, since no such results have been reported in the literature for these alloys yet. It is also of interest to further study the fatigue crack growth behavior and the related propagation mechanisms under dynamic loading condition.

(4) The strain distribution within polycrystalline samples needs to be measured on a more localized scale (i.e., at the grain level). A detailed investigation combining both EBSD and digital image correlation (DIC) to track the local strain distribution during mechanical testing at intermediate strains would prove to be highly valuable in understanding strain hardening phenomena more precisely.

(5) Texture measurement by neutron diffraction coupled with TEM observations will be helpful to understand the relative activity of different deformation modes in varying Y containing magnesium alloys.

(6) The future work about the research of Mg-Zn-Y series alloys should also be extended in the practically applicable conditions, which includes the investigations on creep mechanisms, creep-fatigue interactions, and corrosion resistance, etc.

REFERENCES

[1] C. McGlade, P. Ekins, The geographical distribution of fossil fuels unused when limiting global warming to 2 °C, Nature. 517 (2015) 187–190.

[2] M. McNutt, Climate Change Impacts, Science. 341 (2013) 435.

[3] S.S. Myers, A. Zanobetti, I. Kloog, P. Huybers, D.B. Andrew, A. Bloom, E. Carlisle, L.H. Dietterich, G. Fitzgerald, T. Hasegawa, N.M. Holbrook, R.L. Nelson, M.J. Ottman, V Raboy, H. Sakai, K.A. Sartor, J. Schwartz, S. Seneweera, M. Tausz, Y. Usui, Increasing CO_2 threatens human nutrition, Nature 510 (2014) 139–142.

[4] M. McNutt, The beyond-two-degree inferno, Science. 349 (2015) 7.

[5] S. Chu, A. Majumdar, Opportunities and challenges for a sustainable energy future, Nature. 488 (2012) 294–303.

[6] J. Schmale, D. Shindell, E. von Schneidemesser, I. Chabay, M. Lawrence, Clean up our skies, Nature. 515 (2014) 335–337.

[7] J. Murray, D. King, Climate policy: Oil's tipping point has passed, Nature. 481 (2012) 433–435.

[8] N. Tahreen, D.F. Zhang, F.S. Pan, X.Q. Jiang, D.Y. Li, D.L. Chen, Hot deformation and processing map of an as-extruded Mg-Zn-Mn-Y alloy containing I and W phases, Materials and Design. 87 (2015) 245–255.

[9] A. Macwan, V.K. Patel, X.Q. Jiang, C. Li, S.D. Bhole, D.L. Chen, Ultrasonic spot welding of Al/Mg/Al tri-layered clad sheets, Materials & Design. 62 (2014) 344–351.

[10] W.J. Joost, Reducing vehicle weight and improving U.S. energy efficiency using integrated computational materials engineering, JOM. 64 (2012) 1032–1038.

[11] T.M. Pollock, Weight loss with magnesium alloys, Science. 328 (2010) 986–987.

[12] T.A. Schaedler, A.J. Jacobsen, W.B. Carter, Toward lighter, stiffer materials, Science. 341 (2013) 1181–1182.

[13] N. Tahreen, D.L. Chen, M. Nouri, D.Y. Li, Effects of aluminum content and strain rate on strain hardening behavior of cast magnesium alloys during compression, Materials Science and Engineering A. 594 (2014) 235–245.

[14] Z. Yang, J. Li, J. Zhang, G. Lorimer, J. Robson, Review on research and development of magnesium alloys, Acta Metallurgica Sinica (English Letters). 21 (2008) 313–328.

[15] A.I. Cooper, Cooperative carbon capture, Nature. (2015) 5–6.

[16] N. Tahreen, D.F. Zhang, F.S. Pan, X.Q. Jiang, C. Li, D.Y. Li, et al., Characterization of hot deformation behavior of an extruded Mg-Zn-Mn-Y alloy containing LPSO phase, Journal of Alloys and Compounds. 644 (2015) 814–823.

[17] J. Hirsch, T. Al-Samman, Superior light metals by texture engineering: Optimized aluminum and magnesium alloys for automotive applications, Acta Materialia. 61 (2013) 818–843.

[18] F. Mokdad, D.L. Chen, Strain-controlled low cycle fatigue properties of a rare-earth containing ZEK100 magnesium alloy, Materials & Design. 67 (2015) 436–447.

[19] N. Tahreen, D.L. Chen, M. Nouri, D.Y. Li, Effect of yttrium addition on texture development in a cast Mg-Al-Y magnesium alloy during compression, in: Magnesium Technology 2014, John Wiley & Sons, Inc., 2014: pp. 269–272.

[20] F.A. Mirza, D.L. Chen, Fatigue of rare-earth containing magnesium alloys: A review, Fatigue and Fracture of Engineering Materials and Structures. 37 (2014) 831–853.

[21] G. Garcés, M. Maeso, I. Todd, P. Pérez, P. Adeva, Deformation behaviour in rapidly solidified $Mg_{97}Y_2Zn$ (at.%) alloy, Journal of Alloys and Compounds. 432 (2007) 10–14.

[22] Y.M. Zhu, A.J. Morton, J.F. Nie, Growth and transformation mechanisms of 18R and 14H in Mg-Y-Zn alloys, Acta Materialia. 60 (2012) 6562–6572.

[23] P. Pe, Effect of the LPSO volume fraction on the microstructure and mechanical properties of Mg – Y 2 X – Zn X alloys, (2012) 1085–1093.

[24] J.Y. Lee, D.H. Kim, H.K. Lim, D.H. Kim, Effects of Zn/Y ratio on microstructure and mechanical properties of Mg-Zn-Y alloys, Materials Letters. 59 (2005) 3801–3805.

[25] J. Geng, X. Teng, G. Zhou, D. Zhao, Microstructure transformations in the heat-treated Mg-Zn-Y alloy, Journal of Alloys and Compounds. 577 (2013) 498–506.

[26] Y. Zhang, X. Zeng, L. Liu, C. Lu, H. Zhou, Q. Li, et al., Effects of yttrium on microstructure and mechanical properties of hot-extruded Mg-Zn-Y-Zr alloys, Materials Science and Engineering A. 373 (2004) 320–327.

[27] D.K. Xu, W.N. Tang, L. Liu, Y.B. Xu, E.H. Han, Effect of Y concentration on the microstructure and mechanical properties of as-cast Mg-Zn-Y-Zr alloys, Journal of Alloys and Compounds. 432 (2007) 129–134.

[28] D.K. Xu, L. Liu, Y.B. Xu, E.H. Han, The influence of element Y on the mechanical properties of the as-extruded Mg-Zn-Y-Zr alloys, Journal of Alloys and Compounds. 426 (2006) 155–161.

[29] Z.P. Luo, S.Q. Zhang, Y.L. Tang, D.S. Zhao, On the stable quasicrystals in slowly cooled Mg-Zn-Y alloys, Scripta Metallurgica et Materiala. 32 (1995) 1411–1416.

[30] Z.P. Luo, H.X. Sui, S.Q. Zhang, On the stable Mg-Zn-Y quasicrystals, Metallurgical and Materials Transactions A. 27 (1996) 1779–1784.

[31] D. Levine, P.J. Steinhardt, Quasicrystals. I. Definition and structure, Physical Review B. 34 (1986) 596–616.

[32] D.V. Louzguine-Luzgin, A. Inoue, Formation and Properties of Quasicrystals, Annual

Review of Materials Research. 38 (2008) 403–423.

[33] D. Shechtman, I. Blech, D. Gratias, J.W. Cahn, Metallic phase with long-range orientational order and no translational symmetry, Physical Review Letters. 53 (1984) 1951–1953.

[34] Z. Wang, W. Zhao, Mg-Based Quasicrystals, in: New Features on Magnesium Alloys, n.d.

[35] A. Singh, M. Watanabe, A. Kato, A.P. Tsai, Strengthening in magnesium alloys by icosahedral phase, Science and Technology of Advanced Materials. 6 (2005) 895–901.

[36] J.B. Ok, I.J. Kim, S. Yi, W.T. Kim, D.H. Kim, Solidification microstructure of as-cast Mg–Zn–Y alloys, Philosophical Magazine. 83 (2003) 2359–2369.

[37] A. Singh, M. Watanabe, A. Kato, A.P. Tsai, Microstructure and strength of quasicrystal containing extruded Mg-Zn-Y alloys for elevated temperature application, Materials Science and Engineering A. 385 (2004) 382–396.

[38] A. Singh, Y. Osawa, H. Somekawa, T. Mukai, Effect of microstructure on strength and ductility of high strength quasicrystal phase dispersed Mg-Zn-Y alloys, Materials Science and Engineering A. 611 (2014) 242–251.

[39] D.K. Xu, W.N. Tang, L. Liu, Y.B. Xu, E.H. Han, Effect of W-phase on the mechanical properties of as-cast Mg-Zn-Y-Zr alloys, Journal of Alloys and Compounds. 461 (2008) 248–252.

[40] N. Tahreen, D.F. Zhang, F.S. Pan, X.Q. Jiang, C. Li, D.Y. Li, et al., Influence of yttrium content on phase formation and strain hardening behavior of Mg-Zn-Mn magnesium alloy, Journal of Alloys and Compounds. 615 (2014) 424–432.

[41] N. Tahreen, D.F. Zhang, F.S. Pan, X.Q. Jiang, D.Y. Li, D.L. Chen, Hot Deformation and Work Hardening Behavior of an Extruded Mg–Zn–Mn–Y Alloy, Journal of Materials Science & Technology. 31 (2015) 1161–1170.

[42] Q. Wang, K. Liu, Z. Wang, S. Li, W. Du, Microstructure, texture and mechanical properties of as-extruded Mg-Zn-Er alloys containing W-phase, Journal of Alloys and Compounds. 602 (2014) 32–39.

[43] D.K. Xu, L. Liu, Y.B. Xu, E.H. Han, Effect of microstructure and texture on the mechanical properties of the as-extruded Mg-Zn-Y-Zr alloys, Materials Science and Engineering A. 443 (2007) 248–256.

[44] F. Lu, A. Ma, J. Jiang, D. Yang, Q. Zhou, Review on long-period stacking-ordered structures in Mg-Zn-RE alloys, Rare Metals. 31 (2012) 303–310.

[45] A. Inoue, Y. Kawamura, M. Matsushita, K. Hayashi, J. Koike, Novel hexagonal structure and ultrahigh strength of magnesium solid solution in the Mg–Zn–Y system, Journal of Materials Research. 16 (2001) 1894–1900.

[46] Y. Kawamura, K. Hayashi, A. Inoue, T. Masumoto, Rapidly solidified powder metallurgy $Mg_{97}Zn_1Y_2$ alloys with excellent tensile yield strength above 600 MPa, Mater Trans. 42 (2001) 1172–1176.

[47] M. Matsuda, S. Ii, Y. Kawamura, Y. Ikuhara, M. Nishida, Variation of long-period stacking order structures in rapidly solidified $Mg_{97}Zn_1Y_2$ alloy, Materials Science and Engineering A. 393 (2005) 269–274.

[48] E. Abe, Y. Kawamura, K. Hayashi, A. Inoue, Long-period ordered structure in a high-strength nanocrystalline Mg-1 at% Zn-2 at% Y alloy studied by atomic-resolution Z-contrast STEM, Acta Materialia. 50 (2002) 3845–3857.

[49] F. Qi, D. Zhang, X. Zhang, X. Xu, Effects of Mn addition and X-phase on the microstructure and mechanical properties of high-strength Mg-Zn-Y-Mn alloys, Materials Science and Engineering A. 593 (2014) 70–78.

[50] X. Li, T. Al-Samman, S. Mu, G. Gottstein, Texture and microstructure development during

hot deformation of ME20 magnesium alloy: Experiments and simulations, Materials Science and Engineering A. 528 (2011) 7915–7925.

[51] L. Li, X. Zhang, Hot compression deformation behavior and processing parameters of a cast Mg-Gd-Y-Zr alloy, Materials Science and Engineering A. 528 (2011) 1396–1401.

[52] Y. Xu, L. Hu, T. Deng, L. Ye, Hot deformation behavior and processing map of as-cast AZ61 magnesium alloy, Materials Science and Engineering A. 559 (2013) 528–533.

[53] Q. Chen, X. Xia, B. Yuan, D. Shu, Z. Zhao, J. Han, Hot workability behavior of as-cast Mg-Zn-Y-Zr alloy, Materials Science and Engineering A. 593 (2014) 38–47.

[54] H.Z. Zhao, L. Xiao, P. Ge, J. Sun, Z.P. Xi, Hot deformation behavior and processing maps of Ti-1300 alloy, Materials Science and Engineering A. 604 (2014) 111–116.

[55] H. Liao, Y. Wu, K. Zhou, J. Yang, Hot deformation behavior and processing map of Al-Si-Mg alloys containing different amount of silicon based on Gleebe-3500 hot compression simulation, Materials and Design. 65 (2015) 1091–1099.

[56] G.I. Taylor, Plastic strain in metals, Twenty-Eighth May Lecture to the Institute of Metals. (1938) 307–325.

[57] P.G. Partridge, The crystallography and deformation modes of hexagonal close-packed metals, International Materials Reviews. 12 (1967) 169–194.

[58] Dierk Raabe Materials Science and Engineering - Titanium alloys. (n.d.). Retrieved April 19, 2016, from http://www.dierk-raabe.com/titanium-alloys/

[59] W. Callister, D. Rethwisch, Materials science and engineering: an introduction, 2007.

[60] G.E. Dieter, Mechanical Fundamentals, in: Mechanical Metallurgy - SI Metric Edition, 1988: pp. 1–119.

[61] Y. Wu, W. Hu, Comparison of the solid solution properties of Mg-RE (Gd, Dy, Y) alloys with atomistic simulation, Research Letters in Physics. (2008) 1–4.

[62] M.R. Barnett, A taylor model based description of the proof stress of magnesium AZ31 during hot working, Metallurgical and Materials Transactions A. 34 (2003) 1799–1806.

[63] S.R. Agnew, Ö. Duygulu, Plastic anisotropy and the role of non-basal slip in magnesium alloy AZ31B, International Journal of Plasticity 21 (2005) 1161–1193.

[64] S.R. Agnew, M.H. Yoo, C.N. Tomé, Application of texture simulation to understanding mechanical behavior of Mg and solid solution alloys containing Li or Y, Acta Materialia. 49 (2001) 4277–4289.

[65] S.R. Agnew, C.N. Tome, D.W. Brown, T.M. Holden, S.C. Vogel, Study of slip mechanisms in a magnesium alloy by neutron diffraction and modeling, Scripta Materialia. 48 (2003) 1003–1008.

[66] I. Ulacia, N. V. Dudamell, F. Golvez, S. Yi, M.T. Perez-Prado, I. Hurtado, Mechanical behavior and microstructural evolution of a Mg AZ31 sheet at dynamic strain rates, Acta Materialia. 58 (2010) 2988–2998.

[67] T. Obara, H. Yoshinga, S. Morozumi, {1122}<1123> Slip system in magnesium, Acta Metallurgica. 21 (1973) 845–853.

[68] S.R. Agnew, O. Duygulu, A Mechanistic Understanding of the Formability of Magnesium: Examining the Role of Temperature on the Deformation Mechanisms, Materials Science Forum. 419-422 (2003) 177–188.

[69] R. Reed-Hill, W. Robertson, Deformation of magnesium single crystal by non-basal slip, Journal of Metals Transactions of AIME. 9 (1957) 496–502.

[70] E.W. Kelley, J.W.F. Hosford, Plane strain compression of magnesium and magnesium alloy crystals, Metallurgical Society of American Institute of Mining, Metallurgical and Petroleum Engineers Transactions. 242 (1968) 5–13.

[71] G.E. Totten, D.S. Mackenzie, Handbook of Aluminum Volume 2 - Alloy Production And

Materials Manufacturing, 2003.

[72] S. Lou, D.O. Northwood, Effect of strain aging on the strength coefficient and strain-hardening exponent of construction-grade steels, Journal of Materials Engineering and Performance. 3 (1994) 344–349.

[73] J.H. Hollomon, Tensile Deformation, Transactions of the Metallurgical Society of AIME. 162 (1945) 268–290.

[74] N. Afrin, D.L. Chen, X. Cao, M. Jahazi, Strain hardening behavior of a friction stir welded magnesium alloy, Scripta Materialia. 57 (2007) 1004–1007.

[75] S. Kleiner, P.J. Uggowitzer, Mechanical anisotropy of extruded Mg-6% Al-1% Zn alloy, Materials Science and Engineering A. 379 (2004) 258–263.

[76] G. Garcés, P. Pérez, P. Adeva, Effect of the extrusion texture on the mechanical behaviour of Mg–SiCp composites, Scripta Materialia. 52 (2005) 615–619.

[77] Y. Chino, K. Kimura, M. Mabuchi, Deformation characteristics at room temperature under biaxial tensile stress in textured AZ31 Mg alloy sheets, Acta Materialia. 57 (2009) 1476–1485.

[78] P. Okrutny, Modelling of recovery and recrystallization in magnesium alloys, MSc Thesis, McMaster University, 2010.

[79] R.A. Lebensohn, C.N. Tomé, A self-consistent anisotropic approach for the simulation of plastic deformation and texture development of polycrystals: Application to zirconium alloys, Acta Metallurgica et Materialia. 41 (1993) 2611–2624.

[80] C.N. Tomé, R.A. Lebensohn, U.F. Kocks, A model for texture development dominated by deformation twinning: Application to zirconium alloys, Acta Metallurgica et Materialia. 39 (1991) 2667–2680.

[81] I.J. Beyerlein, R.A. Lebensohn, C.N. Tomé, Modeling texture and microstructural

evolution in the equal channel angular extrusion process, Materials Science and Engineering: A. 345 (2003) 122–138.

[82] C. Tomé, Mechanical response of zirconium-I. Derivation of a polycrystal constitutive law and finite element analysis, Acta Materialia. 49 (2001) 3085–3096.

[83] R.A. Lebensohn, C.N. Tomé, A self-consistent viscoplastic model: prediction of rolling textures of anisotropic polycrystals, Materials Science and Engineering: A. 175 (1994) 71–82.

[84] S.V.S. Narayana Murty, B. Nageswara Rao, B.P. Kashyap, Instability criteria for hot deformation of materials, International Materials Reviews. 45 (2000) 15–26.

[85] H.J. McQueen, J.E. Hockett, Microstructures of aluminum compressed at various rates and temperatures, Metallurgical Transactions. 1 (n.d.) 2997–3004.

[86] Y.V.R.K. Prasad, H.L. Gegel, S.M. Doraivelu, J.C. Malas, J.T. Morgan, K.A. Lark, D. R. Barker, Modeling of dynamic material behavior in hot deformation: Forging of Ti-6242, Metallurgical Transactions A. 15 (1984) 1883–1892.

[87] H.L. Gegel, J.C Malas, S.M Doraivelu, Modeling Techniques Used in Forging Process Design, in: Metals Handbook, ASM, Metals Park, OH, 1988: pp. 417–426.

[88] J. Li, J. Liu, Z. Cui, Characterization of hot deformation behavior of extruded ZK60 magnesium alloy using 3D processing maps, Materials and Design. 56 (2014) 889–897.

[89] Y.V.R.K. Prasad, K.P. Rao, S. Sasidhara, A Compendium of Processing Maps, in: Hot Working Guide, ASM International, 2015.

[90] Y.V.R.K. Prasad, T. Seshacharyulu, Processing maps for hot working of titanium alloys, Materials Science and Engineering: A. 243 (1998) 82–88.

[91] S. Biswas, B. Beausir, L.S. Toth, S. Suwas, Evolution of texture and microstructure during hot torsion of a magnesium alloy, Acta Materialia. 61 (2013) 5263–5277.

[92] P. Šedá, A. Jäger, P. Lejček, P. Romano Triguero, Formation of grain boundaries in magnesium single crystal during equal channel angular pressing, Philosophical Magazine. 94 (2014) 1095–1111.

[93] T. Al-Samman, K.D. Molodov, D.A. Molodov, G. Gottstein, S. Suwas, Softening and dynamic recrystallization in magnesium single crystals during c-axis compression, Acta Materialia. 60 (2012) 537–545.

[94] K.D. Molodov, T. Al-Samman, D.A. Molodov, G. Gottstein, Mechanisms of exceptional ductility of magnesium single crystal during deformation at room temperature: Multiple twinning and dynamic recrystallization, Acta Materialia. 76 (2014) 314–330.

[95] S.E. Ion, F.J. Humphreys, S.H. White, Dynamic recrystallisation and the development of microstructure during the high temperature deformation of magnesium, Acta Metallurgica. 30 (1982) 1909–1919.

[96] S.M. Fatemi-Varzaneh, A. Zarei-Hanzaki, H. Beladi, Dynamic recrystallization in AZ31 magnesium alloy, Materials Science and Engineering A. 456 (2007) 52–57.

[97] T. Al-Samman, G. Gottstein, Dynamic recrystallization during high temperature deformation of magnesium, Materials Science and Engineering A. 490 (2008) 411–420.

[98] Q. Ma, B. Li, E.B. Marin, S.J. Horstemeyer, Twinning-induced dynamic recrystallization in a magnesium alloy extruded at 450 °C, Scripta Materialia. 65 (2011) 823–826.

[99] Q. Ma, B. Li, W.R. Whittington, A.L. Oppedal, P.T. Wang, M.F. Horstemeyer, Texture evolution during dynamic recrystallization in a magnesium alloy at 450° C, Acta Materialia 67 (2014) 102–115.

[100] N. Stanford, D. Atwell, M.R. Barnett, The effect of Gd on the recrystallisation, texture and deformation behaviour of magnesium-based alloys, Acta Materialia 58 (2010) 6773–6783.

[101] F.J. Humphreys, M. Hatherly, Recrystallization and Related Annealing Phenomena, 2004.

[102] B.C. Walter A, Backofen. Wonsiewicz, Plasticity of magnesium crystals, Transactions of the Metallurgical Society of AIME 239 (1967) 1422–1431.

[103] M. Knezevic, A. Levinson, R. Harris, R.K. Mishra, R.D. Doherty, S.R. Kalidindi, Deformation twinning in AZ31: Influence on strain hardening and texture evolution, Acta Materialia 58 (2010) 6230–6242.

[104] X.P. Chen, L.X. Wang, R. Xiao, X.Y. Zhong, G.J. Huang, Q. Liu, Comparison of annealing on microstructure and anisotropy of magnesium alloy AZ31 sheets processed by three different routes, Journal of Alloys and Compounds 604 (2014) 112–116.

[105] Q. Huo, X. Yang, H. Sun, B. Li, J. Qin, J. Wang, et al., Enhancement of tensile ductility and stretch formability of AZ31 magnesium alloy sheet processed by cross-wavy bending, Journal of Alloys and Compounds 581 (2013) 230–235.

[106] M.D. Nave, M.R. Barnett, Microstructures and textures of pure magnesium deformed in plane-strain compression, Scripta Materialia 51 (2004) 881–885.

[107] D. Sarker, J. Friedman, D.L. Chen, Influence of pre-deformation and subsequent annealing on strain hardening and anisotropy of AM30 magnesium alloy, Journal of Alloys and Compounds 611 (2014) 341–350.

[108] A. Levinson, R.K. Mishra, R.D. Doherty, S.R. Kalidindi, Influence of deformation twinning on static annealing of AZ31 Mg alloy, Acta Materialia. 61 (2013) 5966–5978.

[109] X. Yang, Y. Okabe, H. Miura, T. Sakai, Effect of prior strain on continuous recrystallization in AZ31 magnesium alloy after hot deformation, Materials Science and Engineering A 535 (2012) 209–215.

[110] X. Li, P. Yang, L.N. Wang, L. Meng, F. Cui, Orientational analysis of static recrystallization at compression twins in a magnesium alloy AZ31, Materials Science and Engineering A 517 (2009) 160–169.

[111] E.A. Lukyanova, N.S. Martynenko, I. Shakhova, A.N. Belyakov, L.L. Rokhlin, S.V. Dobatkin, et al., Strengthening of age-hardenable WE43 magnesium alloy processed by high pressure torsion, Materials Letters 170 (2016) 5–9.

[112] F.A. Mirza, D.L. Chen, D.J. Li, X.Q. Zeng, Cyclic deformation behavior of a rare-earth containing extruded magnesium alloy: effect of heat treatment, Metallurgical and Materials Transactions A: Physical Metallurgy and Materials Science 46 (2014) 1168–1187.

[113] H. Pan, Y. Ren, H. Fu, H. Zhao, L. Wang, X. Meng, et al., Recent developments in rare-earth free wrought magnesium alloys having high strength: A review, Journal of Alloys and Compounds 663 (2016) 321–331.

[114] N. Tahreen, D.F. Zhang, F.S. Pan, X.Q. Jiang, D.Y. Li, D.L. Chen, Hot deformation and processing map in an Mg-Zn-Mn-Y alloy, in: Magnesium Technology 2016, John Wiley & Sons, Inc., 2016: pp. 183–186.

[115] D. Mumbaraddi, S. Sarkar, S.C. Peter, A review on the synthesis, crystal growth, structure and physical properties of rare earth based quaternary intermetallic compounds, Journal of Solid State Chemistry 236 (2016) 94–115.

[116] R. Cottam, J. Robson, G. Lorimer, B. Davis, Dynamic recrystallization of Mg and Mg-Y alloys: Crystallographic texture development, Materials Science and Engineering A 485 (2008) 375–382.

[117] Y. Chino, K. Sassa, M. Mabuchi, Texture and stretch formability of a rolled Mg-Zn alloy containing dilute content of Y, Materials Science and Engineering A 513-514 (2009) 394–400.

[118] S.M. Zhu, M.A. Gibson, M.A. Easton, J.F. Nie, The relationship between microstructure and creep resistance in die-cast magnesium-rare earth alloys, Scripta Materialia 63 (2010) 698–703.

[119] F.A. Mirza, D.L. Chen, D.J. Li, X.Q. Zeng, Low cycle fatigue of a rare-earth containing extruded magnesium alloy, Materials Science and Engineering A 575 (2013) 65–73.

[120] F.A. Mirza, D.L. Chen, D.J. Li, X.Q. Zeng, Effect of strain ratio on cyclic deformation behavior of a rare-earth containing extruded magnesium alloy, Materials Science and Engineering A 588 (2013) 250–259.

[121] E.A. Ball, P.B. Prangnell, Tensile-compressive yield asymmetries in high strength wrought magnesium alloys, Scripta Metallurgica et Materiala 31 (1994) 111–116.

[122] L.L. Rokhlin, Advanced Light Alloys and Composites, in: R. Ciach (Ed.), Springer Netherlands, Dordrecht, 1998: pp. 443–448.

[123] J. Grobner, R. Schmid-Fetzer, Thermodynamic modeling of the Mg-Ce-Gd-Y system, Scripta Materialia. 63 (2010) 674–679.

[124] G. Shao, V. Varsani, Z. Fan, Thermodynamic modelling of the Y-Zn and Mg-Zn-Y systems, Calphad: Computer Coupling of Phase Diagrams and Thermochemistry 30 (2006) 286–295.

[125] Z.H. Huang, S.M. Liang, R.S. Chen, E.H. Han, Solidification pathways and constituent phases of Mg-Zn-Y-Zr alloys, Journal of Alloys and Compounds 468 (2009) 170–178.

[126] A. Singh, Tailoring microstructure of Mg–Zn–Y alloys with quasicrystal and related phases for high mechanical strength, Sci. Technol. Adv. Mater. 15 (2014) 1-16.

[127] A. Singh, A.P. Tsai, A new orientation relationship OR4 of icosahedral phase with magnesium matrix in Mg–Zn–Y alloys, Scripta Materialia 53 (2005) 1083–1087.

[128] A. Singh, M. Watanabe, A. Kato, A.P. Tsai, Twinning and the orientation relationships of icosahedral phase with the magnesium matrix, Acta Materialia 53 (2005) 4733–4742.

[129] E. M. Padezhnova, E. V. Melnik, R. A. Miliyevskiy, T. V. Dobatkina, V. V. Kinzhibalo, Russian Metallurgy 4 (1982) 185–188.

[130] J. Wang, S. Gao, P. Song, X. Huang, Z. Shi, F. Pan, Effects of phase composition on the mechanical properties and damping capacities of as-extruded Mg-Zn-Y-Zr alloys, Journal of Alloys and Compounds 509 (2011) 8567–8572.

[131] A. Singh, A.P. Tsai, On the cubic W phase and its relationship to the icosahedral phase in Mg-Zn-Y alloys, Scripta Materialia. 49 (2003) 143–148.

[132] Y.M. Zhu, A.J. Morton, J.F. Nie, The 18R and 14H long-period stacking ordered structures in Mg-Y-Zn alloys, Acta Materialia. 58 (2010) 2936–2947.

[133] H. Gao, K. Ikeda, T. Morikawa, K. Higashida, H. Nakashima, Microstructures of Long-Period Stacking Ordered Phase of Mg-Zn-Y Alloy, Materials Transactions 54 (2013) 632–635.

[134] D.H. Ping, K. Hono, Y. Kawamura, A. Inoue, Local chemistry of a nanocrystalline high-strength Mg97Y2Zn1 alloy, Philosophical Magazine Letters. 82 (2002) 543–551.

[135] Z.P. Luo, S.Q. Zhang, High-resolution electron microscopy on the X-Mg12ZnY phase in a high strength Mg-Zn-Zr-Y magnesium alloy, Journal of Materials Science Letters. 19 (n.d.) 813–815.

[136] T. Itoi, T. Seimiya, Y. Kawamura, M. Hirohashi, Long period stacking structures observed in Mg97Zn 1Y2 alloy, Scripta Materialia 51 (2004) 107–111.

[137] M. Yamasaki, M. Sasaki, M. Nishijima, K. Hiraga, Y. Kawamura, Formation of 14H long period stacking ordered structure and profuse stacking faults in Mg-Zn-Gd alloys during isothermal aging at high temperature, Acta Materialia 55 (2007) 6798–6805.

[138] H. Yokobayashi, K. Kishida, H. Inui, M. Yamasaki, Y. Kawamura, Enrichment of Gd and Al atoms in the quadruple close packed planes and their in-plane long-range ordering in the long period stacking-ordered phase in the Mg-Al-Gd system, Acta Materialia. 59 (2011) 7287–7299.

[139] E. Abe, A. Ono, T. Itoi, M. Yamasaki, Y. Kawamura, Polytypes of long-period stacking structures synchronized with chemical order in a dilute Mg-Zn-Y alloy, Philosophical Magazine Letters. (2011) 8.

[140] T. Itoi, T. Suzuki, Y. Kawamura, M. Hirohashi, Microstructure and Mechanical Properties of Mg-Zn-Y Rolled Sheet with a Mg12ZnY Phase, Materials Transactions 51 (2010) 1536–1542.

[141] K. Kishida, H. Yokobayashi, H. Inui, M. Yamasaki, Y. Kawamura, The crystal structure of the LPSO phase of the 14H-type in the Mg-Al-Gd alloy system, Intermetallics 31 (2012) 55–64.

[142] Y.M. Zhu, A.J. Morton, J.F. Nie, The 18R and 14H long-period stacking ordered structures in Mg-Y-Zn alloys, Acta Materialia. 58 (2010) 2936–2947.

[143] E.J. Kirkland, R.F. Loane, J. Silcox, Simulation of annular dark field stem images using a modified multislice method, Ultramicroscopy 23 (1987) 77–96.

[144] S.J. Pennycook, D.E. Jesson, Atomic resolution Z-contrast imaging of interfaces, Acta Metallurgica Et Materialia. 40 (1992).

[145] D.H. Bae, S.H. Kim, D.H. Kim, W.T. Kim, Deformation behavior of Mg-Zn-Y alloys reinforced by icosahedral quasicrystalline particles, Acta Materialia 50 (2002) 2343–2356.

[146] H.J. Chae, B.-S. Kim, Y. Do Kim, T.-S. Kim, Microstructure and mechanical properties of a Mg–Zn4.3Y0.7 alloy powder reinforced by quasi-crystalline particles, Materials Letters 77 (2012) 63–66.

[147] D.H. Bae, M.H. Lee, K.T. Kim, W.T. Kim, D.H. Kim, Application of quasicrystalline particles as a strengthening phase in Mg-Zn-Y alloys, Journal of Alloys and Compounds 342 (2002) 445–450.

[148] R.M. Wang, A. Eliezer, E. Gutman, Microstructures and dislocations in the stressed AZ91D

magnesium alloys, Materials Science and Engineering A. 344 (2003) 279–287.

[149] B. Chen, D. Lin, X. Zeng, C. Lu, Effects of yttrium and zinc addition on the microstructure and mechanical properties of Mg-Y-Zn alloys, Journal of Materials Science. 45 (2010) 2510–2517.

[150] B. Chen, D. Lin, X. Zeng, C. Lu, Microstructure and mechanical properties of ultrafine grained $Mg_{97}Y_2Zn_1$ alloy processed by equal channel angular pressing, Journal of Alloys and Compounds. 440 (2007) 94–100.

[151] L.B. Tong, X.H. Li, H.J. Zhang, Effect of long period stacking ordered phase on the microstructure, texture and mechanical properties of extruded Mg-Y-Zn alloy, Materials Science and Engineering A. 563 (2013) 177–183.

[152] Y. Kawamura, M. Yamasaki, Formation and mechanical properties of $Mg_{97}Zn_1RE_2$ alloys with long-period stacking ordered structure, Materials Transactions. 48 (2007) 2986–2992.

[153] S. Yoshimoto, M. Yamasaki, Y. Kawamura, Microstructure and mechanical properties of extruded Mg-Zn-Y alloys with 14H long period ordered structure, Materials Transactions. 47 (2006) 959–965.

[154] K. Hagihara, A. Klnoshita, Y. Sugino, M. Yamasaki, Y. Kawamura, H.Y. Yasuda, Y. Umakoshi, Plastic deformation behavior of $Mg_{97}Zn_1Y_2$ extruded alloys, Transactions of Nonferrous Metals Society of China (English Edition). 20 (2010) 1259–1268.

[155] Y. Kawamura, T. Kasahara, S. Izumi, M. Yamasaki, Elevated temperature $Mg_{97}Y_2Cu_1$ alloy with long period ordered structure, Scripta Materialia. 55 (2006) 453–456.

[156] X.H. Shao, Z.Q. Yang, X.L. Ma, Strengthening and toughening mechanisms in Mg-Zn-Y alloy with a long period stacking ordered structure, Acta Materialia. 58 (2010) 4760–4771.

[157] American Society for Testing and Materials Annual, “Annual Book of ASTM Standards,” Philadelphia, PA, USA. Sec., 4 (1992) 04–08.

[158] K. Hantzsche, J. Bohlen, J. Wendt, K.U. Kainer, S.B. Yi, D. Letzig, Effect of rare earth additions on microstructure and texture development of magnesium alloy sheets, Scripta Materialia. 63 (2010) 725–730.

[159] N. Stanford, M. Barnett, Effect of composition on the texture and deformation behaviour of wrought Mg alloys, Scripta Materialia. 58 (2008) 179–182.

[160] S.A. Farzadfar, M. Sanjari, I.H. Jung, E. Essadiqi, S. Yue, Role of yttrium in the microstructure and texture evolution of Mg, Materials Science and Engineering A. 528 (2011) 6742–6753.

[161] B. Wang, R. Xin, G. Huang, Q. Liu, Effect of crystal orientation on the mechanical properties and strain hardening behavior of magnesium alloy AZ31 during uniaxial compression, Materials Science and Engineering: A. 534 (2012) 588–593.

[162] K. Hagihara, N. Yokotani, Y. Umakoshi, Plastic deformation behavior of $Mg_{12}YZn$ with 18R long-period stacking ordered structure, Intermetallics. 18 (2010) 267–276.

[163] F. Qi, D. Zhang, X. Zhang, F. Pan, Effect of Y addition on microstructure and mechanical properties of Mg–Zn–Mn alloy, Transactions of Nonferrous Metals Society of China. 24 (2014) 1352–1364.

[164] K. Hagihara, A. Kinoshita, Y. Sugino, M. Yamasaki, Y. Kawamura, H.Y. Yasuda, Y. Umakoshi, Plastic deformation behavior of $Mg_{89}Zn_4Y_7$ extruded alloy composed of long-period stacking ordered phase, Intermetallics. 18 (2010) 1079–1085.

[165] A.A. Salem, S.R. Kalidindi, R.D. Doherty, S.L. Semiatin, Strain hardening due to deformation twinning in α-titanium: Mechanisms, Metallurgical and Materials Transactions A: Physical Metallurgy and Materials Science. 37 (2006) 259–268.

[166] D. Sarker, D.L. Chen, Detwinning and strain hardening of an extruded magnesium alloy during compression, Scripta Materialia. 67 (2012) 165–168.

[167] Y. Xin, X. Zhou, L. Lv, Q. Liu, The influence of a secondary twin on the detwinning deformation of a primary twin in Mg–3Al–1Zn alloy, Materials Science and Engineering: A. 606 (2014) 81–91.

[168] G. Wan, B.L. Wu, Y.D. Zhang, G.Y. Sha, C. Esling, Anisotropy of dynamic behavior of extruded AZ31 magnesium alloy, Materials Science and Engineering: A. 527 (2010) 2915–2924.

[169] S.-H. Choi, J.K. Kim, B.J. Kim, Y.B. Park, The effect of grain size distribution on the shape of flow stress curves of Mg–3Al–1Zn under uniaxial compression, Materials Science and Engineering: A. 488 (2008) 458–467.

[170] S.B. Yi, C.H.J. Davies, H.G. Brokmeier, R.E. Bolmaro, K.U. Kainer, J. Homeyer, Deformation and texture evolution in AZ31 magnesium alloy during uniaxial loading, Acta Materialia. 54 (2006) 549–562.

[171] L. Jiang, J.J. Jonas, A.A. Luo, A.K. Sachdev, S. Godet, Influence of {10-12} extension twinning on the flow behavior of AZ31 Mg alloy, Materials Science and Engineering: A. 445-446 (2007) 302–309.

[172] C.H. Cáceres, A.H. Blake, On the strain hardening behaviour of magnesium at room temperature, Materials Science and Engineering: A. 462 (2007) 193–196.

[173] D. Sarker, D.L. Chen, Dependence of compressive deformation on pre-strain and loading direction in an extruded magnesium alloy: Texture, twinning and de-twinning, Materials Science and Engineering: A. 596 (2014) 134–144.

[174] R.K. Mishra, A.K. Gupta, P.R. Rao, A.K. Sachdev, A.M. Kumar, A.A. Luo, Influence of cerium on the texture and ductility of magnesium extrusions, Scripta Materialia 59 (2008) 562–565.

[175] F.A. Mirza, D.L. Chen, D.J. Li, X.Q. Zeng, Effect of rare earth elements on deformation

behavior of an extruded Mg-10Gd-3Y-0.5Zr alloy during compression, Materials and Design. 46 (2013) 411–418.

[176] L. Jiang, J.J. Jonas, R.K. Mishra, A.A. Luo, A.K. Sachdev, S. Godet, Twinning and texture development in two Mg alloys subjected to loading along three different strain paths, Acta Materialia. 55 (2007) 3899–3910.

[177] D.H. Bae, Y. Kim, I.J. Kim, Thermally stable quasicrystalline phase in a superplastic Mg-Zn-Y-Zr alloy, Materials Letters. 60 (2006) 2190–2193.

[178] K. Hagihara, A. Kinoshita, Y. Sugino, M. Yamasaki, Y. Kawamura, H.Y. Yasuda, Y. Umakoshi, Effect of long-period stacking ordered phase on mechanical properties of $Mg_{97}Zn_1Y_2$ extruded alloy, Acta Materialia. 58 (2010) 6282–6293.

[179] L.L. Rokhlin, Magnesium Alloys Containing Rare Earth Metals: Structure and Properties, CRC Press, 2003.

[180] M. Noda, Y. Kawamura, Thermal Stability and mechanical properties of extruded Mg-Zn-Y alloys with long-period stacking order phase, Materials Science Forum. 654-656 (2010) 611–614.

[181] X. Wang, C. Liu, L. Xu, H. Xiao, L. Zheng, Microstructure and mechanical properties of the hot-rolled Mg–Y–Nd–Zr alloy, Journal of Materials Research. 28 (2013) 1386–1393.

[182] R. Muraliraja, H. Vettrivel, R. Elansezhian, Synthesis and characterization of magnesium alloy added with yttrium and to study the microstructure and mechanical properties, International Journal of Engineering and Innovative Technology 2 (2013) 388–392.

[183] F.A. Mirza, D.L. Chen, D.J. Li, X.Q. Zeng, Effect of rare earth elements on deformation behavior of an extruded Mg–10Gd–3Y–0.5Zr alloy during compression, Materials & Design. 46 (2013) 411–418.

[184] N. Tahreen, D.L. Chen, M. Nouri, D.Y. Li, Influence of aluminum content on twinning and

texture development of cast Mg-Al-Zn alloy during compression, Journal of Alloys and Compounds. 623 (2015) 15–23.

[185] Z.A. Luo, G.M. Xie, Z.Y. Ma, G.L. Wang, G.D. Wang, Effect of yttrium addition on microstructural characteristics and superplastic behavior of friction stir processed ZK60 alloy, Journal of Materials Science & Technology. 29 (2013) 1116–1122.

[186] D. Sarker, J. Friedman, D.L. Chen, Influence of pre-strain on de-twinning activity in an extruded AM30 magnesium alloy, Materials Science and Engineering: A. 605 (2014) 73–79.

[187] D. Sarker, J. Friedman, D.L. Chen, Twin growth and texture evolution in an extruded AM30 magnesium alloy during compression, Journal of Materials Science & Technology. 30 (2014) 884–887.

[188] N. Stanford, D. Atwell, A. Beer, C. Davies, M.R. Barnett, Effect of microalloying with rare-earth elements on the texture of extruded magnesium-based alloys, Scripta Materialia. 59 (2008) 772–775.

[189] J. Bohlen, M.R. Nurnberg, J.W. Senn, D. Letzig, S.R. Agnew, The texture and anisotropy of magnesium-zinc-rare earth alloy sheets, Acta Materialia. 55 (2007) 2101–2112.

[190] M. Lentz, M. Klaus, R.S. Coelho, N. Schaefer, F. Schmack, W. Reimers, B. Clausen, Analysis of the deformation behavior of magnesium-rare earth alloys Mg-2 pct Mn-1 pct rare earth and Mg-5 pct Y-4 pct rare earth by in situ energy-dispersive X-ray synchrotron diffraction and elasto-plastic self-consistent modeling, Metallurgical and Materials Transactions A. 45 (2014) 5721–5735.

[191] N. V. Dudamell, P. Hidalgo-Manrique, A. Chakkedath, Z. Chen, C.J. Boehlert, F. Gálvez, S. Yi, J. Bohlen, D. Letzig, M.T. Pérez-Prado, Influence of strain rate on the twin and slip activity of a magnesium alloy containing neodymium, Materials Science and Engineering

A. 583 (2013) 220–231.

[192] J.P. Hadorn, K. Hantzsche, S. Yi, J. Bohlen, D. Letzig, J.A. Wollmershauser, et al., Role of solute in the texture modification during hot deformation of Mg-rare earth alloys, Metallurgical and Materials Transactions A: Physical Metallurgy and Materials Science. 43 (2012) 1347–1362.

[193] J.F. Nie, Y.M. Zhu, J.Z. Liu, X.Y. Fang, Periodic segregation of solute atoms in fully coherent twin boundaries, Science. 340 (2013) 957–960.

[194] M. Bugnet, A. Kula, M. Niewczas, G.A. Botton, Segregation and clustering of solutes at grain boundaries in Mg-rare earth solid solutions, Acta Materialia. 79 (2014) 66–73.

[195] J.D. Robson, Effect of rare-earth additions on the texture of wrought magnesium alloys: The role of grain boundary segregation, Metallurgical and Materials Transactions A: Physical Metallurgy and Materials Science. 45 (2014) 3205–3212.

[196] A. Kumar, J. Wang, C.N. Tomé, First-principles study of energy and atomic solubility of twinning-associated boundaries in hexagonal metals, Acta Materialia. 85 (2015) 144–154.

[197] L.P. Kurilekh, Recrystallization behavior of solid solutions of metals, Metal Science and Heat Treatment of Metals. 1 (n.d.) 33–36.

[198] M. Yamasaki, K. Hashimoto, K. Hagihara, Y. Kawamura, Effect of multimodal microstructure evolution on mechanical properties of Mg-Zn-Y extruded alloy, Acta Materialia. 59 (2011) 3646–3658.

[199] M. Matsuda, S. Ii, Y. Kawamura, Y. Ikuhara, M. Nishida, Interaction between long period stacking order phase and deformation twin in rapidly solidified $Mg_{97}Zn_1Y_2$ alloy, Materials Science and Engineering A. 386 (2004) 447–452.

[200] D. Sarker, D.L. Chen, Texture transformation in an extruded magnesium alloy under pressure, Materials Science and Engineering A. 582 (2013) 63–67.

[201] H. Mirzadeh, J.M. Cabrera, A. Najafizadeh, P.R. Calvillo, EBSD study of a hot deformed austenitic stainless steel, Materials Science and Engineering A. 538 (2012) 236–245.

[202] F.J. Humphreys, Grain and subgrain characterisation by electron backscatter diffraction, Journal of Materials Science. 36 (2001) 3833–3854.

[203] S. Mitsche, P. Poelt, C. Sommitsch, Recrystallization behaviour of the nickel-based alloy 80 a during hot forming, Journal of Microscopy (2007) 267–274.

[204] I. Basu, T. Al-Samman, Twin recrystallization mechanisms in magnesium-rare earth alloys, Acta Materialia. 96 (2015) 111–132.

[205] I. Basu, T. Al-Samman, Triggering rare earth texture modification in magnesium alloys by addition of zinc and zirconium, Acta Materialia. 67 (2014) 116–133.

[206] I. Basu, T. Al-Samman, G. Gottstein, Shear band-related recrystallization and grain growth in two rolled magnesium-rare earth alloys, Materials Science and Engineering A. 579 (2013) 50–56.

[207] A.L. Oppedal, H. El Kadiri, C.N. Tomé, G.C. Kaschner, S.C. Vogel, J.C. Baird, et al., Effect of dislocation transmutation on modeling hardening mechanisms by twinning in magnesium, International Journal of Plasticity. 30-31 (2012) 41–61.

[208] G.C. Kaschner, C.N. Tome, I.J. Beyerlein, S.C. Vogel, D.W. Brown, R.J. McCabe, Role of twinning in the hardening response of zirconium during temperature reloads, Acta Materialia. 54 (2006) 2887–2896.

[209] G. Proust, C.N. Tome, A. Jain, S.R. Agnew, Modeling the effect of twinning and detwinning during strain-path changes of magnesium alloy AZ31, International Journal of Plasticity. 25 (2009) 861–880.

[210] I.J. Beyerlein, C.N. Tome, A dislocation-based constitutive law for pure Zr including temperature effects, International Journal of Plasticity. 24 (2008) 867–895.

[211] M. Arul Kumar, A.K. Kanjarla, S.R. Niezgoda, R.A. Lebensohn, C.N. Tome, Numerical study of the stress state of a deformation twin in magnesium, Acta Materialia. 84 (2015) 349–358.

[212] C.J. Boehlert, Z. Chen, A. Chakkedath, I. Gutiérrez-Urrutia, J. Llorca, J. Bohlen, et al., In situ analysis of the tensile deformation mechanisms in extruded Mg–1Mn–1Nd (wt%), Philosophical Magazine. 93 (2013) 598–617.

[213] A. Jain, S.R. Agnew, Modeling the temperature dependent effect of twinning on the behavior of magnesium alloy AZ31B sheet, Materials Science and Engineering A. 462 (2007) 29–36.

[214] A. Chapuis, J.H. Driver, Temperature dependency of slip and twinning in plane strain compressed magnesium single crystals, Acta Materialia. 59 (2011) 1986–1994.

[215] S. Sandlobes, S. Zaefferer, I. Schestakow, S. Yi, R. Gonzalez-Martinez, On the role of non-basal deformation mechanisms for the ductility of Mg and Mg-Y alloys, Acta Materialia. 59 (2011) 429–439.

[216] S. Sandlöbes, M. Friák, J. Neugebauer, D. Raabe, Basal and non-basal dislocation slip in Mg-Y, Materials Science and Engineering A. 576 (2013) 61–68.

[217] T. Tsuru, D.C. Chrzan, Effect of solute atoms on dislocation motion in Mg: An electronic structure perspective, Scientific Reports. 5 (2015) 8793.

[218] K.H. Kim, J.B. Jeon, N.J. Kim, B.J. Lee, Role of yttrium in activation of <c + a> slip in magnesium: An atomistic approach, Scripta Materialia. 108 (2015) 104–108.

[219] Z. Wu, W.A. Curtin, The origins of high hardening and low ductility in magnesium, Nature. 000 (2015) 1–6.

[220] C.M. Sellars, W.J. McTegart, On the mechanism of hot deformation, Acta Metallurgica. 14 (1966) 1136–1138.

[221] H. McQueen, N. Ryan, Constitutive analysis in hot working, Materials Science and Engineering: A. 322 (2002) 43–63.

[222] M.A. Jabbari Taleghani, E.M. Ruiz Navas, M. Salehi, J.M. Torralba, Hot deformation behaviour and flow stress prediction of 7075 aluminium alloy powder compacts during compression at elevated temperatures, Materials Science and Engineering A. 534 (2012) 624–631.

[223] S.Y. Jiang, Y.Q. Zhang, Y.N. Zhao, Dynamic recovery and dynamic recrystallization of NiTi shape memory alloy under hot compression deformation, Transactions of Nonferrous Metals Society of China (English Edition). 23 (2013) 140–147.

[224] H. Mirzadeh, Constitutive analysis of Mg-Al-Zn magnesium alloys during hot deformation, Mechanics of Materials 77 (2014) 80–85.

[225] H. Mirzadeh, Constitutive behaviors of magnesium and Mg–Zn–Zr alloy during hot deformation, Materials Chemistry and Physics. 152 (2015) 123–126.

[226] F.A. Slooff, J.S. Dzwonczyk, J. Zhou, J. Duszczyk, L. Katgerman, Hot workability analysis of extruded AZ magnesium alloys with processing maps, Materials Science and Engineering: A. 527 (2010) 735–744.

[227] M. Roostaei, M.H. Parsa, R. Mahmudi, H. Mirzadeh, Hot compression behavior of GZ31 magnesium alloy, Journal of Alloys and Compounds. 631 (2015) 1–6.

[228] M.R. Barnett, Influence of deformation conditions and texture on the high temperature flow stress of magnesium AZ31, Journal of Light Metals. 1 (2001) 167–177.

[229] A. Galiyev, R. Kaibyshev, G. Gottstein, Correlation of plastic deformation and dynamic recrystallization in magnesium alloy ZK60, Acta Materialia. 49 (2001) 1199–1207.

[230] Y.V.R.K. Prasad, K.P. Rao, Processing maps for hot deformation of rolled AZ31 magnesium alloy plate: Anisotropy of hot workability, Materials Science and Engineering

A. 487 (2008) 316–327.

[231] H.C. Xiao, S.N. Jiang, B. Tang, W.H. Hao, Y.H. Gao, Z.Y. Chen, C.M. Liu, Hot deformation and dynamic recrystallization behaviors of Mg–Gd–Y–Zr alloy, Materials Science and Engineering: A. 628 (2015) 311–318.

[232] Y.V.R.K. Prasad, K.P. Rao, Processing maps for hot deformation of rolled AZ31 magnesium alloy plate: Anisotropy of hot workability, Materials Science and Engineering: A. 487 (2008) 316–327.

[233] B. Li, Q. Pan, Z. Yin, Characterization of hot deformation behavior of as-homogenized Al-Cu-Li-Sc-Zr alloy using processing maps, Materials Science and Engineering A. 614 (2014) 199–206.

[234] H.A. Patel, N. Rashidi, D.L. Chen, S.D. Bhole, A.A. Luo, Cyclic deformation behavior of a super-vacuum die cast magnesium alloy, Materials Science and Engineering: A. 546 (2012) 72–81.

[235] H. Asgari, J.A. Szpunar, A.G. Odeshi, Texture evolution and dynamic mechanical behavior of cast AZ magnesium alloys under high strain rate compressive loading, Materials & Design. 61 (2014) 26–34.

[236] S.S. Zhou, K.K. Deng, J.C. Li, K.B. Nie, F.J. Xu, H.F. Zhou, J.F. Fan, Hot deformation behavior and workability characteristics of bimodal size SiCp/AZ91 magnesium matrix composite with processing map, Materials and Design. 64 (2014) 177–184.

[237] I.A. Maksoud, H. Ahmed, J. Rödel, Investigation of the effect of strain rate and temperature on the deformability and microstructure evolution of AZ31 magnesium alloy, Materials Science and Engineering: A. 504 (2009) 40–48.

[238] M.A. Jabbari Taleghani, J.M. Torralba, Hot deformation behavior and workability characteristics of AZ91 magnesium alloy powder compacts-A study using processing map,

Materials Science and Engineering A. 580 (2013) 142–149.

[239] Y.V.R.K. Prasad, Recent Advances in the Science of Mechanical processing, Indian Journal of Technology. 28 (1990) 435–451.

[240] N. Srinivasan, Y.V.R.K. Prasad, P. Rama Rao, Hot deformation behaviour of Mg–3Al alloy-A study using processing map, Materials Science and Engineering: A. 476 (2008) 146–156.

[241] X. Yang, H. Miura, T. Sakai, Dynamic evolution of new grains in magnesium alloy AZ 31 during hot deformation, Materials Transactions. 44 (2003) 197–203.

[242] S. Shekhar, J. Cai, S. Basu, S. Abolghasem, M.R. Shankar, Effect of strain rate in severe plastic deformation on microstructure refinement and stored energies, Journal of Materials Research. 26 (2011) 395–406.

[243] F.C. Frank, On the equations of motion of crystal dislocations, Proceedings of the Physical Society. Section A. 62 (1949) 131.

[244] S. Yin, D.Y. Li, R. Bouchard, Effects of Strain Rate of Prior Deformation on Corrosion and Corrosive Wear of AISI 1045 Steel in a 3.5 Pct NaCl Solution, Metallurgical and Materials Transactions A. 38 (2007) 1032–1040.

[245] Y. Xu, L.-X. Hu, Y. Sun, Hot deformation behavior and microstructure evolution of as-cast AZ91D magnesium alloy without pre-homogenization treatment, Rare Metals. 32 (2013) 338–346.

[246] M. Wang, L. Huang, M. Chen, Y. Wang, Processing map and hot working mechanisms of Cu-Ag alloy in hot compression process, Journal of Central South University. 22 (2015) 821–828.

[247] J. Wang, P. Song, S. Huang, F. Pan, Effects of heat treatment on the morphology of long-period stacking ordered phase and the corresponding mechanical properties of Mg–9Gd–

xEr–1.6Zn–0.6Zr magnesium alloys, Materials Science and Engineering: A. 563 (2013) 36–45.

[248] E.O. Hall, The Deformation and Ageing of Mild Steel: III Discussion of Results, Proceedings of the Physical Society. Section B. 64 (1951) 747–753.

[249] N.J. Petch, The Cleavage Strength of Polycrystals, J. Iron Steel Inst. 174 (1953) 25 – 28.

[250] K. Hagihara, N. Yokotani, Y. Umakoshi, Plastic deformation behavior of Mg12YZn with 18R long-period stacking ordered structure, Intermetallics. 18 (2010) 267–276.

[251] E. Orawan, Nature. 149 (1942) 463.

[252] K. Hagihara, Y. Fukusumi, M. Yamasaki, T. Nakano, Y. Kawamura, Non-Basal Slip Systems Operative in $Mg_{12}ZnY$ Long-Period Stacking Ordered (LPSO) Phase with 18R and 14H Structures, Materials Transactions. 54 (2013) 693–697.

[253] G. Garcés, G. Requena, D. Tolnai, P. Pérez, P. Adeva, J.A. Jiménez, et al., Thermal expansion behaviour of Long-Period Stacking Ordered (LPSO) phase, Revista de Metalurgia. 51 (2015) e043.

[254] A.M. Korsunsky, A.I. Salimon, I. Pape, A.M. Polyakov, A.N. Fitch, Thermal expansion coefficient of mechanically alloyed Al-Cu-Fe quasicrystalline powders, Scripta Materialia. 44 (2001) 217–222.

[255] E. Zhang, W. He, H. Du, K. Yang, Microstructure, mechanical properties and corrosion properties of Mg-Zn-Y alloys with low Zn content, Materials Science and Engineering A. 488 (2008) 102–111.

[256] K. Ma, H. Wen, T. Hu, T.D. Topping, D. Isheim, D.N. Seidman, E.J. Lavernia, J.M. Schoenung, Mechanical behavior and strengthening mechanisms in ultrafine grain precipitation-strengthened aluminum alloy, Acta Materialia. 62 (2014) 141–155.

[257] N. Kumar, R.S. Mishra, Additivity of strengthening mechanisms in ultrafine grained Al-

Mg-Sc alloy, Materials Science and Engineering A. 580 (2013) 175–183.

[258] F. Mirza, D. Chen, A unified model for the prediction of yield strength in particulate-reinforced metal matrix nanocomposites, Materials. 8 (2015) 5138–5153.

[259] C.S. Kim, I. Sohn, M. Nezafati, J.B. Ferguson, B.F. Schultz, Z. Bajestani-Gohari, P. K. Rohatgi, K. Cho, Prediction models for the yield strength of particle-reinforced unimodal pure magnesium (Mg) metal matrix nanocomposites (MMNCs), Journal of Materials Science. 48 (2013) 4191–4204.

[260] N. Tahreen, D.F. Zhang, F.S. Pan, X.Q. Jiang, D.Y. Li, D.L. Chen, Microstructure and texture evolution in a yttrium-containing ZM31 alloy: effect of pre- and post-deformation annealing, Metallurgical and Materials Transactions B. (2015) 1–8.

[261] Z. Zhang, D.L. Chen, Contribution of Orowan strengthening effect in particulate-reinforced metal matrix nanocomposites, Materials Science and Engineering A. 483-484 (2008) 148–152.

[262] Z. Zhang, D.L. Chen, Consideration of Orowan strengthening effect in particulate-reinforced metal matrix nanocomposites: A model for predicting their yield strength, Scripta Materialia. 54 (2006) 1321–1326.

[263] F. Naghdi, R. Mahmudi, J.Y. Kang, H.S. Kim, Contributions of different strengthening mechanisms to the shear strength of an extruded Mg–4Zn–0.5Ca alloy, Philosophical Magazine. 95 (2015) 3452–3466.

[264] M. Yamasaki, K. Hashimoto, K. Hagihara, Y. Kawamura, Effect of multimodal microstructure evolution on mechanical properties of Mg-Zn-Y extruded alloy, Acta Materialia. 59 (2011) 3646–3658.

[265] L.H. Dai, Z. Ling, Y.L. Bai, Size-dependent inelastic behavior of particle-reinforced metal-matrix composites, Composites Science and Technology. 61 (2001) 1057–1063.

[266] K.S. Tun, M. Gupta, Improving mechanical properties of magnesium using nano-yttria reinforcement and microwave assisted powder metallurgy method, Composites Science and Technology. 67 (2007) 2657–2664.

[267] V.C. Nardone, K.M. Prewo, On the strength of discontinuous silicon carbide reinforced aluminum composites, Scripta Metallurgica. 20 (1986) 43–48.

[268] F.A. Mirza, D.L. Chen, An analytical model for predicting the yield strength of particulate-reinforced metal matrix nanocomposites with consideration of porosity, Nanoscience and Nanotechnology Letters. 4 (2012) 794–800.

[269] D. Seidman, E. Marquis, D. Dunand, Precipitation strengthening at ambient and elevated temperatures of heat-treatable Al (Sc) alloys, Acta Materialia. 50 (2002) 4021–4035.

[270] H. Wen, T.D. Topping, D. Isheim, D.N. Seidman, E.J. Lavernia, Strengthening mechanisms in a high-strength bulk nanostructured Cu-Zn-Al alloy processed via cryomilling and spark plasma sintering, Acta Materialia. 61 (2013) 2769–2782.

[271] C. Booth-Morrison, D.C. Dunand, D.N. Seidman, Coarsening resistance at 400°C of precipitation-strengthened Al-Zr-Sc-Er alloys, Acta Materialia. 59 (2011) 7029–7042.

[272] J.F. Nie, Effects of precipitate shape and orientation on dispersion strengthening in magnesium alloys, Scripta Materialia. 48 (2003) 1009–1015.

[273] W.Y. Wang, S.L. Shang, Y. Wang, K.A. Darling, L.J. Kecskes, S.N. Mathaudhu, X.D. Hui, Z.K. Liu, Electronic structures of long periodic stacking order structures in Mg: A first-principles study, Journal of Alloys and Compounds. 586 (2014) 656–662.

[274] M. Yamasaki, K. Hagihara, S.I. Inoue, J.P. Hadorn, Y. Kawamura, Crystallographic classification of kink bands in an extruded Mg-Zn-Y alloy using intragranular misorientation axis analysis, Acta Materialia. 61 (2013) 2065–2076.

[275] X. Zhao, L.L. Shi, J. Xu, Biodegradable Mg-Zn-Y alloys with long-period stacking ordered

structure: Optimization for mechanical properties, Journal of the Mechanical Behavior of Biomedical Materials. 18 (2013) 181–190.

[276] R.J. Arsenault, The strengthening of aluminum alloy 6061 by fiber and platelet silicon carbide, Materials Science and Engineering. 64 (1984) 171–181.

[277] C.S. Goh, J. Wei, L.C. Lee, M. Gupta, Properties and deformation behaviour of Mg-Y2O3 nanocomposites, Acta Materialia. 55 (2007) 5115–5121.

[278] P.J. Withers, T.W. Clyne, An Introduction to Metal Matrix Composites, Cambridge University Press, 1995.

[279] S.F. Hassan, K.S. Tun, M. Gupta, Effect of sintering techniques on the microstructure and tensile properties of nano-yttria particulates reinforced magnesium nanocomposites, Journal of Alloys and Compounds. 509 (2011) 4341–4347.

[280] N. Ramakrishnan, An analytical study on strengthening of particulate reinforced metal matrix composites, Acta Materialia. 44 (1996) 69–77.